An avalanche integrated risk approach : quantification of structural and human vulnerability and otpimisation of protection countermeasures

Philomène Favier

UNIVERSITÉ DE GRENOBLE

THÈSE

Pour obtenir le grade de

DOCTEUR DE L'UNIVERSITÉ DE GRENOBLE

Spécialité : **Sciences de la Terre, Univers et Environnement**

Arrêté ministériel : 7 août 2006

Présentée par

Philomène Favier

Thèse dirigée par **Mohamed Naaim**
et co-encadrée par **David Bertrand et Nicolas Eckert**

préparée au sein **de l'IRSTEA Grenoble et de l'INSA Lyon**
et de **l'école doctorale « Terre - Univers - Environnement »**

Une approche intégrée du risque avalanche : quantification de la vulnérabilité physique et humaine et optimisation des structures de protection.

Thèse soutenue publiquement le **13 octobre 2014**,
devant le jury composé de :

Mme Clémentine Prieur
HDR, Professeur Université de Grenoble, Examinatrice
M. Bruno Sudret
HDR, Professeur ETHZ, Rapporteur
M. Thierry Verdel
HDR, Professeur École des Mines de Nancy, Rapporteur
M. Éric Parent
HDR, ICPEF, Professeur AgroParisTech, Président
M. Alberto Pasanisi
HDR, Chef de Projet EDF R&D, Examinateur
M. Mohamed Naaim
HDR, Directeur de recherche, IRSTEA Grenoble, Directeur de thèse
M. David Bertrand
Dr., Maître de conférences, INSA Lyon, Co-Encadrant de thèse
M. Nicolas Eckert
Dr., ICPEF, IRSTEA Grenoble, Co-Encadrant de thèse

Abstract

Long term avalanche risk quantification for mapping and the design of defense structures is done in most countries on the basis of high magnitude events. Such return period/level approaches, purely hazard-oriented, do not consider elements at risk (buildings, people inside, etc.) explicitly, and neglect possible budgetary constraints. To overcome these limitations, risk based zoning methods and cost-benefit analyses have emerged recently. They combine the hazard distribution and vulnerability relations for the elements at risk. Hence, the systematic vulnerability assessment of buildings can lead to better quantify the risk in avalanche paths. However, in practice, available vulnerability relations remain mostly limited to scarce empirical estimates derived from the analysis of a few catastrophic events. Besides, existing risk-based methods remain computationally intensive, and based on discussable assumptions regarding hazard modelling (choice of few scenarios, little consideration of extreme values, etc.). In this thesis, we tackle these problems by building reliability-based fragility relations to snow avalanches for several building types and people inside them, and incorporating these relations in a risk quantification and defense structure optimal design framework. So, we enrich the avalanche vulnerability and risk toolboxes with approaches of various complexity, usable in practice in different conditions, depending on the case study and on the time available to conduct the study. The developments made are detailed in four papers/chapters.

In paper one, we derive fragility curves associated to different limit states for various reinforced concrete (RC) buildings loaded by an avalanche-like uniform pressure. Numerical methods to describe the RC behaviour consist in civil engineering abacus and a yield line theory model, to make the computations as fast as possible. Different uncertainty propagation techniques enable to quantify fragility relations linking pressure to failure probabilities, study the weight of the different parameters and the different assumptions regarding the probabilistic modelling of the joint input distribution. In paper two, the approach is extended to more complex numerical building models, namely a mass-spring and a finite elements one. Hence, much more realistic descriptions of RC walls are obtained, which are useful for complex case studies for which detailed investigations are required. However, the idea is still to derive fragility curves with the simpler, faster to run, but well validated mass-spring model, in a "physically-based meta-modelling" spirit. In paper three, we have various fragility relations for RC buildings at hand, thus we propose new relations relating death probability of people inside them to avalanche load. Second, these two sets of fragility curves for buildings and human are exploited in a comprehensive risk sensitivity analysis. By this way, we highlight the gap that can exist between return period based zoning methods and acceptable risk thresholds. We also show the higher robustness to vulnerability relations of optimal design approaches on a typical dam design case. In paper four, we propose simplified analytical risk formulas based on extreme value statistics to quantify risk and perform the optimal design of an avalanche dam in an efficient way. A sensitivity study is conducted to assess the influence of the chosen statistical distributions and flow-obstacle interaction law, highlighting the need for precise risk evaluations to well characterise the tail behaviour of extreme runouts and the predominant patterns in avalanche - structure interactions.

Remerciements

J'ai vécu milles choses pendant ma thèse, de la surprise, de l'incompréhension, des questionnements, des réussites, des échecs, des réponses, des doutes, des résultats et je serais encore perdue dans ces atermoiements sans le concours précieux de plusieurs personnes. Mes premières pensées vont d'abord vers mes encadrants. Je souhaite remercier Mohamed Naaim, Mo, mon directeur de thèse pour son optimisme et sa bienveillance sur mes travaux. Il me semble avoir sollicité mes encadrants Nicolas Eckert et David Bertrand plus que de raison ! Merci Nico pour ton exigence scientifique, tes corrections qui m'ont donné du fil à retorde mais qui étaient tellement nécessaires pour m'améliorer. Merci pour ta sympathie, ta présence et prévenance en toute épreuve. Merci David pour m'avoir initié au génie civil et plus concrètement au comportement du béton armé, pour ton enthousiasme envers mon travail, ta disponibilité sans faille et la sympathie que tu m'as accordée.

Merci à mon jury de thèse qui a consacré un temps précieux à la lecture de mon manuscrit et à ma soutenance. Merci à Eric Parent d'avoir présidé mon jury: c'était un honneur pour moi. Merci à messieurs Bruno Sudret et Thierry Verdel d'avoir relu ma thèse, pour les interrogations qu'ils ont relevé sur le manuscrit et l'intérêt qu'ils ont manifesté pour mon travail. Merci à Clémentine Prieur et Alberto Pasinisi d'avoir été examinateurs de ma thèse et pour leurs questions lors de ma soutenance.

Merci à mon école doctorale d'avoir suivi mon travail et à Christine pour l'appui administratif et les encouragements ! Je souhaite remercier toutes les personnes qui ont participé aux bon déroulement administratif de ma thèse : le personnel à Irstea (Corinne, Martine, Alexandra, Thomas, Élodie, Séverine, Valérie ...) et les chefs d'équipe, j'ai apprécié effectuer ma thèse avec Didier en chef d'unité (tes qualités humaines m'ont aidé et merci pour la bière à mon nom) et Florence en chef d'équipe. Les réunions scientifiques avec mon comité et les chercheurs du projet MOPERA ont toujours été enrichissantes et m'ont toujours données un élan, de nouvelles idées, de nouvelles questions: merci donc à Lilliane Bel, Delphine Granger, Ophélie Guin, Mickaël Brun, Vincent Jomelli, Chris Keylock, Frédéric Leone, Philippe Naveau, Eric Parent et mes encadrants.

Je n'oublie pas les doctorants avec qui j'ai partagé de chouettes moments, coups à boire, "geekeries" en tout genre, conférences ou sessions escalade, jardin...: il y a les "vieux doctorants of the dark corridor" (Adeline, Joshua, Paolo, Nejib, Johan), mes contemporains de thèse (Nico, Sandrine, Mathieu, Popo, Amandine, Antoine) et les petits jeunes (Coraline, Pascal, Gaëtan, Raphaël). Merci Isa pour avoir partagé ton bureau avec moi, pour nos discussions qui permettaient de faire avancer la réflexion sur nos sujets de thèse bien proches, pour ta gentillesse et disponibilité envers moi ! Merci en général aux collègues pour m'avoir appris plein de choses techniques, ludiques et scientifiques (Merci Hervé de m'avoir fait découvrir l'instrumentation d'un couloir avalancheux ou la métrologie du Col du Lac Blanc pour étudier la neige soufflée, Xav pour le déclenchement et le ski de rando). Merci aux collègues du labo Fred et Christian. Faire partie de l'association Aski a été une chouette expérience. Je garde tout particulièrement en mémoire les ateliers chocolat de Nicolle et ses minis Paris-Brest lors de ma thèse ; merci Nicolle pour ta générosité et sympathie. Merci à Stéphane, Renaud, Sophie, Dédé, Gillou, Evgeny et tous ceux avec qui j'ai pu

partagé le quotidien à l'Irstea avec le sourire. Je vous souhaite plein de réussites tant professionnelles que personnelles, j'ai beaucoup apprécié le cadeau et vos aides le jour de ma soutenance. Le bouquin photo avec vos touchants messages est simplement génial.

Enfin, je pense à tous mes amis qui m'ont supporté pendant ces années, avec qui j'ai fait de superbes sorties montagnes et/ou de longues et joyeuses soirées, toute cette période a été plus colorée grâce à vous ! Merci à ma famille et belle-famille pour leur soutien, leur bienveillance et leur aide pour le super pot ! Je pense bien fort à Marie, Charlo et Mamoune. Enfin une montagne de merci à toi Flo pour tes encouragements, ton infinie patience, l'équilibre et la joie que tu m'apportes quotidiennement.

Je dédie cette thèse à mamy Suzy, qui se disait paysanne et qui me surestimait affectueusement.

Contents

CHAPTER 1

Introduction

1.1 Casualties due to snow avalanches

Snow avalanches threaten mountain communities and are, at fine spatio-temporal scales, fairly unpredictable. Several winters of the last decades remain in the collective memory as having been very lethal or destructive in mountain valleys. For instance, the Val d'Isère avalanche in February 1970, which has initiated in France a real policy of recognition of avalanche risk at the state level, killed 39 people. Similarly, February 1999 was a black month in Alpine countries: 12 people died in dwellings in Evolène (Switzerland), 38 people were buried in Galtür and Valzür ski resorts (Austria) and 12 people passed away in chalets due to the Péclerey avalanche in Montroc (France) (Ancey et al., 2000).

More recently, a remarkable avalanche cycle occurred in December 2008 in the Southern French Alps (Queyras and Mercantour, France). Several people were buried without any death, but few buildings were partially destroyed and ski resorts isolations, ski lifts and forests damages were reported (Eckert et al., 2010b). Extreme avalanches exceeding the limits of the official avalanche map were also observed in the Piedmont Region in Italy (Maggioni et al., 2009). Also, casualties are recorded every year among back country skiers (Jarry, 2011). All in all, in France, avalanches kill an average of 30 people per year.

Not only do avalanches injure and kill people but they also cost to population and local authorities. As shown in catastrophic events causing materials damages, the decision to protect and at which extent is a difficult question. Decision makers have to determine the protective measures that conjugate safety and economy for populations. Decisions can affect various elements at risk such as ski resorts, buildings and communication axes. For instance, ski resorts can be partially closed due to avalanche risk or avalanche damages. For example, the recent impressive avalanche in Saint-François-Longchamp ski resort nearly destroyed a ski chairlift and the decision was taken to protect the ski tracks with stabilization devices ($260k€$). These were assessed as being less expensive than the damages due to a new potential avalanche ($360k€$) (Roudnitska, 2013).

However, cost-benefit approaches are not as simple to apply to complex systems as to single elements at risk. The example of road closure is relevant. For instance, the access road to the Mont-Blanc tunnel is an important international axe and its closure can cost a lot to French and Italian companies and, more widely, to different actors. At a more local scale, some ski resorts, such as for instance Isola 2000 whose access road often suffers from cut offs, are regularly isolated, inducing consequences difficult to evaluate as a whole. For buildings, economic losses are calculated according to insurance payments due to damages, and to the costs of rescuing and rebuilding (Johannesson and Arnalds, 2001; Fuchs and Bründl, 2005). For the 1998-99 winter, the SLF institute in Davos estimated the material damages in the whole Alpine area to about 1 billion Euros.

1.2 Avalanche risk management

1.2.1 Short term risk versus long term risk

Short-term risk quantification deals with the estimation of avalanche activity at a short temporal horizon (1-5 days). Mainly used by mountain practitioners, short-term risk quantification consists in providing a 1 to 5 index revealing the daily risk of avalanche triggering. Short-term risk quantification is deduced according to meteorological and physical observations and modelling of the snow. Short term risk quantification is not in the scope of this work. In contrast, long term risk quantification aims at providing tools to decision makers in order to manage land use planning and optimize permanent mitigation measures such as defense structures construction. This is what we deal with in this thesis.

1.2.2 From long term risk mapping to risk zoning

Local authorities in charge of population safety are in front of an intricate situation. To manage this natural threat and ensure the most adequate decision making for stake holders, risk to people exposed to snow avalanches must be well quantified. Beyond this human aspect, economical, environmental and cultural issues must also be taken into account. Buildings (hotels, industries, shopping centres, schools, hospitals, places of worship ...) have to be preserved to ensure a socio-economic activity in mountain valleys. On the other hand, land use spread due to increasing area devoted to urbanisation, see for instance the time evolution of urban sprawl in Bessans (Savoie, France) (Fig. 1.1), encourages the development of more accurate risk quantification tools.

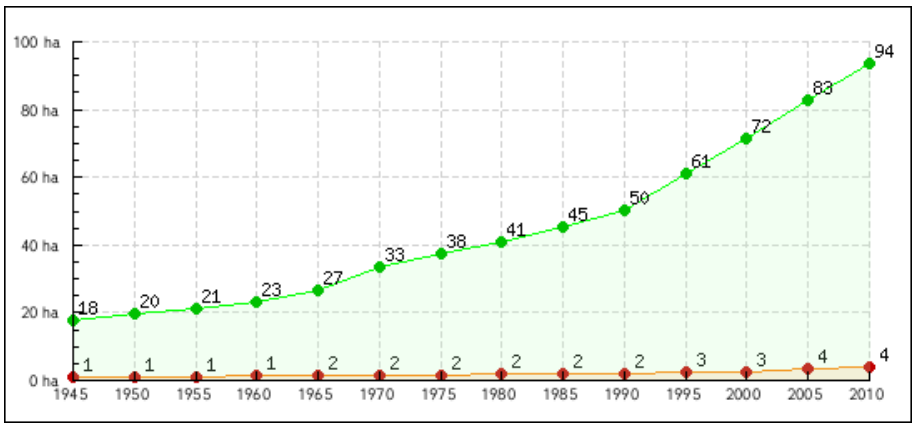

Figure 1.1 – Cumulative evolution of urban sprawl (•), that is to say urbanised area (whatever its use: residential, economic, transport infrastructure), and built surfaces (•) from 1945 to 2010 in Bessans township. Source by: `http://www.observatoire.savoie.equipement-agriculture.gouv.fr`

Current approaches are using the estimation of return periods to delineate land use planning zones. The decision maker needs to define three zones: the red zone corresponds to an interdiction of new constructions, the blue zone corresponds to zones with regulated new constructions subjected to requirements and recommendations (*e.g.* structures resisting to a 30 kPa pressure, no opening in the wall facing the flow, etc.) and the white zone is defined as the zone with no restriction (Givry and Perfettini, 2004). To do so, generally, only high magnitude events are used, defined on the basis of typical return period calculations. A search for normalisation and equal exposition against risk at the European scale has been attempted, but a large diversity of legal thresholds between countries is still observed: 100-year in France, 30- and 300-year in Switzerland, 30- to 100-year depending on regions in Italy (Maggioni et al., 2006), 150-year in Austria and 1000-year in Norway. Arnalds et al. (2004) underlined the original individual risk approach adopted in Iceland in 2000 as a new regulation tool for avalanche hazard zoning, using the estimation of avalanche frequency, runout distribution but also vulnerability of people inside buildings.

In France, in practice, hazard maps are first proposed by avalanche expert (Fig. 1.2(a)) ; then, on this basis, a PPR (Risk Prevention Plan) zoning defining potential interdictions and prescriptions is defined (Fig. 1.2(b)). Hazard assessment to determine potential pressures and runouts includes various steps like analysis of historical data, terrain analysis, analysis of aerial photos, modelling, expert judgement, etc. but no official methodological guide actually exists to systematize the calculation of references avalanches. Besides, in existing methods, no standardised way to take consistently the elements at risk into account, for example by performing cost benefit analyses, is yet available (except in some ways in the Icelandic example).

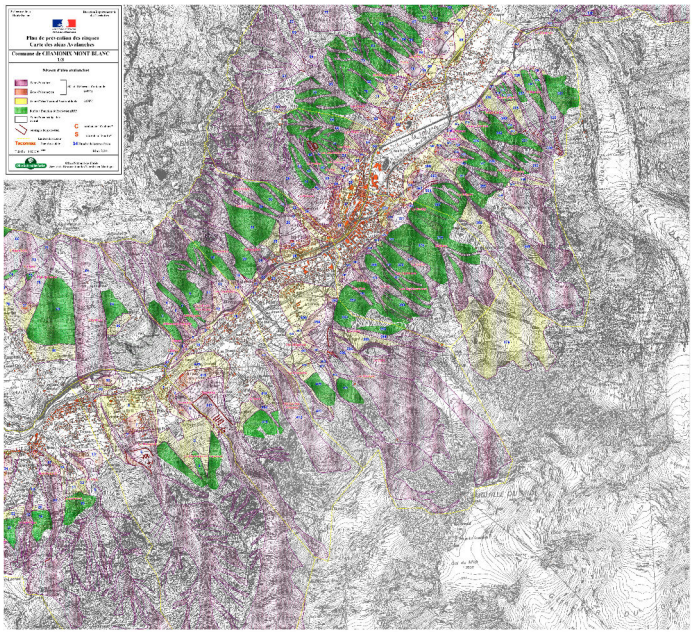

(a) Example of hazard maps.

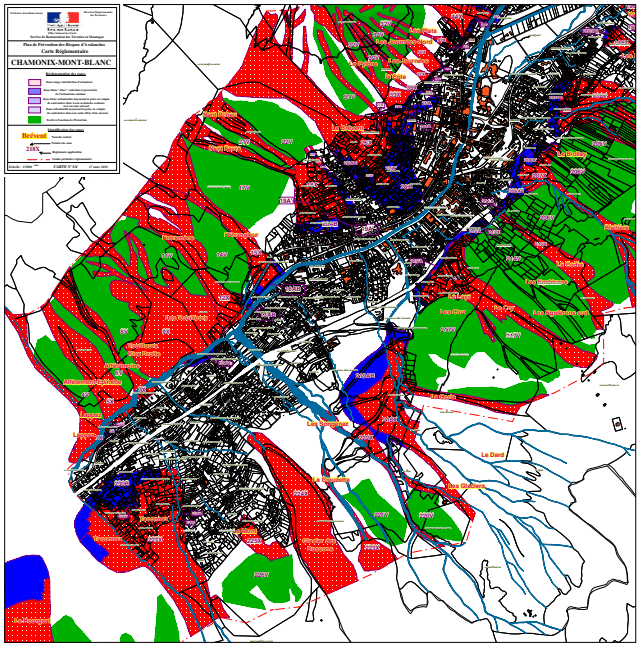

(b) Example of PPR.

Figure 1.2 – Maps concerning the Chamonix valley, Haute-Savoie, France. Source by: `www.haute-savoie.gouv.fr/Politiques-publiques/Environnement-risques-naturels-et-technologiques/Prevention-des-risques-naturels`

1.2.3 Snow avalanche protection

Avalanche protections can be sorted into different types, depending on their action. When the protection prevents the avalanche from triggering in the release area, it is called active protection ; in contrast, when the protection slows down or stops the avalanche once it is triggered, it is called a passive protection. Such protections devices can be temporarily or permanently installed (Tab. 1.1).

Table 1.1 – Usual classification of countermeasures protection against snow avalanches.

	Temporary	Permanent
Passive	warning, closure (road avalanche detector), evacuation plans	deflecting dams, breaking mounds, catching dams, buildings reinforcement, hazard zoning
Active	artificial release (explosive or gas), snow grooming	snow sheds (galleries or tunnels), steel snow bridges, snow nets, terraces, silvicultural measures

Permanent passive structures are under interest for long term land use planning in avalanche prone areas. Historically made according to empirical observations or according to expert knowledge, defence structures design is now gaining interest in the scientific community. The influence of their size and shape on the flow intensity reduction was studied in small scale laboratory experiments and on full-scale experimental sites (Faug et al., 2008; Caccamo, 2012). To better understand their behaviour and improve future design, some researches aim at well determining their dynamical response against avalanches (Berthet-Rambaud et al., 2008; Ousset et al., 2014). Beyond these mechanical questions, optimal design approaches were developed based on a cost-benefit analyse taking into account uncertainty sources within a Bayesian framework (Eckert et al., 2008a, 2009). This approach allows performing the design within the risk evaluation using decision theory.

1.3 Sub-models for risk calculation

As previously explained, current risk approaches rely, for most of them, on incomplete calculations of risk by only considering hazard description. In this section, we will see how to treat elements at risk *via* vulnerability/fragility curves. Second, monovariate (runouts) and multivariate (runout/pressure) snow avalanche models are briefly exposed. Risk quantification as an expected damage will not be introduced here since it is described in the

chapters of the thesis where risk calculation is needed. Furthermore, a detailed presentation of the framework can be found in the review from Eckert et al. (2012) presented in appendix B of the thesis and to which I collaborated at the beginning of my PhD.

1.3.1 Vulnerability assessment and vulnerability/fragility distinction

The need for assessing the vulnerability of elements at risk against avalanches was recently highlighted and is now kept under close research interests. For example, the Irasmos (Integral Risk Management of Extremely Rapid Mass Movements) project was interested in rock avalanches, debris flows, and snow avalanches. Review and development of vulnerability relations was one of the outcome of the project. In that context, Naaim et al. (2008a) made efforts to express available vulnerability curves in a single pressure intensity unit (Fig. 1.3(a)). More recently, Bertrand et al. (2010) obtained some vulnerability relations for reinforced concrete structures impacted by snow avalanches using a displacement-based damage index and a parametric study to investigate the damage domain of a reinforced structure (Fig. 1.3(b)).

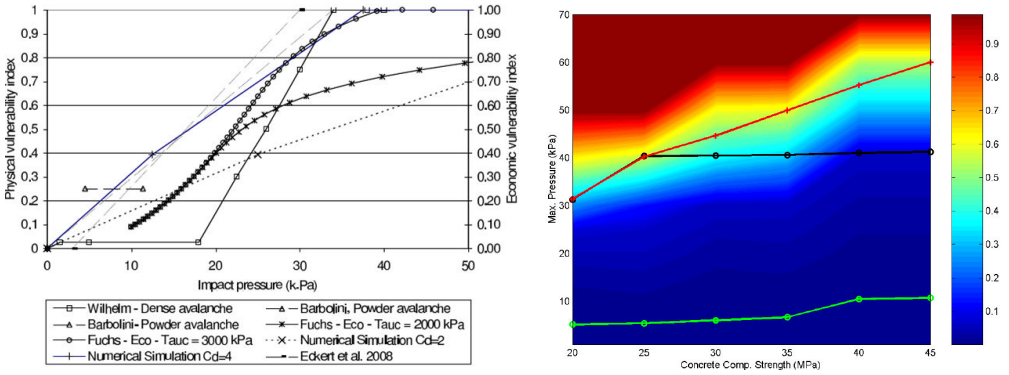

(a) (b)

Figure 1.3 – Example of vulnerability relations: (a) vulnerability curves reviewed in the Irasmos project (Naaim et al., 2008a), (b) vulnerability function according to a displacement damage index obtained for several values of maximum compressive strength of concrete (Bertrand et al., 2010).

Fragility curves are increasing curves providing a $[0, 1]$ failure probability according to a solicitation magnitude of the studied natural hazard. Vulnerability and fragility curves have different definitions. A vulnerability curve provides a damage index conditionally to an intensity value: for instance, Bertrand et al. (2010) expressed a displacement ratio, that is to say, the ratio between the displacement at a given pressure and the ultimate

displacement the structure can tolerate ; others expressed the damage index as the ratio between a reparation cost and the cost of the building (Fuchs et al., 2007a). Fragility curves express a failure probability, *i.e.* a structural limit state exceedence probability, for a given applied pressure.

Today, vulnerability curves exist in several natural hazard engineering domains, but few were obtained with reliability approaches. Examples can be found for rockfalls impacts (Mavrouli and Corominas, 2010a), landslides or debris-flows (Papathoma-Köhle et al., 2012). Seismic engineering vulnerability research figures as exception, since structural reliability studies have been numerous in this field (Ellingwood, 2001; Li and Ellingwood, 2007; Lagaros, 2008; Sudret et al., 2014).

Structural reliability studies of complex structures consist in covering a range of steps from the civil engineering model choice to the statistical treatment of the system. First, the whole complex system is simplified to a single structural element which failure behaviour represents the failure of the whole system. Second, a numerical method to simulate the structure is chosen (analytical approach, Finite Element Analysis, etc.). Third, a failure criterion needs to be established in order to define a damage or a limit state for the structure. Fourth, uncertainties on the inputs of the numerical model have to be considered and modelled by PDF distributions. Finally, two ways for assessing fragility curve can be followed: i) for each hazard intensity, the failure probability is calculated and the fragility curve is discretely built, ii) the resistance (or capacity) of the system is known as the numerical output and the fragility curve is the CDF distribution of the capacity of the studied element. To carry out uncertainty propagation and evaluate the failure probability, Lemaire (2005) gives an overview of current commonly used reliability methods.

In avalanche engineering, such methods have been seldomly used and mostly for the detailed study of reinforced concrete structures, but not to build fragility curves (Kyung and Rosowsky, 2006; Daudon et al., 2013). Note by the way that reinforced concrete is one of the most common construction materials that can be found in moutanious areas ; others are masonries, steel structures or framed buildings. Reinforced concrete is widely used for snow avalanche protection measures (Berthet-Rambaud et al., 2007; Nicot, 2010).

1.3.2 Avalanche models

To better understand avalanche extension, runout distance distribution models have long attracted widespread attention. However, to build risk maps, other quantities are required, mainly pressure fields. Whereas runouts and flow depths can be obtained as direct outputs of avalanche model runs, the derivation of pressure fields requires an additional step.

Three classes of avalanche models

Some statistical approaches, namely the alpha-beta and runout ratio methods use topographical considerations (the typical local slope characteristics) to predetermine avalanche runout positions (Lied and Bakkehoi, 1980; McClung and Lied, 1987), sometimes with explicit references to extreme value theory (Keylock, 2005). Research is still active at a more regional scale (Lavigne, 2013) or in a cross validation perspective (Schläppy et al., 2014).

Statistical approaches have long been opposed to fully deterministic hydraulic-based models. The latters are based on the resolution of hydraulic equations in the framework of continuum mechanics (Savage and Hutter, 1989). The snow avalanche can be considered and modelled as a multilayer flow (Issler, 1997; Naaim, 1998), but, for practical needs, only the dense layer is generally taken into account when modelling (Bartelt et al., 1999). Nowadays, in practice, for deterministic flow modelling, two approaches prevail (Ancey, 2006): the snow avalanche can be considered as a sliding block subjected to a basal friction or can be treated with Saint-Venant equations. Both remain dependant on the choice of rheological friction laws.

To take advantage of numerical hydraulic models developments, statistical-mechanical models are gaining popularity among the avalanche scientists community (Bozhinskiy et al., 2001; Barbolini and Keylock, 2002). This consists in picking up the inputs of deterministic models in statistical distributions. The joint distribution of outputs under interests such as the velocity of the flow or its depth is then obtained. In such studies, Monte Carlo simulations are the predominant method. Last improvements used Bayesian framework to better assess uncertainties in input distributions (Eckert et al., 2007a, 2010c).

Pressure derivation

For the design of defense structures, the dense part of the flow is more crucial as it represents the greatest threat in terms of potential damage due to its high density ($\rho \approx 200-500\ kg.m^{-3}$). The medium velocity of a dense avalanche is around $40\ m.s^{-1}$. Typical dense avalanche deposits can be observed in figure 1.4 threatening back country skiers (a) and exposed buildings (c). Snow avalanche velocities are direct output quantities of avalanche dynamical models. Meanwhile, mechanical structural models need pressure-like inputs expressed in Pascal to determine a wall failure. This paragraph is devoted to the question of pressure derivation.

Several field (Gauer et al., 2007; Sovilla et al., 2008b) or laboratory (Caccamo et al., 2012) experiments have been conducted to assess the avalanche pressure on an obstacle. The col du Lautaret site (Fig. 1.4(b)) and the instrumented mounds in the Taconnaz avalanches path (Ravanat et al., 2012; Bellot et al., 2013) enabled to obtain relevant field data (Thibert et al., 2008; Baroudi and Thibert, 2009). A spatio-temporal variation of the

(a) (b) (c)

Figure 1.4 – Dense avalanches: (a) near a back country skier in the Briançonnais, Écrins, Hautes-alpes, (b) deposit of a dense avalanche in the Irstea experimental site of col du Lautaret, (c) avalanche that occurred after a warming period in january 1980, the Eymendras chalet was destroyed in Le Sappey-en-Chartreuse, Isère (Valla, F.).

avalanche pressure signal is observed (Schaer and Issler, 2001) but, for convenience, it is often assumed that the pressure is uniformly loading the structure and that the maximum pressure over all the loading time is the main relevant feature of the avalanche intensity.

Apart from on-the-field data, numerical models provide velocities. As already explained, avalanche impact pressure is an important data to know when considering obstacle/flow interactions. We want here to know what are the possible relations linking the velocity to the applied pressure on an obstacle. The dynamic pressure in a free surface flow is defined as ρV^2. For a free surface flow, the impact pressure can be expressed as:

$$Pr = C_x \frac{1}{2} \rho v^2 \ , \tag{1.1}$$

where C_x is the total drag coefficient, ρ is the fluid density and v is the flow velocity. The drag coefficient expresses the size and shape of the impacted obstacle considered. For obstacles small enough, the drag coefficient is equal to 2. This calculation is the most common engineering approach but it is admitted that the dynamical pressure is then under-estimated. Thus, the drag coefficient C_x can be expressed according to the empirical formulation of Sovilla et al. (2008a) or the semi-empirical formulation of Naaim et al. (2008b) considering the Reynolds number, the Froude number, the lateral dimension of the obstacle and the flow height of the snow avalanche as additional control parameters.

1.4 Aim of this work and lecture grid

1.4.1 Overview of the work

Grounding on this overview of methods and models potentially usable in snow avalanche risk quantification, we aim in this thesis at addressing the long term risk assessment problem by combining reliability-based fragility curves together with integrated risk assessment. The work done is fully numerical and consists in mixing civil engineering models together within statistical and combined statistical-numerical avalanche models with a common framework. The thesis core is made of 4 chapters, each chapter is intended to be a self-containing journal published article. For instance, the first chapter has been published in *Natural Hazard and Earth System Sciences*, the third is accepted in *Cold Regions Science and Technology*. The two others are not yet submitted but will be soon. The thesis addresses two aspects of the risk analysis: the vulnerability which is treated in the chapters 2-3 and the risk quantification and sensitivity which is tackled in the chapters 4-5. Chapter 6 is a brief general conclusion. My contribution to the four articles consists in all technical developments, and the major part of the writing. As usual, my co-authors/PhD supervisors had a close look on the work and helped me organise and smooth the ideas and the writing.

1.4.2 Chapters content

In Chapter 2, we derive systematic fragility curves associated to different limit states for various reinforced concrete (RC) buildings loaded by an avalanche-like uniform pressure. The work aimed at building fragility curves according to different technologies depending on their boundary conditions. Four limit states were taken into account. Thanks to simple mechanical resolution *via* basic civil engineering abacus and a yield line theory model, we succeed in obtaining a spectrum of forty fragility relations using Monte Carlo simulations. We took advantage of various inputs distributions (normal, log-normal, correlated or not, etc.) to weight the effects of different choices on the fragility curves determination (Sobol indices and a quantitative comparison).

In Chapter 3, we focus on more refined mechanical models for the behaviour of RC walls. We developed a mass-spring model validated according to a finite element model and to limit analysis. The mass-spring model can be seen as a meta-model of the more complex model based on finite element theory. The non-linearities of the materials can well be taken into account and mechanical justifications ensure to stay close to physical reality. One wall was tested, and fragility curves were obtained considering various statistical distributions as inputs. Due to important computation times, we choose methods alternative to the standard Monte Carlo sampling picked up in the reliability toolbox to evaluate fragility

curves.

In Chapter 4, to take advantage of the vulnerability curves set of chapter 2, human fragility curves are proposed, based on the state of the building. Risk was then calculated considering successively human and buildings fragility curves. For various abscissas in the path, risk values obtained are compared to acceptable risk thresholds showing the limits of classical return period based zoning method. A sensitivity index is calculated to understand the influence of the fragility curves on the risk quantification. An optimal design calculation is done on a simple case.

In Chapter 5, an analytical expression of the risk is proposed based on extreme value statistics. More particularly, a generalized Pareto distribution (GPD) is used. The analytical expression guarantees a fast calculation for the risk and the optimal design of a dam. The goal was first to assess the influence of the statistical distributions. Then, two flow-obstacle interaction laws were tested to quantify how the patterns occurring when the avalanche hits an obstacle affect the risk calculation. A sensitivity index is built and shows that the GPD input distribution choice is more influential on the risk than the interaction law choice.

In Chapter 6, we remind the main results and conclusions of the thesis, and we propose perspectives to pursue this work.

CHAPTER 2

A reliability assessment of physical vulnerability of reinforced concrete walls loaded by snow avalanches

Le contenu de ce chapitre a été publié dans *Natural Hazard and Earth System Sciences*, la citation est : Favier, P., Bertrand, D., Eckert, N., and Naaim, M. (2014). A reliability assessment of physical vulnerability of reinforced concrete walls loaded by snow avalanches. *Nat. Hazards Earth Syst. Sci.*, 14:689–704.

Les auteurs souhaitent alerter le lecteur sur le fait que les courbes de fragilité développées dans ce chapitre ne doivent pas être utilisées pour tout type de bâtiments en béton armé mais pour ceux répondant aux même caractéristiques structurelles que celles énoncées et se trouvant dans la gamme des paramètres matériaux et géométriques balayée par les distributions statistiques choisies dans ce chapitre.

Abstract

Snow avalanches are a threat to many kinds of elements (human beings, communication axes, structures, etc.) in mountain regions. For risk evaluation, the vulnerability assessment of civil engineering structures such as buildings and dwellings exposed to avalanches still needs to be improved. This paper presents an approach to determine the fragility curves associated with reinforced concrete (RC) structures loaded by typical avalanche pressures and provides quantitative results for different geometrical configurations. First, several mechanical limit states of the RC wall are defined using classical engineering approaches (Eurocode 2), and the pressure of structure collapse is calculated from the usual yield line theory. Next, the fragility curve is evaluated as a function of avalanche loading using a Monte Carlo approach, and sensitivity studies (Sobol indices) are conducted to estimate the respective weight of the RC wall model inputs. Finally, fragility curves and relevant indicators such a their mean and fragility range are proposed for the different structure boundary conditions analyzed. The influence of the input distributions on the fragility curves is investigated. This shows the wider fragility range and/or the slight shift in the median that has to be considered when a possible slight change in mean/standard deviation/inter-variable correlation and/or the non-Gaussian nature of the input distributions is accounted for.

2.1 Introduction

The increasing urban development in mountainous areas means that issues associated with rockfalls, landslides and avalanches need to be addressed (Naaim et al., 2010). Prospective human casualties and physical civil engineering structures damages are of concern for snow avalanche risk management. Depending on the external loading applied to the structure, that is to say the natural hazard considered (rockfall, landslide, earthquake, etc.), the physical vulnerability of civil engineering structures is usually assessed differently depending on the nature of the failure modes involved. If a relevant failure criterion is defined that represents the overall damage level of the structure, the potential failure of the system can be assessed and even its failure probability if the calculations are performed within a stochastic framework.

Avalanche risk mapping is often carried out by combining probabilistic avalanche hazard quantification (*e.g.*, Keylock, 2005; Eckert et al., 2010c) and vulnerability (deterministic framework) or fragility (probabilistic framework) relations to assess individual risk for people (Arnalds et al., 2004) and buildings (Cappabianca et al., 2008). For instance, the Bayesian framework (Eckert et al., 2009, 2008a; Pasanisi et al., 2012) makes it possible to take into account uncertainties in the statistical modeling assumptions and data availability. On the other hand, a better definition of vulnerability or fragility relations remains a challenge for the improvement of the integrated framework of avalanche risk assessment (Eckert et al., 2012).

A review of vulnerability approaches for alpine hazards (Papathoma-Köhle et al., 2011) mentioned various studies conducted to derive vulnerability relations. Several definitions have been proposed. One point of view is to define the vulnerability of a structure by its economic cost and not its physical damage (Fuchs et al., 2007a), which necessitates an expression for the recovery cost (Mavrouli and Corominas, 2010a). Another point of view suggests that human survival probability inside a building is commonly related to the vulnerability of the building itself by empirical relations (Jónasson et al., 1999; Barbolini et al., 2004a). For instance, Wilhelm (1998) introduced thresholds to build vulnerability relations for five different construction types impacted by snow avalanches, and Keylock and Barbolini (2001) proposed relating the vulnerability of buildings with their position in the avalanche path. More recently, Bertrand et al. (2010) suggested using a deterministic numerical simulation to assess the structural failure susceptibility of reinforced concrete (RC) structures.

To describe the failure probability of civil engineering structures exposed to snow avalanches and thus derive fragility curves, reliability approaches can be considered. For instance, in earthquake engineering (Ellingwood, 2001; Li and Ellingwood, 2007; Lagaros, 2008) or for RC structures subjected to blast loading (Low and Hao, 2001), the latter technique is often used. In hydraulic risk research, some studies focus on assessing dam safety using reliability methods (Peyras et al., 2012). Direct simulations (such as Monte Carlo methods) give robust results but can be time-consuming. As an alternative, simulation-based or surface approximation methods are used to avoid the direct calculation of the failure probability (Lemaire, 2005), but convergence of the algorithm can be cumbersome.

In the snow avalanche context, vulnerability relations are often derived from back-analyzed in situ data, which are often very scarce. These relations give the fraction of destroyed buildings as a function of the avalanche loading. A reliability assessment of vulnerability relations (fragility curve derivation) is therefore a useful complementary tool for examining the interaction between the avalanche and the structures at different scales (avalanche path, urban area, individual house, etc.). This paper attempts to improve risk evaluations by proposing an innovative way to derive refined fragility curves that can be used in snow avalanche engineering.

As RC is the most usual material used to build structures exposed to potential avalanche loadings, herein we focus on this technology. First of all, the RC structure is described. Secondly, the mechanical model of the RC wall and the snow avalanche loading description are exposed. Then, the damage level definitions opted for in the structure limit state description are presented. The next part deals with statistical distributions of the inputs of the deterministic mechanical model. Finally, fragility curves are derived and their sensitivity to input parameters, modeling assumptions and failure criterion are discussed.

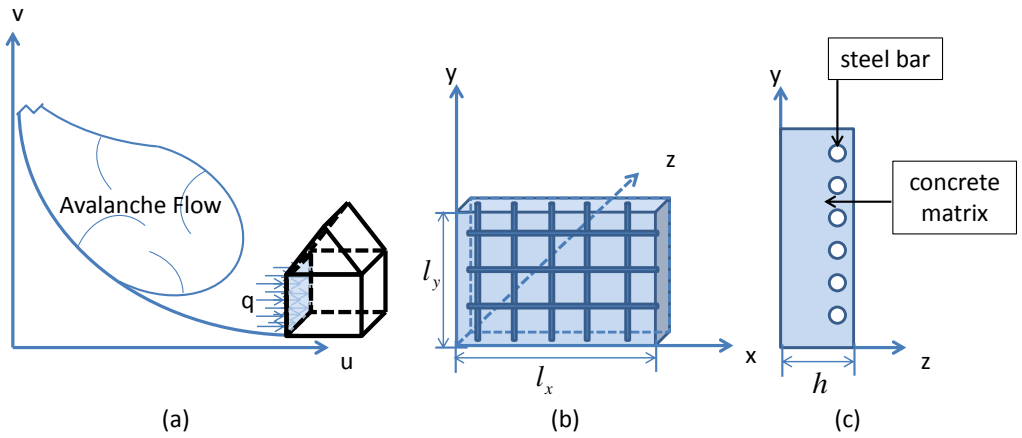

Figure 2.1 – Dwelling house impacted by a snow avalanche: loading applied onto the structure **(a)**; RC wall geometry and orthogonally distributed reinforcement **(b–c)**.

2.2 Methods

To protect people against snow avalanches, French legal hazard zoning defines three regions, which correspond to several levels of danger. The white zone corresponds to the geographic zone where the consequences of an avalanche in terms of structural damage have been estimated negligible. Hence, no specific recommendations related to the ability of the structure to resist to an avalanche are needed. In the red zone, the avalanche return period has been estimated less than 100 yr and thus no construction is allowed. In the last zone (blue zone), civil engineering structures, such as buildings or houses, can be built only within certain restrictions. For the wall facing the avalanche, no opening is allowed and the wall has to resist at least a pressure of 30 kPa. Several technologies are available. As mentioned by Givry and Perfettini (2004), the most common are wooden, masonry, RC or mixed structures. RC technology appears to provide the best value for money. Moreover, RC is usually the most frequently encountered material for such structures and in particular for dwelling houses. The most vulnerable part of a structure built in an avalanche path is the wall facing the flow (Fig. 2.1). Thus, the damage of the entire structure can be assessed from the wall's resistance capacity. Indeed, the pressure applied by the avalanche flow on the structure is balanced almost solely by the wall facing the avalanche. Thus, as a first approximation, the damage of the entire structure is reduced to the damage of the structural elements directly exposed to the load, *i.e.*, a flat vertical RC wall.

2.2.1 RC wall description

First, the features of the wall considered are presented (geometry, mechanical properties of reinforced concrete, boundary conditions). Then, the out-of-plane mechanical response of an RC wall is described. The nature of the damage and the different damage stages the structure undergoes are presented as a function of the loading magnitude. From the physical vulnerability assessment point of view, relevant performance functions dedicated to quantifying the damage level of the RC wall can be proposed. Finally, the wall loading due to a snow avalanche is presented and discussed.

RC wall features

The RC wall is composed of concrete and steel bars. The bars are distributed homogeneously along the horizontal and vertical directions in the region of the wall where tensile stresses can develop (Fig. 2.1b–c). The number of steel bars is calculated from the steel density (ρ_s) needed to ensure the resistance of the RC wall. The usual sizes of dwelling houses situated in mountainous regions have been considered. Depending on the construction solution chosen, the RC wall boundary conditions can vary from one dwelling to another. The modeling of such various technologies of construction is considered in the boundary conditions of the wall. Three kinds of boundary conditions are usually encountered. Each edge of the wall can be considered either simply supported or clamped or free (*e.g.*, can move without any constraint). From a mechanical point of view, concrete strength differs from compressive to tensile regimes. The characteristic compressive strength (f_{c28}) is generally 10 times greater than the tensile strength (f_t). The compressive strength allowable for calculation is defined as f_{bc} by the Eurocode 2 (Committee, 2004), as a function of the loading time parameter, *i.e.*, the creep consideration, θ and the safety factor γ_b described below:

$$f_{bc} = \frac{0.85 f_{c28}}{\theta \gamma_b}. \tag{2.1}$$

Steel's behavior exhibits two typical limits. First, the yield strength (f_y) exceeding corresponds to the development of permanent strain inside steel; secondly, the ultimate tensile strain (ϵ_{uk}) highlights the ability of steel to undergo more or less substantial yield strain before failure. The RC behavior is a combination of the two materials. Figure 2.2 depicts the typical evolution of an RC member subjected to a monotonic loading. Four stages can be identified. The first stage represents the elastic response of the RC wall. The second stage corresponds to crack appearance and growth in the tensile zone of concrete. Once the crack distribution is fully developed (beginning of stage 3), the opening of the cracks continues. For higher loading and for low reinforced concrete, the capacity of the RC wall is only controlled by the resistance of the steel bars. When a steel bar starts

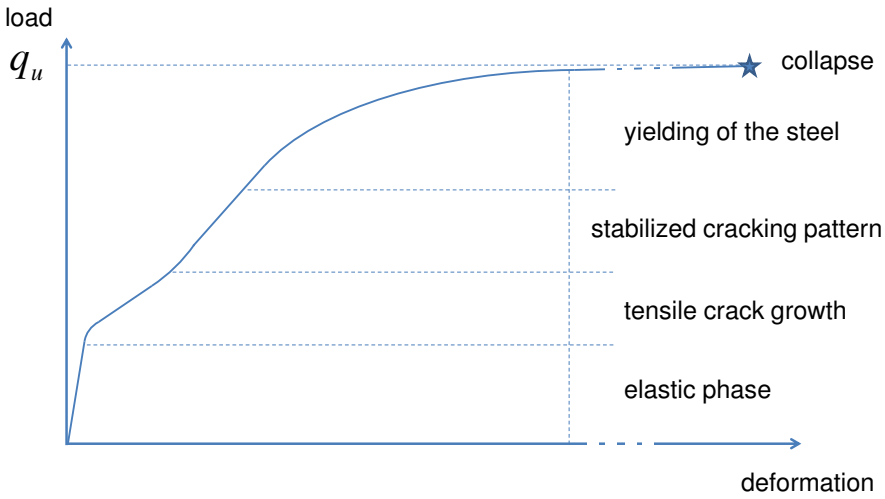

Figure 2.2 – Typical mechanical response of RC members subjected to a pushover test (monotonic loading until the collapse of the system), derived from (Favre et al., 1990, p. 343).

to undergo plastic strain, it is the beginning of the fourth stage. The end of the stage 4 corresponds to the collapse of the RC wall, where strains are concentrated through yield lines that can be described as macro-cracks. At the scale of the RC member, this last stage ends when a typical fracture line pattern develops over the entire RC structure. This failure mechanism induces the structure's loss of equilibrium, leading to its collapse.

Limit state definitions

The structural failure is assumed to be due to excessive bending of the wall. The RC wall collapses under a bending failure mode. The first damage level is defined as when the RC wall is no longer elastic. See for instance the European standard dedicated to the design of RC members: the Eurocode 2 provides mechanical design recommendations for several types of loadings. In this paper, the mechanical states used to describe the damage level of the structure are inspired from the Eurocode 2. The second and third damage levels are defined from Eurocode 2 (Mosley et al., 2007), where typical safety coefficients are proposed. Finally, the collapse of the RC wall is modeled by yield line theory (Johansen, 1962). It allows for calculating the ultimate pressure that the structure can support before

Table 2.1 – Safety coefficients on steel and concrete strength for ULS and ALS calculations (Committee, 2004).

	ULS safety coefficient	ALS safety coefficient
Steel	$\gamma_s = 1.15$	$\gamma_s = 1$
Concrete	$\gamma_b = 1.5$	$\gamma_b = 1.15$

collapse. The first three stages are defined from the local mechanical balance of the cross section where the highest bending moment arises, whereas stage 4 considers the whole failure pattern of the wall.

Elastic limit state

The first crack in the concrete defines the upper limit of stage 1. Beyond the first stage upper limit, the RC wall is no longer elastic. This limit is defined as when the tensile strength inside the concrete is reached.

Ultimate limit state (ULS)

This mechanical state is defined in the Eurocode 2 regulation and concerns the safety of people inside buildings and that of the building itself. In this paper, the Eurocode 2 terminology is used, but it can be a bit confusing. Indeed, the ULS does not correspond to the "real" ultimate resistance of the RC wall, which is here assessed by the yield line theory (see Sect. 2.2.1). From the Eurocode 2, the ULS is related to potential loadings that can arise during the "normal" life of the RC wall. The loadings are either permanent or transitory but not exceptional. Thus, the safety factors associated to the ULS loading are calculated based on "normal" life of the structure. Under bending, the ultimate limit state is obtained when either the concrete reaches its ultimate compressive strain or the steel its ultimate tensile strain.

Accidental limit state (ALS)

When dimensioning, the ALS differs from the ULS only in the loading description. Loadings are assumed exceptional (*i.e.*, accidental) and not usual or "normal" as for the ULS. The probability of occurrence of such loadings is often low and explains why the safety factors are lower than in the ULS case and thus the margin to support the loading is lower (Table 2.1). Using ALS as a structural limit state the structure could reach consists in applying a different multiplicative safety coefficients on the strength of the two materials comparing to those applied in the ULS approach.

Collapse

Finally, the collapse of the structure is characterized by its failure pattern. Under bending, yield lines develop through the RC member, leading to the structure's collapse. In order to obtain the ultimate load, the yield line theory is used, which is based on limit analysis theory (see for instance Nielsen and Hoang, 2011). In the literature, some theoretical and experimental studies have been compared. These studies proposed collapse failure patterns as a function of boundary conditions (Sawczuk and Jaeger, 1963). Favre et al. (1990) provide theoretical solutions for RC slabs under various geometrical configurations.

Snow avalanche loading

Different types of avalanche flows can be observed in the Alps, inducing various loadings on the impacted structures. Spatial and temporal changes in snow avalanche loadings were experimentally observed and measured. For instance, small-scale experiments were conducted to reproduce the granular behavior of snow and study its interaction with obstacles (Faug et al., 2010). Moreover, real-scale experiments have been conducted to measure the pressure magnitudes reached by dense avalanche flows (Thibert et al., 2008) and powder avalanches (Sovilla et al., 2008a).

An open question concerning the physical vulnerability assessment of civil engineering structures is whether the problem should be considered with a dynamical approach or a quasi-static approach. Various studies (Daudon et al., 2013) have considered that the dynamic effect has to be taken into account, whereas others have obtained vulnerability results assuming quasi-static approaches (Bertrand et al., 2010). In addition, in some cases (powder avalanches for instance) negative pressures can arise during the loading and thus can modify the failure mode of the structure considered. However, as already suggested, the type of avalanche controls the type of loading (quasi-static or dynamic), and here the avalanche type is considered as dense, which cannot generate negative pressures.

To determine whether a dynamic or a quasi-static approach has to be considered, a modal analysis has to be performed to compare avalanche loading and structural natural periods. In this paper, it is assumed that the duration of the accidental loadings is not creating dynamical effects. Thus, the pressure of the avalanche is supposed to be quasi-static, as proposed by Bertrand et al. (2010). Moreover, a uniform pressure distribution is applied to the wall even if vertical variations are observed (Baroudi et al., 2011). The pressure is uniformly distributed on the entire facing wall, along x and y axes. Due to the quasi-static assumption, the response of the RC wall is calculated considering the maximal pressure reached over time. The time variation is not considered because only the peak pressure for a quasi-static approach is relevant. The assumption of uniform pressure distribution is conservative, since the maximum is applied over the entire vertical, whereas

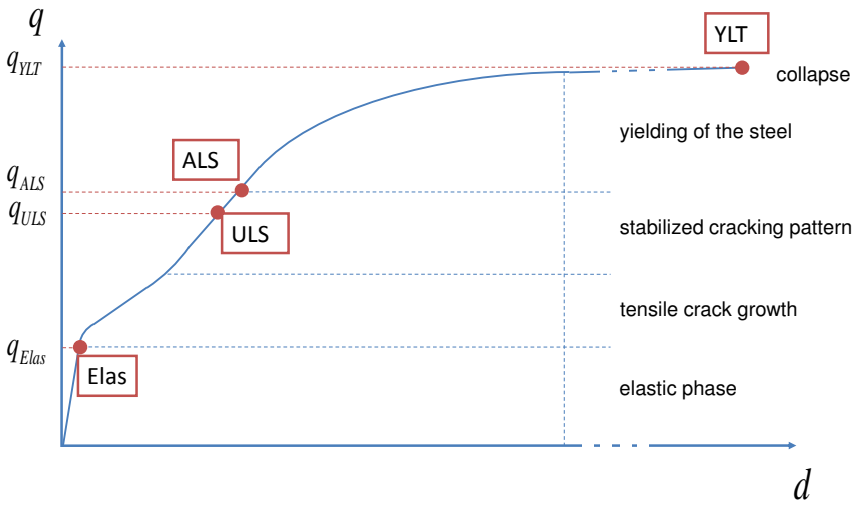

Figure 2.3 – Transitions between each damage level (Elas: elastic limit; ULS: ultimate limit state; ALS: accidental limit state; YLT: yield line theory).

in reality it decreases with the vertical coordinate.

2.2.2 Mechanical approaches

Figure 2.3 depicts the transitions between each damage level (Elas: elastic limit; ULS: ultimate limit state; ALS: accidental limit state; YLT: yield line theory). For each point, a loading pressure ($q_{\text{Elas}}, q_{\text{ULS}}, q_{\text{ALS}}, q_{\text{YLT}}$) can be calculated. For the first three cases, the load is obtained from the mechanical balance of the cross section, which is subjected to the maximal bending moment inside the RC wall (Fig. 2.4). For the collapse load, yield line theory is used.

RC wall design under bending

Bending moment expression

First, the loss of RC elasticity is related to crack appearance when the tensile strength of concrete is exceeded. At this stage, the steel contribution in the overall behavior can be ignored. The bending moment can thus be expressed as

$$M_{\text{Elas}} = \frac{f_t l_x h^2}{6}. \tag{2.2}$$

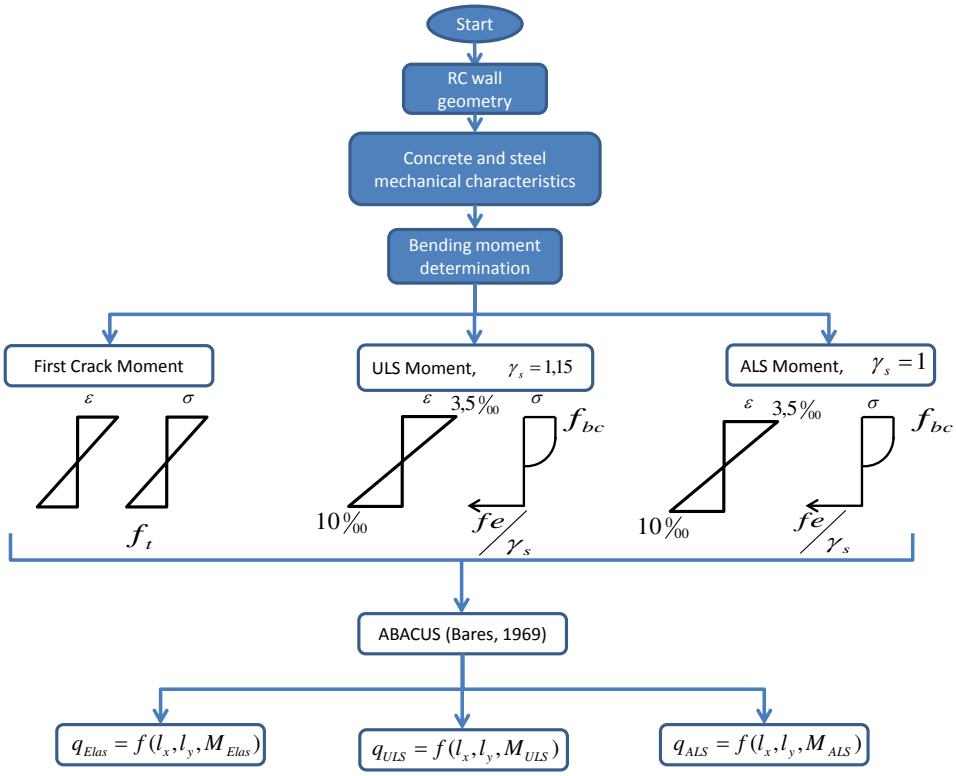

Figure 2.4 – Flowchart to calculate loading pressure related to each moment based on damage levels (Elas/ULS/ALS): first levels include geometry, mechanical characteristics and moment calculation; then, by inverting the Bares abacus (Bares, 1969), the corresponding loads are deduced.

The second (third) damage limit is attained when the bending moment defined by the ULS (ALS) is reached. In this case, the following assumptions are made:

- Sections remain planar during loading.
- No slip can occur between concrete and steel.
- The strain is linear along the thickness.
- Concrete's tensile strength is ignored ($f_t = 0$).
- The ultimate compressive strain of the concrete (ϵ_{bc}) and the ultimate tensile strain of the steel (ϵ_{uk}) are limited to 3.5 ‰ and 10 ‰, respectively.

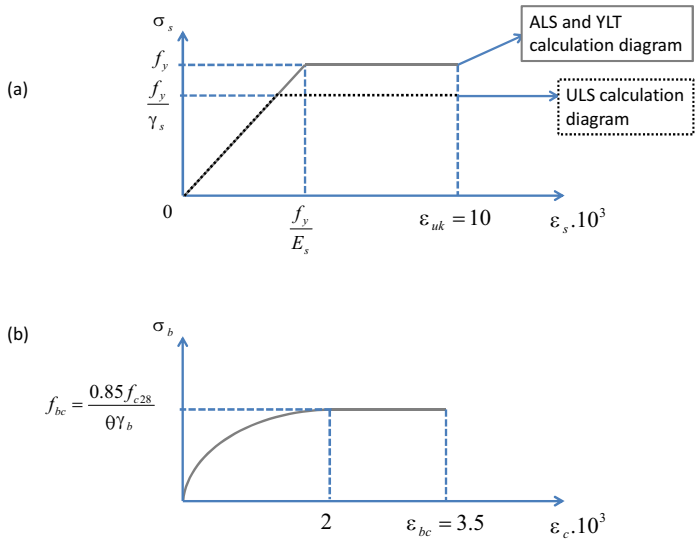

Figure 2.5 – Strain–stress calculation diagrams of the steel: perfect elasto-plastic grey diagram for the ALS and YLT calculations, black dotted line for the ULS calculation diagram where the steel yield strength is modified by the safety coefficient γ_s **(a)**, and strain–stress calculation diagram of the concrete **(b)**.

As functions of the ULS and the ALS, concrete and steel strengths change with the safety coefficients (γ_b and γ_s). As a consequence, the corresponding maximal bending moments also change. Figure 2.5 depicts assumed behaviors of the concrete and the steel.

The RC wall design consists in attaining the maximum strengths in concrete and in the steel at the same time. The compressive strength of concrete f_{bc} (Eq. 2.1) is estimated: no creep effect is taken into account ($\theta = 0.85$), and the safety coefficient $\gamma_b = 1.15$. According to assumptions previously made, the Eurocode 2 supplies the coefficient $\mu_{AB} = 0.186$. Thus, knowing the effective depth of the RC cross section d, the corresponding moment per linear meter developed in the section can be calculated:

$$M_{AB} = \mu_{AB} d^2 f_{bc}. \tag{2.3}$$

Next, by knowing the lever arm $z \approx 0.9d$, the amount of steel (*i.e.*, the percentage of steel inside concrete if normalized by the section area) needs to ensure that the balance of the bending moment is equal to

$$A_s = \frac{M_{AB}}{z \frac{f_y}{\gamma_s}}, \tag{2.4}$$

where $\gamma_s = 1.15$ for ULS. The ULS and ALS bending moments differ in the value taken

by the safety coefficient γ_s. Finally, the ULS and ALS ($\gamma_s = 1.0$) bending moments are expressed as

$$M_{\text{ULS}} = M_{\text{AB}}, \tag{2.5}$$

$$M_{\text{ALS}} = A_s z \frac{f_y}{\gamma_s}. \tag{2.6}$$

Boundary conditions

When the RC wall is subjected to a uniform pressure, the spatial distribution of bending moments depends on the boundary conditions of each wall edge. Many combinations can be considered (free edge, clamped edge or simply supported edge). Bares (1969) proposed a useful abacus that gives the maximal bending moments developed in elastic rectangular plates for numerous configurations of boundary conditions.

In this paper, the derivation of vulnerability relations is carried out within a reliability framework. Thus, to calculate the failure probability of the RC wall, many runs are needed. By using the abacus to assess the RC wall's resistance capacity, the computational time to perform a single run is very low, which makes it possible to use robust but computationally intensive reliability methods such as Monte Carlo simulations. Ten boundary conditions were implemented (1 to 10, cf. Table 2.2). A linear spline is fitted to extrapolate coefficients from available coefficients (β_x and β_y) provided by the abacus. Knowing the limit bending moment for each damage stage, the corresponding pressure is deduced for each direction x and y:

$$q^x = \frac{M}{\beta_x l_x^2}, \tag{2.7}$$

$$q^y = \frac{M}{\beta_y l_y^2}. \tag{2.8}$$

RC wall collapse (yield line theory)

The ultimate resistance of RC slabs under uniformly distributed pressure can be derived from the classical yield line theory (Johansen, 1962). This theory provides the collapse mechanism of the RC wall. Under an external loading, cracks will develop to form a pattern of "yield lines" until a mechanism is formed. A yield line corresponds to a nearly straight line along which a plastic hinge has developed. To perform the yield line theory algorithm, the bending moment along yield lines needs to be calculated. The bending moment per unit length along those lines remained constant and equal to the moment calculated in Eq. (2.6). Indeed, as we are considering a uniform and equal reinforcement along the horizontal and vertical directions, the steadiness is verified. Then the energy

Table 2.2 – Maximum bending moment coefficients (β_x, β_y) for a rectangular plate subjected to an uniform load. The Poisson's ratio $\nu = 0.15$ and $\frac{l_x}{l_y} = 0.5$.

Boundary conditions	β_x	β_y
(1) four simply supported edges	0.0991	0.0079
(2) simply supported on the two large edges clamped on the two small edges	0.0835	0.0088
(3) simply supported on one large edge clamped on the three other edges	0.0550	0.0045
(4) one free large edge clamped on the three other edges	$-\nu \times \beta_y$	0.0268
(5) one free large edge simply supported on the three other edges	$-\nu \times \beta_y$	0.0575
(6) clamped on one small edge simply supported on the three other edges	0.0908	0.0084
(7) simply supported side by side clamped on the two other edges	0.0570	0.0040
(8) four clamped edges	0.0405	0.0024
(9) one free large edge/one clamped large edge simply supported on the two small edges	$-\nu \times \beta_y$	0.0288
(10) one free large edge/one simply supported large edge clamped on the two small edges	$-\nu \times \beta_y$	0.0361

balance between external and internal forces is calculated. According to the assumed yield line pattern, each adjacent plate can rotate. The plates rotate around axes defined by the edges of the slab and the yield lines. During the rotation, energy is dissipated inside the material by yielding. The dissipated energy is calculated as $M_{\mathrm{p}}^{i}\theta_i L_i$, where M_{p}^{i} is the plastic moment of the yield line considered i, θ_i the magnitude of the angle of rotation, and L_i the length of the yield line. The ultimate load is calculated from the equality between the external energy (W_{ext}) and the internal energy (W_{int}). In order to find the most likely collapse pattern, the kinematic theorem is used. It consists in determining the failure pattern minimizing the collapse load. Thus, the following equations are derived:

$$\begin{cases} W_{\mathrm{int}} = \sum_{i=1}^{n_L} \vec{M}_{\mathrm{p}}^{i}.\vec{\theta}_i.L_i \\ W_{\mathrm{ext}} = q \iint \delta(x,y)\mathrm{d}x\mathrm{d}y \end{cases}, \tag{2.9}$$

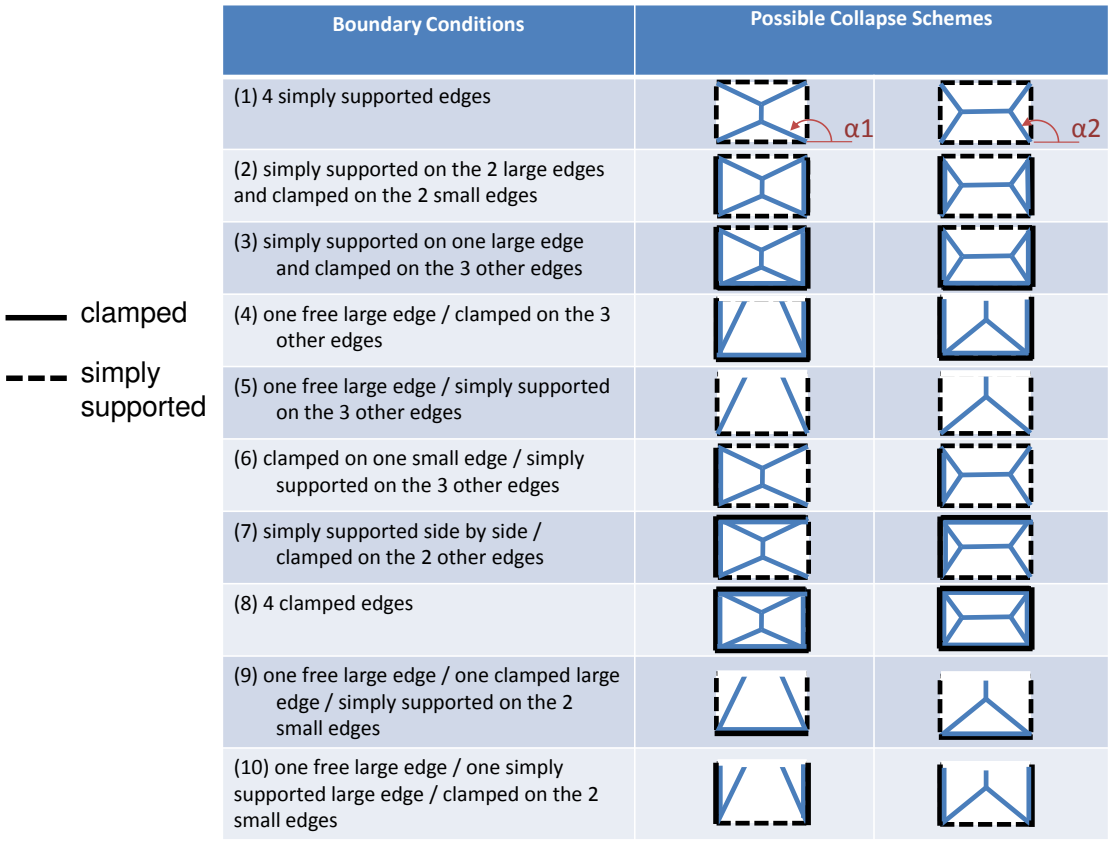

Figure 2.6 – Failure patterns according to several boundary conditions when considering yield line theory.

where n_L is the number of yield lines, $\delta(x, y)$ is the displacement field of the slab and q is the uniform load applied on the slab. Various failure patterns were considered as functions of the boundary conditions (Fig. 2.6). For each boundary condition, two failure patterns are mainly observed (Fig. 2.6, col. 2 and 3). Each pattern depends on an angle α_1 or α_2 calculated in order to minimize the energy.

2.2.3 Reliability framework

The structure's safety cannot be assessed from a deterministic point of view because several properties of the system are uncertain. Thus, the study is performed in a reliability framework.

Failure probability definition

The failure probability P_f is defined as the probability for the resistance of the structure r to be less than or equal to an event size s:

$$P_\mathrm{f} = P[r \leq s] = \int_{-\infty}^{s} f_\mathrm{R}(r)\mathrm{d}r. \tag{2.10}$$

To solve Eq. (2.10), the probability density function of the resistance $f_\mathrm{R}(r)$ needs to be known. The Monte Carlo algorithm is used to generate data samples. Depending on what it is calculated with, it is a robust but time-consuming method. By randomly generating N variables from the input probability distributions, N mechanical runs can be performed. Thus, the probability density function of the response can be approximated by the Monte Carlo integral: $\hat{P}_f$. The central limit theorem provides a $(1-\alpha)$ asymptotic confidence interval reflecting a significance level of α:

$$\hat{P}_f \left(1 - z_{1-\alpha/2}\frac{\sqrt{\hat{P}_f(1-\hat{P}_f)}}{\sqrt{N}}\right) \leq P_f \leq \hat{P}_f \left(1 + z_{1-\alpha/2}\frac{\sqrt{\hat{P}_f(1-\hat{P}_f)}}{\sqrt{N}}\right),$$

where $z_{1-\alpha/2}$ is the α quantile of the normal distribution.

Sobol's index

Sobol's index provides the contribution of inputs to model outputs. It consists in quantifying the contribution of each input variable to the entire system's variability. It is based on a variance sensitivity analysis (Sobol, 2001). Saltelli et al. (2010) provide different numerical estimates and a comparison between their efficiency. For independent input variables, Sobol's first-order sensitivity coefficient S_i is equal to the total effect index $S_{\mathrm{T}i}$. Considering Y as the model output and X as the vector of inputs, Sobol's indices are defined as

$$S_i = \frac{V_{X_i}(E_{X_{\sim i}}(Y|X_i))}{V(Y)}, \tag{2.11}$$

$$S_{Ti} = 1 - \frac{V_{X_{\sim i}}(E_{X_i}(Y|X_{\sim i}))}{V(Y)}, \tag{2.12}$$

where V is the variance and more particularly V_{X_i} is the variance of the argument taken over X_i, $V_{X_i}(E_{X_{\sim i}}(Y|X_i))$ is the expected reduction in variance that would be obtained if X_i could be fixed.

According to Saltelli et al. (2010), Jansen (1999) provides the most efficient estimator of Eq. (2.12) through the approximation

$$\hat{S_{Ti}} = \frac{1}{2N}\sum_{j=1}^{N}(f(\mathbf{A})_j - f(\mathbf{A}_B^{(i)})_j)^2, \tag{2.13}$$

where $Y = f(X_1, X_2, \ldots, X_k)$, $\mathbf{A}$ and $\mathbf{B}$ are an $N \times k$ matrix of input factors and $\mathbf{A}_B^{(i)}$ is a matrix where column i comes from matrix $\mathbf{B}$ and all other $k-1$ columns from matrix $\mathbf{A}$.

Table 2.3 – Distribution parameters of material inputs.

Variable	Mean	Standard deviation
l_x (m)	8.0	0.4
l_y (m)	4.0	0.2
h (m)	0.2	0.01
f_{c28} (MPa)	30	1.5
f_y (MPa)	500×10^6	25×10^6
f_t (MPa)	2	0.1

2.2.4 Vulnerability assessment

Statistical distributions of inputs need to be defined. Here, six input variables were chosen and their distributions were determined: l_x, l_y, h, f_{c28}, f_y and f_t. Different sets of distributions are used: a set of normal independent distributions, a more realistic distribution provided by the Joint Committee on Structural Safety (2001) (JCSS) and intermediate cases. Thus, building cumulative distribution functions of mechanical capacity load outputs allows for fragility curves to be assessed.

Statistical description of inputs

Normal distributions

First, to analyze the effect of each variable separately, a normal distribution describes each variable. Low and Hao (2001) provided several references identifying distributions for material inputs involved in a reinforced concrete slab problem. Mirza and MacGregor (1979) assumed normal distributions to model the variability/uncertainty regarding the sizes of slabs. After in situ experiments, a coefficient of variation of 0.05 is suggested and the designed value is adopted as the mean distribution value. To carry out a first statistical description of the proposed model, a coefficient of variation of 0.05 is assumed for all the inputs considered, leading to the means and standard deviations provided in Table 2.3.

JCSS distributions

As reported by the JCSS, correlations between input variables can be taken into account. Steel's yield strength is still independent and follows a normal distribution. On the other hand, the tensile strength (f_t) and the compressive strength of the concrete (f_{bc}) distributions are deduced from the basic concrete compression strength (f_{c28}) distributions. For a

Table 2.4 – Table presenting the marginal distributions of independent material inputs for the JCSS distribution case. Other inputs are computed according to Eqs. (2.14), (2.15) and (2.16) of Sect. 2.2.4.

Variable	Mean	Standard deviation
l_x (m)	8.0	0.4
l_y (m)	4.0	0.2
h (m)	0.2	0.01
f_y (MPa)	560×10^6	30×10^6

ready-mixed concrete type with a $C25$ concrete grade, based on the given parameters, the values of m, v, s, n are $m = 3.65$, $v = 3$, $s = 0.12$ and $n = 10$, and t_v is a random variable from a Student distribution for v degrees of freedom:

$$f_{c28} = \exp(m + t_v s(1 + \frac{1}{n})^{0.5}). \tag{2.14}$$

Then, f_t and f_{bc} are calculated with λ, Y_1 and, Y_2. λ is a factor taking into account the systematic variation of in situ compressive strength and the strength from standard tests. Finally, $(Y_i)_{i=1,2}$ are lognormal variables representing additional variations due to special placing, curing, and hardening of the concrete. In our case, α_c is considered equal to $\frac{0.85}{\theta\gamma_b}$:

$$f_{bc} = \alpha_c f_{c28}^{\lambda} Y_1, \tag{2.15}$$

$$f_t = 0.3 f_{bc}^{2/3} Y_2. \tag{2.16}$$

For all parameters, the marginal mean and standard deviation were set according to the JCSS recommendation (Table 2.4). Difference with the previous case (Table 2.3) concerns (f_{c28}) for which they are higher in this case.

Intermediate distributions

To bridge the gap between the realistic JCSS distributions case and the normal independent choice, seven intermediate distributions were considered, differing from each other in terms of distribution type and/or covariance matrix:

- A lognormal distribution for three multiplicative variables: the tensile strength and the compressive strength of concrete, and the steel yield strength with parameters of Table 2.5. Means and standard deviations are the same as for the normal case.
- A lognormal distribution for the tensile strength and the compressive strength of concrete, and the steel yield strength with parameters of Table 2.6. Means and standard deviations are the same as for the JCSS case.

Table 2.5 – Table presenting the marginal lognormal distributions used for the tensile strength and the compressive strength of concrete, as well as the steel yield strength. Means and standard deviations are the same as in Table 2.3. The parameters μ_{LN} and σ_{LN} are the resulting parameters of the lognormal distributions.

Variable	Mean	Standard deviation	μ_{LN}	σ_{LN}
f_{t} (MPa)	2	0.1	0.69	0.05
f_{c28} (MPa)	30	1.5	3.40	0.05
f_y (MPa)	500×10^6	25×10^6	20.03	0.05

Table 2.6 – Marginal JCSS-based lognormal distributions used for the tensile strength and the compressive strength of concrete, as well as the steel yield strength.

Variable	Mean	Standard deviation	μ_{LN}	σ_{LN}
f_{t} (MPa)	2.38	0.76	0.82	0.31
f_{c28} (MPa)	38.9	6.11	3.65	0.16
f_y (MPa)	560×10^6	30×10^6	20.14	0.053

- A lognormal distribution for the tensile strength and the compressive strength of concrete, and the steel yield strength. According to the Table 2.6, standard deviations are multiplied by 2 to emphasize lognormal distributions asymmetry.

- A normal joint distributions for all the variables with variance–covariance matrix deduced from the JCSS distributions and the means from Table 2.3.

- A normal joint distribution for the six parameters l_x, l_y, h, f_{c28}, f_y and f_{t} using mean and standard deviation from Table 2.3 and correlation coefficients (covariance) of the JCSS case. The main correlation is the relation between f_{c28} and f_{t}: $\rho(f_{\mathrm{c28}}, f_{\mathrm{t}}) = 0.31$; others are lower than 0:01, *i.e.*, close to independence.

- A normal joint distribution for the six parameters l_x, l_y, h, f_{c28}, f_y and f_{t} using mean, standard deviation and correlation coefficients (covariance) of the JCSS case.

- Uncorrelated JCSS distributions: to assess the effect of correlation on the JCSS case, each modeled variable was selected independently to break down dependencies.

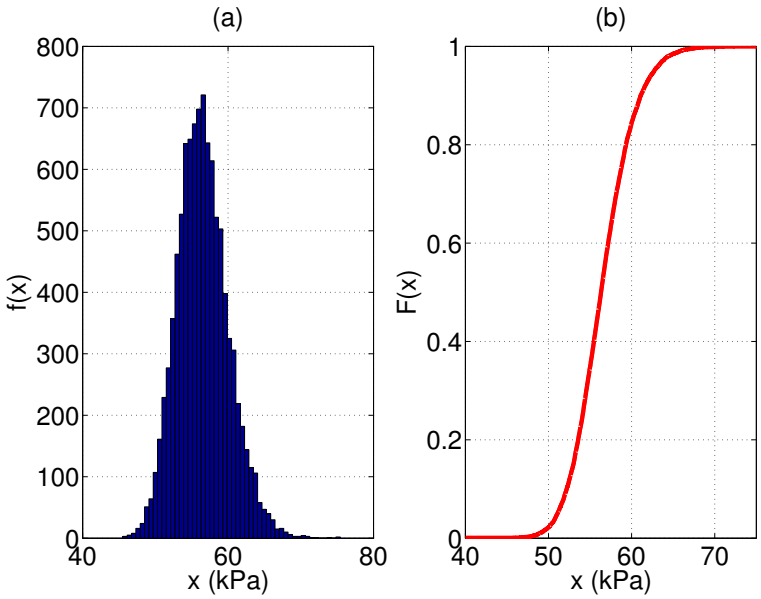

Figure 2.7 – Output histogram of the ULS case for a rectangular wall with one free edge and three clamped edges with normal independent inputs **(a)**, and the cumulative distribution function associated **(b)**.

Fragility curves derivation

A fragility curve $F(x)$ is a monotonic curve providing a failure probability as a function of the magnitude of a loading, here a pressure applied, hence the cumulative distribution function $F(x)$ of the failure probability for the load x. The usual way to compute fragility curves is to set a pressure and vary the inputs from their statistical distributions. Thus, for each pressure a failure probability is obtained to build the fragility curve. In this paper, the approach is somewhat original because failure probabilities are derived from an inverse resolution. First, the structure capacity of resistance is found; then, by abacus inversion, a load distribution is assessed. Finally, the cumulative distribution function of the latter distribution makes it possible to link a failure probability to a pressure. As an example, Fig. 2.7 depicts an output histogram of the ULS case for a rectangular wall with one free edge and three clamped edges with normal independent inputs and the fragility curve associated through its cumulative distribution function.

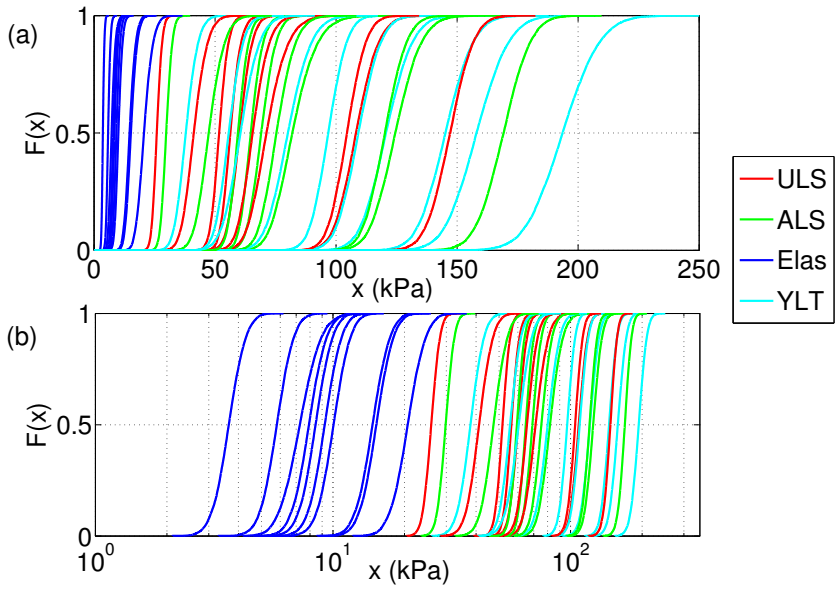

Figure 2.8 – Fragility curves according to boundary conditions sorted by failure criterion: **(a)** linear frame and **(b)** semi-log frame.

2.3 Results

2.3.1 Fragility curves with uncorrelated normally distributed inputs

Overview of all configurations

Using 10 000 runs per curve, smooth fragility curves are obtained. Figure 2.8 depicts fragility curves according to explored boundary conditions. They are sorted by the four failure criteria. Two visual groups are formed. First, all the curves representing the elastic limit state are gathered at low pressure loads. By considering the minimum 2.5 % quantile and their maximum 97.5 % quantile, their fragility range is $[2.8, 27.2]$ (kPa). They do not interfere with fragility curves of the other failure criteria. On the other hand, the ULS, ALS and YLT fragility curves are defined on a range from 22.7 kPa to 218.6 kPa. It is interesting to note that the ALS fragility curves are scaled from the ULS curves by the safety factor 1.15. This is easily explained by the definition itself of the ALS failure criterion.

Another point of view can be taken by plotting the same data according to the description of their boundary conditions (Fig. 2.9). Sets of fragility curves can be deduced. The four weakest structures present free edges. Rectangular walls with one free edge are

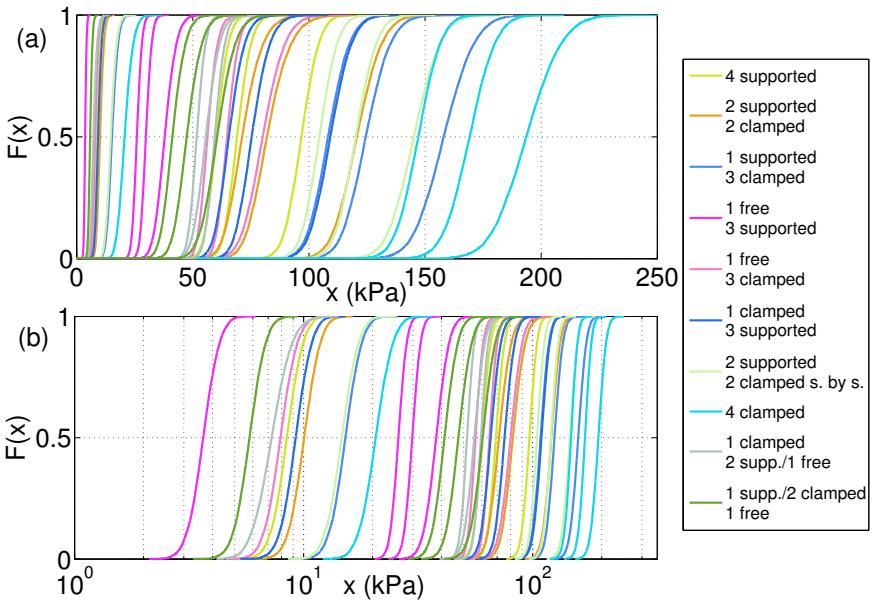

Figure 2.9 – Fragility curves according to boundary conditions sorted by boundary conditions: **(a)** linear frame and **(b)** semi-log frame.

sorted from the weakest by their boundary conditions as below: (1) one free edge and three supported edges; (2) one supported edge, two clamped edges and one free; (3) one clamped edge, two supported edges and one free*; and (4) one free edge and three clamped edges (*exception for the YLT limit state where 3 and 4 are exchanged). Then the second set of curves gathers the rectangular wall with supported edges ((5) four supported edges, (6) one clamped edge and three supported ones, (7) two supported edges and two clamped ones, (8) two supported edges and two clamped edges side by side, and (9) one supported edge and three clamped ones). Finally, the less vulnerable rectangular wall has four clamped edges.

Equation (2.17) provides the p quantile of each vulnerability curve:

$$F(x) = \Pr(X \leq x) = p. \tag{2.17}$$

The previous equation allows considering a more quantitative approach. Table 2.7 sums up the 50 % quantiles and similar conclusions as described above are set up. The fragility range is defined as an interval: the lower bound is the 2.5 % quantile and the upper bound is the 97.5 % quantile of the fragility curve, which could be considered as very useful quantitative thresholds for engineering applications.

Table 2.7 – The 50 % quantile of the CDF fragility curves according to boundary conditions and failure criterion, and (2.5 %, 97.5 %) quantile defining a fragility range (kPa).

Boundary conditions	Elas	ULS	ALS	YLT
(1) four simply supported edges	8.4	60.2	69.3	97.0
	(6.5, 10.9)	(52.3, 69.1)	(60.2, 79.5)	(85.5, 109.5)
(2) simply supported on the two large edges clamped on the two small edges	10.0	71.6	82.4	121.0
	(7.7, 13.0)	(59.4, 87.6)	(68.3, 100.7)	(104.8, 139.1)
(3) simply supported on one large edge clamped on the three other edges	15.2	108.6	124.9	158.5
	(11.6, 19.7)	(95.0, 124.2)	(109.3, 142.8)	(138.8, 180.2)
(4) one free large edge clamped on the three other edges	7.8	56.0	64.4	80.5
	(6.0, 10.3)	(49.9, 63.7)	(57.4, 73.2)	(66.6, 96.7)
(5) one free large edge simply supported on the three other edges	3.6	26.0	29.9	38.1
	(2.8, 4.7)	(22.7, 29.6)	(26.1, 34.1)	(30.9, 46.7)
(6) clamped on one small edge simply supported on the three other edges	9.2	65.8	75.7	109.5
	(7.1, 11.9)	(56.0, 77.6)	(64.4, 89.2)	(95.6, 124.7)
(7) simply supported side by side clamped on the two other edges	14.6	104.7	120.4	145.5
	(11.2, 19.2)	(93.1, 117.6)	(107.1, 135.3)	(128.3, 164.4)
(8) four clamped edges	20.7	147.9	170.0	194.0
	(15.6, 27.5)	(133.3, 163.4)	(153.3, 187.9)	(171.1, 219.2)
(9) one free large edge / one clamped large edge simply supported on the two small edges	7.2	51.9	59.7	55.9
	(5.3, 10.3)	(43.2, 58.9)	(53.2, 67.8)	(47.2, 65.8)
(10) one free large edge / one simply supported large edge clamped on the two small edges	5.8	41.4	47.6	60.9
	(4.4, 7.5)	(33.5, 50.8)	(38.5, 58.5)	(48.9, 74.1)

Table 2.8 – Quantiles of fragility curves illustrated in Fig. 2.13.

Approach	$Q_{2.5\,\%}$	$Q_{50\,\%}$	$Q_{97.5\,\%}$	$Q_{97.5\,\%}$–$Q_{2.5\,\%}$
Deterministic		55.5		0
JCSS	44.9	62.4	86.8	41.9
JCSS independent	45.3	62.6	86.8	41.6
Normal independent	50.2	56.3	64.3	14.1
Correlated normal	50.3	56.3	64.0	13.6
Normal, correlation and variance from JCSS case	33.7	56.6	79.4	45.7
Lognormal, mean and variance from normal case	51.3	56.2	63.6	12.3
Normal, correlation, variance and mean from JCSS case	42.8	63.3	84.5	41.7
Lognormal, mean and variance from JCSS case	45.2	62.4	86.2	41.0
Lognormal, mean and variance (×4) from JCSS case	32.0	60.3	114.6	82.6

An example: one free edge and three clamped edges

To investigate Monte Carlo confidence interval quantification, a focus on a particular case was required. The selected case is the rectangular wall with one free edge and three clamped edges (Fig. 2.10). The four limit state fragility curves can be distinguished together with Monte Carlo confidence intervals. As mechanical runs are not time-consuming, the number of calls N can be high enough to make numerical uncertainty negligible. Thus 10 000 runs induce thin confidence intervals near the curve, giving confidence in all the numerical results provided.

2.3.2 Parametric study

This section is devoted to the analysis of total Sobol indices. As each of the input variables is independent, their sum is equal to 1. Sensitivity pie charts of outputs according to the input distribution can be plotted (Fig. 2.11). Four input parameters influence the fragility assessment based on the elastic failure criterion: f_{t}, l_x, l_y and h. The variable h is the predominant variable affecting the elastic-based failure probability. The ULS and ALS have the same sensitivity pie charts. Three input parameters are involved in the variability of ULS- and ALS-based failure probabilities: l_x, l_y and f_{c28}. f_{c28} seems to be the variable influenced the most by these outputs. This indicates which variables should be considered

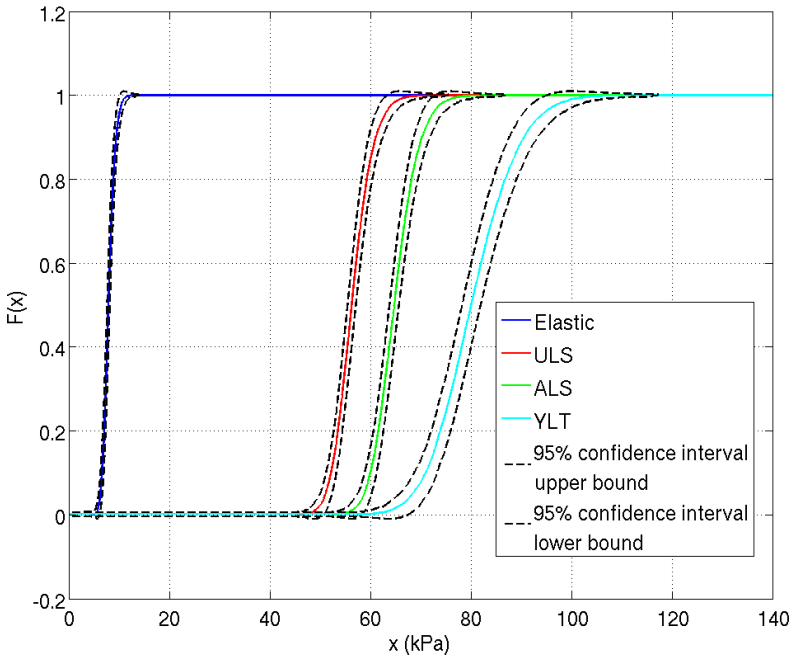

Figure 2.10 – Vulnerability curves and their 95 % confidence intervals from Monte Carlo simulations of a slab with one free edge and three clamped edges.

with the greatest care while designing a structure in practice, depending on the chosen failure criterion.

2.3.3 Sensitivity to input distributions choice

Fragility curves are highly dependent on the input distributions used. Outcomes were obtained from the two first distributions previously described (Fig. 2.12). As a general overview, more elaborated distributions induce greater spread in fragility curves. Their fragility ranges have a higher amplitude than the range derived from independent normal approaches. One explanation is that taking into account correlations makes certain "extreme" combinations of inputs more likely than in the independent case. Another explanation lies in the number of variables considered: the more numerous they are, the more uncertainties are taken into account, and also the larger the fragility range of the fragility curves is.

To ascertain and detail this conclusion, Fig. 2.13 focuses on the ULS example for the same boundary conditions. It appears clearly that, from the deterministic point of view (a simple 0–1 response if the fragility limit is attained or is not attained) to the JCSS-based approach, fragility curves have wider fragility ranges. Quantiles at 2.5 %, 50 % and 97.5 %

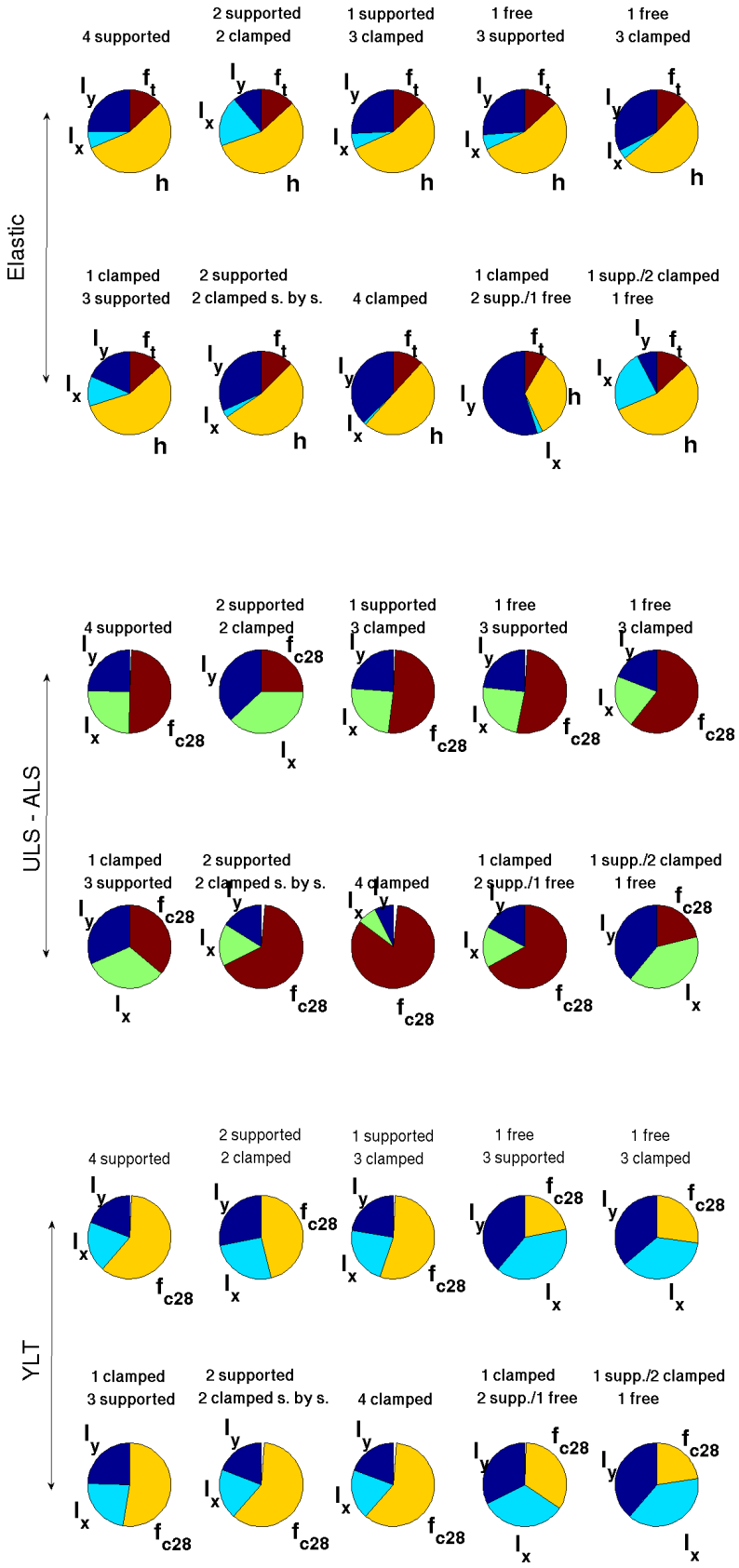

Figure 2.11 – Sensitivity pie charts for the elastic, ULS (ALS) and YLT failure criteria.

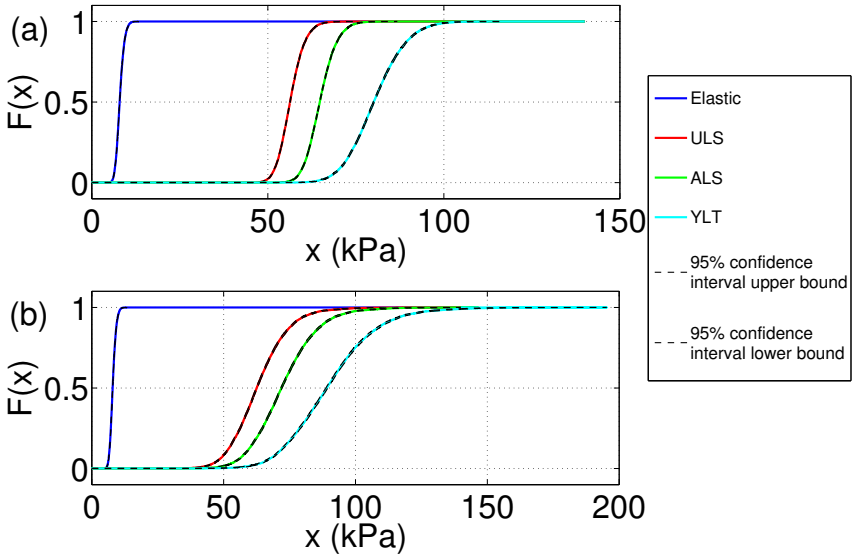

Figure 2.12 – Comparison of fragility curves from different input distributions of a slab with one free edge and three clamped edges: **(a)** normal independent distributions, **(b)** JCSS distribution.

support these results (Table 2.8). Note, however, that the more complex case (*i.e.*, the JCSS case), despite its wider spread, shows higher (and thus "safer") modal values, and therefore simpler approaches (normal or lognormal inputs) can be used in practice, at least as first approximations.

The 50 % quantile depends nearly only on the means of the three material parameters f_y, f_{c28} and f_t. Indeed, the 50 % quantile remains fully constant to ~ 56 kPa regardless of the covariance matrix for Gaussian inputs with f_y, f_{c28} and f_t centered on their nominal values 500×10^6, 30 and 2 MPa, respectively. Switching to the JCSS leads to a higher 50% quantile ~ 62 kPa independent of the correlation structure. In addition, the 50 % quantile remains nearly unchanged with independent lognormally distributed inputs with the same mean even if these, by definition, introduce non-symmetry into the problem. This asymmetry effect is, however, visible when the standard deviation is multiplied by 2. By the way, the fragility range is logically also increased (Table 2.8).

All in all, the fragility range and fragility curves shape changes mainly according to the marginal variances, much higher in the different JCSS cases, with covariance between the different inputs and marginal distribution types having less influence.

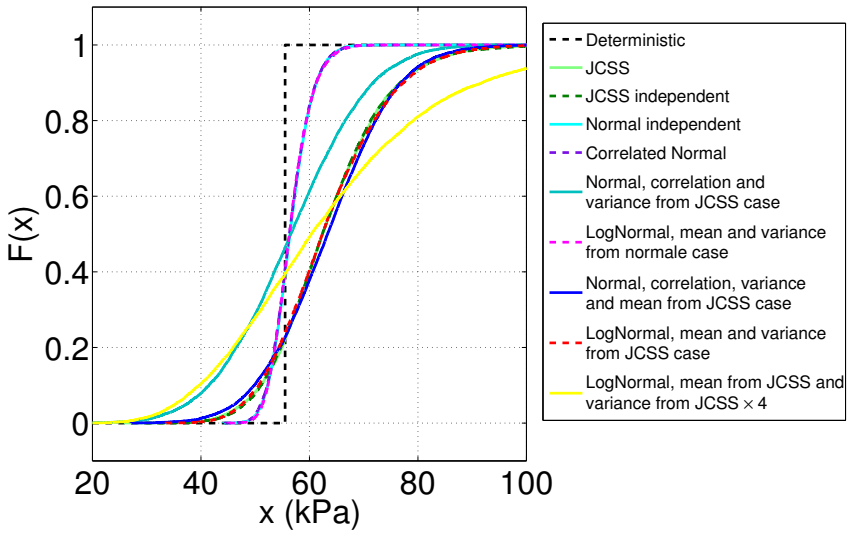

Figure 2.13 – Comparison between a deterministic approach and fragility curves computed with different input distributions. Fragility curves are here calculated for a slab with one free edge and three clamped edges under ULS considerations.

2.4 Conclusion

The proposed approach can be considered as a comprehensive framework providing fragility curves for RC walls exposed to a snow avalanche pressure load. It could be considered with benefits for other sorts of problems and in particular for other types of civil engineering structures (structures with different materials, structures built using another technology, etc.) or natural hazards.

In detail, the influence of the boundary conditions and of the stochastic input distributions were systematically investigated, so as to provide robust fragility curves for various building types. Their most useful application may be individual risk assessment, including sensitivity analyses, for which the main concern is to evaluate the survival probability as a function of space for a hypothetical individual within different building types.

Four limit states based on the RC wall's mechanical response were considered: three local (cross-section scale) and one global (wall scale). For instance, the distinction between the ULS, concerning the safety of people, and the real collapse, where the structure is no longer standing, could lead to considering different thresholds for risk boundary assessment, leading to refined risk maps taking into account the winter usage of each building.

It has also been shown that, from a statistical point of view, stochastic input distri-

butions strongly influence the shape of the fragility curves. Hence, mean and standard deviation of each variable, independent or correlated variables as well as the number of variables considered, constitute important factors in the variability of fragility curves. This sensitivity to the input parameter distributions highlights that it seems important to consider and describe precisely the uncertainty sources for each application.

The deterministic simulations were carried out through simplified and effective mechanical models in terms of CPU time. This allowed using the Monte Carlo method, which gave robust results for the failure probability assessment. Probabilistic input distributions are provided by the literature, but no statistical inference has been performed. Future work should therefore take real data into consideration and a Bayesian approach could then be appropriate to update the information conveyed by numerical simulations (Eckert et al., 2009).

Finally, it should be noted that more sophisticated mechanical models for civil engineering structures exist, based on the finite-element (FE) method, which can simulate the structure in greater detail and in particular describe how the damage field evolves when material nonlinearities develop inside the concrete and the steel reinforcement. However, these FE models are often more complex (*i.e.*, in term of convergence) and time-consuming. Hence, they may be less well adapted to a generic individual risk base approach, but more useful for studies deriving refined fragility curves for specific structures included in precise engineering projects.

2.5 Acknowledgements

The authors thank the ANR research program MOPERA (Modélisation probabiliste pour l'Etude du Risque d'Avalanche – avalanches.irstea.fr/mopera-projet/) and the MAP3 ALCOTRA INTERREG program for financially supporting this work. The authors are also grateful to Regis Monnard for fruitful discussions. We also thank Dr. Lasaponara (handling editor) and the two anonymous referees for their constructive comments used to improve the paper. Edited by: R. Lasaponara Reviewed by: three anonymous referees

2.6 Appendix: Nomenclature

Table 2.9 – Nomenclature.

ρ_{s}	density of steel
l_x	length of the slab
l_y	height of the slab
h	thickness of the slab
f_{c28}	cylinder characteristic compressive strength of concrete (age, 28 days)
f_{bc}	compressive strength of concrete
f_{t}	tensile strength of concrete
f_{y}	steel yield strength
ϵ_{uk}	ultimate tensile strain of the steel
γ_{b}, γ_{s}	safety coefficients on concrete and steel strength
$q_{\mathrm{ULS}}, q_{\mathrm{ALS}}, q_{\mathrm{Elas}}, q_{\mathrm{YLT}}$	characteristic loading at the ultimate limit state, at the accidental limit state, at the first cracks of the concrete in the tensile zone and at the collapse
ϵ_{bc}	ultimate compressive strain of the concrete
θ	loading time parameter
M_{AB}	rational dimensioning moment
μ_{AB}	ULS rational dimensioning coefficient
d	effective depth of the RC cross section
z	lever arm in the section
β_y, β_x	Bares coefficient
ν	Poisson coefficient
W_{int}	internal virtual work
W_{ext}	external virtual work
n_{L}	number of yield lines
M_{p}^i	unitary plastic moment along the ith line
L_i	length of the ith line
θ_i	rotation angle of the ith element
$\delta(x, y)$	displacement matrix
q	uniform load
α_1, α_2	angles of YLT patterns
P_{f}	failure probability
r	resistance of the structure
s	solicitation
α	significance level of confidence interval
$f_{\mathrm{R}}(r)$	probability density function of the resistance
S_i	first-order Sobol sensitivity coefficient
S_{Ti}	total Sobol sensitivity coefficient
α_{c}	coefficient from the JCSS distribution

CHAPTER 3

Reliability-based physical vulnerability assessment of a RC wall impacted by snow avalanches using a nonlinear SDOF model

Le contenu de ce chapitre a vocation à être soumis après travail à *Reliability Engineering and System Safety*, les auteurs sont : Favier, P., Bertrand, D., Eckert, N., Ousset, I. and Naaim, M..

Abstract

As often in reliability engineering, the CPU time required to obtain accurate and robust results is the main issue. Here, the objective is to propose a simplified modelling of the RC structure keeping the involved physics and especially the dynamic nature of the structure's mechanical response. This paper presents the assessment of the physical vulnerability of a Reinforced Concrete (RC) wall subjected to an avalanche loading within a reliability framework. A Single Degree-Of-Freedom (SDOF) model is used to describe the dynamical response of the RC member. The non-linear behaviour of the material is taken into account by a Moment-Curvature approach which allows describing the overall bending response of the RC wall until the collapse. The deterministic SDOF model is validated by Finite Element Analysis (FEA) and by limit analysis.

A reliability analysis is conducted in order to derive fragility curves providing the limit state reach as function of avalanche pressure. A performance analysis is carried out which underlines the necessity to use efficient numerical models in terms of computation time. For our case of snow avalanche loadings, a SDOF model seems to be an interesting option to derived rapidly fragility curves keeping a sufficient accuracy. Several reliability methods (Monte-Carlo, Kernel smoothing, Taylor expansion) are used and compared suggesting that non parametric methods (not based on parametrized families of probability distributions) have a good potential to approach fragility curves. Finally, the sensitivity to strength parameters (material tensile and compressive strengths, reinforcement ratio) and to loading parameters are proposed. It highlights that both have influences on the fragility curve derivation; the loading rate has also a significant influence on both the shape and the mode of the fragility curve. Discussion is proposed with regards to the seldom fragility curves available in this field.

Keywords: Vulnerability Relations; Fragility Curves; RC Wall; Reliability; Natural Hazard; Snow Avalanche; Risk; SDOF model; Finite Element Analysis.

3.1 Introduction

Nowadays, risk analysis is more and more used in order to help decision makers. In safety domains, such as natural hazards prevention and mitigation engineering, the construction of hazard models together with vulnerability relations are needed. Vulnerability relations are used to represent a degree of damage of the considered system, or fragility curves which express the probability to reach a given limit state. Vulnerability curves are deterministic in opposition to fragility curves which are probabilistic.

In the context of avalanche risk mitigation, technical prescriptions for buildings lying in dangerous runout zones impose that the part of the structure facing the snow flow has to resist to pressures up to 30kPa. Several kind of construction technologies can be used to achieve this resistance (masonry, wood or metallic structures, etc.). In a first step, only reinforced concrete is considered in this paper. Indeed, most of usual constructions which can be found in the Alps are built with this composite material. Thus, this paper deals with the definition of the fragility curves for RC walls impacted by a snow avalanche. For a given magnitude of avalanche loading, a fragility curve provides the probability that the

RC wall would reach a given damage level.

Until now, very few fragility curves established within the context of snow avalanche risk are available. Indeed, most studies dedicated to the assessment of physical vulnerability to snow avalanches are dealing only with vulnerability curves and not fragility curves (Papathoma-Köhle et al., 2011). Vulnerability relations are often empirically assessed, based on historical observations (Keylock and Barbolini, 2001; Barbolini et al., 2004a; Cappabianca et al., 2008). Because these relations were deduced from scarce data which can be site dependent, the accuracy and the generalization of such relations is questionable. Recently, in order to propose an alternative way to derive vulnerability curves, Finite Element Analysis (FEA) was used to described the damage level of typical RC structures subjected to an avalanche pressure field (Bertrand et al., 2010). The main advantage of numerical approaches is to define and control accurately the studied structure (geometry, resistance, reproducibility, etc.).

Second, fragility curves are non homogeneously used with natural or anthropic hazards. For instance, the failure probability quantification of structures within an industrial context is currently undertaken (explosions (Low and Hao, 2001; Nassr et al., 2012), geotechnical works (Mollon et al., 2013), etc.). Besides, for multistorey buildings exposed to earthquake loadings, the probability to overpass a drift limit according to the peak ground acceleration is very often described *via* reliability-based fragility curves (Ellingwood, 2001; Kyung and Rosowsky, 2006; Li and Ellingwood, 2007; Lagaros, 2008). However, for rockfalls (Mavrouli and Corominas, 2010a,b), landslides or debris flows (Papathoma-Köhle et al., 2012), tephra falls (Spence et al., 2005), fragility curves are seldom used and vulnerability relations are preferred.

The failure probability assessment is based on the well-established framework of reliability analysis (Lemaire (2005)). Once the deterministic model and the failure criterion of the system are chosen, the uncertainties related to the random variables are propagated through the mechanical model to calculate the failure probability. Usually, simulation methods are used. These methods are more or less based on the Monte-Carlo approach and give robust results. However, they can be time consuming depending on the rapidity of the deterministic model. In some cases, if too many runs are needed to get a good accuracy of the failure probability or if the deterministic model is not effective enough in terms of CPU time, approximation methods can be alternatively used in order to lower the number of simulation calls. However, the convergence is not always ensured, depending, *inter alia*, on the non linearity of the deterministic model and on the number of random variables involved.

Alternative models to highly time-consuming models are preferred in reliability analysis. Reducing the calculation time can be made by performing simplifying assumptions on the mechanical model together with keeping the involved physics. Reinforced concrete

structures are broadly studied and various numerical models exist to describe the mechanical response of the structure and possibly its failure. For snow avalanche loadings, FEA have already been used in order to better understand the interaction between the avalanche and the RC structure. For instance, a FEA has been performed on deflective RC walls of the protection system of Taconnaz (Berthet-Rambaud, 2004; Ousset et al., 2013). Besides, typical structure geometries have been considered for residential buildings, *i.e.* three vertical walls with a U-like shape (Bertrand et al., 2010). Within a stochastic framework, the main drawback of these approaches is the CPU time needed to performed a single simulation. As an alternative, the mechanical capacity of a RC structure can be estimated using classical civil engineering abacuses allowing the use of reliability analysis. Thus, for a wide range of boundary conditions, the failure probability calculation of RC slabs impacted by snow avalanches has been proposed by Favier et al. (2014a). The main assumption consists in supposing that the response of the structure is quasi-static. Nevertheless, this approach does not account for potential inertial effects or strain rate effects due to the dynamical nature of the loading.

In order to find a compromise between simplified time effective models and refined models but time consuming, RC structures can be described using Single-Degree-of-Freedom (SDOF) approaches (Biggs, 1964). The structure is modeled by an equivalent mass and an equivalent spring. This approach has been largely used and validated in the field of structures subjected to blast loads (Ngo et al., 2007; Jones et al., 2009; Carta and Stochino, 2013). In this paper, a simply supported RC wall is considered and modeled by a SDOF approach. The model is able to describe the ultimate state of the RC wall, *i.e.* its collapse which corresponds to the ultimate bending moment which can be undergone. A FEA and limit analysis are used to validate the ultimate mechanical state predicted by the SDOF model. Then, several inputs of the SDOF model are randomized and a reliability analysis is performed in order to established fragility curves according to various simulation and approximation methods. A comparison of the relevance and efficacy of the reliability methods is proposed. Finally, a parametric study is presented which underlines the relation between random input variables and, particularly, the effect of variable correlations and the coefficients of variation of each variable.

3.2 Deterministic SDOF model

3.2.1 RC wall description

Geometry and loading

The considered RC wall is rectangular with a length L of 8m, a width b of 1m and a thickness h of 20cm (Figure 3.1a). The RC wall is simply supported along the two smaller

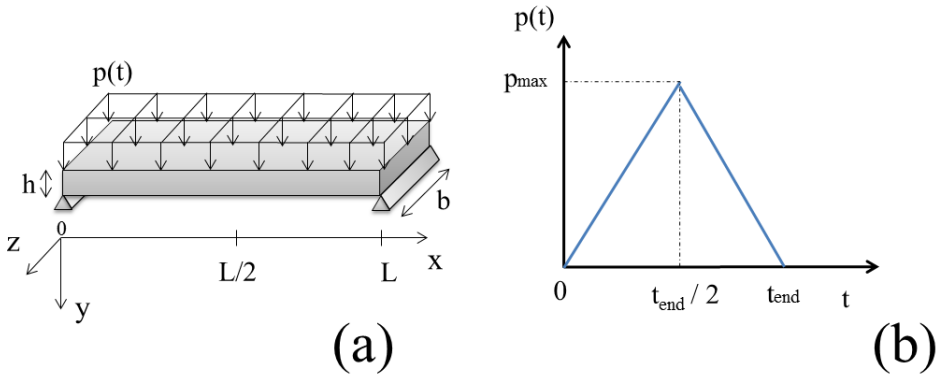

Figure 3.1 – Simply supported RC wall (a) and time evolution of the pressure (b).

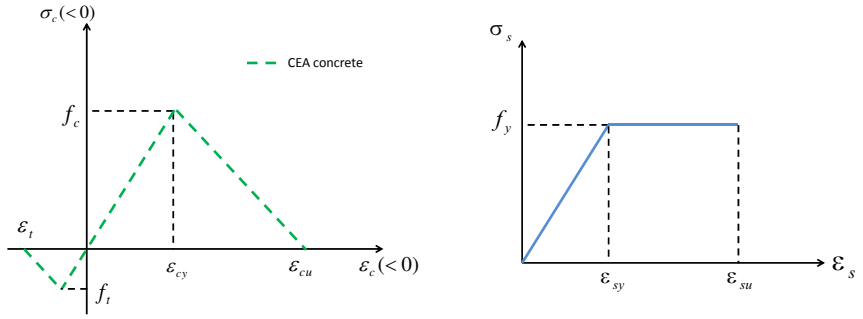

(a) Concrete. (b) Steel.

Figure 3.2 – Stress-strain relations for concrete (a) and steel (b).

edges. This boundary condition allows considering the system as a 2D problem and thus the RC wall can be assimilated to a simply supported beam.

The snow avalanche applies an uniform pressure $p(t)$ along the y axis which evolves through time from 0s to t_{end} up to the maximal pressure P_{max} which is reached for $t_{end}/2$. This time evolution is shown in figure 3.1b. The loading rate ($\frac{p_{max}}{t_{end}}$) is fixed at 0.3 kPa.s^{-1}.

Steel and concrete

Many stress-strain relations for concrete and steel are available in the literature (Bazant and Oh (1983); Mazars (1986); De Borst and Guitiérrez (1999); Wang and Hsu (2001); CEB-FIP (2010), etc.). As a function of the problem assumptions (cyclic loading, 3D formulation, etc.), the evolutions of the stress-strain relations can be more or less complex.

In this paper, the concrete and steel behaviour laws are piecewise linear relations describing the evolution of stress (σ_{xx}) as a function of strain (ϵ_{xx}) along the longitudinal axis x of the slab (Figure 3.2a).

The behaviour laws proposed by Leprêtre et al. (1988) have been used. The elastic part of the behaviours laws is described by the Young modulus of steel (E_s) and concrete (E_c). For concrete, compressive and tensile responses have been distinguished (Figure 3.2a). Under compression regime, the stress (σ_c) increases as a function of the strain (ϵ_c) up to the compressive strength of concrete (f_c) which corresponds to a strain of ϵ_{cy}. Then a negative hardening compressive behaviour develops. When the ultimate compressive strain (ϵ_{cu}) is reached, $\sigma_c = 0$. Under tensile regime, the same behaviour is qualitatively used. The tensile strength of concrete (f_t) and the ultimate tensile strain of concrete (ϵ_t) are involved. The strain associated to f_t equals $\epsilon_{ty} = f_t/E_c$. For steel, the behaviour law is supposed elastic perfectly plastic (Figure 3.2b). f_y is the yielding stress associated to the yield strain ϵ_{sy} and ϵ_{su} is the ultimate strain of steel.

Reinforced concrete is a composite material for which the quantity of steel included within concrete plays a major role. The steel reinforcement ratio (ρ_r) is defined as the ratio between the steel area (A_s) on the cross-section surface ($h \times b$) and equals 0.4%. Figure 3.3a depicts a cross sectional view of the RC wall.

3.2.2 SDOF model

The pressure is applied out-of-plan of the RC wall and thus bending and shearing efforts exist through cross-sections. Because the loading is uniformly applied and the time of loading is quite higher than the fundamental frequency of the structure (5Hz, thus an oscillation period of 0.2s), it can be assumed that the failure mode occurs by excessive bending at midspan (Figure 3.4c). Thus, it justifies to use SDOF modelling to represent the RC wall mechanical response.

The proposed SDOF model corresponds to a mass-spring system loaded by a uniform pressure (Figure 3.4a-b). An equivalent concentrated mass (M_{eq}) is maintained by a spring of stiffness K_{eq}. The expressions of M_{eq} and K_{eq} are deduced respectively from the deformed shape (Biggs, 1964) and from the Moment-Curvature relationship presented in the section 3.2.2. Finally, no viscous damping has been considered because, if the structure collapses, the failure criteria will be necessarily achieved during the loading phase and thus it is not necessary to account for the post peak oscillation regime.

Elasto-plastic overall response

The elasto-plastic behaviour of the SDOF model can be represented by a bilinear Load-Displacement curve which is derived from the Moment-Curvature ($M - \chi$) relationship

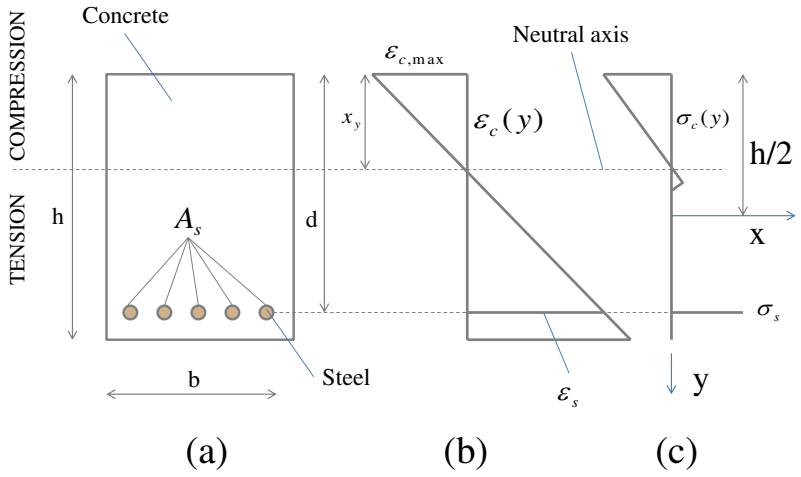

Figure 3.3 – Cross-section of the RC beam (a), stress diagram (b), strain diagram (c).

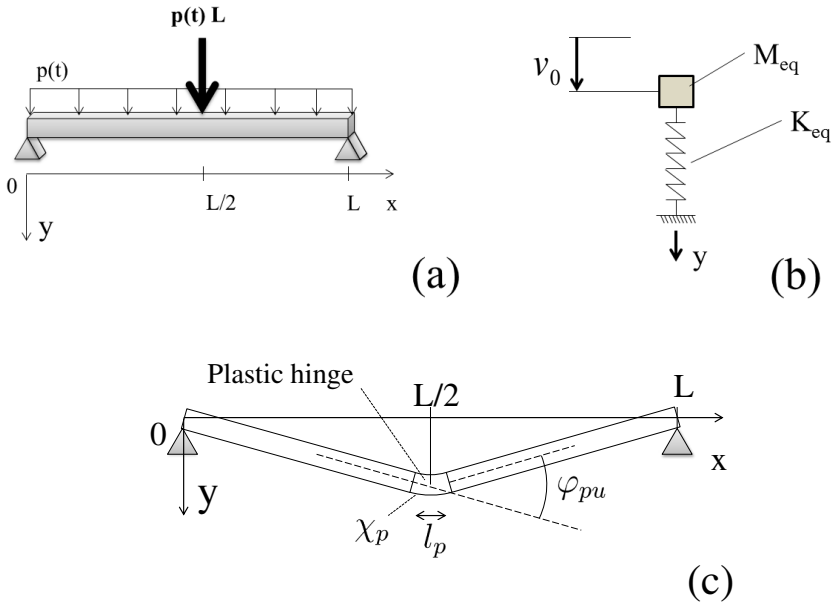

Figure 3.4 – Simply supported beam (a), mass-spring system (b) and failure mode of the RC wall (c).

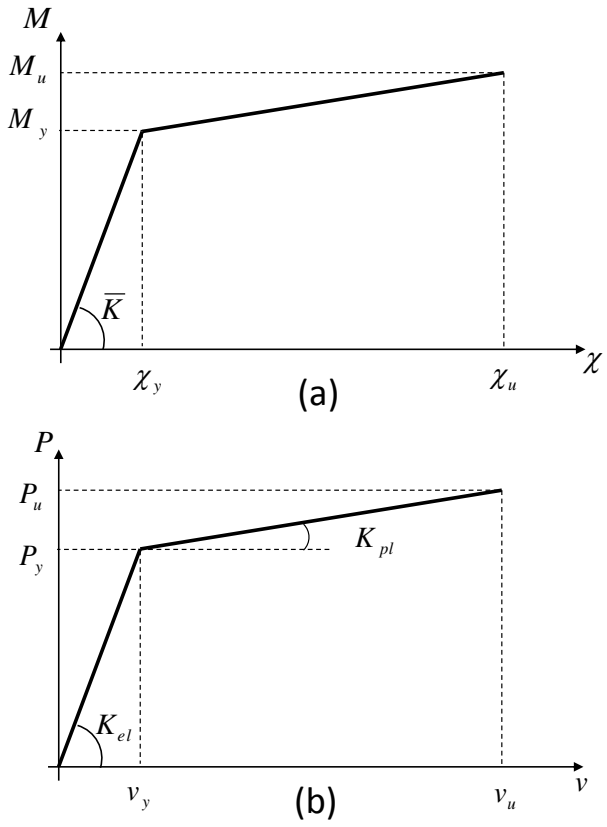

Figure 3.5 – Bending moment - Curvature relation (a) and load-displacement relation of the SDOF model (b).

deduced at the cross-section scale (*cf.* paragraph 3.2.2). The bending moment M_y corresponds to the beginning of either steel yielding or concrete crushing depending on the reinforcement ratio. The ultimate bending moment M_u corresponds to the achievement of the ultimate strain value either within concrete or steel. Related curvatures are χ_y and χ_u.

The first part of the Load-Displacement bilinear curve represents the elastic response and the second part is the plastic response of the RC wall. Two forces are respectively expressed such as $P_y = \frac{8M_y}{L}$ and $P_u = \frac{8M_u}{L}$ which can be transformed into a uniform pressure as $p = P/L$ (Figure 3.4a). Then, the expression of the midspan displacement corresponding to the transition from elastic to plastic is

$$v_y = \frac{5P_yL^3}{384\overline{K}} \ , \tag{3.1}$$

where $\overline{K} = \frac{M_y}{\chi_y}$ which is the bending stiffness of the RC wall. The ultimate midspan displacement is deduced from

$$v_u = v_y + \frac{1}{4}(\chi_u - \chi_y)\, L\, l_p \ , \tag{3.2}$$

where l_p is the plastic hinge length (Figure 3.3c) which can be estimated by the relation $l_p = d + 0.05L$ (Mattock, 1967) where d is the effective depth of the cross-section (Figure 3.3a). Finally, the Load-Displacement curve (Figure 3.5b) has two stiffnesses which are defined such as

$$K_{el} = \frac{P_y}{v_y} \ , \tag{3.3}$$

$$K_{pl} = \frac{P_u - P_y}{v_u - v_y} \ . \tag{3.4}$$

Moment-Curvature relationship

The curvature, defined as $\chi = \frac{\partial^2 v_o}{\partial x^2}$ where v_o is the midspan displacement, is obtained assuming that the strain distribution along the y axis follows classical Euler-Bernoulli assumptions which means that sections remain plane and orthogonal to the neutral axis during the loading of the RC wall (Figure 3.3b). Thus, the curvature can be calculated by

$$\chi = \frac{\epsilon_c(y = -\frac{h}{2})}{x_y} = \frac{\epsilon_s(y = d - \frac{h}{2})}{d - x_y} \ , \tag{3.5}$$

where x_y is the neutral axis depth. x_y is deduced from the translational mechanical balance along x of the cross-section which can be expressed by the equation

$$b\int_0^{x_y}\sigma_c dy = \sigma_s A_s + b\int_{x_y}^{h}\sigma_c dy \ . \tag{3.6}$$

The Moment-Curvature relationship is constructed step by step by calculating the position of the neutral axis for a given strain distribution, *i.e.* a given curvature χ, which fulfil the condition of equation 3.6. Then, the bending moment is calculated from

$$M(\chi) = b\int_0^{x_y}\sigma_c(d-y)dy \ . \tag{3.7}$$

At the end of the process, M_y, M_u, χ_y and χ_u are identified on the $M-\chi$ curve and used to derive the Load-Displacement curve of the SDOF model.

Equations of motion

By applying the fundamental principle of dynamics, the mechanical balance of the SDOF leads to the following differential equations. For the elastic phase ($0 < v_o < v_y$), it comes:

$$M_{el}\frac{d^2v_o(t)}{dt^2} + K_{el}v_o(t) = P(t) \ , \tag{3.8}$$

and, for the plastic phase ($v_y < v_o < v_u$):

$$M_{pl}\frac{d^2v_o(t)}{dt^2} + K_{pl}v_o(t) + (K_{el}-K_{pl})v_y = P(t) \ , \tag{3.9}$$

where $P(t)$ is the time evolution of the external force deduced from the uniform pressure $p(t)$ applied to the RC wall. In order to solve through time equations 3.8 and 3.9, usual Newmark's algorithm technics have been used (Newmark, 1959).

3.2.3 Validation

Finite Element Analysis

In order to validated the SDOF model, a Finite Element simulation of the RC wall response to avalanche loading has been undertaken with the computational software Cast3M (Millard, 1993). The analysis is carried out in 2D (plane stress). Concrete (resp. steel) is meshed using eight node quadrilateral (resp. two node segment) finite elements (Figure 3.6a). 100 finite elements are placed along the x axis and 10 along the y axis. A perfect adhesion between concrete and steel is supposed and thus no slip can occurs. The same behaviour laws previously described are adopted but formulated here in plane stress conditions.

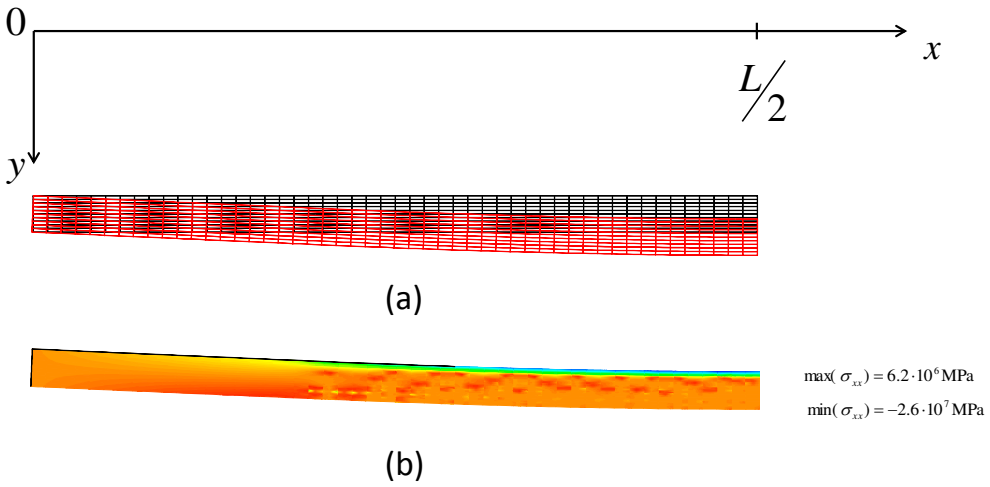

Figure 3.6 – Mesh of the FEA in black and deformed shape in red (a) and stress field (σ_{xx}) at the collapse pressure (b).

A uniform pressure is applied. As for a pushover test, the loading increases linearly up to reach either the ultimate strain within steel or concrete. Thus, the midspan displacement can be expressed as a function of the pressure applied. The stress field at the collapse is depicted in figure 3.6b.

Furthermore, a modal analysis has been carried out. The first (resp. the second) mode of vibration has a frequency of 4.92Hz (resp. 19.64Hz) which match the theoretical values 4.91Hz (resp. 19.63Hz).

Limit analysis

The ultimate resistance of RC slabs under uniformly distributed pressure can be derived from the classical yield line theory (Johansen, 1962) which also provides the collapse mechanism of the RC member. Under an external loading, macrocracks will develop to form a pattern of "yield lines" until a mechanism is formed and leads to the collapse. A yield line corresponds to a nearly straight line along which a plastic hinge develops where the bending moment becomes constant and equals the plastic bending moment. The ultimate pressure is deducted from the energy balance between external and internal energies. The external energy coming from the loading and the internal energy is due to energy dissipation within the yield lines.

For a one-way simply supported slab, the only collapse mechanism that can arise is

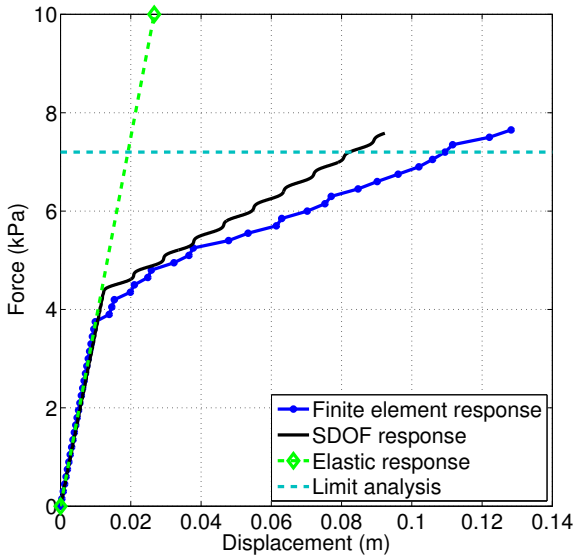

Figure 3.7 – Load-displacement curve obtained with FEA and SDOF model. The green curve represents the elastic response of a beam loaded by a uniform pressure.

depicted in figure 3.4c. Under an uniform pressure, a single yield line would develop at mispan and thus, for a given arbitrary midspan rotation θ, the internal work ($2\theta M_p$) equals the external work ($2\int_0^{\frac{L}{2}} \theta\, x\, q dx = \theta\frac{qL^2}{4}$) and finally leads to the ultimate pressure $q_{YLT} = \frac{8M_p}{L^2}$ where M_p is the plastic bending moment of the RC member. M_p can be obtained by (Favre et al., 1990):

$$M_p = A_s\, f_y\, 0.9\, d\ , \tag{3.10}$$

which leads to $M_p = 57.5$ kN.m and finally $q_{YLT} = 7.2$ kN.m^2.

Results comparison

Table 3.1 summarizes inputs of FE and SDOF models and Table 3.2 gives a comparison of ultimate displacement, ultimate pressure and computation time. Results are compared in figure 3.7 which demonstrates that Load-displacement curves of both models are in good agreement. The elastic regime is accurately reproduced by the SDOF model. Moreover, the ultimate pressure is also well predicted. The limit analysis gives the same result. A slight difference can be noticed concerning the ultimate displacement which is higher in the case of the FEA. It can be explained by the formulation of the behaviours laws. Indeed, in the case of FEA, the plane stress assumption leads to enable stress redistribution which

Parameters	Symbol	Value
Length	L	8 m
Width	b	1 m
Thickness	h	20 cm
Concrete cover	e_{exc}	4 cm
Mass density (S)	ρ_s	7500 $kg.m^{-3}$
Mass density (C)	ρ_c	2500 $kg.m^{-3}$
Young modulus (S)	E_s	200 GPa
Young modulus (C)	E_c	30 GPa
Poisson ratio (S)*	ν_s	0.3
Poisson ratio (C)*	ν_c	0.2
Ult. tensile strain (S)	ϵ_{su}	0.01
Ult. compressive strain (C)	ϵ_{cu}	-0.0035
Ult. tensile strain (C)	ϵ_t	$3f_t/E_c = 4.10^{-4}$
Ult. tensile strength (C)	f_t	4 MPa
Ult. compressive strength (C)	f_c	30 MPa
Reinforcement ratio	ρ_r	0.4%
Yield strength (S)	f_y	500 MPa
Ult. bi-compressive strength (C)*	f_{bic}	$1.15f_c$

Table 3.1 – Parameter values for models comparison (* only needed in the FEM model due to plane stress formulation). The following notations are adopted : Ult. means Ultimate, S (resp. C) means Steel (resp. Concrete).

cannot be accounted for by the SDOF approach and leads to a the stiffer response of the SDOF. Within a reliability context, those observations ensure the SDOF model to provide conservative and hence safe results for ultimate state prediction of the RC wall.

Finally, the computational time of each approach is compared (Table 3.2). With the same computer, a computation time of 40 minutes is needed for the FE analysis whereas the SDOF model runs and finish calculations in less than half a minute. Limit analysis can be time effective but only provides the ultimate pressure.

3.3 Vulnerability assessment

3.3.1 Failure probability

In a reliability framework, model inputs (x) allows defining the Probability Density Function (PDF) $f_R(r)$ which represents the structure resistance (or structure capacity) and

Models	Ult. pressure	Ult. displacement	Comp. time
SDOF	7.58 kPa	0.0923 m	~ 35 s
FEA	7.65 kPa	0.1283 m	~ 40 min
Limit Analysis	7.56 kPa	–	~ 0.2 s

Table 3.2 – Ultimate displacement, ultimate pressure and CPU time provided by the three approaches.

where r is the capacity of the structure for a given input vector x. For a solicitation s, the failure probability is obtained by (Lemaire, 2005)

$$P_f(s) = P(r \leq s) = \int_{-\infty}^{s} f_R(r)\,\mathrm{d}r \tag{3.11}$$

The capacity r of the RC wall is defined by the ultimate pressure p_u. The fragility curve is the Cumulative Density Function (CDF) of the structure capacity according to the ultimate pressure limit state and gives the failure probability as a function of the pressure magnitude applied to the structure (p). In the following, PDF inputs distributions are presented. Then, the different methods to derive fragility curves are exposed.

3.3.2 Inputs statistical distributions

Two classes of inputs are considered as random variables: geometrical (L, b and h) and strength (f_t, f_c, f_y and ρ_r) parameters. The mean value of the input vector refers to the deterministic case (Table 3.1). The inputs variables are supposed either independent or correlated.

First, input distributions are normal PDF and no correlation is supposed between random variables. Values of Coefficients Of Variation (COV) are considered through three typical cases. First, 5% is often used when no specific COV values are available (Tab. 3.3, sets (1.α.a)). Second, values can be proposed from literature justifications (sets (2.β.b)). The last set (sets (3.γ.c)) corresponds to the deterministic point of view (COV=0).

Then, random variable correlation is assumed between strength parameters (f_t, f_c and f_y). The variable correlation is taken into account following the Joint Comity of Structural Safety recommendations (Joint Committee on Structural Safety, 2001).

Marginal PDF distributions

To describe geometrical uncertainties, normal distributions are largely assumed (Lu et al., 1994; Val et al., 1997; Low and Hao, 2002; Kassem et al., 2013). COV are usually taken in a range from 0.01 to 0.07. Three sets (1, 2, 3) of COV are tested using normal distributions (Table 3.3).

Inputs	Mean	COV		
		set 1	**set 2**	**set 3**
L	8m	0.05	0.03	determ.
b	4m	0.05	0.03	determ.
h	20cm	0.05	0.03	determ.
		set α	**set β**	**set γ**
ρ_r	0.4%	0.05	0.03	determ.
		set a	**set b**	**set c**
f_t	4MPa	0.05	0.18	determ.
f_c	30MPa	0.05	0.18	determ.
f_y	500MPa	0.05	0.08	determ.

Table 3.3 – Marginal distributions of inputs parameters. "determ." means deterministic which corresponds to a COV equals to zero. In the case of independent variables, normal distributions are used.

Concerning strength parameters, in a first approximation, normal distributions with a COV of 0.05 are considered (set a). In a second step, more realistic COV are used (set b). For the compressive strength of concrete f_c the normal distribution is an usual choice (Mirza et al., 1979; Val et al., 1997; Low and Hao, 2001, 2002) and COV ranging between 0.11 and 0.18 are generally used. Here, a COV of 0.18 is used. For the tensile strength of the concrete, a normal distribution with a COV of 0.18 can also be assumed (MacGregor et al., 1983). Finally, for f_y, normal, lognormal or beta distributions are often proposed (MacGregor et al., 1983) and the COV varies from 0.08 to 0.11 (Val et al., 1997). In the paper, a normal distribution is adopted and the COV equals 0.08. All these choices are summarized in Table 3.3.

Eventually, no datum is already available about the reinforcement ratio's COV. Because ρ_r is defined from geometrical parameters, a normal PDF is assumed and COV is supposed equal to 0.03 or 0.05, depending on the set considered (Table 3.3).

Strength parameters correlation

The case of strength parameter correlation is also considered. The JCSS (Joint Committee on Structural Safety, 2001) proposed more realistic distribution descriptions by accounting for their potential dependencies.

The concrete tensile strength (f_t) is expressed according to the compressive strength of the concrete f_c. The distribution of f_c is deduced from the basic concrete compression strength f_{c28} distribution. For a ready-mixed concrete type with a $C25$ concrete grade, it

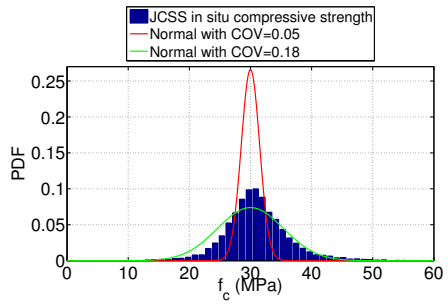

(a) Concrete compressive strength parameter f_c.

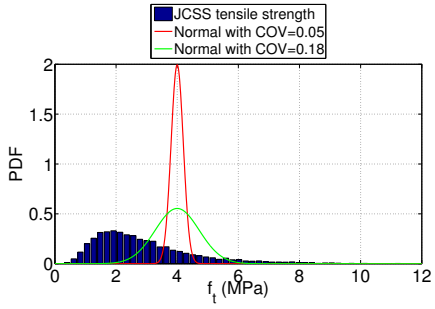

(b) Concrete tensile strength parameter f_t.

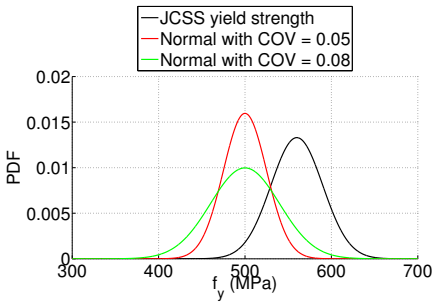

(c) Steel yield strength parameter f_y.

Figure 3.8 – Statistical distributions for f_c, f_t and f_y according to Tab. 3.3, and comparison with JCSS distributions.

yields:

$$f_{c28} = exp(m + t_v s(1 + \frac{1}{n})^{0.5}), \tag{3.12}$$

where the values of the parameters m, v, s, n are: $m = 3.65$, $v = 3.0$, $s = 0.12$, $n = 10$ and, t_v is a random variable from a Student distribution with v degrees of freedom. Then, f_t and f_c are calculated with λ, Y_1 and, Y_2. The parameter λ is taken equal to 0.96 and is a factor taking into account the systematic variation of *in situ* compressive strength and the strength from standard tests. The coefficient α_c equals 0.92. Finally, $(Y_i)_{i=1,2}$ are log-normal variables representing additional variations due to special placing, curing, and hardening of the concrete:

$$f_c = \alpha_c f_{c28}^{\lambda} Y_1, \tag{3.13}$$

$$f_t = 0.3 f_c^{2/3} Y_2, \tag{3.14}$$

where Y_1 and Y_2 means are 1 and their respective coefficients of variation are 0.06 and 0.3. For all other parameters, the marginal mean and standard deviation were also set according to the JCSS recommendation.

For the yield strength of steel (f_y) and based on JCSS assumptions, a normal distribution can be adopted with a mean of 560 MPa and a COV of 0.054. Figure 3.8 depicts strength parameter distributions used in this paper and underlines observed differences related to f_y and f_t PDF definitions.

3.3.3 Reliability methods

From inputs PDF distributions (x) and by propagating uncertainties through the deterministic model (M), output PDF distribution ($f_R(r)$) can be obtained ((Saltelli et al., 2004; Faivre et al., 2013)). As the capacity r of the RC wall is defined by the ultimate pressure p_u, the output PDF distribution can be noted ($f_{p_u}(p_u)$). Two approaches are considered. Either the output is described through the direct approximation of its PDF or by the estimation of the output's moments (mean and variance). In order to perform these calculations, effective methods exist such as Kernel Smoothing (KS) or Taylor Expansion (TE) (Lemaire, 2005).

Kernel Smoothing

Direct MC simulations of input variables can provide a discrete PDF distribution of model's outputs. However, the resulting curve is a piecewise linear function. KS allows approximating the output PDF distribution considering a normal kernel function K

such as

$$\hat{f_{p_u}}(p_u) = \frac{1}{nh_K} \sum_{i=1}^{n} K\left(\frac{p_u - p_u^{(i)}}{h_K}\right) , \tag{3.15}$$

where $p_u^{(i)}$ is the i^{th} component of the output sample of ultimate pressure of size n and the kernel function is expressed as

$$K(x) = \frac{1}{\sqrt{2\pi}} e^{-\frac{1}{2}x^2} , \tag{3.16}$$

and h_K is the optimal bandwidth which is evaluated with *Silverman* rule (Wand and Jones, 1995).

Taylor Expansion

Mean and variance of the output vector of a model M can be calculated directly from MC simulations but this can be time consuming. TE allows approximating the output moments of the model more quickly. The moment approximations suppose that the mean of the output (μ_{p_u}) can be well estimated by model TE around the input mean (μ_x). The mean ($\hat{\mu}_{p_u}$) and variance ($\hat{\sigma}^2_{p_u}$) of the output p_u are approximated though the following expressions:

$$\hat{\mu}_{p_u} = M(\mu_x) + \frac{1}{2} \sum_{i,k=1}^{m} \frac{\partial^2 M}{\partial x_i \partial x_k}(\mu_x)\, \mathbb{C}_{ik} , \tag{3.17}$$

$$\hat{\sigma}^2_{p_u} = \sum_{i,k=1}^{m} \frac{\partial M}{\partial x_i}(\mu_x) \frac{\partial M}{\partial x_k}(\mu_x)\, \mathbb{C}_{ik} , \tag{3.18}$$

where m is the number of input variables, μ_x is the mean of the input vector x and $\mathbb{C}_{ik}$ is the ik component of the variance-covariance matrix of x. The non linearity of the deterministic model should not be too strong in order to ensure a satisfactory approximation of the second partial derivatives of the model and, hence, of the results $\hat{\mu}_{p_u}$ and $\hat{\sigma}^2_{p_u}$ provided by this method. If no covariances is considered ($\mathbb{C}_{ik} = 0$ if $i \neq k$), preceding equations can be rewritten more simply as

$$\hat{\mu}_{p_u} = M(\mu_x) + \frac{1}{2} \sum_{i=1}^{m} \frac{\partial^2 M}{\partial x_i^2}(\mu_x)\, \mathbb{C}_{ii} , \tag{3.19}$$

$$\hat{\sigma}^2_{p_u} = \sum_{i=1}^{m} \left(\frac{\partial M}{\partial x_i}(\mu_x)\right)^2 \mathbb{C}_{ii} . \tag{3.20}$$

3.3.4 Fragility curves derivation

Four methods are proposed to derive fragility curves. First, non-parametric approaches are exposed (crude MC simulations and MC simulations combined with Kernel Smoothing (KS)) and then parametric estimation methods are presented (TE-based method and Maximum Likelihood Estimation (MLE) method). Non parametric approaches consist in a direct estimation deriving the fragility curve without performing any assumptions regarding the form of the output function. Parametric approaches consist in assuming the shape of the output PDF distribution and approximating its constitutive parameters. The OpenTURNS software is dedicated to the treatment of the uncertainty, risk and statistics, its extensive reliability methods library was used to build fragility curves.

Empirical CDF *via* crude MC simulations (ECDF)

Fragility curves can be assessed directly by crude MC simulations such as

$$\hat{P}_f(p_u) = \frac{1}{n}\sum_{i=1}^{n} I\left((p_u^{(i)} \leq p_u\right) \ , \tag{3.21}$$

where p is the external pressure applied to the RC wall, $p_u^{(i)}$ corresponds to the ultimate pressure of the i^{th} simulated RC wall, and n is the number of simulations. The indicator function $I(p_u \geq p_u^{(i)})$ equals 1 if the structure collapses and 0 otherwise. Because of CPU time limitations, the resulting Empirical CDF (ECDF) is often a rough but robust approximation. Another limitation is that the ECDF is non differentiable and non strictly monotonous.

MC using KS approximation (MCKS)

By contrary to crude MC approaches, smoothing methods allows obtaining strictly monotonous and bijective curves. An approximation of the fragility curve can be expressed integrating out equation (3.15), which gives the following expression

$$\hat{P}_f(p_u) = \int_{-\infty}^{p_u} \hat{f_{p_u}}(q)\,\mathrm{d}q \ . \tag{3.22}$$

TE using log-normal and normal CDF (TECDF)

If the shape of the fragility curve is postulated (normal or lognormal CDF), the CDF distribution can be deduced from its first ($\hat{\mu}_{p_u}$) and second ($\hat{\sigma}_{p_u}$) central moments approximation based on TE (Equations (3.17) and (3.18)). For an assumed normal CDF F_N, the following expression comes

$$\hat{P}_f(p_u) = F_N(p_u|\hat{\mu}_{p_u}, \hat{\sigma}_{p_u}) = \phi\left(\frac{p_u - \hat{\mu}_{p_u}}{\hat{\sigma}_{p_u}}\right) \ , \tag{3.23}$$

where $\phi(x) = \int_{-\infty}^{x} \frac{1}{\sqrt{2\pi}} e^{\frac{-u^2}{2}} \mathrm{d}u$ is the CDF of the standard normal distribution.

For an assumed log-normal CDF, the estimators $(\mu_{\hat{LN}}, \sigma_{\hat{LN}})$ are deduced from the following relations:

$$\mu_{\hat{LN}} = \log\left(\frac{\hat{\mu}_{p_u}^2}{\sqrt{\hat{\sigma}_{p_u}^2 + \hat{\mu}_{p_u}^2}}\right) \quad \text{and} \quad \sigma_{\hat{LN}} = \sqrt{\log\left(\frac{\hat{\sigma}_{p_u}^2}{\hat{\mu}_{p_u}^2}\right) + 1} \ . \tag{3.24}$$

A random variable has a log-normal CDF distribution ($\mu_{\hat{LN}}$ and $\sigma_{\hat{LN}}$) if its logarithm has a normal PDF with mean $\mu_{\hat{LN}}$ and standard deviation $\sigma_{\hat{LN}}$. Then, the fragility curve can be approximated by the log-normal CDF F_{LN}

$$\hat{P}_f(p_u) = F_{LN}(p_u|\mu_{\hat{LN}}, \sigma_{\hat{LN}}) = \phi\left(\frac{\log(p_u) - \mu_{\hat{LN}}}{\sigma_{\hat{LN}}}\right) \ . \tag{3.25}$$

MLE using log-normal and normal CDF (MLECDF)

From the MC sampling, the output CDF can be also fitted assuming the fragility curve shape. MLE allows calculating estimators $\hat{\mu_j}^{MLE}$ and $\hat{\sigma}_j^{MLE}$ for the normal or the log normal CDF. $\hat{\mu_j}^{MLE}$ and $\hat{\sigma}_j^{MLE}$ aim at maximizing the probability of having obtained the sample actually at hand (Fisher, 1922). Fragility curves are expressed as:

$$\hat{P}_f(p_u) = F_j(p_u|\hat{\mu_j}^{MLE}, \hat{\sigma}_j^{MLE}) \ , \tag{3.26}$$

where $\hat{\mu_j}^{MLE}$ and $\hat{\sigma}_j^{MLE}$ are, respectively, the mean and variance MLE estimate of the output PDF; j equals N (resp. LN) in the case of a normal (resp. log-normal) CDF.

3.4 Results

3.4.1 Reliability methods comparisons

The comparison between each methods is carried out using the input PDF defined by the set $(1.\alpha.a)$ where all COVs are fixed to 0.05. For the reliability methods using MC simulations (ECDF, MLECDF and MCKS), the number of simulations is set to respectively 30, 300 and $1,000$. The ECDF method is the most robust and its accuracy increases with the MC sample size. Thus, the reference fragility curve is derived by the $1,000$ simulations ECDF sample (Figure 3.9a).

Depending on the expected fragility range (the pressure range on which the CDF increases from ≈ 0 to ≈ 1), a large number of simulations can be needed to obtain smooth fragility curves. Since the MCKS method by definition smooths the CDF curve approximation, fewer simulations than with ECDF method are required to obtain a valid

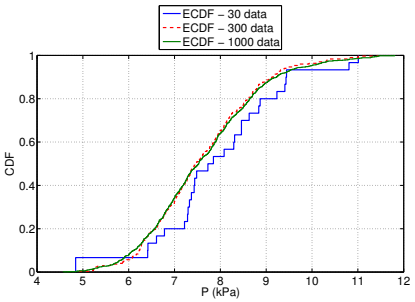

(a) ECDF method

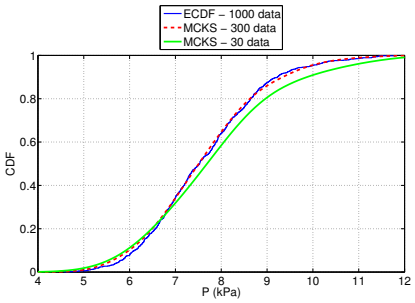

(b) MCKS method

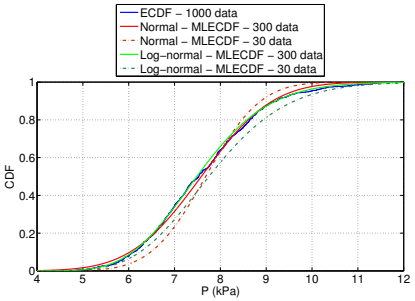

(c) MLECDF method for normal and log-normal assumed CDF

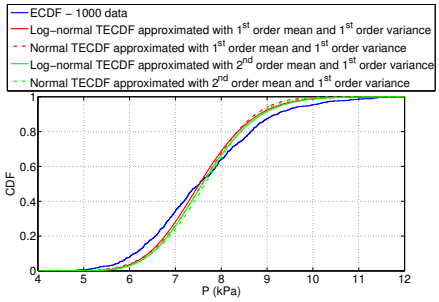

(d) TECDF method for 1^{st} and 1^{nd} order approximations of $\hat{\mu_{p_u}}$ and $\hat{\sigma_{p_u}}$.

Figure 3.9 – Reliability methods comparisons.

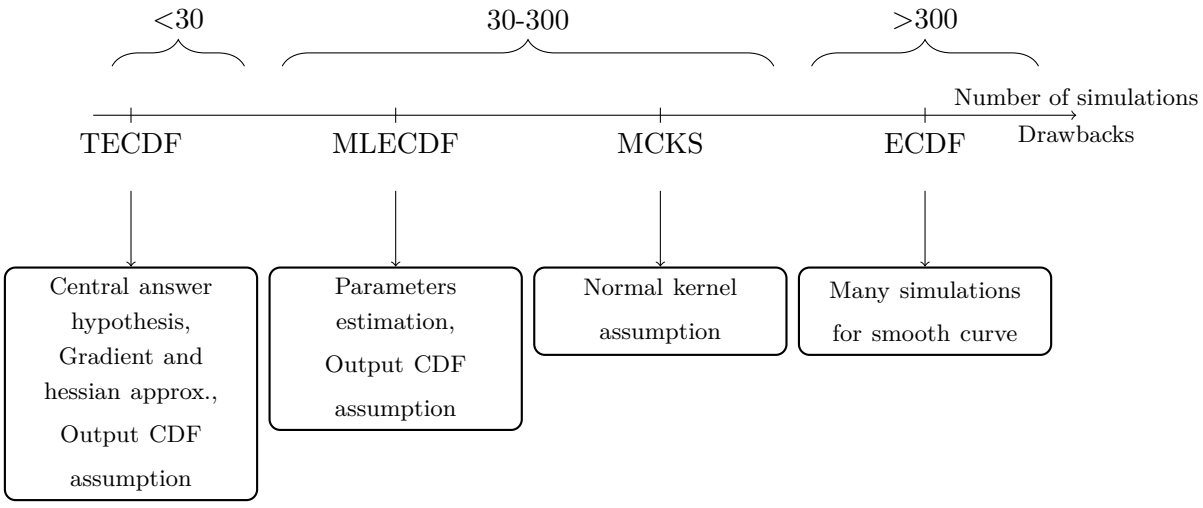

Figure 3.10 – Advantages and drawbacks of each method to derive fragility curves

curve (Figure 3.9b). The same conclusion can be drawn in the case of MLECDF method, which by definition always lead to smooth curves. A significant effect of the assumed output CDF can be noticed for low simulation numbers but it disappeared when 300 simulations are performed (Figure 3.9c).

In the case of the TECDF method, the approximation of the first and the second centred moments combined with normal or log-normal CDF needs only 15 simulations at the 1^{st} order. One simulation allows approximating the mean at the 1^{st} order and 14 simulations allow approximating the variance at the 1^{st} order. The 2^{nd} order mean estimation needs 113 simulations. For TECDF method, the approximation of fragility curve exhibits slight differences compared to the ECDF fragility curve whatever the assumed output CDF (Figure 3.9d). This method is based on the assumption that a good estimator of the output mean of the model can be calculated with the mean of input variables (central answer). This assumption is fully valid when the deterministic model is linear. Thus, the observed differences can be due to the non-linearity of the SDOF model. Nevertheless, if non linearities of the deterministic model are not too significant, few simulations are needed which allows deriving quickly fragility curves. The efficiency and drawbacks of each methods are summed up in the scheme of figure 3.10. To conduct the sensibility analysis of fragility curves, the kernel smoothing method is a good compromise. It allows to take into account possible non-linearities of the deterministic model and to obtain smooth curves without too much MC simulations and without any assumption on the shape of the fragility curve.

3.4.2 Fragility curve sensitivity to inputs

Input PDF effect

Four cases are considered. First, all COVs are set to 0.05 (set $1.\alpha.a$). Second, COVs are set to their maximal value deduced from the literature (set $1.\alpha.b$). Intermediate COV values (set $2.\beta.b$) are used for the third case. These latter combinations involve independent random variables. The last case used JCSS PDF distributions (set $2.\beta.J$, J refering to section 3.3.2) where correlation between strength parameters is accounted for. The derived fragility curves are depicted in figure 3.11.

Independent input PDFs give similar fragility curves when they are centered around the same nominal values. For the three independent cases, the 50% quantile is similar and the fragility range, defined as the interval between the 2.5% and 97.5% quantile, varies slightly (Table 3.4). The more the COV have important values, the more the fragility curve is spread. Finally, correlations between strength parameters induce a shift of the fragility curve toward higher pressures.

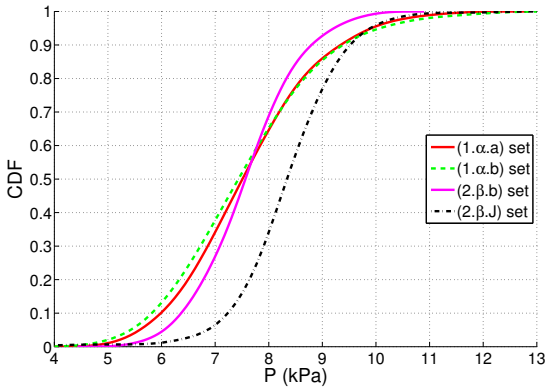

Figure 3.11 – Vulnerability depending on types of statistical inputs PDF based on MCKS method.

Input PDF set	2.5%	50%	97.5%
set $(1.\alpha.a)$	5.6	7.5	9.9
set $(1.\alpha.b)$	5.4	7.4	10.1
set $(2.\beta.b)$	6.0	7.6	9.2
set $(2.\beta.J)$	6.9	8.3	9.9
set $(3.\alpha.a)$	6.7	7.57	8.4
set $(3.\gamma.a)$	6.9	7.59	8.2
set $(3.\gamma.c)$	(-)	7.56	(-)

Table 3.4 – The 2.5%, 50% and 97.5% quantiles (in kPa) of the fragility curves according to the input PDF reference set. J refers to section 3.3.2.

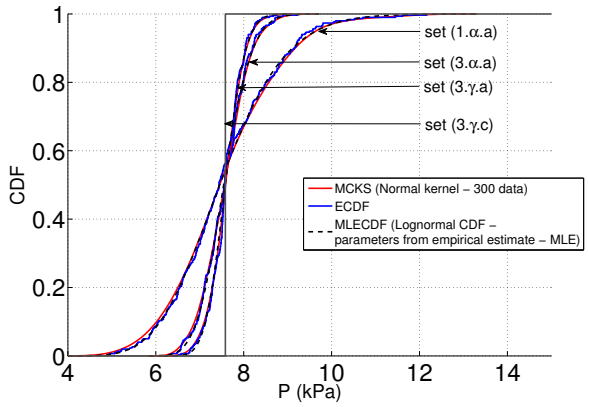

Figure 3.12 – Effect on fragility curves of the number and the class of input parameters. The black curve corresponds to the determinist case. Red (resp. blue and black dashed) curves are derived from MCKS (resp. ECDF and MLECDF) method.

Number and class of random variables

Three combinations of input PDFs are considered. First, the deterministic case (set $3.\gamma.c$) is taken as the reference fragility curve. Second, only geometrical inputs are supposed deterministic (set $3.\alpha.a$). Third, only the material strength parameters are described as random variables (set $3.\gamma.a$). Finally, all the input variables are considered as random variables (set $1.\alpha.a$). Results are presented in figure 3.12.

The number of inputs random parameters controls the fragility curve spreading (Tab. 3.4). If the geometrical uncertainties are not considered, the fragility range drops from $[5.6 - 9.9]$ kPa to $[6.7 - 8.4]$ kPa. Assuming the reinforcement ratio as deterministic, the fragility range drops from $[6.7 - 8.4]$ kPa to $[6.9 - 8.2]$ kPa. The more random input variables are considered, the more wide is the fragility range. Finally, one can notice the asymmetry of the fragility range even if inputs distributions are symmetric (normal PDFs).

3.4.3 Effect of physical parameters

Length effect

The ultimate pressure value (p_u) is significantly influenced by the nominal length of the RC wall (Figure 3.13a). The longer the RC wall is, the lower the ultimate pressure is ($P_u = \frac{8M_u}{L}$). The 2.5%, 50% and 97.5% quantiles underline the fragility curve spreading (Table 3.5). In a semi log-scale, the fragility range is almost the same for each fragility

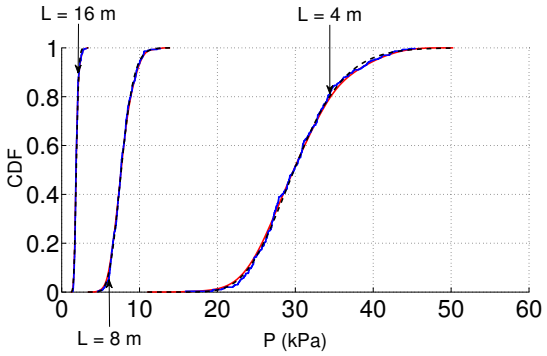

(a) Linear scale.

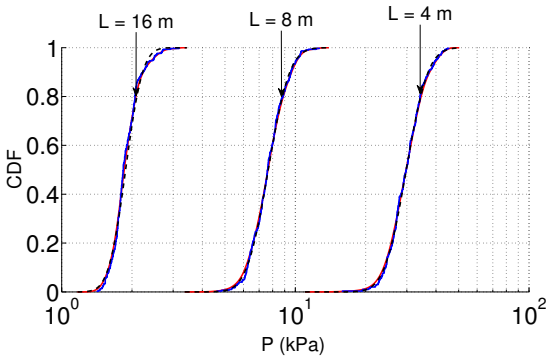

(b) Semi Log scale.

Figure 3.13 – Effect of the length of the RC wall on fragility curves. Red (resp. blue and black dashed) curves are derived from MCKS (resp. ECDF and MLECDF (log-normal)) method.

RC wall length (L)	2.5%	50%	97.5%
4 m	22.4	29.79	40.3
8 m	5.6	7.45	9.9
16 m	1.5	1.85	2.4
Reinforcement Ratio (ρ_r)			
0.3%	5.2	5.8	6.2
0.4%	6.9	7.6	8.2
0.5%	8.6	9.3	9.9
1.8%	17.4	18.8	20.4

Table 3.5 – The 2.5%, 50% and 97.5% quantiles (in kPa) of the fragility curves according to the length and reinforcement ratio.

curve (Figure 3.13b). If the fragility range spreading is normalized by the 50% quantile ($(Q_{97.5\%} - Q_{2.5\%})/Q_{50\%}$) it leads to 0.48, 0.58 and 0.60 for respectively 16m, 8m and 4m.

Reinforcement ratio

The influence of reinforcement ratio is explored for several typical values. Lower the reinforcement ratio is, lower the ultimate pressure is (Figure 3.14). The values of the 50% quantile are presented in Table 3.5. In a semi-log scale (Figure 3.14b), fragility range spreading is almost the same for each fragility curves respectively to the 50%-quantile.

Because, the reinforcement ratio plays an important role in the failure mode of the structure, high density reinforcement ratio is tested (1.8%). For a low reinforcement ratio ($< 1\%$), the failure of the RC member occurs by reaching the ultimate stain within steel. On the contrary, for a high reinforcement ratio, the concrete reaches its ultimate strain first. This aspect is implicitly taken into account by the Bending moment-Curvature relationship. Nevertheless, for highly reinforced RC members, the failure mode can change depending on the magnitude of traversal shearing forces (along y axis) and, thus, a bending failure mode can be questionable when the length of the RC wall becomes small.

Loading rate effect

Depending on the structure mechanical features and the snow avalanche loading, inertial effects can develop and modify the structural response through time. For all the previous results, a loading rate of 0.3 kPa.s^{-1} has been used. In order to assess the SDOF model sensibility to loading rate, higher values were tested: 6 and 10 kPa.s^{-1}. Resulting fragility curves are depicted in figure 3.15. For higher loading rates, inertial effects are more predominant, which leads to an artificial increase of the structure strength. However, this

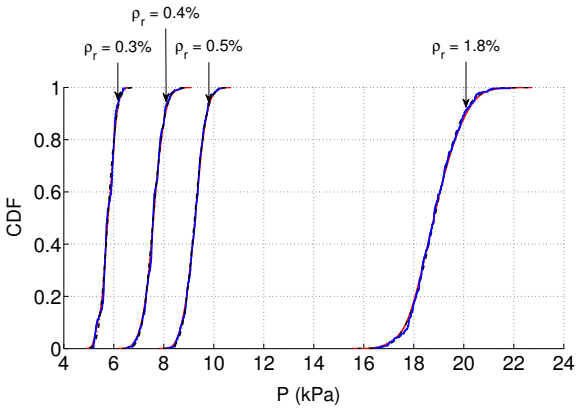

(a) Linear scale.

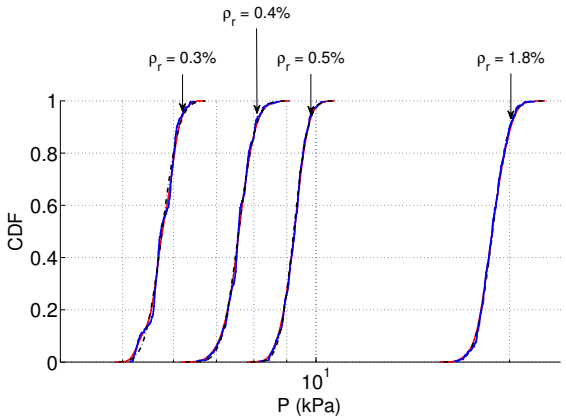

(b) Semi Log scale.

Figure 3.14 – Effect of the reinforcement ratio on fragility curves. Red (resp. blue and black dashed) curves are derived from MCKS (resp. ECDF and MLECDF (log-normal)) method.

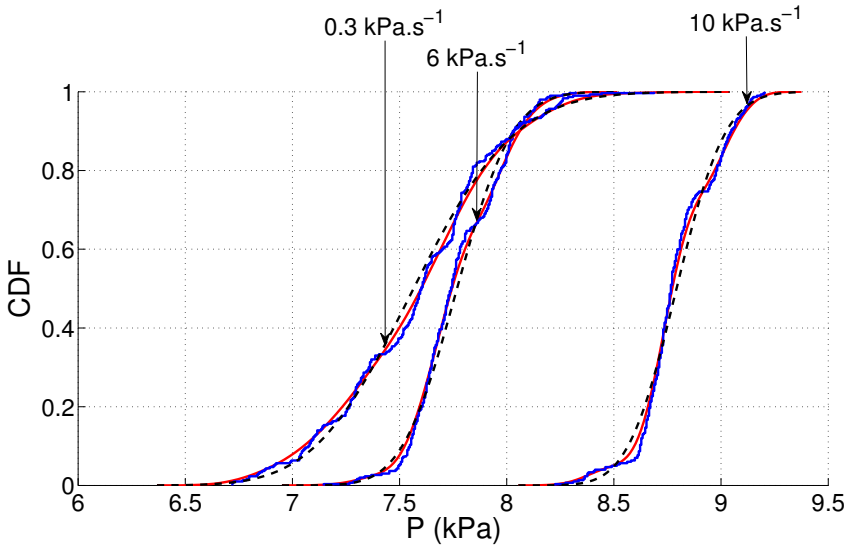

Figure 3.15 – Loading rate effect on the fragility curve. Red (resp. blue and black dashed) curves are derived from MCKS (resp. ECDF and MLECDF (log-normal)) method.

result should be used with caution. In this paper, a triangular shape describes the time evolution of the loading. Thus, for high loading rates, the duration of the applied pressure becomes shorter. The limit case is the Dirac loading signal which induces an impulsive response of the structure. The energy transferred to the structure is low and the collapse of the structure can occur only for higher pressures than in the static case. Obviously, in the case of higher loading duration, for instance using a trapezoidal loading signal, the fragility curves would be significantly affected.

3.4.4 Comparison to Favier et al. (2014a)'s fragility curves

Based on classical design engineering approach, (Favier et al., 2014a) proposed to obtain ultimate pressures related to typical limit states of the RC structure. Four limit states have been defined (Elast, ULS, ALS and YLT). The limit state "Elast" is related to the reaching of the elastic limit within the RC member. "ULS" (resp. "ALS") is based on the classical definition of the ultimate (resp. accidental) limit state given in the Eurocode 2, which allows calculating the ultimate pressure considering safety coefficients related to strength parameters of the RC member. The last limit state allows obtaining the collapse

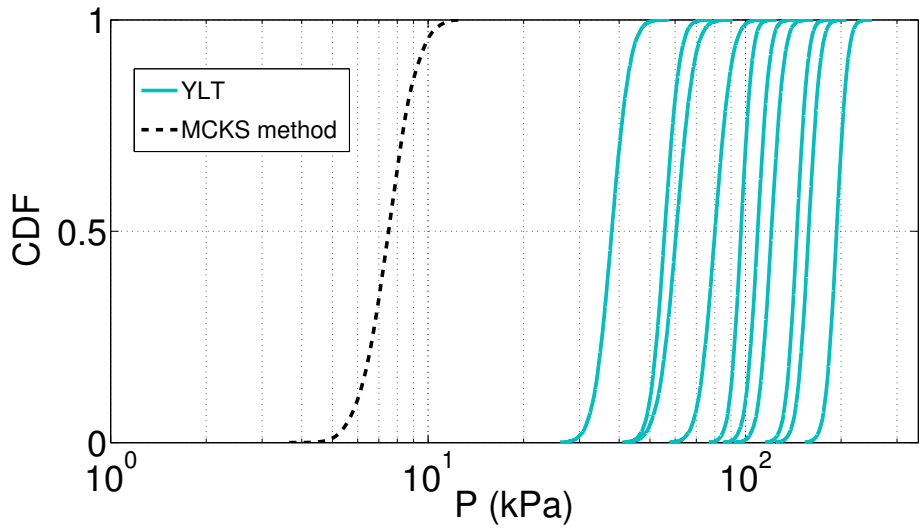

Figure 3.16 – Fragility curves comparison with Favier et al. (2014a)'s study.

pressure deduced from the classical yield line theory ("YLT"). Several boundary conditions were investigated (clamped, supported, free and combination of these latter).

The comparison with our results is presented in figure 3.16. The same input PDFs have been considered in both studies where COVs equal to 0.05 for all random variables (set $1.\alpha.a$). The derived fragility curve shows that the structure collapses for lower pressure values compared to Favier et al. (2014a) which is mainly due to boundary conditions. Indeed, one-way slab configuration lead to lower structural capacity compared to those considered by Favier et al. (2014a).

3.4.5 CDF Tails

Methods presented in this study allows defining accurately the central response of the fragility range. An important aspect, for instance in structure design, is the estimation of the extremal quantile of the fragility curve. For instance, in a risk analysis framework, it is important to determine accurately very low quantiles of the fragility curve which correspond to the lowest loadings for which collapse cannot be excluded. To improve the estimation of these low quantiles and symetrically of the high quantiles, in the studied case,

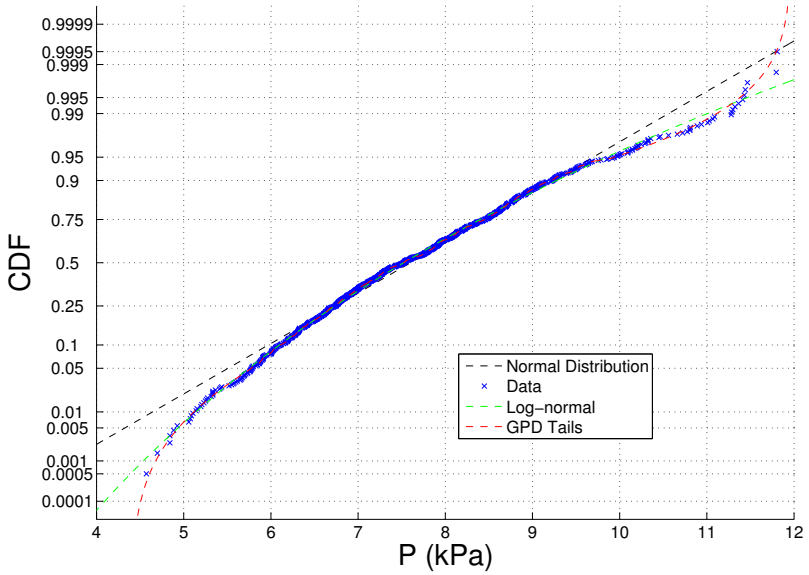

Figure 3.17 – GPD fitting of the tails and data generated by MCKS method (central anwser).

the two tails of the sample are assumed to follow a Generalized Pareto Distribution (GPD) statistical distribution (Coles, 2001) which is the suitable distribution for exceedances of high thresholds (Pickands, 1975). For the middle of the sample (90% of the data), the MCKS method is used to fit data. The figure 3.17 depicts the results of this approach (MCKS + GPD tail) to full parametric approaches (normal and log-normal). It underlines that even if the full parametric approaches will be relevant to estimate the central part of the fragility curve, they may lead to wrongly estimate very high / low quantiles. If these are really important, extrapolation beyond the empirical sample should be performed rather with specific approaches as the GPD extreme value based one.

3.5 Conclusions

This paper presents solutions to derive fragility curves to snow avalanches within a reliability framework. A one-way simply supported RC wall exposed to snow avalanche loadings has been considered. A deterministic model based on mass-spring system equivalence has been used. The ability of the SDOF model to predict the RC wall mechanical response has been validated by FEA and limit analysis comparisons. Using a SDOF approach allows reducing significantly the CPU time (70 times faster than FEM simulations) needed to perform a single simulation and allows accounting for the physics involved up to the collapse of the structure during the interaction between the wall and the avalanche.

Four methods have been proposed to derive fragility curves. ECDF and MCKS are mainly based on MC simulations. For TECDF and MLECDF methods, the shape of the fragilty curve is the main assumption. The fragility curves are obtained following two steps: (1) postulate CDF functions (lognormal or normal CDF) and (2) calculate parameters of the CDF by maximum likelihood estimation or by Taylor expansion approximation. All methods give similar results whatever the configuration considered at least for the core of the distribution. If very low / high quantiles are needed, our preliminary GPD application approaches should be accounted, focusing on specific techniques from EVT. This could be considered for structural engineering when very low failure probability are of interest.

The advantages and drawbacks of each methods have been identified. This framework could be used for a large range of reliability-based engineering applications. The simplified mechanical model allows to reduce computation time. The choice of well adapted reliability methods is crucial. It will mainly depend on the available calculation time and the expected accuracy of the fragility curve (good definition of the central behaviour, better description of the tails...). From our specific engineering field, systematic fragility curves have been derived. They supplement the seldom curves already available.

Parametric studies have underlined that fragility curves are very sensitive to physical

parameters such as the RC wall's geometry, its reinforcement ratio or the loading features. In particular, the fragility range spreading can strongly vary. From a relative point of view, if the fragility range is normalized by the 50% quantile, the relative fragility spreading remains almost the same.

By definition, snow avalanche is a dynamic loading which can involve inertial effects during the mechanical response of the structure. As a function of the structure's mechanical features (stiffness and mass distribution) and the loading characteristic time, the loading rate can influence significantly the fragility curve, especially for flexible civil engineering structures which might develop fundamental periods close to the typical time variation of the pressure applied. If the fundamental period of the structure is lower than typical loading time, the structure mechanical response can be supposed quasi-static and thus classical engineering methods of design can be used. Otherwise, dynamic effects have to be accounted by the deterministic model.

As a perspective, the main difficulty concerns the modelling of the avalanche pressure which can vary significantly as a function of meteorological conditions and specially in terms of pressure magnitude and typical time of variation. Pressure magnitude is implicitly taken into account by the fragility curves but the time of variation can have a significant influence on the structure mechanics. The structure mechanical features are generally better known than the avalanche loading time evolution. Thus, further researches accounting for several typical time evolutions of the pressure might be of specific interest to highlight the influence of avalanche loadings.

Then, the application of this approach to other types of structures is forecasted. Different technologies (masonry, timber, metallic, etc) with more complex geometries might be investigated using these approaches. The challenge will remain to propose simplified mechanical models able to account the main involved phenomenon with a reduce CPU time.

Acknowledgment

The authors are very grateful to the ANR research program MOPERA (Modélisation probabiliste pour l'Etude du Risque d'Avalanche - avalanches.irstea.fr/mopera-projet/) and the MAP3 ALCOTRA INTERREG program for financially supporting this work.

CHAPTER 4

Sensitivity of avalanche risk to vulnerability relations

Le contenu de ce chapitre a été soumis après révision pour publication dans *Cold Regions Science and Technology*, les auteurs sont : Favier, P., Eckert, N., Bertrand, D., and Naaim, M..

Abstract

Long-term avalanche risk assessment is of major importance in mountainous areas. Individual risk methods used for zoning and defense structure design are now gaining popularity in the effort to overcome the major drawbacks of approaches based on high return period events only. They require, for instance, precise vulnerability relations, whereas available knowledge mostly consists in coarse curves inferred from a few catastrophic events. In this paper, we first considerably expand the vulnerability curve sets in use today for reinforced concrete buildings and humans inside them. To do so, we take advantage of the results of a comprehensive reliability analysis of various building types subjected to avalanche loads, and we adapt them to humans inside buildings using different link functions. The fragility curves obtained propose refined destruction (building) / death (people) rates as a function of avalanche pressure that can be used in the risk context exactly like deterministic vulnerability curves.

Second, since land use planning should be done for a reasonably large class of buildings rather than for a very precise single building type, this study shows how a comprehensive risk sensitivity to vulnerability/fragility relation analysis can be conducted. Specifically, we propose bounds and indexes for individual risk estimates and optimally designed defense structures of both theoretical (quantifying uncertainty/variability that cannot be simply expressed in a probabilistic way) and practical (minimal/maximal plausible values) aspects. This is implemented on a typical case study from the French Alps. The results show that individual risk estimates are extremely sensitive to the choice of the vulnerability/fragility relation, whereas optimal design procedures may well be more robust, in accordance with mathematical decision theory. These two outcomes are of crucial importance in practice. For example, the individual risk for buildings and people at various positions in the runout zone spreads over several orders of magnitude. For risk zoning, this suggests that the usual (tri)centennial choice may be seen as optimistic since only abscissas above the 1000-year return period are below standard risk acceptance levels with certainty according to plausible variations of human fragility. On the other hand, the optimal height of a protective dam can be more precisely determined, promoting the use of cost-benefit analyses in avalanche engineering.

Keywords: snow avalanche; building vulnerability and fragility; human fragility; risk bounds; risk sensitivity; optimal design sensitivity; acceptable risk.

4.1 Introduction

Snow avalanches are a serious threat to mountain communities. For their inhabitants, land use planning and zoning are crucial steps that define where it is "reasonably" safe to build. Standard engineering procedures generally consider high return periods as reference design events, *e.g.* the commonly used 30-, 100- and 300-year return period events. For planners, zoning then results from the combination of these with additional social and political considerations. However, this is a simplified means of handling the multivariate danger resulting from impact pressure, flow depth or deposit volume within a single avalanche event, that is to say, all the tangible quantities that describe hazard intensity. Furthermore, high return period-based zoning methods do not explicitly take into account the elements

at risk and/or possible budgetary constraints, which does not guarantee that unacceptable exposure levels cannot be reached and/or that the mitigation choices made are optimal.

To overcome these limitations, an integrated quantitative risk evaluation is an appealing additional instrument. This approach is based on a solid formalism (Eckert et al., 2012), for individual or collective risk mapping. Individual risk mapping consists in evaluating the expected damage for a typical element at risk at any position in an avalanche path (Keylock et al., 1999). In contrast, collective risk mapping implies considering a two- to three-dimensional hazard description together with all elements potentially impacted. In both cases, zoning then includes both hazard and elements at risk. Another possible outcome of a quantitative risk approach is the optimal design of mitigation measures based on risk minimisation, that is to say, a cost-benefit assessment performed throughout the hazard distribution and, if possible, over a continuous space of potential decisions to be taken. Mitigation measures of maximal economic efficiency can then be chosen (Eckert et al., 2008a, 2009; Rheinberger et al., 2009). As a consequence of these advantages over purely hazard-oriented approaches (high return periods), integral risk management is now gaining popularity among stakeholders, and has increasing importance in practice (Bründl et al., 2009).

Specifically, risk quantification requires combining the model describing avalanche hazard with a quantitative assessment of consequences for one or several elements at risk. The avalanche hazard model consists in the distributions of the characteristics of avalanches that can occur in the site studied. These distributions are (at least partially) site-specific and have to be estimated with historical events as much as possible. Two main approaches exist for workable distributions. "Direct" statistical inference can be used to fit explicit distributions on relevant avalanche data, mainly runout distances (Lied and Bakkehoi, 1980; McClung and Lied, 1987; Keylock, 2005; Eckert et al., 2007b; Gauer et al., 2010). As an alternative, richer but more computationally intensive, statistical-dynamical approaches include hydrodynamical modelling within the probabilistic framework (Barbolini and Keylock, 2002; Ancey et al., 2004; Eckert et al., 2008b), which can be seen as an extension of Salm's method (Salm et al., 1990) to multivariate random inputs. They ensure the joint distribution of all variables of interest, including the spatio-temporal pressure field variable (Eckert et al., 2010c). These accurate intensity distributions can then be combined with the damage susceptibility of elements at risk *i.e.* the vulnerability relation.

Vulnerability curves are increasing curves with values within the range $[0, 1]$, expressed as functions of hazard intensity. When studying avalanche-prone areas, the diversity of elements (people, buildings, infrastructures, etc.) exposed implies the use of several curves to represent the overall damage potential. For alpine hazards, existing vulnerability relations mainly focus on buildings. Most of them have been assessed according to field data (Papathoma-Köhle et al., 2010; Schwendtner et al., 2013; Cappabianca et al., 2008).

These empirical curves have drawbacks in that they are based on scarce underlying data (interpolated with statistical regressions, adding potential approximation errors) and to be somewhat site-dependent (because of different technology choices in different countries, for example). More generally, they sometimes fail to provide trustworthy and unique quantitative damage levels in relation to hazard intensity.

As a consequence, in the specific case of snow avalanches, numerical approaches have recently emerged to evaluate the vulnerability of buildings more systematically (Bertrand et al., 2010). Indeed, numerical approaches have the major advantage of being implementable whenever needed for as many building types/configurations as necessary, providing a set of vulnerability relations that can be used for risk evaluation. Among existing numerical approaches, the one detailed in Favier et al. (2014a) made it possible to obtain fragility curves according to typical limit states of different building types. Limit states are defined according to relevant ultimate mechanical characteristics for the building studied, *e.g.* a maximum allowed displacement or an ultimate strength for a composite material. The limit state definition remains, however, a difficult task, depending on the interaction between the hazard and the building (dynamical or quasi-static solicitation) and on the failure scale chosen (local, semi- local, or global).

The distinction between fragility curves and vulnerability curves is important. For a given hazard intensity, fragility curves provide a probability of exceeding a limit state (crudely speaking, a destruction probability), whereas a vulnerability curve provides a deterministic damage index or rate. As stated above, Favier et al. (2014a) studied the collapse behaviour of a building within a reliability framework, providing fragility relations quantifying the probability that the entire building would be completely destroyed. On the other hand, in the literature, vulnerability curves are often easier to interpret in terms of a ratio of a building that fails. It is noteworthy that a fragility estimate can be seen as a conditional expectancy, averaging over the influence of certain factors possibly included in the "full", multidimensional, deterministic vulnerability relation (Eckert et al., 2012). As a consequence, from a mathematical point of view, vulnerability and fragility curves can be treated and used similarly in the risk framework. However, their intrinsic difference may induce different interpretations in practice that should be kept in mind while comparing risk estimates obtained with the two approaches.

Decision-makers typically need to link the vulnerability of buildings to the vulnerability of the people inside them. By definition, human vulnerability is always expressed as a fragility, *i.e.* as a probability of an individual death as a function of snow avalanche intensity. To do that, some studies have suggested multiplying building vulnerability/fragility (the distinction is not always clearly made) by a particular coefficient (Wilhelm, 1998). However, usually, human fragility has been for the most part assessed using past events (Jónasson et al., 1999; Arnalds et al., 2004; Keylock and Barbolini, 2001; Barbolini et al.,

2004a), so that existing curves mainly consist in empirical lethality rates brought together by smoothing approximations. Section 4.2.1 provides a comprehensive review of existing relations. Their scarcity shows how necessary it is to transpose recent advances in building physical vulnerability/fragility assessment to human fragility assessment.

According to these observations, the first objective of this paper is to provide an updated review of available vulnerability/fragility relations for reinforced concrete (RC) buildings and humans inside them (Sect. 4.2). Indeed, RC is a commonly used material in areas endangered by snow avalanches, which ensures reasonable safety in areas with high exposure to avalanche pressure, *i.e.* in areas where up to 30 kPa snow avalanche impact pressures are expected. From this RC vulnerability/fragility curve set, and, specifically, from the fragility curves of Favier et al. (2014a), we then deduce a large set of human fragility curves. Linking fragility relations for buildings to human death rates has rarely been done, and we propose four quantitative methods to achieve this goal.

Another major problem in many individual and total risk assessments for land use planning is that the exact technology of existing buildings and/or potential new buildings to be built in the future is unknown or, at least, intrinsically variable. As a consequence, it may not be easy to choose the relevant vulnerability/fragility relation among those in existence today, even though this choice may have a considerable influence on the final risk estimates. The second objective of the paper is therefore to study and quantify risk sensitivity to the choice of the vulnerability/fragility relation, which has never been attempted to date to our knowledge. The study was conducted on individual risk for mapping/zoning purposes and within a decisional procedure aiming at minimising risk with a defense structure construction.

In Sect. 4.3, we detail how bounds for risk or optimal solutions to the risk minimisation problem taking into account the variability or (mis)specification of vulnerability/fragility relations can be defined and derived from our systematic building and human fragility curve sets. In Sect. 4.4, we apply this methodology to a case study from the French Alps, illustrating how vulnerability/fragility sensitivity logically provides high risk bounds for buildings and humans inside them as well as for optimal protection design. This range of plausible values should be preferred to single values with low robustness for zoning and the design of defense structures. Section 4.5 discusses the major outcomes of the study, specifically those highly relevant for practice, including comparison with acceptable levels and with the results of standard engineering approaches using 30-, 100-, 300- year, etc. return periods as design events. Section 4.6 summarises and concludes.

4.2 From building vulnerability to human fragility

4.2.1 Review of vulnerability and fragility relations for snow avalanches

Physical vulnerability and fragility relations for buildings

Wilhelm (1998) assessed the damage susceptibility of five types of buildings to dense avalanche flows: light construction, mixed construction ("chalets"), masonry, concrete buildings with reinforcement and reinforced concrete buildings. To build damage susceptibility curves, his study assumed that four typical pressures needed to be known: p_u, corresponding to the general damage threshold, *i.e.* valid for every building type, p_{ui}, corresponding to the specific damage threshold of the building considered, p_{ai}, corresponding to the specific demolition limit and p_{oi}, corresponding to the specific destruction limit.

Barbolini et al. (2004a) proposed relations for buildings impacted by mixed snow avalanches (*i.e.* snow avalanches composed of two layers, a dense bottom layer and a powder upper layer). These result from linear fits on two well-documented events in Tyrol, Austria and are provided as functions of avalanche impact pressure and flow depth. Buildings considered are "partly reinforced". Vulnerability relations are derived by introducing a specific loss function in addition to the degree of damage evaluated by expert assessment. The specific loss $V_b(P)$ corresponds to the vulnerability of the building b function of the impact pressure P:

$$V_b(P) = \begin{cases} 0.0297P & if\ P \leq 34\ kPa \\ 1 & if\ P > 34\ kPa\ . \end{cases} \tag{4.1}$$

Fuchs et al. (2007b) implemented a monetary-based method to assess the vulnerability of buildings and humans, providing expected damage expressed in CHF, the Swiss currency unit, for several avalanche scenarios. Finally, a numerical approach was adopted by Bertrand et al. (2010). The method consists first in defining a damage index. Exceedence of a typical value on this index leads to the failure of the building. By scanning possible input values of the numerical building model, vulnerability curves are obtained. Updating the review by Cappabianca et al. (2008), Table 4.1 sums up all these vulnerability relations available for buildings. The approach chosen by each author is specified (*e.g.* empirical or numerical modelling).

In an attempt to systematize and increase this limited set, Favier et al. (2014a) related uniform pressure on a reinforced or partially reinforced concrete wall to failure probabilities. The goal of the study was to obtain fragility curves for buildings impacted by a uniform dense avalanche using a reliability approach. A reliability approach consists in considering probabilistic inputs of a deterministic model to study the occurrence of the

output studied. Four typical engineering limit states of RC were considered. By assuming the material behaviour as imperfectly known (at a certain reasonable level of uncertainty), the probability for reaching one of the four limit states was assessed. The wall was assumed to collapse due to flexural failure. The four limit states considered were:

- the **elastic** limit state (Elas) which defines the step between the reversibility and the irreversibility of building damage. In the case of the RC under flexural strain and low reinforcement, it is quantified by the appearance of the first cracks in the concrete under tensile stresses.
- the **ultimate limit state** (ULS) defined as the onset of plastic yield within steel. This limit state is Eurocode 2-based and is characterized by the calculation of the maximum plastic moment developed in the section combined with safety coefficients applied on the material parameters' behaviour.
- the **accidental limit state** (ALS) corresponds to the calculation of the maximum plastic moment developed in the section combined with lower safety coefficients than those used in the ULS, *i.e.*, it is a "less safe" limit state.
- the **collapse** is described by the yield line theory (YLT) (Johansen, 1962): this is assumed to occur when a complete failure pattern composed of yield lines develops throughout the wall and leads to the collapse of the RC building.

A wall was modelled, considering ten different boundary condition configurations representing construction technology choices. The four edges of the wall were successively assumed to be clamped, simply supported or free. Hence, the ten configurations are: four supported; two supported and two clamped; one supported and three clamped; one free and three supported; one free and three clamped; one clamped and three supported; two supported and two clamped side by side; four clamped; one clamped, two supported and one free; one supported, two clamped and one free. As already assumed in Favier et al. (2014a), these ten configurations can be associated with ten building types. Thus, 40 fragility relations were computed (Figure 4.1(a)). Figure 4.1(b) compares them to empirical and numerical literature-based vulnerability relations (see Sect. 4.5.1 for discussion).

Human fragility relations (lethality rates)

It should be remembered that, by definition, human vulnerability is always expressed as a fragility, *i.e.* an individual probability of death (lethality rate) as a function of snow avalanche intensity. For instance, if the pressure is considered as representing snow avalanche intensity, human fragility is $V_p(P)$, where V_p is the probability of death for people and P is the pressure considered.

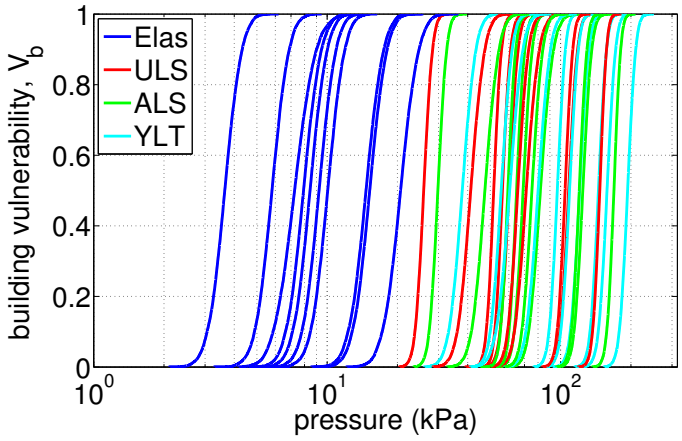

(a) Vulnerability relations from reliability analysis as a function of the limit state choice for different building types (Favier et al., 2014a). One wall with ten boundary conditions is considered together with four different limit states: Elas is the elastic limit state, ULS is the ultimate limit state, ALS is the accidental limit state and YLT is the collapse of the building.

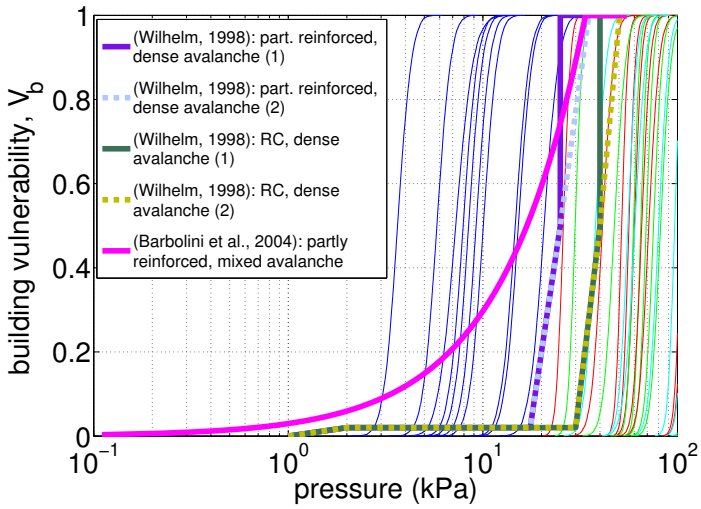

(b) Comparison with other relations from literature (see text for details).

Figure 4.1 – Vulnerability relations for buildings comparing historical/reliability-based relations (semi-log frame). $V_b(P)$ is either a probability (reliability point of view) or a damage level (deterministic point of view). Interpretation of Wilhelm (1998)'s work: (1): vulnerability is 1 for pressure above p_{ai}; (2): vulnerability linearly rises from p_{ai} to the specific destruction limit pressure p_{oi} where it reaches 1.

Table 4.1 – Summary of considered vulnerability approaches (RC is Reinforced Concrete).

element at risk	approach(data)	max. vuln.	avalanche type	ref.
building (Figure 4.1)				
partly reinforced and RC	empirical (Swiss data)	1.0	dense	Wilhelm (1998)
partly reinforced	empirical (Austrian data)	1.0	mixed	Barbolini et al. (2004a)
RC	numerical - deterministic	1.0	dense	Bertrand et al. (2010)
RC	numerical - reliability	1.0	dense	Favier et al. (2014a)
human inside building (Figure 4.2)				
partly reinforced and RC	empirical (Swiss data)	0.46	dense	Wilhelm (1998)
weak timber or concrete	empirical (Icelandic data)	1.0	dense	Keylock and Barbolini (2001)
partly reinforced	empirical (Austrian data)	0.27	mixed	Barbolini et al. (2004a)
weak timber or concrete	empirical (Icelandic data)	0.95	dense	Arnalds et al. (2004)

Fragility of people inside buildings was assessed in Barbolini et al. (2004a) by fitting linear least square regressions on data from two well-documented events in Tyrol, Austria. The resulting probability of being killed by a mixed avalanche inside a building as a function of impact pressure is:

$$V_p(P) = \begin{cases} 0 & if\ P \leq 5\ kPa \\ 0.0094P - 0.0508 & if\ 5 < P \leq 34\ kPa \\ 0.27 & if\ P > 34\ kPa\ . \end{cases} \tag{4.2}$$

For each building hit by the avalanche, the authors summarised: the degree of damage to the building, the impact pressure applied to it, the number of people inside it and the number of victims. The degrees of damage levels correspond to: 1: no visible damage to structural elements, damage to frames, windows, etc.; 2: failed chimneys, attics, or gable walls; damage or collapse of roof; 3: heavy damage to structural elements; 4: partial or complete failure of the building.

Two other well-documented events in Súðavik and Flateyri, Iceland, were used by Jónasson et al. (1999) to assess empirical human fragility relations. Considering the same data, Arnalds et al. (2004) provided a continuously differentiable probability of being killed by an avalanche $V_p(v)$ as a function of avalanche speed v:

$$V_p(v) = \begin{cases} kv^2 & if\ v < v_1 \\ c + \frac{a}{v-b} & if\ v \geq v_1\ , \end{cases} \tag{4.3}$$

where, $k = 0.0013$, $c = 0.95$, $a = 1.151$, $b = 18.61$ and $v_1 = 23.0$ m.s^{-1}.

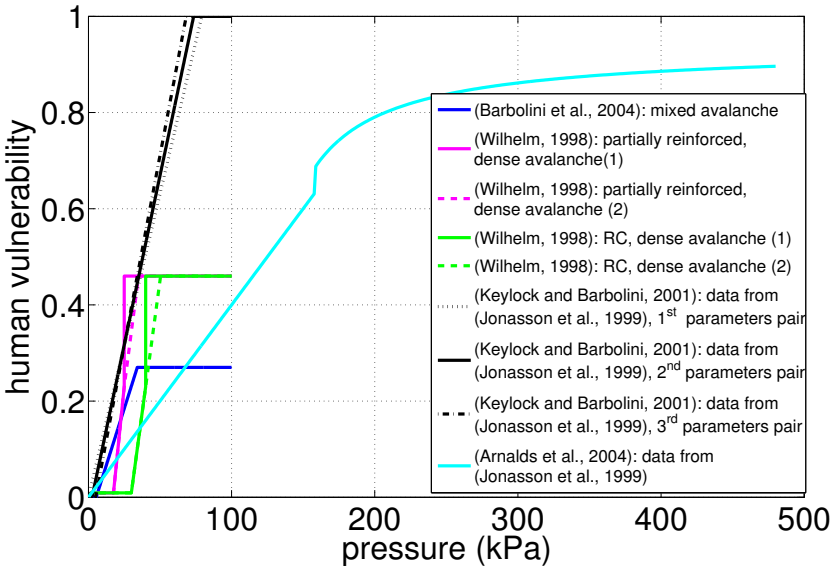

Figure 4.2 – Vulnerability relations from the literature for people inside reinforced or partially reinforced buildings. Arnalds et al. (2004) is added assuming $P = \rho v^2$ with $\rho = 300 kg.m^{-1}$. Keylock and Barbolini (2001) parameter pairs in Eq. (4.4): 1^{st}, $(C_1, C_2) = (0, 79.2)$; 2^{nd}, $(C_1, C_2) = (2.5, 73.5)$; 3^{rd}, $(C_1, C_2) = (5, 68.3)$ (kPa).

Jónasson et al. (1999) specified that most of the houses in the Icelandic villages threatened by avalanches are fairly weak timber or concrete structures with relatively large windows facing the mountainside. This means that this relation is valid for people inside any such constructions, but may not be easy to apply in other European countries where RC is more common.

Based on this study, Keylock and Barbolini (2001) proposed fragility relations for people inside similar buildings with pressure as an index variable instead of velocity:

$$V_p(P) = \begin{cases} 0 & if\ P \leq C_1 \\ \frac{P - C_1}{C_2 - C_1} & if\ C_1 < P \leq C_2 \\ 1 & if\ P > C_2\ . \end{cases} \tag{4.4}$$

C_2 is calculated as a function of C_1 so that the average fragility remains equal to 0.29. Three parameter pairs are proposed: $(C_1; C_2) = \{(0; 79.2),\ (2.5; 73.5),\ (5; 68.3)\}$ (kPa). As mentioned by Keylock and Barbolini (2001), for pressures lower than C_1, the avalanche is insufficiently powerful to cause substantial damage and it is assumed that no fatalities would occur within the building; otherwise, for sufficiently high pressures (higher than C_2), the avalanche is expected to cause 100% fatalities.

Finally, as the only formulation not based on past events, Cappabianca et al. (2008)

took into consideration Wilhelm (1998), *i.e.* they used a 0.46 factor to relate the fragility of a person in a building to the building vulnerability/fragility.

Figure 4.2 and Table 4.1 summarise these relations from the literature for people inside buildings, showing how rare these relations are. This also highlights the differences in terms of the methods that were used to derive these relations, and in terms of data quality and the country and avalanche events on which the calculations were based. For instance, the building technology variability among and within countries, on which inhabitant fragility is largely dependent, makes direct comparisons between the different curves difficult. The extension of the reliability-based approach of Favier et al. (2014a) presented below is an attempt to fill the gaps by focusing on people within RC buildings.

4.2.2 How can one relate building vulnerability/fragility to lethality rates?

To take advantage of the systematic curves shown in Figure 4.1, we suggest herein four ways to derive additional fragility relations for people, connecting the structural fragility of the building to the lethality rates of humans inside buildings. Four methods are proposed, sorted into three categories. The two empirically based connection methods aim at providing a coefficient deduced from historical data which can link the two fragility relations. The ULS-based approach suggests directly using the building fragility relations obtained with a human safety-based definition of building failure. A more exploratory method takes advantage of knowing four different probabilities of reaching different limit states for each building under study. We call this semi-empirical, or the degree-damage approach.

Empirically

- As indicated above, Wilhelm (1998) and Cappabianca et al. (2008) suggested choosing a 0.46 reduction coefficient linking building vulnerability/fragility to human fragility. Figure 4.4(b) applies this approach to the set of building fragility curves at our hand.

- According to Arnalds et al. (2004), this reduction coefficient can be evaluated as a function of avalanche pressure (Figure 4.3(a)):

$$V_p(P) = \alpha(P) \times V_b(P), \tag{4.5}$$

  where V_p is the human fragility inside a building, V_b is the vulnerability/fragility of the building and (P) is the pressure value considered. The coefficient $\alpha(P)$ resulting

from this approach may be valid under certain assumptions only, according to the validity of Arnalds et al. (2004)' relations. Nevertheless, we assume here that $\alpha(P)$ remains a good link between the probability of building failure and the probability of death inside the building for all structures considered in the reliability study of Favier et al. (2014a). To be as close as possible to the conditions of Arnalds et al. (2004), we assessed $\alpha(P)$ from the weakest configuration considered in Favier et al. (2014a), the RC wall with one free edge and three supported edges. The resulting human fragility curves are plotted in Figure 4.4(a).

Using ULS considerations

By definition, the Eurocode limit state, if not exceeded, ensures the safety of people in Eurocode-based design buildings. By calculating the probability for the building to reach the ULS, we obtain a maximum probability for the people inside the building to be killed, resulting in the human fragility curves of Figure 4.4(d). Note that this approach corresponds to the previous approach with a constant $\alpha(P) = 1$, but a different building fragility relation based on the ULS criterion instead of building collapse.

Semi-empirically

Let us consider the four degrees of damage defined by Barbolini et al. (2004a), to obtain vulnerability curves in relation to buildings' degree of damage. A linear regression is used to link the building's degree of damage to the vulnerability of the people inside it:

$$V_p(DD) = \begin{cases} 0.0297 & if\ DD \leq 1.34 \\ 0.0851DD - 0.1140 & if\ DD > 1.34\ . \end{cases} \tag{4.6}$$

Here, we assume that the four damage degrees defined in this study correspond to the four structural limit states as the referred to above elastic limit state, ultimate limit state, accidental limit state and collapse in the reliability-based approach of Favier et al. (2014a). The fragility for the people inside buildings is simply:

$$V_p(P) = \sum_{i=1}^{4} V_b^i(P) \times V_p(DD_i)\ , \tag{4.7}$$

where $V_b^i(P)$ is the probability for the building b under the pressure P to overpass the limit state i, *i.e.* the i^{th} degree of damage DD_i, and $V_p(DD_i)$ is the probability of death in a building at the i^{th} degree of damage DD_i according to the fit of Eq. (4.6) depicted in Figure 4.3(b). The resulting human fragility curves are plotted in Figure 4.4(c).

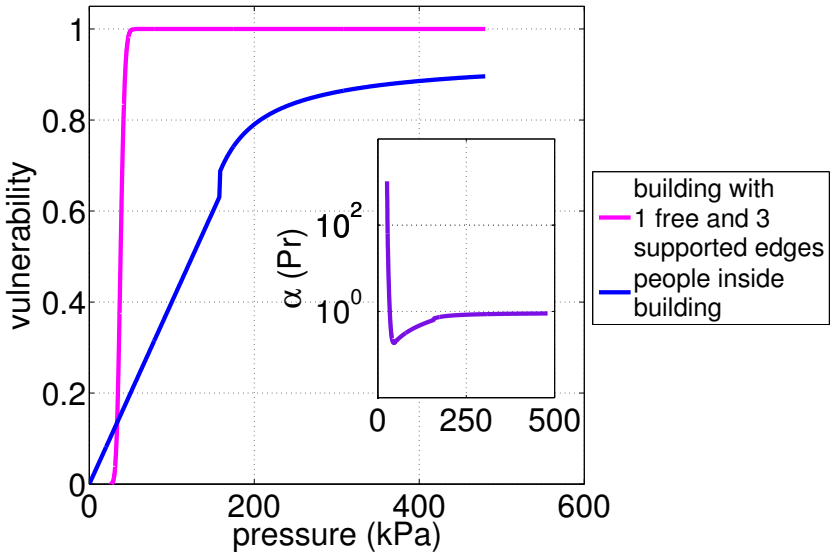

(a) Empirical link function: coefficient $\alpha(P)$ depending on avalanche pressure (kPa). $\alpha(P)$ is Arnalds et al. (2004)'s ratio linking people fragility to Favier et al. (2014a) fragility relation for a RC building with one free edge and three supported edges.

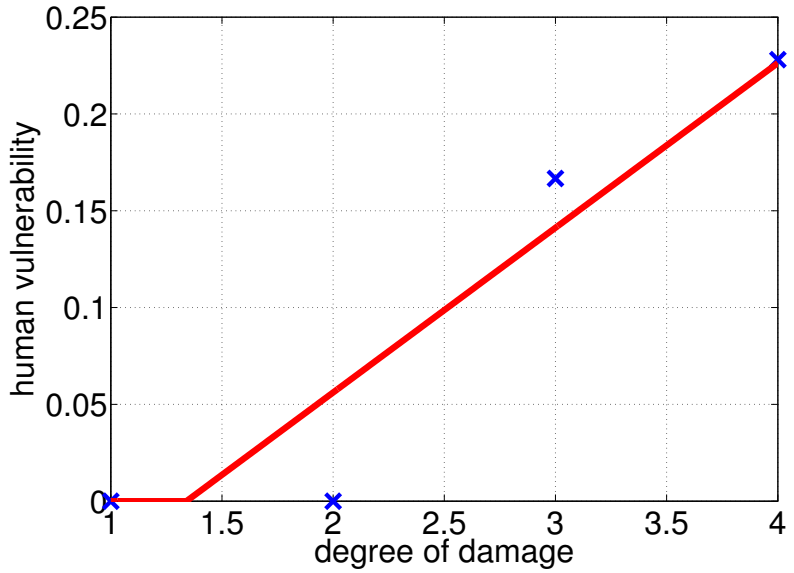

(b) Semi-empirical link function for people inside buildings according to the degree of damage: (1): no visible damage to structural elements, damage to frames, windows, etc.; (2): failed chimneys, attics, or gable walls; damage or collapse of roof; (3): heavy damage to structural elements; (4): partial or complete failure of the building. Data from Barbolini et al. (2004a)

Figure 4.3 – Link functions between building vulnerability/fragility and human fragility.

4.2.3 Four sets of reliability-based fragility curves for humans inside buildings

The resulting four sets of human fragility curves are monotonous and differentiable (Figure 4.4). They differ from each other mainly in their maximum probability of death, ranging from $\simeq 0.41$ (degree-damage approach) to 1 (ULS approach). In addition, two types of shape can be distinguished. The human fragility curves obtained with Wilhelm's and the ULS approaches have a classical sigmoidal shape, increasing from 0 to their maximum value within a pressure range depending on the building configuration considered. In other words, these two curve sets look quite similar to the building fragility curves from which they were derived, except that, with Wilhelm's approach, human fragility is bounded at 0.46. The two other sets obtained with the degree-damage and Arnalds's approaches show more original shapes, variable from one building configuration to another, illustrating the more complex way they were evaluated. Nevertheless, the pressure range on which they rise from 0 to their maximum value remains similar to the pressure ranges of the two other sets, simply showing the underlying fragility curves for buildings from which they all derive.

4.3 Evaluating risk sensitivity to vulnerability/fragility relations

4.3.1 Formal risk framework

In the following, risk is first quantified in a "static" perspective, which consists in calculating expected damage in order to obtain annual destruction rates for buildings and annual death rates for the people inside them. Second, a "dynamic" decisional framework is set by taking into account a potential countermeasure, a dam in the runout zone. Monetary costs for the building value and dam construction are necessary together with the dam effect on the hazard intensity distribution, so as to evaluate the remaining residual risk as a function of the dam height, and to determine the dam height that minimises this risk. All static and dynamic computations are made in an individual risk perspective, focusing on a single element at risk (building or person). However, whereas static computations are made at the annual time scale, dynamic computations are made over the long term using an actualisation term that accounts for the dam amortisation period.

"Static" risk without countermeasures

Risk is broadly defined in natural hazards as the expected damage, in accordance with mathematical theory (*e.g.*, Merz et al. (2010) for floods, Mavrouli and Corominas (2010b)

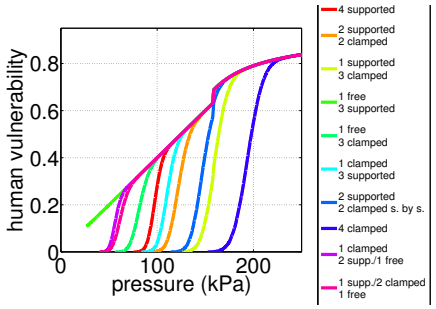

(a) Using Arnalds et al. (2004) approach: a multiplicative coefficient depending on the pressure is applied on building fragility.

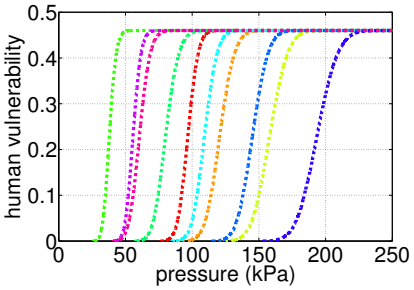

(b) Using Wilhelm (1998) approach: a constant coefficient is applied on building fragility.

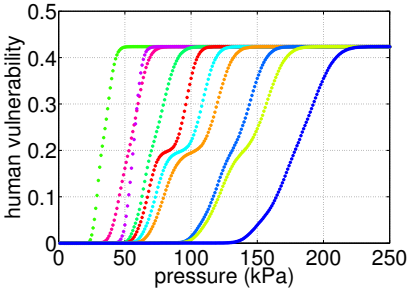

(c) Using the degree damage approach based on Barbolini et al. (2004a) (Eq. (4.7)).

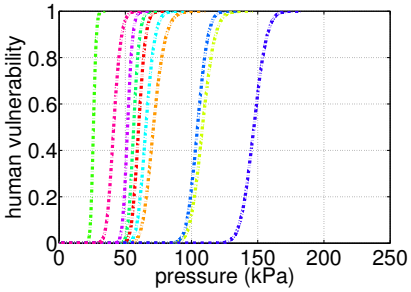

(d) Using the ULS approach: $\alpha(Pr) = 1$, and $V_b(Pr)$ is given by the ULS fragility curves.

Figure 4.4 – Human fragility relations derived from the building fragility curve set. The legend refers to the ten building types of the reliability-based approach which differ from each other in the boundary conditions of their four edges: four supported; two supported and two clamped; one supported and three clamped; one free and three supported; one free and three clamped; one clamped and three supported; two supported and two clamped side by side; four clamped; one clamped, two supported and one free; one supported, two clamped and one free.

for rockfall, Jordaan (2005) in engineering, etc.). Following the notations of Eckert et al. (2012), the specific risk r_z for an element at risk z is:

$$r_z = \lambda \int p(y) V_z(y)\ dy\ , \tag{4.8}$$

where λ is the annual avalanche rate, that is to say, the annual frequency occurrence of an avalanche, $p(y)$ is the (potentially multivariate) avalanche intensity distribution (runout, flow depth, etc.) and $V_z(y)$ is the vulnerability-fragility of the element z towards the avalanche intensity y. By definition, the specific risk is expressed in year^{-1}.

Classically, in a two-dimensional cartesian framework, avalanche intensity is defined by the joint distribution $p(P, x_{stop})$ of pressure fields P and runout distances x_{stop}. The specific risk $r_z(x_b)$ for the element z at the x_b abscissa is then:

$$r_z(x_b) = \lambda \int p(P|x_b \leq x_{stop}) p(x_b \leq x_{stop}) \times V_z(P)\ dP\ . \tag{4.9}$$

This holds since $p(P, x_{stop}) = p(P|x_b \leq x_{stop}) p(x_b \leq x_{stop})$, where $p(P|x_b \leq x_{stop})$ is the pressure distribution at abscissa x_b knowing that x_b has been reached by an avalanche and $p(x_b \leq x_{stop})$ is the probability for the element at x_b to be reached by an avalanche.

According to our approach, the vulnerability of a building is simply the fragility of its wall facing the avalanche, defined by one of the relations illustrated in Figure 4.1(a). The resulting annual probability of the building at the abscissa x_b reaching its limit state (one of the four defined above, and used in the specific $V_b(P)$ relationship considered) is:

$$r_b(x_b) = \lambda \int p(P|x_b \leq x_{stop}) p(x_b \leq x_{stop}) \times V_b(P)\ dP\ , \tag{4.10}$$

and the annual probability of death for somebody inside a building at abscissa x_b is:

$$r_p(x_b) = \lambda \int p(P|x_b \leq x_{stop}) p(x_b \leq x_{stop}) \times V_p(P)\ dP\ , \tag{4.11}$$

with $V_p(P)$ one of the human fragility relations in Figure 4.4.

Decisional framework: minimising residual risk

To study the sensitivity of decisional procedures to vulnerability relations, the classical example of the optimal design of a dam height (Eckert et al., 2008a) is reconsidered, with the fragility curve set from Figure 4.1. The approach minimises the long-term costs obtained by summing up the construction costs and the expected damage at the building abscissa x_b. This is analogous to the precursor work of Van Danzig (1956) for maritime dykes in Holland, and it is based on an extensive mathematical theory (Von Neumann and Morgenstern, 1953; Raiffa, 1968). Hence, the residual risk at the abscissa x_b and with a protective dam h_d is:

$$R_b(x_b, h_d) = C_0 h_d + C_1 A \lambda \int p(P|x_b \leq x_{stop}, h_d) \times p(x_b \leq x_{stop}, h_d) \times V_b(P)\ dP\ , \tag{4.12}$$

where C_0 and C_1 are, respectively, the value of the dam per metre height in €$\cdot m^{-1}$ unit and the value of the entire threatened building situated at abscissa x_b in €(the monetary currency used herein). The notation ".$|h_d$" denotes that runout and pressure distributions are now modified in the runout zone, conditional to the dam height h_d. $A = \sum_{t=1}^{+\infty} \frac{1}{(1+i_t)^t}$ is the actualisation factor to pass from annual to long-term costs, with i_t the interest rate for the year t. So the unit for $R_b(x_b, h_d)$ we consider is €.

Note that the residual risk $R_b(x_b, h_d)$ is no more than $C_0 h_d + C_1 A r_b(x_b, h_d)$, with $r_b(x_b, h_d)$ the specific risk for the building at the abscissa x_b with the dam height h_d, highlighting that the approach remains based on individual risk (a single building at abscissa x_b is considered at risk). A similar computation or formalism could easily be proposed and implemented with humans inside buildings as elements at risk, but this would imply monetising human life, and we prefer to avoid this ethically contestable issue at this stage.

4.3.2 Hazard distribution

Outputs of a statistical-dynamical model

In Eqs. (4.9-4.12), avalanche hazard is expressed by the joint distribution of runout distances and pressure fields. To calculate this, we use the statistical-dynamical model developed by Eckert et al. (2010c) to easily sample from $p(P, x_{stop})$. In this model, the avalanche is (rather classically) modelled by a shallow-water approximation of the mass and momentum conservation equations supplemented by a Voellmy friction law (Naaim et al., 2004) . Additionally, a statistical model considers the depth and the length of the release area, the abscissa of release and the friction coefficients as random input variables, so as to provide the joint distribution of runout distance and velocity spatio-temporal fields as outputs. Independently, the frequency parameter (mean annual avalanche rate) λ is defined within a Poisson model of occurrences, a rather usual assumption (*e.g.* McClung (2003); Eckert et al. (2007a); Lavigne et al. (2012)). It has recently been proven on case studies using independent validation data from tree-ring sampling that this statistical-dynamical model can provide good approximations of the magnitude-frequency relationship in the runout zone (Schläppy et al., 2014).

Pressure evaluation

To feed the vulnerability relations with the statistical-dynamical simulations, velocities must be converted into pressures. For a free surface flow, the impact pressure can be expressed as:

$$P = C_x \frac{1}{2} \rho v^2 \ , \tag{4.13}$$

where C_x is the drag coefficient, ρ is the fluid density and v is the flow velocity. For snow avalanches, the drag coefficient C_x can now be expressed in rather realistic ways according, *e.g.*, to the empirical formulation of Sovilla et al. (2008a) or the semi-empirical formulation of Naaim et al. (2008c). These depend on the Froude number of the flow, highlighting the potentially high impact pressures exerted by flows close to rest. Here, to greater simplicity, we instead use a constant drag coefficient of 2. The dynamic pressure on the impacted wall considered is then ρV^2, a common approximation in engineering. Note, however, that our approach can easily be employed with other drag coefficient assumptions than ours, as soon as C_x can be readily evaluated for each simulation in the statistical-dynamical set-up, as demonstrated in Eckert et al. (2010c).

Optimal design computations: obstacle / flow interaction and delta propagation

For the decisional risk calculations, one must also compute the residual risk for each dam height, which requires the quantification of the dam effects on the flow. According to Faug et al. (2008), semi-empirical relations can be used to account for the effect of a vertical dam on snow avalanche flows. Typically, it has been found that the normalised velocity at the dam abscissa and the normalised flow height are linked through:

$$\frac{v_{h_d}^2(x_d)}{v_0^2(x_d)} = 1 - \frac{\alpha h_d}{2h} \ , \tag{4.14}$$

where $v_{h_d}(x_d)$ is the velocity at the dam abscissa with a dam height h_d, $v_0(x_d)$ is the velocity at the dam abscissa without the dam, h is the flow height at the dam abscissa and $\alpha = 0.14$ is the energy dissipation coefficient determined by Faug et al. (2008) on the basis of small and real-scale flow experiments and energy budget considerations.

Once the modified velocity at the dam abscissa is known, one must propagate the effect of the dam on the avalanche characteristics along the entire runout zone. A simple method consists in assuming a delta propagation. This approach suggests that the velocity decrease is propagated homogeneously throughout the velocity profile after the dam. First, the difference of velocities $\delta_{velocity}$ at the dam abscissa is calculated. Then this delta is subtracted from the rest of the velocity profile:

$$\delta_{velocity} = v_0(x_d) - v_{h_d}(x_d) \tag{4.15}$$

Hence, for any abscissa x in the path, the velocity $v_{h_d}(x)$ of the avalanche with the dam height h_d is:

$$v_{h_d}(x) = \begin{cases} \max\left((v_0(x) - \delta_{velocity}), 0\right) & if\ x \geq x_d \\ v_0(x) & else \ , \end{cases} \tag{4.16}$$

whith $v_0(x)$ the velocity of the avalanche at the x abscissa with no dam.

Finally, the optimal dam height h_{opt} is found by minimising the residual risk expressed in Eq. (4.12):

$$h_{opt} = \underset{h_d}{\text{argmin}}(R_b(x_b, h_d)) \ , \tag{4.17}$$

where the function argmin gives the height h_d at which R_b is minimal for a building abscissa position x_b.

4.3.3 Quantifying sensitivity to vulnerability/fragility: bounds and indexes

Since the objective of the paper is to study how risk estimates and optimal design values vary across vulnerability formulations, we now propose quantitative sensitivity indicators that may illustrate some theoretical (general) and practical (local, for case studies) aspects.

Fragility-based risk bounds for buildings

As detailed in Sect. 4.2, in Favier et al. (2014a), four limit states were used to calculate probabilities for buildings to reach different limit states, and, hence, as surrogates of destruction probabilities as a function of the pressure load. This was done for 10 building configurations differing in their boundary conditions, providing as many as 40 fragility relations. By evaluating Eq. (4.10) with these 40 relations throughout the runout zone, a set of 40 individual risk curves $r_b(x_b)$ representing different evaluations of annual destruction rates is obtained. The main advantage of doing this is to build plausible intervals for risk taking into account a certain variability in the response of the RC building considered to the avalanche load. Hence, as an outline for operational applications aiming at assessing the risk of a building being destroyed, relevant intervals can be determined, taking into account imperfect knowledge of the most relevant failure state and/or the variability within a reasonably large building class.

Specifically, a useful but very large interval can be delimited by, as the upper bound, the risk for the "weakest" building (in terms of geometry / boundary conditions) to reach the elastic state, and, as the lower bound, the risk for the "strongest" building to reach the collapse state. Another relevant risk interval, less wide and which enables to remain consistent among limit states use is defined by: as the lower bound, the risk of the strongest building collapsing, and, as the upper bound, the risk of the weakest building collapsing, and, similarly, with the three other limit states considered, providing four specific limit state intervals whose union corresponds to the overall interval defined above.

Fragility-based risk bounds for humans

By developing new human fragility relations in Sect. 4.2, we have increased the number of available relations relating avalanche hazard to a probability of death for people inside buildings. As for buildings, evaluating Eq. (4.11) with these curves makes it possible to obtain various individual risk curves for people inside buildings in the runout zone.

This panel of human risk curves reflects the same uncertainty/variability sources as for building fragility, but taking into account the additional uncertainty resulting from the choice of the link function between human and building fragility. This implies that the assumptions made above to set a link function have to be kept in mind when interpreting human risk results. However, with this approach, sensitivity towards fragility relations of human risk estimates can at least be quantified, a crucial point in practice. As for buildings, this can be done with upper/lower bounds, either with all the human fragility curves illustrated in Figure 4.4 together or distinguishing the four sets, corresponding to Figure 4.4 a-d, depending on the link function: empirically based - Arnalds's, empirically-based - Wilhelm, ULS or degree-damage.

Sensitivity indexes in risk minimisation (optimal design)

Finally, to assess the sensitivity to building fragility relations of optimal dam heights, we evaluate the spread of the solutions based on Eq.(4.17) towards the 10 relations corresponding to the 10 building configurations through:

$$\delta_{h_{opt}} = \frac{h_{opt,max} - h_{opt,min}}{\overline{h_{opt}}} \ , \tag{4.18}$$

where $h_{opt,max} = \max_{i=1,...10} h_{opt,i}$ (resp. min), with $h_{opt,i}$ the optimal value minimising the residual risk obtained in Eq.(4.17), when considering the i^{th} fragility curve for modelling the fragility of building b. We compute this index for the four limit states separately, and for different positions x_b in the runout zone.

We compare $\delta_{h_{opt}}$ to the risk spread that is similarly quantified with the indicator δ_R calculated for the 10 fragility relations, for each limit state, as:

$$\delta_R = \frac{max(R(x_b, 0)) - min(R(x_b, 0))}{\overline{R(x_b, 0)}} \ . \tag{4.19}$$

The notation $R(x_b, 0)$ indicates that the risk spread over fragility relations is evaluated at the abscissa x_b without any countermeasure ($h_d = 0$).

4.3.4 Numerical risk computations

Classically, Eqs. (4.10) and (4.11) are discretely solved for the element z under study (the building or people inside the building) by the Monte Carlo integral:

$$r_z(x_b) \approx \lambda \frac{1}{N} \sum_{k=1}^{N} I\{x_{stop_k} \geq x_b\} \frac{1}{N'} \sum_{k=1}^{N'} V_z(P_k | x_{stop_k} \geq x_b) \ . \tag{4.20}$$

with N the number of simulations made with the statistical-dynamical model, P_k the pressure for the k^{th} simulation at the x_b abscissa, I the indicator function equals to 1 if x_b is exceeded and 0 if not and N' the number of simulated runouts exceeding the x_b abscissa: $N' = \sum_{k=1}^{N} I\{x_{stop_k} \geq x_b\}$. As $V_z(P_k | x_{stop_k} < x_b) = 0$, Eq. (4.20) can be rewritten:

$$r_z(x_b) \approx \lambda \frac{1}{N} \sum_{k=1}^{N} V_z(P_k) \ . \tag{4.21}$$

The corresponding 95% asymptotic confidence interval is $r_z \pm 1.96\sqrt{\frac{r_z(1-r_z)}{N}}$. Similarly, for various dam heights, Eq. (4.12) is numerically evaluated through:

$$R_b(x_b, h_d) \approx C_0 h_d + C_1 A \lambda \frac{1}{N} \sum_{k=1}^{N} V_z(P_k) \ . \tag{4.22}$$

4.4 Application of risk sensitivity analysis to a case study

4.4.1 Case study presentation

To study the influence of vulnerability curves on the risk and decisional calculations, we reuse the case study presented by Eckert et al. (2009, 2010c). The data and topography come from an avalanche path in the village of Bessans, in the Savoie department of the French Alps. The abscissa position is evaluated in the 2D-plane of the avalanche path starting at the top of the path (Figure 4.5). The runout zone has always been free of permanent habitations, but, due to demographic pressure, it may become impossible to ban construction in the future, provided the risk is estimated to be low enough in the current state or after construction of a defense structure. Therefore, the abscissa position x_d of the dam to be potentially built is $1,956.5$ m, which is the beginning of the runout zone. The building (and people inside the building) abscissa x_b considered for individual risk evaluation varies between the dam abscissa and $2,500$ m.

To be less dependent on the case study in our conclusions, we will not often refer to abscissas in the path studied, but, instead, to the corresponding return period T. For instance, we will evaluate $r_b(T)$, and $r_p(T)$ for T up to $1,000$ years instead of $r_b(x_b)$ and $r_p(x_b)$. For comparison with current land use planning policies based on high return periods (See Sect. 4.5.3), the runout abscissas {1,953.7; 2,004; 2,064; 2,125.2; 2,164; 2,203.9 and 2,242.1} m corresponding to typical runout periods of {2; 5; 10; 30; 100; 300 and 1,000} years will be specifically studied (the first one is just before the dam abscissa).

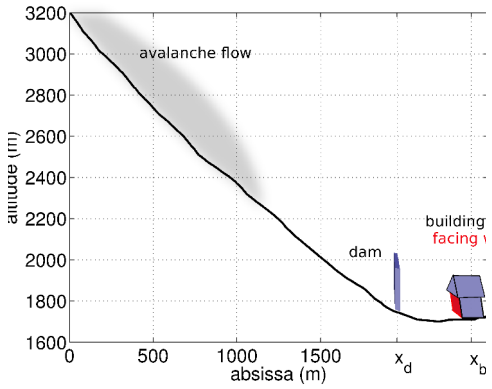

Figure 4.5 – 2D topography of the path studied (Bessans township, French Alps). x_d is the abscissa where dam construction is envisaged, and x_b is the abscissa of the building at risk. The facing wall is highlighted in red as its failure is assumed to be representative of the failure of the whole building.

The one-to-one mapping between runout distance and return period results from Eq. (4.23):

$$T = \frac{1}{\hat{\lambda}(1 - \hat{F}(x_{stop}))} \ , \tag{4.23}$$

where $\hat{\lambda}$ is the avalanche rate estimator and $\hat{F}(x_{stop})$ is the estimated cumulative distribution function of the runout distance, approximated by the runout outputs from statistical-dynamical model simulations conditional to model parameter estimates. These estimates (best guesses, traditionally denoted by a "hat") have been obtained using Bayesian inference as detailed in Eckert et al. (2010c). For numerical evaluations (Sect. 4.3.4), $N = 20,000$ predictive simulations conditional to these estimates were used.

For the decisional computations, the construction cost for the dam and the building value (single element at risk) were set to, respectively, $5,530$ € $\cdot$ m^{-1} and $3 \cdot 10^6$ €. A is fixed to 25, which is obtained with a constant interest rate $i_t = 4\%$. Eight abscissa positions x_b in the path were studied for possible building positions: $\{1,966.5;\ 1,971.5;\ 1,976.5;\ 1,981.5;\ 1,986.5;\ 1,991.5;\ 1,996.5$ and $2,001.5$ m$\}$ (resp. corresponding to a runout period of $\{2.3;\ 2.5;\ 2.8;\ 3.1;\ 3.5;\ 3.9;\ 4.3$ and 4.8 years$\}$). These relatively low values were chosen so that the dam would have a greater chance to demonstrate its effectiveness. Indeed, for buildings situated at positions very rarely reached by avalanches, it is very unlikely that a large defense structure will be economically sound.

4.4.2 Individual risk range for buildings

Figure 4.6 depicts the building risk curves obtained as functions of the runout return period abscissa for a wall with one free edge and three clamped edges, our weakest configuration. Given that a very large number of simulations is used for numerical risk evaluations ($N = 20,000$), confidence intervals are (very) small for low return periods. On the other hand, they become very large for high return periods because the runout exceedence probability is very small, so that only very few events among the simulated set provide non-zero values. For instance, the lower bounds drop to zero as soon as it becomes possible that no simulation reaches the corresponding abscissa with pressure sufficient to provide a non-zero destruction probability for the building considered (it should be remembered that the probability of reaching the limit state is, somewhat abusively, considered the same as the destruction probability). However, these confidence intervals are numerical artefacts which do not reflect epistemic uncertainty regarding the concrete behaviour and/or variability among different elements at risk. They could be reduced even further if necessary (*e.g.* for practice) with more simulations and/or with more efficient approximation methods, so that they would not be considered in the following.

Globally, risk decreases with the runout return period, a trivial result. Also, for a given runout return period, the risk is higher when the elastic limit state is considered than when the ULS is considered, etc. for the two other limit states. This is simply a natural consequence of the definition of the four limit states along the pushover test curve (see Favier et al. (2014a)). Specifically, in the log-scale in Figure 4.6, the four risk curves quasi-linearly decrease with T for return periods up to 500 years, and then decrease faster and drop to zero, except the elastic limit state-based risk curve for which the linear decrease goes on even for T longer than $1,000$ years. The linear shape in the log scale signifies a quasi-exponential decay of runout exceedence probabilities for the case study, whereas the risk drops to zero as soon as there are close to zero avalanches with impact pressures strong enough to be associated with significantly non-zero probabilities of reaching the limit state considered. With the elastic limit state, these probabilities remain high for the few avalanches that reach very high return periods.

When all building configurations are considered together (Figure 4.7), most of these conclusions remain true. For instance, even if the variability of building configurations considered adds "noise", in general, we still have Elas-based risk > ULS based risk > ALS based risk > YLT based risk. Nevertheless, for a given return period, risk estimates are lower than in Figure 4.6 because the nine additional building configurations considered are stronger, inducing lower probabilities of reaching each limit state. Hence, the pattern of decay in risk is generally, with regards to Figure 4.6, shifted to the left. For instance, the annual probability of reaching YLT or even ULS is extremely small for $T > 300$ years

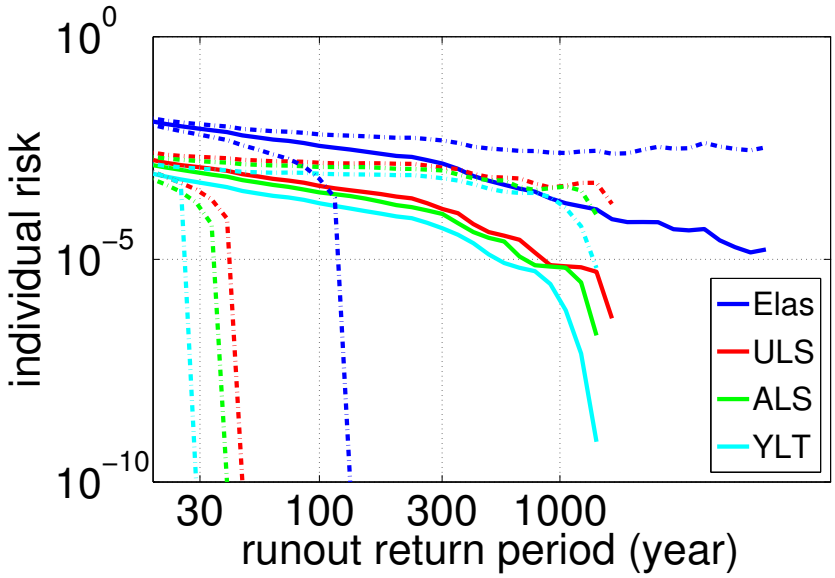

Figure 4.6 – Risk (annual limit states reach probability, solid lines) and associated 95% confidence interval (dotted lines) for a wall with one free edge and three clamped edges. The four limit states defined in the text are considered (semi-log frame). On the x-axis, the runout return period is considered instead of the abscissa position in the path. In the runout zone, the lower bound confidence intervals quickly drop to zero.

with the strongest buildings considered herein.

The resulting risk bounds are therefore very large, showing an overall high sensitivity to the limit state considered, and, for a given limit state, to the building configuration. In other words, risk estimates are highly sensitive to the choice of fragility relations, so that global bounds over the four limit states may be excessively large to be useful in practice. Hence, Figure 4.8 displays risk intervals as a function of the limit state choice, and Table 4.2 resumes the thus-obtained bounds for classical high return period abscissas.

For example, for $T = 100$ years, the risk estimates range from $4.5 \cdot 10^{-3}$ (very high, with the weakest building and the Elas limit state) to $5.5 \cdot 10^{-7}$ (very small, with the strongest building and the YLT limit state), indeed an interval that is too large to be meaningful. Restricting ourselves to the ULS and ALS, more realistic and useful intervals are obtained, but still very wide: $[1.3 \cdot 10^{-5} - 1.5 \cdot 10^{-3}]$ and $[5 \cdot 10^{-6} - 1.2 \cdot 10^{-3}]$, respectively.

For $T = 1,000$ years, the lower bound for risk estimates is non-zero only with the Elas limit state. The upper bound is $\simeq 3 \cdot 10^{-4}$ with the Elas limit states and $\simeq [3 - 5 \cdot 10^{-5}]$ with the other limit states.

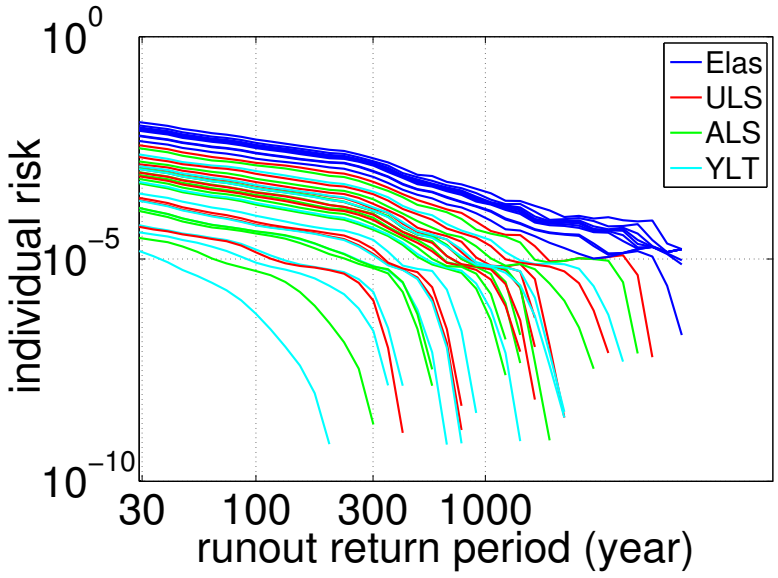

Figure 4.7 – Risk (annual probability of reaching the limit state considered) in the runout zone for the ten building types and the four limit states defined in the text (semi-log frame).

Table 4.2 – Minimal and maximal individual risk values (annual destruction rate bounds) for a building at typical return period abscissas T_z where z is the corresponding return period (in years). These bounds are derived from the reliability curve sets and are given as function of the four limit states considered.

		T_2	T_5	T_{10}	T_{30}	T_{100}	T_{300}	T_{1000}
Elastic	*min*	0.12	0.058	0.028	0.0041	0.0017	$6.7 \cdot 10^{-4}$	$8.0 \cdot 10^{-5}$
	max	0.28	0.14	0.074	0.011	0.0045	0.0017	$3.1 \cdot 10^{-4}$
ULS	*min*	0.0048	0.0016	$5.3 \cdot 10^{-4}$	$4.8 \cdot 10^{-5}$	$1.3 \cdot 10^{-5}$	$1.1 \cdot 10^{-6}$	0
	max	0.10	0.047	0.022	0.0033	0.0015	$5.1 \cdot 10^{-4}$	$4.9 \cdot 10^{-5}$
ALS	*min*	0.0029	$8.9 \cdot 10^{-4}$	$2.9 \cdot 10^{-4}$	$2.7 \cdot 10^{-5}$	$5.0 \cdot 10^{-6}$	$2.6 \cdot 10^{-9}$	0
	max	0.091	0.040	0.019	0.0028	0.0012	$4.1 \cdot 10^{-4}$	$3.8 \cdot 10^{-5}$
YLT	*min*	0.0017	$4.6 \cdot 10^{-4}$	$1.4 \cdot 10^{-4}$	$1.3 \cdot 10^{-5}$	$5.5 \cdot 10^{-7}$	0	0
	max	0.071	0.031	0.014	0.0020	$8.9 \cdot 10^{-4}$	$3.0 \cdot 10^{-4}$	$2.8 \cdot 10^{-5}$

4.4.3 Individual risk range for humans inside buildings

Similarly, our human vulnerability relations allow obtaining a range of human risk curves that translates the same uncertainty/variability sources as for building fragility, but taking into account the additional uncertainty resulting from the choice of the link function

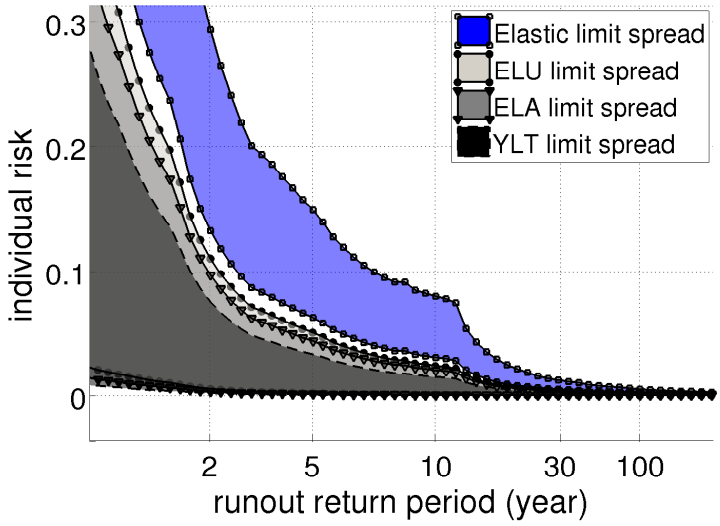

Figure 4.8 – Risk bound definition, *i.e.* annual destruction probability bound definition: delimited by the risk for the weakest building and the risk for the strongest building of reaching each of the four limit states (linear frame).

between human and building fragility (Figure 4.9). Again, the substantial width of the resulting risk intervals/bounds highlights the strong variability of human risk estimates depending on the choice of the fragility curve, and more particularly on the choice of the type of building (boundary conditions, materials properties, etc.) and the human-building link function (Figure 4.10).

Globally, one has an exponential-like pattern of decay of human risk curves similar to that of building risk curves, with very low values reached for (nearly) all building configurations / link functions for $T > 1,000$ years only (see Sect. 4.5.3 for discussion). For a given human-building link function, human risk estimates differ from each other as a function of the building configuration, exactly like the risk for building estimates. From one link function to another, human risk curves are less separated than, for buildings, from one limit state to another. Nevertheless, globally, human risk estimates obtained with Wilhelm's approach are the lowest (the most "optimistic" due to the small maximum value of human fragility it postulates). On the other hand, the ULS approach generally provides the highest estimates, whereas the Arnalds and degree-damage approaches provide less separated values spread in between. However, these are only general rules because, due to the strong influence of building configuration, there are many exceptions (Figure 4.9).

For example, for $T = 100$ years, the Wilhelm, degree-damage and Arnalds approaches

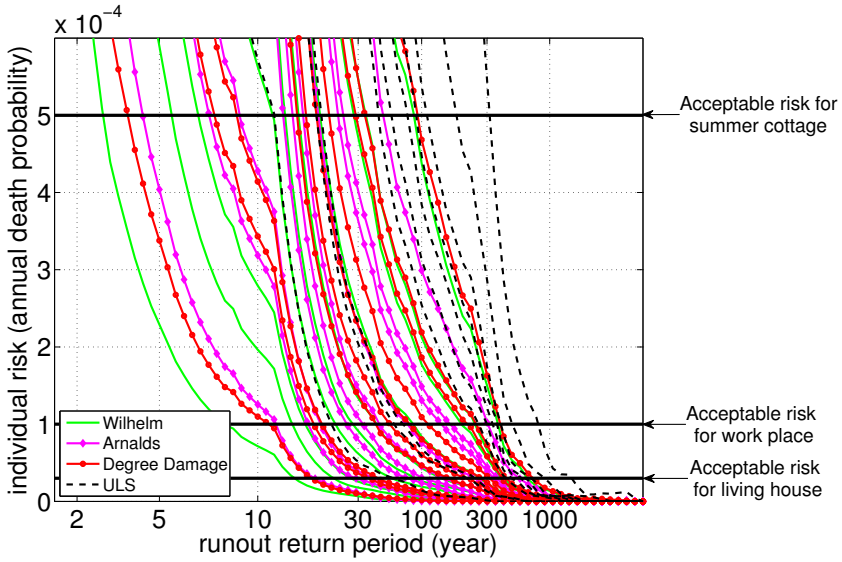

Figure 4.9 – Risk (annual probability of death) in the runout zone for the four adapted human curve sets from the literature obtained in Section 4.2.2 and illustrated in Figure 4.4. They are compared with acceptable risk levels defined by Jónasson et al. (1999): in a dwelling, the acceptable risk is $0.3 \cdot 10^{-4}$; in a work place, $1 \cdot 10^{-4}$; in a summer cottage, $5 \cdot 10^{-4}$.

propose close maximum risk estimates within the $[3 - 5 \cdot 10^{-4}]$ range, whereas the ULS approach does not exclude risk estimates as high as $1.5 \cdot 10^{-3}$. For $T = 1000$ years, maximum predicted values are closer, within a factor of 5: $\simeq 1 \cdot 10^{-5}$ with the Arnalds approach,$\simeq 1.5 \cdot 10^{-5}$ with the Wilhelm and degree-damage approaches, and $\simeq 5 \cdot 10^{-5}$ with the ULS approach.

4.4.4 Optimal design range

Figure 4.11 depicts residual risk functions (long-term expected costs) given by Eq. (4.12) for two limit states and the 10 building configurations. For the elastic limit state, all risk curves clearly decrease with h_d up to close to 15 m optimal dam heights and confused with the asymptotic construction cost for higher dam heights. With the limit state provided by the yield line theory, risk curves show more variable shapes, ranging from curves similar to the elastic limit state curves to strictly increasing curves. As a consequence, optimal heights are more dispersed, and even do not exist with the "strongest" buildings. Indeed, it is not economically efficient to try to reduce the solicitations encountered by these buildings, since they are already strong enough to avoid collapse in most cases. This

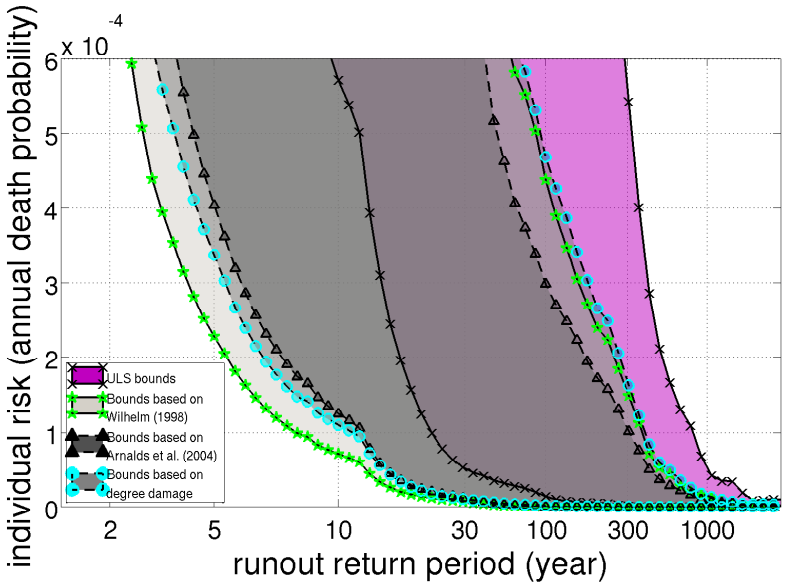

Figure 4.10 – Risk bound definition (annual death probability bound definition): for each of the four human vulnerability curve sets obtained in Section 4.2.2 and illustrated in Figure 4.4. The risk bounds are delimited, for a given return period abscissa, by the lowest risk value (strongest building) and the highest risk value (weakest building).

Table 4.3 – Minimal and maximal individual risk values (annual death rate bounds) for a human inside a building at typical return period abscissas T_z where z is the corresponding return period (in year). Results of three upon four of the adapted human vulnerability approaches detailed in Section 4.2.2 are provided. The ULS interval is provided in Table 4.2 (same as for the building).

		T_2	T_5	T_{10}	T_{30}	T_{100}	T_{300}	T_{1000}
Wilhelm	*min*	$8.2 \cdot 10^{-4}$	$2.3 \cdot 10^{-4}$	$7.2 \cdot 10^{-5}$	$6.6 \cdot 10^{-6}$	$2.7 \cdot 10^{-7}$	0	0
	max	0.035	0.015	0.0068	0.0010	$4.4 \cdot 10^{-4}$	$1.5 \cdot 10^{-4}$	$1.4 \cdot 10^{-5}$
Arnalds	*min*	0.0015	$4.0 \cdot 10^{-4}$	$1.3 \cdot 10^{-4}$	$1.1 \cdot 10^{-5}$	$4.4 \cdot 10^{-7}$	0	0
	max	0.027	0.011	0.0051	$7.4 \cdot 10^{-4}$	$3.0 \cdot 10^{-4}$	$1.0 \cdot 10^{-4}$	$8.3 \cdot 10^{-6}$
Degree Damage	*min*	0.0011	$3.4 \cdot 10^{-4}$	$1.1 \cdot 10^{-4}$	$1.0 \cdot 10^{-5}$	$1.6 \cdot 10^{-6}$	$6.7 \cdot 10^{-8}$	0
	max	0.037	0.016	0.0073	0.0011	$4.7 \cdot 10^{-4}$	$1.6 \cdot 10^{-4}$	$1.5 \cdot 10^{-5}$

shows that a full decisional treatment of the problem is not always possible, depending on when the building failure is assumed to occur and on the building configuration chosen.

Figure 4.12 depicts the risk sensitivity index δ_R function of the decisional sensitivity $\delta_{h_{opt}}$ for the four limit states and for eight different (close) building positions in the runout zone. Each point represents the normalised spread over the 10 building types investigated

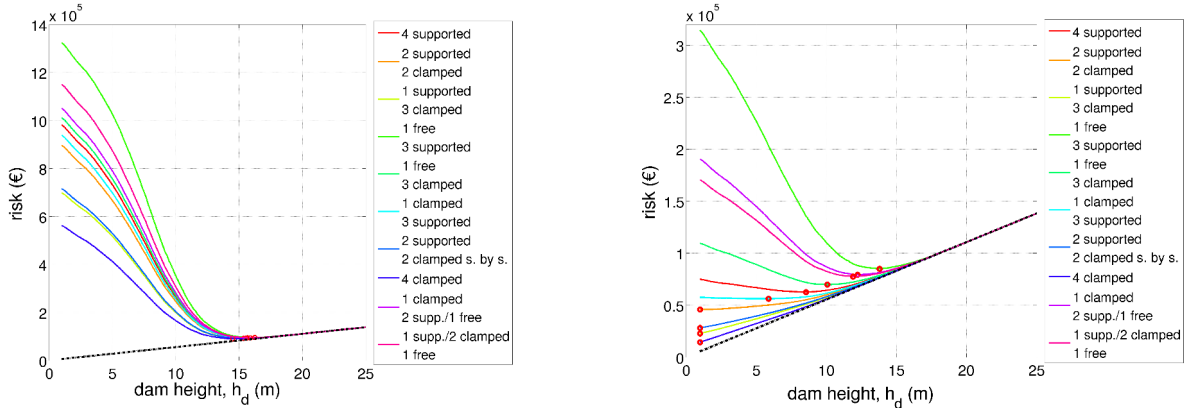

(a) Elastic limit state (Elas)

(b) Collapse (YLT)

Figure 4.11 – Residual risk (expected loss over the long-term in €) curves as a function of the dam height provided by Eq. (4.12) for two reliability-based fragility curves sets: a) Elastic limit state, b) Yield line theory. For each curve, a red circle (○) denotes optimum (minimum risk). Abscissa position considered for the building is 1,966.5 m, corresponding to a return period of 2.3 years (just beyond the dam).

for a specific building position in the runout zone. Substantially, $\delta_{h_{opt}}$ is always around ten times lower than δ_R, a point that argues in favour of much higher robustness of optimal design approaches with regards to "static" risk evaluations (see Sect. 4.5.4 for discussion). In greater detail, two scatter-plot groups are observed: an elastic limit state scatter-plot around $\delta_R \simeq 1$ and another limit state scatter-plot around $\delta_R \simeq 3$, confirming that the risk spread is lower with the elastic limit state than with the other limit states, as already suggested by Figure 4.11. Note also that, for the close building positions investigated, significant variations of $\delta_{h_{opt}}$ compared to the variations of δ_R occur, since, for a given limit state, δ_R is nearly constant, whereas the optimal design sensitivity index varies from 0 to 0.5.

4.5 Discussion

4.5.1 Reliability-based fragility relations versus empirical vulnerability relations

Building vulnerability relations from the literature rise from 0 to 1 over the $[0-50]$ kPa range (Figure 4.1(b)), whereas some of the reliability-based fragility relations of (Favier et al., 2014a) reach 1 above $250kPa$ only (Figure 4.1(a)). Thus, it seems at first glance that buildings damaged by avalanches that were reported in the literature were more vul-

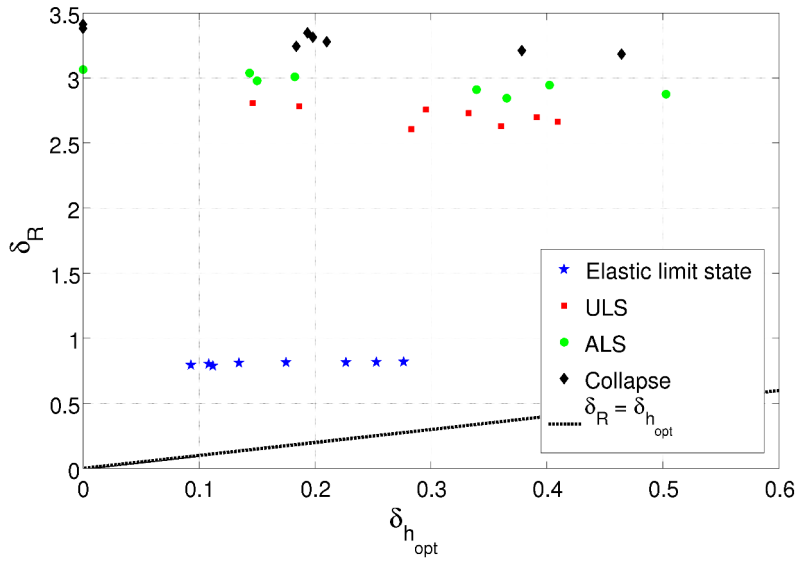

Figure 4.12 – Sensitivity of optimal height to building fragility relations for the four limit states considered (Eq. (4.18)) versus sensitivity of risk (Eq. (4.19)). Eight abscissa positions in the path were considered for the exposed building, corresponding to runout return periods between 2.3 and 4.8 years.

nerable than those considered in (Favier et al., 2014a) and in the present study. This statement remains questionable, however, since buildings reported in the literature and the numerically designed buildings in Favier et al. (2014a) are not essentially similar, in addition to the already discussed variability in technology choices between and within countries that affects empirical relations. For instance, differences in concrete grade, in percentages of reinforcement or in the size of the buildings considered could explain differences between empirical vulnerability and reliability- based fragility to a given pressure load.

Another explanation could be a methodological bias: the vulnerability curves reported in the literature provide damage levels as a function of impact pressures retrieved by expertise and back-analyses of real events, whereas numerical fragility curves result from limit states based on mechanical theory whose exceedence probabilities are considered identical to destruction probabilities. Hence, even if exactly the same building could be studied with the two approaches, it is presumable that the same vulnerability/fragility curve would not be obtained. Note also that the failure mode in Favier et al. (2014a) study was assumed to be the flexural mode, making fragility curves conditional to this assumption. Other failure definitions could have provided different fragility estimates.

Comparing empirical vulnerability relations and Favier et al. (2014a) fragility relations in the risk calculation results in Figure 4.13. For a given runout abscissa/return period, risk estimates based on literature vulnerability relations are high. They correspond to those obtained, with the fragility approach, with the "strongest" building configurations and the elastic limit state definition (the most pessimistic and conservative of the four limit states considered) or with weaker building configurations and the elastic ULS/ALS limit state definition (more "optimistic"). For example, literature-based risk estimates are $\simeq [8 \cdot 10^{-4} - 3 \cdot 10^{-3}]$ at the centennial abscissa and still $\simeq [2 \cdot 10^{-5} - 2 \cdot 10^{-4}]$ at the millennial abscissa (Table 4.4). Again, this shows that the characteristics of the vulnerability/fragility relation used (modal value, spread, pressure range within which it rises from 0 to 1, etc.) are directly propagated on risk estimates, making those highly sensitive to the choice of the vulnerability/fragility relation.

However, the general shape of the risk curves with the literature vulnerability relations is essentially similar to the shape of the risk curves with the reliability-based fragility curves (exponential decay with the runout return period abscissa, Figure 4.13). This suggests that the fragility relations can be used to supplement the empirical vulnerability curves, for instance within the risk framework. Indeed, their intrinsic differences in terms of interpretation (deterministic damage index for the empirical vulnerability curves - destruction probability for the fragility relations) is then totally smoothed in the integral calculation (Eckert et al., 2012), as illustrated by the different estimates we have obtained for the case study.

Table 4.4 – Individual risk values (annual destruction rate) for a building at typical return period abscissas T_z where z is the corresponding return period (in year) with the five considered vulnerability curves from the literature.

	T_2	T_5	T_{10}	T_{30}	T_{100}	T_{300}	T_{1000}
Barbolini et al. (2004a)	0.17	0.080	0.041	0.0062	0.0025	0.0010	$1.5 \cdot 10^{-4}$
Wilhelm (1998), part. RC (1)	0.071	0.031	0.014	0.0021	$9.0 \cdot 10^{-4}$	$3.1 \cdot 10^{-4}$	$3.1 \cdot 10^{-5}$
Wilhelm (1998), part. RC (2)	0.063	0.027	0.012	0.0018	$7.6 \cdot 10^{-4}$	$2.6 \cdot 10^{-4}$	$2.4 \cdot 10^{-5}$
Wilhelm (1998), RC (1)	0.11	0.051	0.024	0.0036	0.0015	$5.7 \cdot 10^{-4}$	$5.8 \cdot 10^{-5}$
Wilhelm (1998), RC (2)	0.096	0.043	0.020	0.0030	0.0013	$4.7 \cdot 10^{-4}$	$4.8 \cdot 10^{-5}$

Regarding human vulnerability of mountain community inhabitants, quantitatively linking it to the structural vulnerability/fragility of housing buildings is a very important issue in avalanche engineering practice. As for the buildings themselves (and even more rarely), human fragility relations have been, in the past, mainly empirically assessed on the basis of well-documented catastrophic events, leading to survival/death rates as a function of impact pressure. An appealing alternative has been presented herein to simply derive

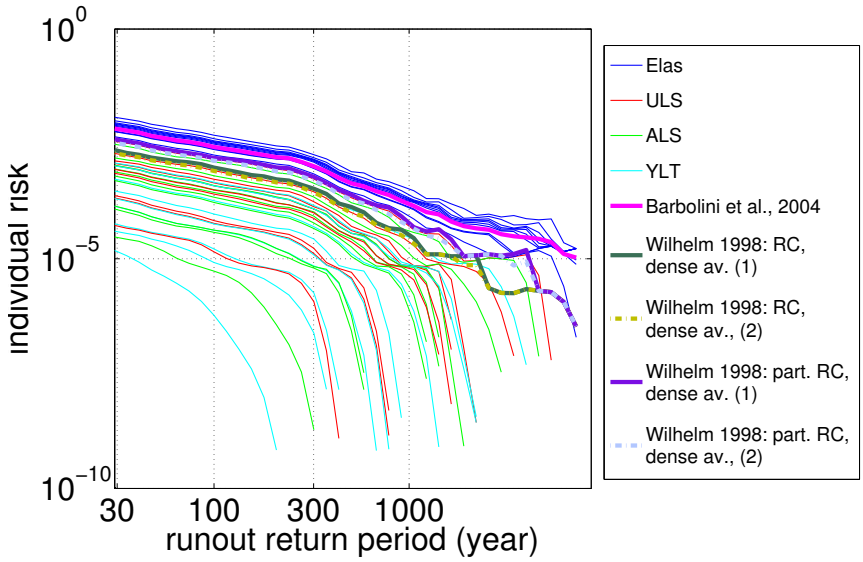

Figure 4.13 – Risk (annual destruction probability) for a building in the runout zone with the literature curves, versus risk with reliability-based fragility curves: YLT, ALS, ULS and Elas curves from Favier et al. (2014a)).

human fragility relations from building fragility curves in a systematic way, assuming various (three or four) simple deterministic link functions based on existing work. Therefore a large set of human fragility curves, a function of the link function and the building configuration, were obtained.

The strong assumptions made to evaluate these curves must be kept in mind while using and interpreting them. Specifically, the rather simple link functions used herein are arguably oversimplified preliminary proposals that could be reconsidered in future studies. However, as for buildings, these have been sufficient to obtain fragility curves that have shapes similar to the shapes of the empirical literature curves (although highly dependent on the building configuration and link function), which promotes their use as an advantageous supplement to the scarce relations available to date. Furthermore, our human fragility curves were clearly essential to conduct our risk to vulnerability sensitivity study on a typical case study.

4.5.2 Risk sensitivity to vulnerability/fragility (mis)specification

Vulnerability/fragility relations are one of the key ingredients of a quantitative risk assessment, directly controlling buildings and individual risk estimates for humans inside buildings, which are the crucial outputs required for avalanche risk zoning in practice.

Our application has abundantly illustrated how highly sensitive to the choice of vulnerability/fragility relation these are, whereas existing RC buildings are never perfectly known. Indeed, existing RC buildings are composed of two materials (concrete and steel) whose behaviours may be described somewhat inaccurately. Besides, the proportion of steel together with its arrangement within the concrete matrix can add other uncertainties to the building description (the same building will never be exactly reproduced).

Furthermore, from a more predictive point of view, risk zoning for land use planning should not only focus on existing buildings, but should also anticipate the possible construction of a reasonably large class of new construction and still account for the same uncertainties. From land use planners' perspective, it is also difficult to know the exact, most suitable building configuration to choose, as well at the best limit state to concentrate on to ensure the safety of building inhabitants together with reasonable architectural recommendations. This all makes the application of one single curve among the existing curve set a tricky, if not impossible, task.

How then should this uncertainty/variability and the related high sensitivity of risk estimates be handled in practice? If this variability/uncertainty could be expressed in a probabilistic way, the risk framework would easily account for it as an additional source of randomness to average over. This is illustrated with different examples by Eckert et al. (2012). For instance, if ϕ is the additional source of "noise" to be considered (*e.g.* a parameter of the hazard or vulnerability model), then, one simply needs to evaluate the Bayesian-like risk:

$$r'_z(x_b) = \int r_z(x_b, \phi).p(\phi)d(\phi), \tag{4.24}$$

where $r_z(x_b, \phi)$ is, for example, the risk estimates provided by Eq. ((4.9)) with the parameter value ϕ and $p(\phi)$ its probability distribution . However, in the case of the choice of a vulnerability/fragility relation, this probabilistic response is presumably not possible. This is the reason why we chose a "bound approach" instead: ten boundary conditions were considered, providing ten vulnerability relations for each limit state. Propagating these curves through the risk calculation allowed us to propose risk bounds, *i.e.* risk estimate ranges that are valid for different boundary conditions and/or different thresholds above which the building is assumed to fail (limit state).

The width of these intervals precisely quantifies the strong variability of building and human risk estimates according to the choice of the fragility curve, and more particularly, to the choice of the type of building (boundary conditions, material properties, etc.). Bounds are large even for positions in the path only reached by rare avalanches (*e.g.* Figure 4.10 for humans), and even higher if the results provided by empirical curves are considered together with the fragility curves (Tables 4.3 and 4.4).

In detail, risk bounds can be refined focusing on one type of variability/uncertainty only. For buildings, the overall interval mixing all limit states and configurations may be too large (Figure 4.8), requiring additional assumptions to provide usable values in practice, such as fixing the considered limit state. For humans inside buildings, the four link functions provide partially imbricated intervals (Figure 4.10), so that, instead of setting the link function, making additional reasonable assumptions regarding the building configuration considered may more efficiently reduce the width of risk bounds.

4.5.3 Comparison with acceptable levels and high return period design events

To go even further in terms of the practical outcomes of the study, the high return period abscissas currently used as legal risk assessment limits were compared to the abscissas where risk estimates provided by our approach are acceptable according to Jónasson et al. (1999). Acceptable risk values from Jónasson et al. (1999) are: in a dwelling: $0.3 \cdot 10^{-4}$; in a work place: $1 \cdot 10^{-4}$; in a summer cottage: $5 \cdot 10^{-4}$ (Figure 4.9).

Table 4.5 displays abscissa intervals in the path where these conditions are fulfilled. The interval spread corresponds to the evaluation of risk estimates with our different human fragility relations. This shows that acceptable risks for dwellings can be observed for houses situated above $2,086.5$ m in the avalanche path for the most "optimistic" human fragility relation, but only above $2,255.5$ m for the most "pessimistic". This corresponds to runout return periods of $[11.9 - 1,955]$ years. Similarly, abscissa intervals of $[2,043.6 - 2,235.1]$ m and $[1,969.6 - 2,205.5]$ m (respectively corresponding to runout period of $[8 - 693.7]$ years and $[2.4 - 336]$ years), depending on the choice of the fragility relation, correspond to acceptable risk thresholds for, respectively, a work place and a summer cottage.

Again, in addition to dramatically highlighting the sensitivity of risk estimates to the choice of the vulnerability/fragility relation, this clearly illustrates the limit of return period-based approaches for human risk zoning. Depending on the vulnerability/fragility relation, traditional return period-based zoning thresholds can overestimate the risk as well as underestimate the risk, an obviously critical problem. For instance, the acceptable risk threshold of $0.3 \cdot 10^{-4}$ (in a residential house or building) is reached for 13 out of 40 fragility-based risk curves before attaining the reference centennial abscissa, but only abscissa positions above the $1,000$-year return period are associated with risk estimates lower than $0.3 \cdot 10^{-4}$ with all fragility relations. Hence, only these can be considered as fully safe for our typical case study if one takes into account all the possible range of variability of human fragility relations that this study has suggested.

Table 4.5 – Abscissa / return periods $[min; max]$ intervals fulfilling the three Jónasson et al. (1999) requirements of acceptable risk for the four approaches detailed in section 4.2.2 (four sets of human fragility curves depending on the link function). The interval width highlights the sensitivity to the fragility relation.

		Living house: $< 0.3 \cdot 10^{-4}$	Work place: $< 1 \cdot 10^{-4}$	Summer cottage: $< 5 \cdot 10^{-4}$
Wilhelm	$x_{stop}(m)$	$[2,086.5; 2,228.4]$	$[2,043.6; 2,210.5]$	$[1,969.6; 2,159.3]$
	$T(years)$	$[11.9; 592.6]$	$[8.0; 379.8]$	$[2.5; 87.2]$
Arnalds	$x_{stop}(m)$	$[2,098.6; 2,223.6]$	$[2,075.1; 2,204.4]$	$[1,993.8; 2,140.5]$
	$T(years)$	$[14.2; 532.2]$	$[10.8; 336.9]$	$[4.0; 49.6]$
Degree Damage	$x_{stop}(m)$	$[2,096.9; 2,232.0]$	$[2,070.7; 2,212.0]$	$[1,984.7; 2,161.5]$
	$T(years)$	$[13.9; 610.7]$	$[10.5; 387.0]$	$[3.4; 91.9]$
ULS	$x_{stop}(m)$	$[2,146.7; 2,255.5]$	$[2,109.0; 2,235.1]$	$[2,074.1; 2,205.5]$
	$T(years)$	$[57.2; 1959.8]$	$[18.4; 708.0]$	$[10.8; 339.4]$

4.5.4 Optimal design sensitivity versus risk sensitivity

A decision can modify the hazard distribution, and implementing this modification within the risk framework can make it possible to determine the decision that minimises risk. This requires additional assumptions regarding the decision's effects on avalanche flows, in the present case how the perturbation at the dam abscissa is propagated further along the path. Depending on the avalanche type and the dam shape, different optimal designs could have been obtained, but we focused on the simple case (dense avalanche, vertical dam, etc.) herein described by Faug et al. (2008). This was enough for the purpose of this study: implement the sensitivity to vulnerability/fragility study up to the decisional analysis. The case study has shown that the sensitivity to vulnerability/fragility relations is much lower when decisional output values are sought than when risk estimates are the quantities studied. Specifically the difference between the minimum and maximum values for risk (depending on the building fragility relationship considered) was 10 times greater than for the optimal design value.

The choice of the vulnerability/fragility curve is therefore much more important when calculating risk than for an optimal design procedure. This conclusion was already reached in Eckert et al. (2009), but with a much smaller number of vulnerability/fragility relations. More generally, this is not a surprising result since it is in accordance with decision theory where robustness of optimality towards classes of cost/loss functions is well known (Abraham and Cadre, 2004). Our building and human fragility curve sets do not correspond exactly to the mathematical definition of classes, but they are close. More importantly, the practical outcomes of this finding are great: if the objective of the study is to find the decision (let's say, the mitigation measure) that minimises risk rather than having an exact estimate of the risk, then a rougher estimate of the vulnerability/fragility relation

may be sufficient. This is another point arguing in favour of the use of the systematic but presumably oversimplified fragility relation set, and also for the promotion of cost benefit analyses / optimal design approaches in avalanche engineering.

4.6 Conclusion and outlooks

In a nutshell, few relations reflecting vulnerability/fragility to snow avalanches currently exist for buildings, and even fewer for humans inside buildings. Furthermore, these relations were mainly derived from catastrophic historical events whose characteristics do not often correspond to paths where refined risk estimates are needed. In this study, systematic reliability analyses of buildings impacted by avalanche loads were used to deduce large sets of building and human fragility relations according to avalanche pressure. By comparison to empirical back analyses, this approach is powerful and infinitely reproducible, allowing the existing knowledge to be supplemented as needed.

Second, this new large set of curves was used to produce a comprehensive sensitivity to vulnerability/fragility relation analysis up to the design of a defence structure. To do so, we promoted the ability of the risk framework to accommodate differences between vulnerability/fragility, and proposed bounds and indexes of both theoretical (quantifying uncertainty/variability that cannot be simply expressed in a probabilistic way) and practical (minimum/maximum plausible values) aspects. In a typical case study, we clearly showed how highly risk estimates are sensitive to the choice of the vulnerability/fragility relation, whereas optimal design procedures may be more robust. Even if a certain case-study dependence may exist, requiring more studies for wider generalisation, these results enhance our overall understanding of avalanche risk and may therefore well be worth considering by avalanche engineers. For instance, they clearly show that current runout return period-based zoning policies can be far from the quantification of true risk. Specifically, comparisons with acceptable risk levels has highlighted the variability of abscissas in the path where the acceptable risk threshold is exceeded. For example, for the case study, only abscissas above the $1,000$ year return period may be considered as fully safe.

The generally high sensitivity to vulnerability/fragility relations that has been highlighted emphasizes the need for reliable relations, that is to say accurate and systematically available relations for a large variety of building types, provided *e.g.*, by fully numerical approaches. The application presented in this paper was undertaken for a relatively large class of RC buildings, but using a rather simple numerical engineering approach. Hence, the results are subjected to all the inherent approximations and assumptions. For example, the fragility relations were assessed under the assumption of quasi-static pressure loads only, which is questionable in some typical situations. In the future, a more complex mechanical building model could be developed to study a particular geometry and carefully

propagate confidence intervals up to risk quantification, taking into account additional epistemic uncertainties and/or variability sources within the various processes involved.

Similarly, we worked with hazard distributions calibrated on a typical case study, but in a simple (x,z) geometry (no lateral spread), and with only one building or human taken into account in an individual risk perspective. For real risk mapping and optimal design of mitigation measures in already urbanised areas, this is not enough, and expanding the approach to a 2D to 3D avalanche hazard model is still required. Combining its outputs with more advanced mechanical models accurately describing the existing buildings, as discussed above, would definitely help refine the quantification of risk to humans and buildings, and, therefore, be very useful for managing risk in the most delicate case studies.

4.7 Acknowledgements

The authors thank the ANR research program MOPERA (Modélisation probabiliste pour l'Étude du Risque d'Avalanche - www.avalanches.fr/mopera-projet/) and the MAP3 Alcotra Interreg program for funding this work. The authors are also grateful to P. Gauer and two anonymous referees whose constructive comments helped to improve the paper.

CHAPTER 5

Avalanche risk evaluation and protective dam optimal design using extreme value statistics: simple analytical formulae and sensitivity study to hazard modeling assumptions

Le contenu de ce chapitre a vocation à être soumis après travail à *Journal of Glaciology*, les auteurs en sont : Favier, P., Eckert, N., Bertrand, D., Faug, T. and Naaim, M..

Abstract

In snow avalanche long term forecasting, existing risk-based methods remain difficult to use in a real engineering context. Yet, they make use of debatable assumptions for hazard modelling. In this work, we address these limitations by expanding a quasi analytical decisional model so as to obtain simple risk formulae to quantify risk and perform the optimal design of an avalanche dam in a quick and efficient way. These may be usable in a variety of situations, as soon as a very generic additive cost model with a constant damage susceptibility is found suitable. Specifically, the exponential runout model is replaced by the generalised Pareto distribution (GPD) that has theoretical justifications that promotes its use for modelling the different possible runout tail behaviours. Regarding the defence structure - flow interaction, a simple law based on kinetic energy dissipation is confronted to a law based on the volume stored upstream of the dam whose flexibility make it able to cope for various types of snow. We finally show how a detailed sensitivity study can be conducted, leading intervals and bounds for risk estimates and optimal design values.

Application on a typical case study from the French Alps demonstrates that it is often not easy to fit a robust runout tail distribution on the basis of the data only, making the forecasted high return levels badly constrained. A profile likelihood approach can tackle this difficulty, but residual risk estimates and optimal dam heights remain highly variable towards possible runout tail types. Similarly, a very high sensitivity to the avalanche-dam interaction law exists: the energy dissipation one generally postulates a higher risk reduction, but the flexility of the volume catch one makes the case of high deposit shape angles due to wet snow flows an exception to this rule. Also, with this law, the higher complexity of the dependency to the dam height makes that no solution to the optimal design problem exists over a large range of abscissas in the runout zone. The highest sensitivity to the runout tail type and interaction law is fond at abscissas of legal importance for hazard zoning (return periods of $10 - 1,000$ years), a crucial result for practice. This all suggests that the tail behaviour of extreme runouts, as well as the energy dissipation and deposition patterns occurring when an avalanche hits an obstacle should be reinvestigated to reduce uncertainty levels in operational contexts.

Keywords: Snow Avalanche; Individual Risk; Defense Structure; Risk Minimisation; Extreme Value Statistics; Runout return period; Interaction Law; Uncertainty Quantification and Propagation.

5.1 Introduction

Snow avalanche long term forecasting for risk mapping and the design of defense structures is generally done on the basis of high magnitude events defined by their return period *e.g.* Salm et al. (1990). Such purely hazard-oriented approaches do not explicitly consider elements at risk (buildings, people inside, etc.), and neglect possible budgetary constraints. Therefore, they do not guarantee that unacceptable exposition levels and/or unacceptable costs cannot be reached. This is well demonstrated in Favier et al. (2014b) by confronting standard hazard zone limits with acceptable risk levels as defined in Jónasson et al. (1999). To overcome these limitations, risk based zoning methods (Keylock et al., 1999; Arnalds

et al., 2004) and cost-benefit analyses (Fuchs et al., 2007a) have emerged recently in this field, allowing socioeconomic considerations to be included into the analysis (Bründl et al., 2009) in a proper mathematical framework (Eckert et al., 2012).

Risk quantification requires combining the model for avalanche hazard with a quantitative assessment of consequences for the elements at risk. The hazard distribution is (at least partially) site-specific, and two main approaches exist to determine it. "Direct" statistical inference can be used to fit explicit probability distributions on avalanche data, mainly runout distances (Lied and Bakkehoi, 1980; Eckert et al., 2007b; Gauer et al., 2010). As an alternative, richer but more computationally intensive, statistical-dynamical approaches include hydrodynamical modelling within the probabilistic framework (Barbolini and Keylock, 2002; Meunier and Ancey, 2004; Eckert et al., 2008a). They lead the joint distribution of all variables of interest, including the one of spatio-temporal pressure fields (Eckert et al., 2010c).

Consequences for elements at risk are estimated using vulnerability relations, *i.e.* increasing curves with values in $[0-1]$ quantifying, for various types of elements at risk (people, buildings, infrastructures ...), the expected damage as function of avalanche intensity. The latter is generally expressed in terms of impact pressure, but sometimes also of flow depth or velocity (Barbolini et al., 2004a). Existing vulnerability to snow avalanche relations have been historically assessed empirically, by back-analysis of well documented events (Keylock and Barbolini, 2001; Papathoma-Köhle et al., 2010), but numerical approaches have emerged recently to evaluate more systematically the vulnerability of buildings, deterministically (Bertrand et al., 2010), or within a reliability framework (Favier et al., 2014a).

To conduct a cost benefit analysis between various mitigation solutions and, for instance, minimize the residual risk after the construction of a defense structure, effects of such structures on avalanche flows must also be quantified. This is complex because fundamental physical processes are involved (propagating jumps, dead zones and airborne jets), which are still not fully understood. This makes the full modelling of the interaction between avalanches and various defense structure types such as dams currently impossible with state of the art depth-averaged models for avalanche propagation (Bartelt et al., 1999; Naaim et al., 2004). However, for this purpose, semi-empirical analytic equations could be developed to describe the runout shortening caused by dam-like obstacles. These laws were established for walls spanning the whole width of the incoming flow with the help of simple theoretical arguments combined with small-scale laboratory tests on granular avalanches. For high Froude number incoming flows (fast dry snow avalanche), a simple linear relation between the runout shortening and the dam height relative to the incident flow was evidenced (Hakonardottir, 2000; Faug et al., 2003) and partly verified on available full-scale observations (Faug et al. (2008)). For low Froude number flows (very slow

avalanche), the runout shortening was found to be a function of the volume stored upstream of the dam relative to the total avalanche volume (Faug et al. (2004a)). These two existing interaction laws correspond to idealized situations for which the runout shortening is caused by either the local dissipations of kinetic energy (purely inertial regime) or the volume reduction due to storage of the snow upstream of the dam (purely gravitational regime). In real world, however, both process may coexist, and other semi-empirical, more complex laws for the runout shortening may be used (Faug et al., 2003; Faug, 2004).

A specific difficulty remains poorly addressed in the avalanche community. Long term forecasting deals with high magnitude events, by definition rare, whereas available data series are short and lacunar, when they exist. Hence, robust methods to extrapolate beyond the observational records should, in principle, be used. For this, statistical models based on extreme value theory (EVT) are ideal candidates because of their strong mathematical justifications (Leadbetter et al., 1983; Embrechts et al., 1997; Coles, 2001). They are therefore commonly used, *e.g.*, in hydraulic engineering to evaluate high return period discharges, *e.g.* Katz et al. (2002). Specifically, for univariate random numbers, block maxima (see, *e.g.*, Coles (2001) for a synthesis of the original work of Fisher, Tippett and Gnedenko) and exceedences above high thresholds (Pickands, 1975) converge, under rather mild regularity conditions, to well known distributions of three types: heavy tailed (Fréchet type), light tailed (Gumbel type) and bounded (Weibull type). These can be summarised into one unique class of limit models, namely Generalized Extreme Value (GEV) distributions for block maxima, and Poisson - Generalized Pareto Distributions (GPD) for Peak Over Threshold (POT) exceedences. Both approaches are asymptotically equivalent, leading to the same prediction of high return levels.

For multivariate random numbers, the class of limit models is not unique, but analogous convergence results exist, providing properties to be satisfied by multivariate extremes, *e.g.*, Resnick (1987). These include asymptotic dependance/independence measures indicating how two marginal tails of distributions are related (Coles et al., 1999; Schlather and Tawn, 2003). The approach can be generalised to the infinite dimension case of spatial processes (De Haan, 1984; Naveau et al., 2009).

The univariate EVT framework is more or less behind most of the statistical approaches to high return period avalanche evaluation, even if it not always explicitly advocated. For instance, Ancey (2012) has discussed the behaviour of extreme avalanches with regards to outliers' theory. Also, the runout ratio approach of McClung and Lied (1987) where normalized runouts of extremes avalanches collected over a sample of paths are fitted by a Gumbel distribution may be seen as a specific application of the block-maxima GEV approach. More recently, available runout samples have been studied in search for some systematic behaviour of the tail of their distribution, which could give valuable insights for practice. Indeed, results showed a Weibull type more often than not (Keylock, 2005).

Critically, however, the strong dependency of runouts on local topography makes that exceptions arise, precluding from general conclusions, and making extrapolations beyond the highest recorded value speculative as soon as the paths topography is irregular. This is well shown in Eckert et al. (2009) with long range simulations highlighting strong discontinuities in the runout distribution tail linked to very local changes in path's concavity. Finally, the use of univariate EVT is emerging for characterizing avalanche cycles (clusters of events, generally during a winter storm), but with specific difficulties due to the discrete nature of the data (Eckert et al., 2010b, 2011).

The framework of multivariate EVT has not been, up to now, used for snow avalanches, except in a simplified way for a few engineering studies, (Naaim et al., 2010), and, from a slightly different perspective, to evaluate in a spatial context extreme snowfall (Blanchet and Davison, 2011; Gaume et al., 2013) and subsequent avalanche release depths (Gaume et al., 2012), taking into account dependence between close measurement stations to refine predictions. Hence, evaluation of the joint distribution of rare avalanche flow depths, velocities, runouts, etc. generally rely on the statistical-dynamical models previously introduced. In them, the inter-variable dependence is strongly constrained by the physical equations used (mass and momentum conservation, flow rheology, etc.) within the numerical model (Bartelt et al., 1999; Naaim et al., 2004). This has some evident advantages, but also the limitation of being not necessarily consistent with the limit results of EVT, making the most extreme events predicted questionable, whereas their validation on the basis of observations remains a challenging task (Schläppy et al., 2014).

More generally, existing risk-based methods available for engineers in the snow avalanche field suffer from strong limitations. On the one hand, standard cost-benefit analyses generally consider a limited value of potential actions/decisions, and, even more critically, reduce the hazard distribution to one or a few scenarios. The retained choice may therefore be far from optimal, and even be inappropriate in case of a strong sensitivity to the retained hazard scenarios. Application exist mostly in the domains of defense structure efficiency assessment, (Wilhelm, 1997; Fuchs and Bründl, 2005; Margreth and Romang, 2010), and risk to traffic roads minimization (Margreth et al., 2003; Hendrikx and Owens, 2008). Existing risk based methods that well consider the full hazard distribution mainly address the question of zoning for land use planning purposes (Keylock et al., 1999; Barbolini et al., 2004b). However, as for the statistical-dynamical models on which they rely, they do not benefit from the theoretical justifications of extreme value statistical models. Furthermore, they remain so computationally intensive that strong simplifying assumptions are generally made to reduce the numerical burden, *e.g.* a linear relation between avalanche release depth and impact pressure in the runout zone in Cappabianca et al. (2008). And even so, they remain little used by practitioners because of their inherent complexity, difficult to conciliate with operational constraints.

Up to now, at our knowledge, only two exceptions consistently combine all the elementary bricks of the risk framework within a single decisional perspective more or less based on EVT. In Rheinberger et al. (2009), a quantitative comparison of organisational (temporary) and structural (permanent) risk to traffic road reduction options is performed. In Eckert et al. (2008a) the size of the avalanche dam that maximizes the economical benefit of its construction in a land use planning application is searched. These approaches work at more than reasonable computational costs since they are nearly fully analytical. Yet, some drawbacks can be found. In Rheinberger et al. (2009), the different competing decisions are too different from each others to allow a sound representation of the risk as function of decision. In Eckert et al. (2008a), the decision space is continuous and simpler and, hence, better accounted for, but this arises because only the case of a dam interacting with fast dry snow avalanches (Faug et al., 2008) is considered. Furthermore, in both papers, only the relatively simple case of light runout tails is considered: Gumbel block maxima in Rheinberger et al. (2009), and Poisson Exponential exceedences of the dam position in Eckert et al. (2008a). And even if a Bayesian analysis is made in Eckert et al. (2008a) to take data quantity into account in the decisional procedure, little attention in given in both papers to the question of model uncertainty and sensitivity of risk estimates and related minimisation rules to its choice.

On this basis, the first objective of this paper is to expand the pre-existing dam decisional procedure of Eckert et al. (2008a) to make it workable under much less restrictive assumptions regarding hazard distribution and interaction law, but keeping the idea to develop fully analytical risk equations easily usable in practice. Specifically, to address the question of well describing runout tails within the EVT framework, we consider the full class of Poisson-GPD models of which the exponential case used previously is only a very particular case. Similarly, regarding the interaction laws for runout shortening, we will confront the simple formulation based on energy dissipation used before to the one based on the retained volume developed in Faug et al. (2004a). This latter is suitable for slow flows and more flexible thanks to an additional free parameter representing the deposit shape angle from the horizontal. This framework leads different analytical formulae based on extreme value statistics to quantify risk and perform the optimal design of an avalanche dam in a quick and efficient way. These may be usable in a variety of situations faced in the engineering practice as soon as a very generic additive cost model is adopted to express losses to elements at risk and construction costs in the same monetary currency. All computations are made in an individual risk perspective, focusing on a single element at risk (say a building) and over the long range using an econometric actualisation term that accounts for the dam amortizing duration.

The second objective of the paper is to implement these formulae on a real case study (a path from the French Alps), where, as usual for real applications, available data is

seldom and presumably imperfect. This makes strong uncertainties regarding estimates of the runout model and, more generally, regarding the different modelling assumptions unavoidable, *e.g.* which flow regime should be considered in priority for the dam design. Hence, we show how results can be provided in terms of intervals/bounds usable by the engineers to fairly quantify and represent the impact of different uncertainty sources on risk zoning and defense structure design values, in the spirit of the work made by Favier et al. (2014b) for vulnerability relations, but, as said before, at much lower computational costs (analytical evaluation here, versus numerical in (Favier et al., 2014b)). These intervals/bounds result from different techniques of uncertainty propagation/quantification suitable for different types of uncertainty/variability, depending, for instance, if these are expressible in a quantitative probabilistic way or not. In fine, from a wider perspective, we use our case study to discuss the sensitivity of risk quantification and minimisation procedures to avalanche hazard modelling choices.

In what follows, Sect. 5.2 presents the elementary bricks of the work. Sect. 5.3 details the application of our approach on the chosen case study. Sect. 5.4 discusses the outcomes of the work, potential outlooks and concludes.

5.2 Methods

5.2.1 Runout models based on extreme value statistics

In this subsection, we present the extreme value statistical model class we are working with, and how its parameters can be fitted on the data. For practitioners willing not to worry with the technical difficulties, most of the computations can be performed with existing routines in open-source statistical softwares like *R*.

POT modelling

The Poisson GPD Peak Over Threshold (POT) approach is now commonly used in hydrology to estimate high quantiles (Parent and Bernier, 2003a; Naveau et al., 2014), and has gained recent interest for analysing related processes such as debris flows (Nolde and Joe, 2013). The reason is that Pickands (1975) has shown that the Poisson GPD class of models includes all limit models for independent exceedences of asymptotically high thresholds. In practice, this "only" means choosing a sufficiently high threshold and, if necessary, decluster possibly dependent exceedences (Coles, 2001) before fitting the model parameters. Specifically, it writes as follows.

The number a_t of threshold exceedences on a winter period follows a Poisson distribu-

tion with parameter λ:

$$f(a_t|\lambda) = \frac{\lambda^{a_t}}{a_t!}\exp(-\lambda). \tag{5.1}$$

The intensity of exceedences follows a Generalized Pareto Distribution (GPD). In our case, the avalanche runout abscissa x_{stop_0} is the intensity variable of interest. The 0 index refers to the fact that no protective measure is considered (natural activity of the avalanche phenomenon). Hence, the probability density function of avalanche runouts exceeding the x_d dam abscissa (the "d" index denotes that the the chosen threshold corresponds here to the position where a dam construction is envisaged, but other choices are straightforward) is:

$$f\left(x_{stop_0} - x_d|\rho,\beta,x_{stop_0} > x_d\right) = \begin{cases} \rho\left(1-\beta\left(x_{stop_0}-x_d\right)\right)^{\frac{\rho}{\beta}-1} & \text{if} \quad \beta \neq 0 \\ \rho\exp(-\rho(x_{stop_0}-x_d)) & \text{if} \quad \beta = 0 \end{cases}. \tag{5.2}$$

In practice, two different GPD parametrization are used, with the correspondence $\xi = -\frac{\beta}{\rho}$ and $\sigma = \frac{1}{\rho}$. The (σ,ξ) couple is more interpretable in terms of physics (σ is a scale parameter and ξ a dimensionless shape parameter), whereas the (ρ,β) couple is computationally more convenient (Parent and Bernier, 2003b). As a consequence, we will deal with the latter for inference only, and, with the former, in the rest of the analysis. Notably, the ξ parameter fully characterises the shape of the GPD tail. A heavy tail associated to the Fréchet domain corresponds to $(\xi > 0)$. The light (exponential) tail (Gumbel domain) is the $(\xi = 0)$ limit case, and $(\xi < 0)$ characterizes the bounded tail of the Weibull domain.

The one-to-one mapping between runout distance beyond x_d and return period T results, for $\lambda T > 1$, from equation:

$$T = \frac{1}{\lambda\left(1-F(x_{stop_0})\right)}\ , \tag{5.3}$$

where λ is the avalanche exceedence rate of the abscissa x_d (mathematical expectancy of the Poisson distribution), and $F(x_{stop_0})$ the cumulative distribution function of unperturbed (without dam) runout distances beyond the abscissa x_d.

Replacing $F(x_{stop_0})$ by its expression given by the integral of Eq. (5.2) leads the $(1-1/\lambda T)$ quantile (also denoted return level) corresponding to the return period T fully analytically, an enormous advantage for practice:

$$x_T|(x_T > x_d) = \begin{cases} x_d + \frac{\sigma}{\xi}((\lambda T)^{\xi}-1) & \text{if} \quad \xi \neq 0 \\ x_d + \sigma\ln(\lambda T) & \text{if} \quad \xi = 0 \end{cases}. \tag{5.4}$$

This expression shows well the crucial role of the sign of the ξ parameter: positive values lead to "explosive" increments of the return level with T, faster than in the exponential

case ($\xi = 0$), for which this increase is log-linear with T. On the contrary, in the Weibull case ($\xi < 0$), the quantile tends, for high values of T, to the limit return level $x_d + \sigma/\xi$.

Likelihood maximisation

To get estimates $\hat{\lambda}$ and $\hat{F}(x_{stop_0}) = F(\hat{\rho}, \hat{\beta})$ (best guesses, traditionally denoted by a "hat") for λ and $F(x_{stop_0})$, respectively, the standard procedure is to use likelihood maximisation, *i.e.* to determine the parameter values that maximise the probability of having observed the data actually at hand. For the Poisson distribution, $\hat{\lambda}$ is simply the mean exceedence rate, *i.e.* $\hat{\lambda} = \dfrac{m}{T_{obs}}$ where $m = \sum_{t=1}^{T_{obs}} a_t$ is the number of recorded exceedences of the x_d abscissa during the T_{obs} winters of observation.

The Generalized Pareto log-likelihood $l(\rho, \beta)$, the logarithm of the probability density function seen as function of model parameter, is, for $\beta \neq 0$:

$$l(\rho, \beta) = n \log \rho + \left(\frac{\rho}{\beta} - 1\right) \sum_{i=1}^{n} \log\left(1 - \beta\left(x_{stop_{0_i}} - x_d\right)\right), \tag{5.5}$$

where $x_{stop_{0_i}}$, i in $[1, n]$, is an independant and identically distributed (iid) sample of the distribution $f(x_{stop_0})$.

The partial derivative according to ρ is:

$$\frac{\partial l}{\partial \rho} = \frac{n}{\rho} + \frac{1}{\beta} \sum_{i=1}^{n} \log\left(1 - \beta\left(x_{stop_{0_i}} - x_d\right)\right). \tag{5.6}$$

It follows that the maximum log-likelihood estimate for ρ is: $\hat{\rho} = \dfrac{n}{S_n(x_{stop_0}, \hat{\beta})}$, where $S_n(x_{stop_0}, \beta) = -\frac{1}{\beta} \sum_{i=1}^{n} \log\left(1 - \beta\left(x_{stop_{0_i}} - x_d\right)\right)$. The estimate $\hat{\beta}$ of β is obtained numerically, knowing $\rho = \hat{\rho}$, leading the log-likelihood maximum: $\hat{\beta} = \max_{\beta} l(\hat{\rho}, \beta)$.

Classical theory of statistical estimation relies on asymptotic properties resulting from suites of experiments. It provides standard errors for the maximum likelihood estimates trough:

$$var(\theta) = [-E[H(l|\theta)]]^{-1} \tag{5.7}$$

where E denotes the mathematical expectation and $H(l|\theta)$ is the so-called Hessian matrix of the log-likelihood l indexed by the parameters θ (traditional generic notation).

Specifically, the expression of the (negative) Hessian of the GPD is (see, *e.g.*, Coles (2001)):

$$-H(l|\theta) = \begin{pmatrix} \frac{n}{\rho^2} & \frac{1}{\beta}\left(\sum_{i=1}^{n} \frac{(x_{stop_{0_i}} - x_d)}{\left(1-\beta(x_{stop_{0_i}} - x_d)\right)} - S_n(x_{stop_0}, \beta)\right) \\ sym. & -\frac{2\rho}{\beta^2}\left(\sum_{i=1}^{n} \frac{(x_{stop_{0_i}} - x_d)}{\left(1-\beta(x_{stop_{0_i}} - x_d)\right)} + S_n(x_{stop_0}, \beta)\right) + \left(\frac{\rho}{\beta} - 1\right) \sum_{i=1}^{n} \frac{(x_{stop_{0_i}} - x_d)^2}{\left(1-\beta(x_{stop_{0_i}} - x_d)\right)^2} \end{pmatrix}, \tag{5.8}$$

where *sym* denotes that the matrix is symmetrical. Since maximum likelihood estimates are asymptotically Gaussian, these standard errors allow constructing asymptotic confidence intervals for the estimated parameters easily, so as to fairly represent the uncertainty resulting from the limited data sample available.

Model selection and profile likelihood maximisation

The Poisson - Exponential model is a very specific (limit) case of the Poisson - GPD one ($\xi = 0$), with a different writing of the likelihood according to Eq. (5.2). This implies that two different likelihood minimisations must be carried out and that, then, a model selection tool must be employed to discriminate between the best fitted exponential and GPD (Fréchet or Weibull) models. An usual way to do that is to implement a likelihood ratio test based on the D deviance statistics, *i.e.* two times the logarithm of the ratio of the two maximized likelihoods. Specifically, if $\ell_1(M_1)$ is the maximised log-likelihood corresponding to the exponential distribution ($\beta = 0$) and $\ell_0(M_0)$ the maximised log-likelihood corresponding to the GPD distribution ($\beta \neq 0$):

$$D = 2\left\{\ell_1(M_1) - \ell_0(M_0)\right\} = 2\left\{n \log\left(\sum_{i=1}^{n}\left(x_{stop_{0_i}} - x_d\right)\right) - n \log\left(S_n\left(x_{stop_0}, \hat{\beta}\right)\right) + \hat{\beta} S_n\left(x_{stop_0}, \hat{\beta}\right)\right\} . \tag{5.9}$$

The model choice is then made according to the value of D. Its asymptotic distribution is the one degree of freedom χ^2 law. The null hypothesis is the choice of the exponential model, whereas the alternative hypothesis is the GPD model with $\xi \neq 0$ (Fréchet or Weibull). The null hypothesis is rejected at the $\alpha\%$ significance level if $D > c_{\alpha_{\chi^2}}$ where $c_{\alpha_{\chi^2}}$ is the $1-\alpha\%$ quantile of the one degree of freedom χ^2. Specifically, the 95%-quantile of the one degree of freedom χ^2 law is 3.841.

Yet, this may not be enough for choosing a model among the GPD class. Indeed, the shape parameter ξ (or β) is often difficult to estimate on real data whereas $\hat{\sigma}$ and the estimates $\hat{\xi}$ are linked. As a consequence, the likelihood is often very flat around the optimum $(\hat{\sigma}, \hat{\xi})$ provided by the maximisation of Eq. (5.5), so that different couples (σ, ξ) may well fit the data rather similarly. To explore the practical implication of that, and, hence, go on with the uncertainty/sensitivity analysis to hazard model choice, we hereafter test different couples obtained by solving the profile likelihood maximisation for various possible values ξ_0 as:

$$\hat{\sigma}(\xi_0) = \underset{\sigma}{\operatorname{argmin}} \left(-\sum_{i=1}^{n} log f\left(\sigma \mid x_i, \xi_0\right) \right) . \tag{5.10}$$

5.2.2 Avalanche-dam interaction laws

This sub-section deals with the semi-empirical analytic laws governing the influence of a dam on avalanche-flows, with a specific focus on runout shortening.

It is rarely possible (for economical and/or environmental reasons) to design a catching dam that could stop all avalanches at all times. Some avalanches might overflow the dam and flow downstream. One way of quantifying the residual risk related to overflow is to estimate the avalanche runout shortening, $x_{xtop}(h_d) - x_{stop_0}$, caused by the dam, where $x_{xtop}(h_d)$ and x_{stop_0} are the maximum runout distances with dam and without dam, respectively, and h_d is the dam height. Depending on the flow regime of the incoming avalanche and the size of the dam, the physical processes involved in the dam-avalanche interaction are expected to vary. Studying the details of the involved mechanics in this interaction is beyond the scope of this paper. In what follows, we shortly present two semi-empirical analytic equations that were previously developed and tested on small-scale laboratory experiments about granular avalanches (Faug et al., 2003; Faug, 2004), and which will be used in the present work.

Runout shortening by energy dissipation

A first interaction law was established to relate the maximum runout distance downstream of a dam, $x_{stop}(h_d)$ relative to the maximum runout distance without dam, x_{stop_0}, to the dam height h_d relative to the thickness of the incident avalanche-flow h_0 as:

$$\frac{x_{stop}(h_d) - x_d}{x_{stop_0} - x_d} = 1 - \alpha \frac{h_d}{h_0}. \tag{5.11}$$

α is the energy dissipation coefficient quantifying the dam efficiency. It is assumed to be constant and equal to 0.14 in the present study.

This interaction law was initially developed by Faug et al. (2003), further justified and verified by Faug et al. (2008), and previously used for risk and optimal design computations by Eckert et al. (2008a, 2009, 2012). It is expected to be valid when local dissipations of kinetic energy prevail, which is generally verified under two conditions: (i) fast dry snow avalanches (inertial regime) characterized by relatively high Froude numbers (around $5 - 10$) and (ii) a dam height not too high in order to prevent the formation of shocks upstream of the dam. If the dam height is too high, typically h_d/h_0 around $5 - 11$ for Froude numbers in the range $5 - 10$, propagating waves are likely to be formed upstream of the dam which may lead to important volumes of snow retained upstream of the dam.

A positivity constraint exists with this interaction law, *i.e.* $h_d < \frac{h_0}{\alpha}$. For higher dams, all avalanches are stopped. For instance, for an incident avalanche flow $h_0 = 1m$, h_d varies with Eq. (5.11) in the $[0\ m, 7.14\ m]$ interval. As stated previously, another critical upper value for the dam height that avoids the formation of shocks upstream of the dam can also be determined according to the Froude number of the flow. In theory, this critical value can be lower or greater than $\frac{h_0}{\alpha}$, the upper bound due to the positivity constraint in Eq. (5.11). In this paper, however, we consider that we investigate only Froude number

ranges for which the minimal height for shock formation is higher than $\frac{h_0}{\alpha}$, so that we avoid the problem of determining it precisely, and only consider the positivity constraint directly linked to Eq. (5.11).

Runout shortening by volume catch

We propose to test also another interaction law, initially developed by Faug et al. (2004a) as well. As Eq. (5.11), this interaction law relates the maximum runout distance downstream of the dam, $x_{stop}(h_d)$ relative to the runout distance without dam, x_{stop_0}, to the dam height. However, it is somewhat different because it is based on the idea that the runout shortening is mainly driven by the volume reduction. Hence, the runout shortening can be related to the difference between the total volume of the avalanche flow V and the volume retained upstream of the dam V_s. As a natural deposit, caused by friction with the bottom, is likely to occur with or without the presence of the obstacle (Faug, 2004), the volume retained upstream of the dam is the sum of this natural volume due to friction, V_{stop}, and the volume retained by the obstacle only, $V_{obs}(h_d)$, which depends on the dam height (Figure 5.1).

Specifically, under the assumption of a very slow avalanche (Froude number less than or around 1), the following equation was proposed by Faug et al. (2004a):

$$\frac{x_{stop}(h_d) - x_d}{x_{stop_0} - x_d} = \left(1 - \frac{V_{obs}(h_d)}{V - V_{stop}}\right)^n \tag{5.12}$$

where n can be either 1/2 or 1/3 ,depending on the characteristics of the upstream storage zone (confined or not). For a confined storage zone, $n = 1/2$ is more suitable. Furthermore, the reasonable assumption that V_{stop} is much smaller that V_{obs} yields:

$$\frac{x_{stop}(h_d) - x_d}{x_{stop_0} - x_d} = \left(1 - \frac{V_{obs}(h_d)}{V}\right)^{1/2} . \tag{5.13}$$

Finally, by assuming that the volume $V_{obs}(h_d)$ stored upstream of the dam roughly has a triangular shape forming a line inclined at constant slope ϕ with the horizontal, one can explicitly relate the retained volume to the dam height h_d when the deposit zone upstream of the dam is confined and of constant width ℓ_{fz}. However, the shape of the deposit V_{obs} might depend on the snow type: dry snow (fast flow - Eq. (5.14) (a)) versus more humid and, hence, heavier snow (slower flow - Eq. (5.14) (b)), so that one may expect two situations to occur, described by the following equation:

$$V_{obs}(h_d) = \frac{\ell_{fz} \times h_d^2}{2\ tan(\alpha_s)} \text{ with } \alpha_s = \psi_{fz} - \phi \begin{cases} \phi < 0 \text{ (Table 5.1}a\text{)} \\ \phi \geq 0 \text{ (Table 5.1}b\text{)} \end{cases} , \tag{5.14}$$

since the length L of the deposit upstream the dam is simply $L = \frac{h_d}{\tan(\alpha_s)}$.

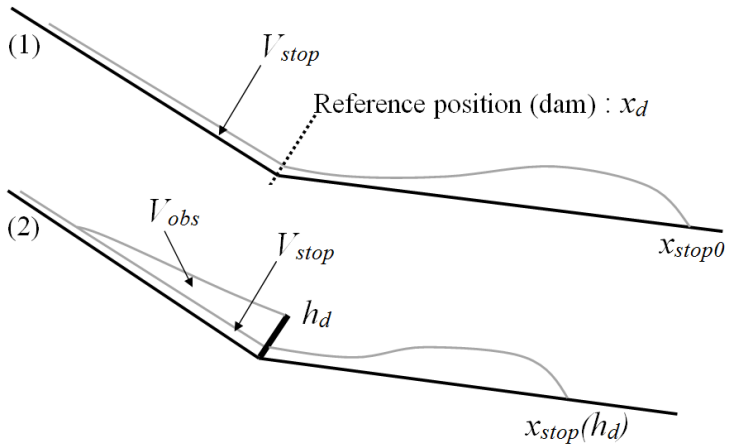

Figure 5.1 – Definition of deposited volumes without (1) and with (2) obstacle (dam of height h_d at the abscissa x_d), inspired by Faug et al. (2004a).

These two cases are considered because, for heavy humid snow (very slow flows), the friction coefficient, classically denoted as μ in the avalanche literature, should be high (*e.g.* Naaim et al. (2013)), resulting in larger deposits with a deposit line above the horizontal plane. In contrast, dry cold snow should flow faster and give a lower friction coefficient, resulting in shorter deposits with a deposit line below the horizontal plane. All assumptions and notations regarding runout shortening by volume catch are outlined in Table 5.1 where the angle of snow deposit ϕ is the angle with the horizontal measured in the inverse trigonometric wise.

In practice, the volume stored upstream of the dam is smaller or equal to the incident avalanche volume leading the constraint $h_d < \left(\frac{V \times 2\tan(\alpha_s)}{\ell_{fz}}\right)^{1/2}$. Furthermore, in a given path, and knowing the dam width, we can write: $A_a = V/\ell_{fz}$. The positivity constraint associated to Eq. (5.13) then becomes: $h_d^2 \ell_{fz} < 2V \times \tan\alpha_s$, which is equivalent to $h_d < (2A_a \tan\alpha_s)^{1/2}$. For example, for an incident volume $V = 50,000\ m^3$, $\phi = 0°$, $\psi_{fz} = 10°$ and $\ell_{fz} = 100\ m$, h_d may vary in the $[0 - 18.7]$m interval.

Finally, all these considerations highlight that the runout shortening according to volume catch relation is much more flexible than the one regarding energy dissipation. Indeed, whereas in Eq. (5.11) and Eqs. (5.12), (5.13), (5.14) an avalanche scenario is a flow depth / volume, respectively, with the volume catch relation, one has, in addition, the deposit angle ϕ (value and sign) to choose/specify, according to the snow type one considers.

Table 5.1 – Difference in deposit shape assumed in this study between "dry" and "humid" snow avalanches, $\phi = 0°$ is the limit case between these. Other given ϕ values are those considered in text.

Dry snow (a)	Humid snow (b)
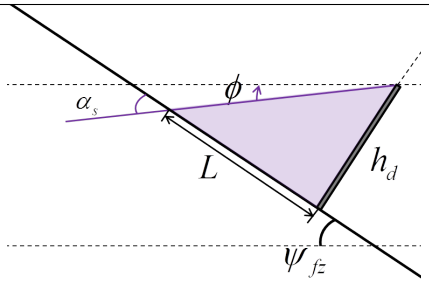	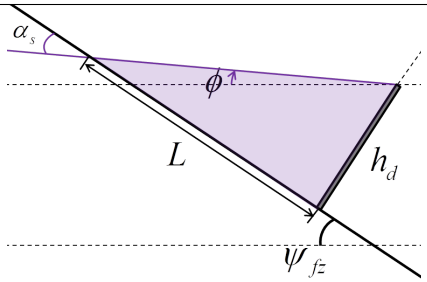
fast flow / low friction snow	slower flow / highly frictional snow
deposit line below the horizontal line	deposit line above the horizontal line
$\phi = -20°, -40°$	$\phi = 0°, 3°, 6°, 9°$ ($\phi < \psi_{fz}$ mandatory)

5.2.3 Individual risk and optimal design based on its minimisation

This subsection presents the general risk and optimal design framework we work within and goes up to the combination of our POT hazard model with the two studied interaction laws. This leads analytical formulae for the residual risk as function of the dam height for the different considered runout tail types and interaction laws.

Specific risk

Among natural hazards, risk is broadly defined as an expected damage, in accordance with mathematical theory (*e.g.*, Merz et al. (2010) for floods, Mavrouli and Corominas (2010b) for rockfall, Jordaan (2005) in engineering, etc.). Following the notations of Eckert et al. (2012), the generic notation for the specific risk r_z for an element at risk z is:

$$r_z = \lambda \int p(y) V_z(y)\ dy\ , \tag{5.15}$$

where λ is the annual avalanche rate, *i.e.* the annual frequency occurrence of an avalanche, $p(y)$ is the multivariate avalanche intensity distribution (runout, flow depth, etc.) and $V_z(y)$ is the vulnerability of the element z to the avalanche avalanche intensity y. $V_z(y)$ can be either a damage level or a destruction probability, depending if a deterministic or a probabilistic (relability based) point of view is adopted. By definition, the specific risk unit at the annual time scale is $[year^{-1}]$.

In accordance with our hazard and interaction law model specifications, we describe avalanche flow within a two-dimensional cartesian frame. In it, avalanche intensity is

classically defined by the joint distribution $p(y) = p(P, x_{stop_0})$ of spatio-temporal pressure fields P and runout distances x_{stop_0}. The specific risk $r_b(x_b)$ for the element b at the x_b abscissa is then:

$$r_b(x_b) = \lambda \int p(P|x_b \leq x_{stop}) p(x_b \leq x_{stop}) \times V_b(P)\ dP\ , \tag{5.16}$$

where the notation ".|." classically denotes a conditional probability. Notations x_b, V_b, and r_b (indice b) indicate that the typical element at risk we consider is a building, see Sects. 5.3 for details (numerical values) and 5.4 for discussion.

We consider only building abscissas such as $x_b > x_d$, a natural choice in practice (one would'nt build higher in the path for evident safety reasons) which makes the link with our POT approach. Hence, the λ avalanche rate in Eq. (5.16) can be assimilated to the occurrence rate in Eq. (5.1). Also, the over threshold $x_b > x_d$ condition should appear in all risk equations (Eq. (5.16) and the following), but it is dropped, for simplicity.

Finally, note that Eq. (5.16) holds since the pressure distribution $p(P|x_b > x_{stop_0}) = \delta(0)$, so that $p(P, x_{stop_0}) = p(P|x_b \leq x_{stop_0}) p(x_b \leq x_{stop_0})$, with $p(P|x_b > x_{stop_0})$ the pressure distribution at abscissa x_b knowing that the abscissa x_b is not reached, $\delta(0)$ the Dirac distribution in zero, $p(P|x_b \leq x_{stop_0})$ the pressure distribution at abscissa x_b knowing that the abscissa x_b has been reached by an avalanche and $p(x_b \leq x_{stop_0})$ is the probability for x_b to be reached by an avalanche.

Residual risk and optimal design

The dam optimal design approach we consider minimizes the long term costs obtained by summing up the construction costs and the expected damages for the building at abscissa x_b. In has been proposed in avalanche engineering by Eckert et al. (2008a, 2009), in analogy to the precursor work made by Van Danzig (1956) for maritime dykes in Holland and by Bernier (2003) for river dams. All this work ground itself on an extensive mathematical theory (Von Neumann and Morgenstern, 1953; Raiffa, 1968). Hence, the long term costs with a protective dam h_d are:

$$\begin{aligned} R(x_b, h_d) =& C_0 h_d + C_1 A \lambda \int p(Pr|h_d, x_b \leq x_{stop}) \\ & \times p(x_b \leq x_{stop|h_d}) \times V_z(Pr)\ dPr\ , \end{aligned} \tag{5.17}$$

where C_1 and C_0 are, respectively, the value of the building at risk at abscissa x_b in €, the monetary currency we work with, and the value of the dam per meter height in $€.m^{-1}$. $A = \sum_{t=1}^{+\infty} \frac{1}{(1+i_t)^t}$ is the actualisation factor to pass from annual to long term risk with i_t is the interest rate for the year t. The unit of the long term costs $R(x_b, h_d)$ is therefore $[e]$.

The notation ".$|h_d$" in Eq. (5.17) denotes that runout and pressure distributions are now modified in the runout zone, conditional to the dam height h_d. As a consequence, for a fixed h_d value, the long term costs correspond to the residual risk after the dam construction.

By the way, $R_b(x_b, h_d)$ is nothing more than $C_0 h_d + C_1 A r_b(x_b, h_d)$, with $r_b(x_b, h_d)$ the specific residual risk at the annual time scale for the building at the abscissa x_b with the dam height h_d. This highlights that the approach remains individual risk based, with one single element at risk at abscissa position x_b. Note also that the damages caused to the dam by successive avalanches and the consecutive reparation costs do not appear explicitly in (5.17). In fact, they are included in the C_0 evaluation through the definition of a suitable amortizing period, a straightforward econometrical computation. Yet, a strong underlying assumption is made: in case an avalanche severely damages or even destroys the dam, the dam still reduces the hazard for this specific avalanche event according to Eqs. (5.11) or (5.13), and is repaired immediately after.

Strong simplifications occur if the additional assumption of a constant "step" vulnerability function is made. The worst-case scenario is that the damage is maximal as soon as the element at risk is attained, whereas the considered element at risk remains obviously undamaged if the avalanche does not reach its abscissa. The integral in Eq. (5.17) is then reduced to $P((x_{stop} - x_d) > x_b - x_d | h_d)$, the probability of exceeding the abscissa x_b with a protective dam height h_d, so that:

$$R(x_b, h_d) = C_0 h_d + \lambda C_1 A \left(1 - F\left(x_b - x_d | h_d\right)\right) \ , \tag{5.18}$$

where $F(x_b - x_d | h_d)$ is the cumulative distribution function of runouts in x_b with a protective dam height h_d. This is the key assumption to keep a fully analytical decisional model with our POT approach, see below.

Eq. (5.18) can first be regarded as a residual risk function that, for a fixed value of h_d, varies according to the x_b position. It is then a linear function of the non exceedence probability $F(x_b - x_d | h_d)$ showing the decrease of the residual risk in the runout zone as one goes further and further away downstream. This directly represents/illustrates the coupling of the interaction law with the probabilistic POT hazard model.

Second, Eq. (5.18) can be regarded as total costs depending on the dam height h_d at a fixed x_b position, for instance a specific position of the runout zone which has some legal meaning (such as the limit of a hazard zone), or a position where a real element at risk / building is situated. The optimal dam height from a stake holder's perspective is then simply:

$$h_{opt} = \underset{h_d}{\operatorname{argmin}}(R_b(x_b, h_d)) \ , \tag{5.19}$$

where the function argmin gives, for a given x_b, the height h_d at which R_b is minimal.

Explicit risk formulae with the energy dissipation interaction law

According to Eq. (5.11), under the constraint $h_d < \frac{h_0}{\alpha}$, one has $P(x_{stop} - x_d > x_b - x_d | h_d) = P\left(\frac{x_{stop_0} - x_d}{1 - \alpha\frac{h_d}{h_0}} > x_b - x_d\right)$. In other words, the random variable $x_{stop} - x_d | h_d$ remains GPD distributed, with the same shape parameter ξ than $x_{stop_0} - x_d$, but with the reduced scale parameter $\sigma(1 - \alpha\frac{h_d}{h_0})$. The expression of the residual risk for the Poisson - GPD model is straightforward:

$$R(x_b, h_d) = \begin{cases} C_0 h_d + \lambda C_1 A \left(1 + \dfrac{\xi(x_b - x_d)}{\sigma(1 - \alpha\frac{h_d}{h_0})}\right)^{\frac{-1}{\xi}} & \text{if} \quad \xi \neq 0 \\ C_0 h_d + \lambda C_1 A \exp\left(\dfrac{-(x_b - x_d)}{\sigma(1 - \alpha\frac{h_d}{h_0})}\right) & \text{if} \quad \xi = 0 \end{cases} . \tag{5.20}$$

Explicit risk formulae with the volume catch interaction law

According to Eq. (5.13), under the constraint $h_d < (2A_a \tan\alpha_s)^{1/2}$, one has this time $P(x_{stop} - x_d > x_b - x_d | h_d) = P\left(\frac{x_{stop_0} - x_d}{\left(1 - \frac{h_d^2}{2A_a tan\alpha_s}\right)^{1/2}} > x_b - x_d\right)$. Hence, $x_{stop} - x_d | h_d$ is once again still GPD distributed, but with this time the reduced scale parameter $\sigma\left(1 - \frac{h_d^2}{2A_a \tan\alpha_s}\right)^{1/2}$. This time, the residual risk writes:

$$R(x_b, h_d) = \begin{cases} C_0 h_d + \lambda C_1 A \left(1 + \dfrac{\xi(x_b - x_d)}{\sigma\left(1 - \frac{h_d^2}{2A_a \tan\alpha_s}\right)^{1/2}}\right)^{\frac{-1}{\xi}} & \text{if} \quad \xi \neq 0 \\ C_0(h_d) + A\lambda C_1 \left(\exp\left(\dfrac{-(x_b - x_d)}{\sigma\left(1 - \frac{h_d^2}{2A_a \tan\alpha_s}\right)^{1/2}}\right)\right) & \text{if} \quad \xi = 0 \end{cases} , \tag{5.21}$$

where $tan(\alpha_s) = \tan(\psi_{fz} - \phi)$ and ϕ is arbitrary negative for dry cold snow avalanches and positive for humid snow avalanches, with the standard limit case $\phi = 0$ (Table 5.1).

Solutions to the risk minimisation problem

Sadly, none of these risk equations provide analytical solutions to Eq. (5.19). As a consequence, this is the only place of the work where a numerical search is required, spanning,

for a fixed x_b position, the possible values of h_d according to the positivity constraints of each interaction law. With the energy dissipation law, as already demonstrated in (Eckert et al., 2008a) in the Poisson-Exponential case, this is easy because of the (rather) nice shape of the residual risk function over a relatively large range of building positions and model parameter values. The residual risk decreases with increasing dam heights for dam heights below a single (rather) clear optimum, and increases with increasing dam heights above the optimum. Only exception is when one considers building positions too far down in the path. The dam is then useless making the optimal choice to be $h_d = 0m$

For the volume catch interaction law, however, things are not that simple because of the higher complexity of the dependency of $R(x_b, h_d)$ to h_d. Therefore, different typical cases can be encountered for plausible parameter values: no optimum, one "pseudo" optimum due to the positivity constraint, and the "good" case of a minimum residual risk arising as an optimal compromise between losses and construction costs. Yet, in the latter case, relative maximum residual risks can also be observed. These different cases are detailed/examplified in Appendix 5.6.1. For our application, we identified which of them occurred in all configurations we tested, and only dam heights truly minimising the risk were kept. These correspond to optimal compromises between construction costs and losses, but also to the pseudo optimums, *i.e.* dam heights just sufficient to stop all avalanches before the considered building position.

5.2.4 Quantifying uncertainty and sensitivity: intervals, bounds and indexes

Since one objective of the paper is to quantify how risk estimates and optimal design values vary across runout tail distribution types and avalanche-dam interaction laws, we propose in this subsection different intervals, bounds and indexes suitable for taking into account different types of uncertainty/variability. These intervals, bounds and indexes may be usable by engineers in risk zoning and defense structure design to represent sensitivity to available data resulting from parameter estimates standard errors, and/or sensitivity to non probabilistic model uncertainty. They have also wider interest, being somewhat interpretable in terms of respective weight of the different ingredients of the decisional analysis.

In the core of the paper, and with regards to the difference to be made between model parameters and their estimates on the basis of the available data, all risk computations are performed under the classical paradigm of statistical inference. This means that we plug the maximum full/profile likelihood estimates $(\hat{\lambda}, \hat{\xi}, \hat{\sigma})$ or $(\hat{\lambda}, \hat{\sigma}(\xi_0))$ in the Poisson - GPDs/Exponential distribution functions, and we evaluate return levels and risk functions accordingly, considering $R(h_d, \hat{\lambda}, \hat{\xi}, \hat{\sigma})$ or $R(h_d, \hat{\lambda}, \hat{\sigma}(\xi_0))$. Here, and in all what follows, the

notation ξ_0 indicates that the GPD shape parameter is chosen and that the profile likelihood is maximised conditionally to its choice. Discussion with regards to the alternative Bayesian paradigm is provided in Sect. 5.4 and Appendix 5.6.3.

Propagating uncertainty on parameter estimates

To quantify the uncertainty resulting from the limited data sample available, the usual approach is to propagate parameter standard errors (Eq. (5.7)) up to the quantities of interest. Starting from the MLE estimates for the Poisson - GPD model and the associated asymptotic variance-covariance matrix, different methods exist in the literature to evaluate confidence intervals for high return levels. Appendix 5.6.2 presents how the arguably two most common of them can be adapted to our profile likelihood case, where the shape parameter value ξ_0 results from a more or less arbitrary modelling choice rather than from inference.

Bounds and sensitivity indexes to the runout tail shape

From a different perspective, to evaluate the influence of the runout tail shape, we evaluate Eqs. (5.20) and (5.21) according to the range of ξ_0 values provided by the profile likelihood maximisation procedures. We do that without dam, and also for a given dam height and interaction law. From these set of values (one for each ξ_0), retaining the maximum and minimum risk value at each abscissa leads risk bounds function of the abscissa, interaction law and dam height. They constitute plausible upper/lower bounds for the risk taking into account the variability of risk estimates towards runout distribution tail types. To summarise the spread at the abscissa x_b, the sensitivity index $\delta_{R(x_b,h_d)}$ is evaluated:

$$\delta_{R(x_b,h_d)} = \frac{\max\limits_{\xi_0}\left(R(x_b,h_d)\right) - \min\limits_{\xi_0}\left(R(x_b,h_d)\right)}{\overline{R(x_b,h_d)}} \tag{5.22}$$

with $\overline{R(x_b,h_d)}$ the mean value evaluated at the abscissa x_b with the dam height h_d. Note that with the different interaction laws at our hand (energy dissipation and volume catch with varying deposit shape angles), different values of $\delta_{R(x_b,h_d)}$ can de obtained.

To do a similar evaluation for the optimal design procedure, we also search, for a given position x_b and interaction law, the solution h_d^* of (5.19) for each possible value ξ_0. The solution spread towards runout tail shapes is quantified from the minimum, maximum and mean optimal height at the abscissa x_b, denoted $h_d^*(x_b)$ as:

$$\delta_{x_b,h_d^*} = \frac{\max\limits_{\xi_0}\left(h_d^*(x_b)\right) - \min\limits_{\xi_0}\left(h_d^*(x_b)\right)}{\overline{h_d^*(x_b)}} \ . \tag{5.23}$$

Finally, to confront risk and optimal design sensitivity to the ξ_0 choice, we evaluate the same sensitivity index function of abscissa and interaction law as:

$$\delta_{x_b,R(h_d^*)} = \frac{\max_{\xi_0}\left(R(h_d^*(x_b))\right) - \min_{\xi_0}\left(R(h_d^*(x_b))\right)}{\overline{R(h_d^*(x_b))}} \ , \tag{5.24}$$

where $R(h_d^*(x_b))$ denotes the minimum residual risk at the abscissa x_b given $h_d = h_d^*(x_b)$. Note that the latter index is somewhat different to the one provided by eq. (5.22) where h_d was fixed once for all. This time, for each value ξ_0, the dam height considered to evaluate the risk is different, as it is the one that locally minimises the residual risk.

Bounds and sensitivity index to the avalanche/dam interaction law

Similarly, to evaluate the sensitivity to the choice on one interaction law instead of another, we evaluate, for a given runout tail (ξ_0 is fixed), abscissa x_b, and dam height h_d, the spread between the possible risk estimates as:

$$\delta'_{R(x_b,h_d)} = \frac{\max_{IL}\left(R(x_b,h_d)\right) - \min_{IL}\left(R(x_b,h_d)\right)}{\overline{R(x_b,h_d)}} \ , \tag{5.25}$$

where IL is the short-name for the interaction laws considered: the volume catch interaction law with various deposit angles, plus, potentially, the energy dissipation interaction law.

5.3 Application and results

5.3.1 Case study

The case study selected is the same as in Eckert et al. (2008a), a real path from the French avalanche database situated in the township of Bessans, in the Savoie department. It has a vertical drop of $1,175$ m from its top to the Arc river, is only very slightly channelled and the average slope is steep. The runout zone that consists in the gentle slope preceding the Arc River ($x = 1,763$ m in the (x,z) 2D-plane starting at the top of the path) is rather regular, making the use of a simple stochastic model for runout distances such as the POT-GPD possible.

The most extreme runout distance recorded corresponds to the Arc River, but, beyond it, the terrain remains rather flat, making it potentially possible for extreme avalanches to reach higher abscissas. This runout zone is, up to now, free from permanent habitations. However, due to demographic pressure, it may become urbanizable in the future, provided risk is estimated to be low enough in the current state or after a permanent defense structure construction. Hence, we study the potential risk reduction by a dam at the

abscissa which corresponds to the beginning of the runout zone according to a classical slope criterion. In the whole work, $x_d = 1,550\ m$ and $\psi_{fz} = 10°$ are therefore fixed. During the 1973-2003 time period, 28 avalanches exceeding x_d were recorded by the local forestry service.

The risk evaluation and sensitivity analysis is performed all over the runout zone. However, for being less case-study dependant in our conclusions, specific positions of legal importance are studied, corresponding to return periods of 10 - 1000 years. These are evaluated with Eq. (5.4) conditionally to "reasonable" GPD shape parameter values ξ_0 (see below).

The construction cost for the dam and the building value (the single element at risk we consider) were set to, respectively, $5,530\ €.m^{-1}$ and $300,000\ €$. A is fixed to 25, which is obtained with a constant interest rate $i_t = 4\%$. In all risk minimisation calculations, the x_b building position is fixed, but a range of positions is investigated. The bounds of this range correspond to the shortest decennial runout and to the longest centennial runout we evaluate according to data and choices made regarding possible GPD shape parameters.

5.3.2 Fitted runout distance - return period relationships

Without dam

The maximum likelihood method supplies estimates for the Poisson ($\hat{\lambda} = 0.904$) and the GPD parameters (Table 5.2). The likelihood ratio test rejects the exponential distribution to the benefit of the GPD distribution at the 5% significance level. The negativity of the MLE estimate $\hat{\beta}$, or, identically, the positivity of $\hat{\xi}$, indicates that the best fitted GPD distribution belongs to the Fréchet domain and has therefore a heavy tail. However, the MLE estimate $\hat{\xi}_{MLE}$ is close to 1.1, suggesting a tail so heavy that it is presumably untrustful since ξ values above 0.5 are known to be extremely rare in environmental systems. Furthermore, the associated standard error is very high (Table 5.2). As a consequence, the high return levels predicted on the basis of the MLE estimates are presumably unrealistic and, anyhow, the associated confidence intervals provided by the two uncertainty propagation methods we have implemented are so large that they are practically useless (Tables 5.4 and 5.5). These results highlight that it is presumably not possible to fit a reliable runout tail for this case study on the basis of the data only.

Our profile likelihood approach introduces extra-data information into the analysis through the choice of a ξ_0 value, somewhat arbitrary, but at least in a realistic range. Figure 5.2(a) shows the negative profile log-likelihood curves corresponding to the different values tested. It confirms that the likelihood of the data sample under the GPD model is very flat around the MLE couple, so that a wide range of other couples may be nearly as suitable in terms of data fitting (Table 5.3). This is even clearer when the different

fitted models are confronted to the data (Figure 5.2(b)). We may just note that the minimum negative log-likelihood increases with decreasing values of ξ_0, suggesting a little more confidence in a heavy tail (positive shape parameter) than in other runout types (null or negative shape parameter, Table 5.3).

The ξ_0 choice, however, considerably impacts the estimated runout distance - return period relationship, for instance the high return levels of interest for hazard mapping (Figure 5.2(c)). ξ_0 values lower than 0.5 provide $\hat{x_{100}}$ - $\hat{x_{1000}}$ return levels arguably plausible from the perspective on an expert analysis of the path. On the contrary, these are clearly too high for $\xi_0 > 0.5$, as expected with regards to the poor confidence we may have in ξ_0 values above 0.5. As a consequence, in the following, we concentrate our analysis on $\xi_0 = \{-0.3; -0.1; 0; 0.1; 0.3; 0.5\}$, *i.e.* on a range of plausible values containing the three different runout tail types, but with more weight on the heavy tail Fréchet type, according to the information the data seem to contain. Furthermore, in the same spirit, when a single value is required, we focus on $\xi_0 = 0.3$.

In more details, one may note that the concave/convex shape of return level plots with positive/negative ξ_0 values, respectively, makes return levels higher in the Weibull domain ($\xi_0 < 0$) for low return periods, but much higher in the Fréchet domain ($\xi_0 > 0$) for high return periods. For the same shape parameter absolute value $|\xi_0|$, the Frechet/Weibull return level plots cross on the straight line corresponding to the exponential case ($\xi_0 = 0$, leading to a linear behavior in log scale). For our case study, this crossing is obtained for return periods of $50 - 500$ years, depending on $|\xi_0|$.

Regarding return levels confidence intervals due to parameter uncertainty, Tables 5.4 and 5.5 illustrate how the two methods detailed in Appendix 5.6.2 perform in our case for $\hat{x_{10}}$ and $\hat{x_{100}}$. Both approaches show well that the uncertainty becomes higher and higher for increasing return periods, a classical and intuitive result. Also, for high return periods, the uncertainty literally explodes for very high ξ_0 values, in accordance with what was already observed for the MLE. More interestingly, the delta approach does not provide return level confidence intervals for negative shape parameters, and leads unrealistically large return level confidence intervals for slightly positive shape parameters (the zero case seems trustful since the computation is performed with the exponential likelihood rather than with the GPD one). These problems related to the variance covariance matrix approximation do not show with the deviance based approach, for which plausible return level confidence intervals are evaluated for all the ξ_0 values tested. In addition, even for very high ξ_0 values, the high return level confidence intervals provided by the deviance approach are much narrower than with the delta approach. These advantages are partly attributable to the fact that the deviance approach does not impose symmetry for return level confidence intervals. Hence, all in all, the deviance based method seems to perform much better than the delta method in our profile likelihood context.

In Tables 5.4 and 5.5, the $\hat{\xi_{MLE}}$ column provides return level confidence intervals with ξ_0 set to the MLE in the profile likelihood maximisation. If ξ is not set, with both approaches, the confidence interval is much larger, which illustrates well the additional uncertainty resulting from having one more free parameter to estimate (or, in contrast, the uncertainty reduction by the "arbitrary" choice of ξ_0). For example, with the deviance approach (in that case, a more classical full likelihood uncertainty propagation), the confidence intervals for $\hat{x_{10}}$ (resp. $\hat{x_{100}}$) is $CI_{\hat{x_{10}}} = [1,586 - 1,707.8]$ m (resp. $CI_{\hat{x_{100}}} = [1,762.6 - 3,714.6]$ m) when the uncertainty on $\hat{\xi_{MLE}}$ is taken into account, *i.e.* intervals much larger than those displayed in Table 5.5.

With a fixed dam height

Figure 5.3 shows the impact on the return level plots of the two interaction laws (and of the deposit shape angle for the volume catch interaction law) for different dam heights and GPD parameterisations, the latter being provided by the profile likelihood maximisation with different ξ_0 choices. Logically, for both interaction laws, return levels decrease for increasing value of the dam height h_d, which simply illustrates the ability of the dam in reducing the hazard in the runout zone.

Furthermore, for a fixed GPD parametrisation and dam height, the energy dissipation law generally evaluates a higher return period for a given path abscissa than the volume catch interaction law. This first suggests that the dam is more efficient in protecting potential elements at risk under the assumption of a dam-avalanche interaction governed by energy dissipation rather than by volume catch. An exception to this rule is, however, observed for the "extreme" deposit angle shape $\phi = 9°$ (just below the 10° local slope, which is its maximal possible value), that is to say, the case catching the highest volume of snow behind the dam. For instance, in case where $h_d = 6$ m, $\ell_{fz} = 100$ m and $\phi = 9°$ (Figure 5.3(b)), all avalanches are stopped by the dam, whereas, with a similar dam height, a few exceedences are still observed with the energy dissipation law. This highlights well the higher flexibility of the volume catch interaction law due to the additional parameter ϕ.

Regarding the influence of ξ_0, Figure 5.3, shows well that, for all dam heights and interaction laws, the similar features discussed before as function of the sign of ξ_0 without dam remain true. Simply, the crossing of the different return level plots on the exponential straight line for the same $|\xi_0|$ values occurs for return levels that slightly decrease with the dam height. This traduces that all interaction laws and dam heights impacts the scale of the runout distance distribution only: $x_{stop} - x_d > x_b - x_d | h_d$ remain always GPD distributed with ξ_0 shape parameter whatever the dam height and interaction law considered.

Table 5.2 – Maximum likelihood estimates and respective standard errors for the GPD parameters with the two possible parametrisations

	Maximum-likelihood estimates	Standard errors
ρ	0.1165	0.0223
β	-0.1284	0.0079
ξ	1.1018	0.3372
σ	8.5826	2.7957

Table 5.3 – Full and profile likelihood estimates. *nll* is the minimum negative log-likelihood in each case. * is the exponential case ($\xi_0 = 0$).

ξ_0	$\hat{\sigma}(\xi_0)$	$-2\ nll$
-0.3	86.86	280.9
-0.1	56.63	272.0
0 *	43.1679 ($\hat{\rho}_{MLE} = 0.0232$)	266.8
0.1	31.72	261.3
0.3	17.58	250.9
0.5	12.29	243.9
0.7	10.21	240.2
0.9	9.18	238.5
$\hat{\xi}_{MLE} = 1.1018$	$\hat{\sigma}_{MLE}$ =8.5826	238.1
1.3	8.20	238.4

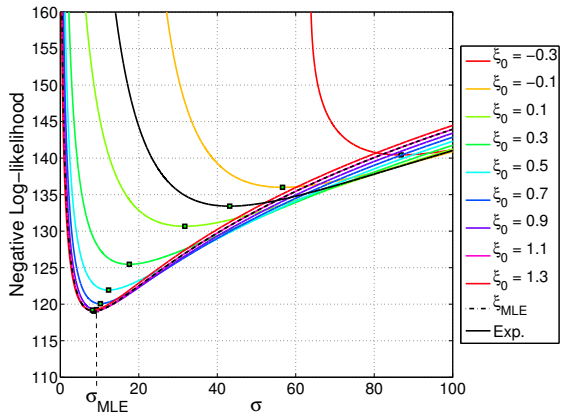

(a) Profile negative log-likelihoods: green square markers denote the minimum of each curve.

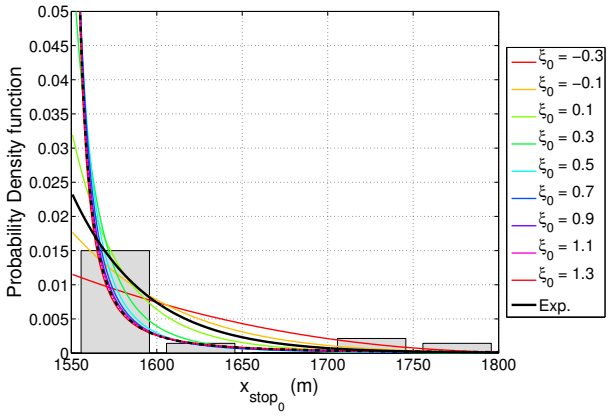

(b) Density functions provided by the profile likelihood minimisation method versus histogram of original data.

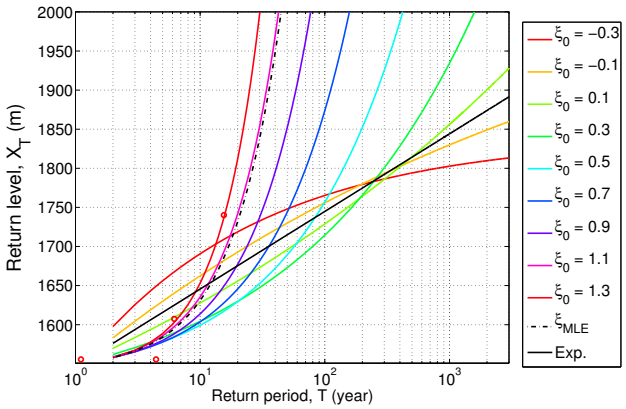

(c) Return level plots provided by the profile likelihood minimisation method versus original data in red circles (○).

Figure 5.2 – Model fit and checking: negative log-likelihood curves, density plots and return level plots. *Exp* is the exponential case ($\xi_0 = 0$).

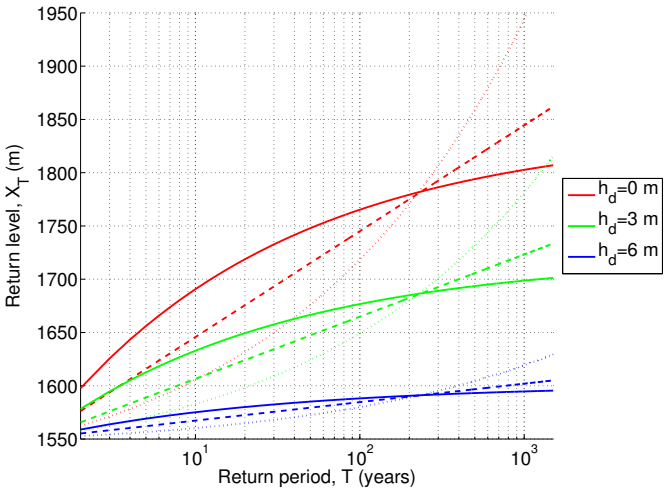

(a) With the energy dissipation interaction law. $h_0 = 1\ m$, $\alpha = 0.14$.

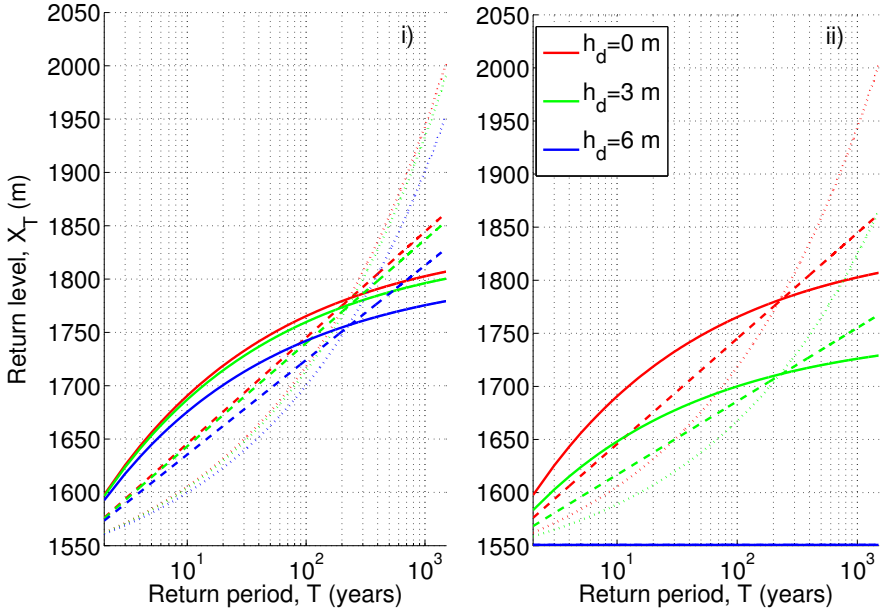

(b) With the volume catch interaction law, $V = 50,000\ m^3$, $\ell_{fz} = 100\ m$: (i) "intermediate" case: $\phi = 0°$ (standard volume storage), and (ii) "optimistic" case: $\phi = 9°$ (maximal volume storage and, hence, runout shortening with "humid" snow). In that case, for $h_d = 6\ m$, all avalanches are stopped by the dam.

Figure 5.3 – Runout distance - return period relationships for different dam heights, the two interaction laws and three possible GPD parameterisations provided by the profile likelihood maximisation. Solid line: $\xi_0 = -0.3$, dashed line: $\xi_0 = 0$, dotted line: $\xi_0 = 0.3$).

Table 5.4 – Return levels and corresponding 95% confidence intervals from the delta method; * same calculation with the specific exponential formulae ($\xi_0 = 0$); ▲ negative diagonal terms in the approximate variance-covariance matrix $V_{x_T}(\xi_0)$, see Appendix 5.6.2.

ξ_0	-0.3▲	-0.1▲	0 *	0.1	0.3	0.5	0.7	0.9	$\hat{\xi_{MLE}}$	1.3
$\hat{x_{10}} \pm z_{\frac{\alpha}{2}}\sqrt{V_{x_T}(\xi_0)}$ (m)	1,690.6 /	1,662.6 /	1,645.6± 38.65	1,628.8± 843.30	1,605.5± 50.12	1,600.0± 36.74	1,604.2± 38.68	1,614.4± 47.29	1,630.9± 62.54	1,654.7± 85.88
$\hat{x_{100}} \pm z_{\frac{\alpha}{2}}\sqrt{V_{x_T}(\xi_0)}$ (m)	1,765.2 /	1,756.0 /	1,744.8± 73.76	1,731.2± 1,948.4	1,718.4± 150.54	1,759.7± 150.93	1,877.3± 227.98	2,127.8± 414.60	2,655.68± 838.6	3,744.5± 1775.2

Table 5.5 – Return levels and corresponding 95% confidence intervals ($[CI]$, [*lower bound*−*upper bound*]) from the deviance method (Appendix 5.6.2); * same calculation with the specific exponential formulae ($\xi_0 = 0$).

ξ_0	-0.3	-0.1	0 *	0.1	0.3	0.5	0.7	0.9	$\hat{\xi_{MLE}}$	1.3
$\hat{x_{10}}$ (m)	1,690.6	1,662.6	1,645.6	1,628.8	1,605.5	1,600	1,604.2	1,614.4	1,630.9	1,654.7
$[CI]$ (m)	[1,668 – 1,731]	[1,636 – 1,707]	[1,617 – 1,693]	[1,601 – 1,675]	[1,583 – 1,648]	[1,579 – 1,641]	[1,581 – 1,649]	[1,586 – 1,669]	[1,594 – 1,701]	[1,606 – 1,747]
$\hat{x_{100}}$ (m)	1,765.2	1,756	1,744.8	1,731.2	1,718.4	1,759.7	1,877.3	2,127.8	2,655.7	3,744.5
$[CI]$ (m)	[1,732 – 1,827]	[1,707 – 1,838]	[1,687 – 1,840]	[1,668 – 1,837]	[1,649 – 1,848]	[1,671 – 1,932]	[1,736 – 2,152]	[1,877 – 2,622]	[2,165 – 3,624]	[2,735 – 5,723]

5.3.3 Residual risk estimates

Influence of the GPD ξ_0 shape parameter

According to Eq. (5.18), residual risk is a linear function of exceedence probability, so that most noticeable features in residual risk plots directly derive from what is observable on return level plots. For instance, Figure 5.4 shows the influence of the dam height h_d on the risk reduction with a fixed ξ_0 shape parameter whereas Figure 5.5 illustrates, with a constant dam height, the influence of the GPD parametrisation, with the ξ_0 parameter taken in the $[-0.3 - 0.5]$ interval.

In Figure 5.4, with both interaction laws, the residual risk reduction as function of the dam height increase is clear, *e.g.* from 74,993€ with no dam to 57,201€ with $h_d = 1m$, 35,124€ with $h_d = 3m$ and 33,676€ with $h_d = 5m$ for a building situated at a position corresponding to the centennial runout without dam ($x_b = 1,718.4$) and the energy dissipation law. Here, ξ_0 is fixed to 0.3, which is, as said before, a potentially

sensible choice since it is positive but not too high.

In Figure 5.5(a), the GPD shape parameter influence is also clear: the Fréchet-type values tested ($\xi_0 > 0$) provide the lowest residual risk estimates for buildings situated just above the dam abscissa but lead by far the highest risk estimates further down in the path, and vice versa for the Weibull-type values ($\xi_0 < 0$). The exponential case where $\xi_0 = 0$ provides intermediate residual risk estimates, and, for one given $|\xi_0|$, all estimates are the same only for the abscissa position at which the Fréchet and Weibull-type return level plots cross the exponential straight line.

Figure 5.5(b) summarises, for the same constant dam height and the two interaction laws, the variability of risk estimates towards runout distribution tail types, *i.e.* on the plausible ξ_0 range $[-0.3 - 0.5]$, slightly positive on average. The resulting lower and upper risk bounds may be very valuable insights for practice. For example, for $h_d = 6m$ and the energy dissipation law, the residual risk is estimated to be in the interval $[33,180 - 37,389]$€for a building situated at a position corresponding to the centennial runout without dam (and $\xi_0 = 0.3$). The width of the inter-bounds interval depends on the position in the path: it is minimal for "intermediate" abscissas where the different risk curves lead similar estimates, and is much larger when Fréchet/Weibull-type risk estimates strongly diverge.

The $\delta_{R(x_b,h_d)}$ sensitivity index (Eq. (5.22)) more quantitatively ascertains the spread of risk bounds towards ξ_0 values. Figure 5.5(c) shows that it varies as function of the considered building position and interaction law, but that, with the two interaction laws, the relative difference between risk estimates can be as high as 200%. This indicates that considerable errors can be made if the ξ_0 value for which the risk is minimal is chosen instead of the one maximizing the risk at the considered abscissa, and vice versa. For each interaction law, $\delta_{R(x_b,h_d)}$ has two modes as function of x_b. The first (closer to x_d) corresponds to the position where Weibull type estimates are the highest with regards to Fréchet type ones, and the second mode, further down in the path, to the opposite case. For very high abscissas, all estimates drop to zero, eventually reducing the sensitivity to the runout tail shape. The local minimum between the two modes in $\delta_{R(x_b,h_d)}$ corresponds to the region in the path previously discussed where all risk estimates are similar.

Influence of the the interaction law and of the ϕ deposit shape angle

Regarding the respective efficiency of the two interaction laws in reducing risk, conclusions made with return level plots remain obviously true here. For all dam heights, the energy dissipation interaction law predicts a strong risk reduction with regards to the no-dam case, residual risk drops sharply for abscissas just above the dam and this effect is all the more marked that the dam is high. With a standard deposit shape angle $\phi = 0°$,

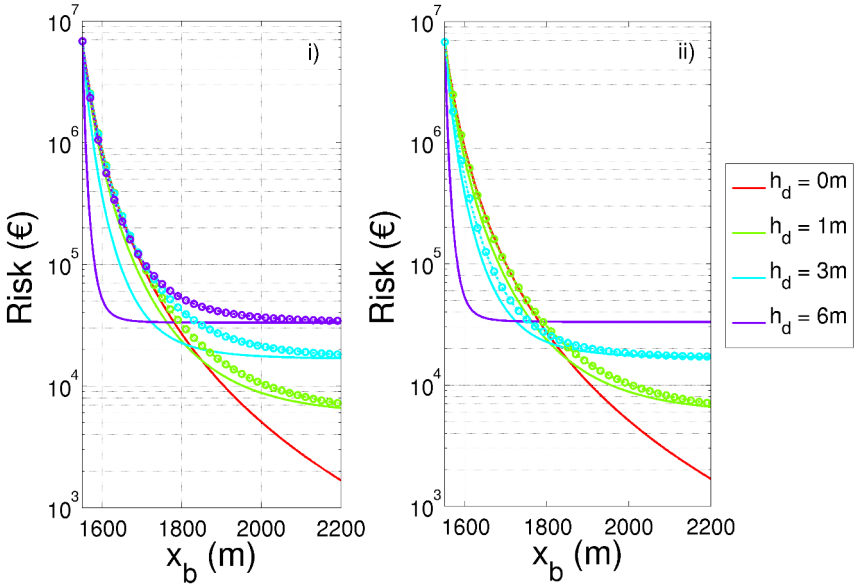

Figure 5.4 – Residual risk functions with $\xi_0 = 0.3$ for various dam heights h_d with the energy dissipation interaction law (solid line, $h_0 = 1\ m$, $\alpha = 0.14$) and the volume catch interaction law (dashed line with circles, $V = 50\ 000\ m^3$, $\ell_{fz} = 100\ m$), (i) intermediate case $\phi = 0°$, and (ii) "optimistic case" $\phi = 9°$.

the volume catch interaction law predicts a much weaker risk reduction for a given dam height, with residual risk estimates dropping at much lower pace as one goes further down in the path (Figure5.4 (i)).

As already stated in the previous 5.3.2 subsection, the only exception to the higher efficiency of the energy dissipation interaction law with regards to the volume catch one occurs for "extremal" volume storages, *e.g.* with $\phi = 9°$ in Figure 5.4 (ii). In that case, with moderate dam heights $(1 - 3m)$, the two interaction laws lead rather similar risk estimates, and, for $h_d = 6\ m$, the volume catch interaction law predicts even a higher risk reductions since all avalanches are stopped before or at the dam abscissa. As a consequence, for a given abscissa in the path, low and high risk bounds obtained towards possible runout tails are much higher for a given dam height with the energy dissipation law than with the volume catch one (Figure 5.5(b)). Also the pattern in resulting sensitivity index is shifted to the right with the volume catch interaction law, with higher values further down in the path (Figure 5.5(c)) .

To further quantify the effect of ϕ on the risk estimation, Figure 5.6 systematically investigates the $h_d = 5.5\ m$ case, and $\ell_{fz} = 50$ m, which stays within the validity range of the two interaction laws for all ϕ values (for the volume catch interaction law, the

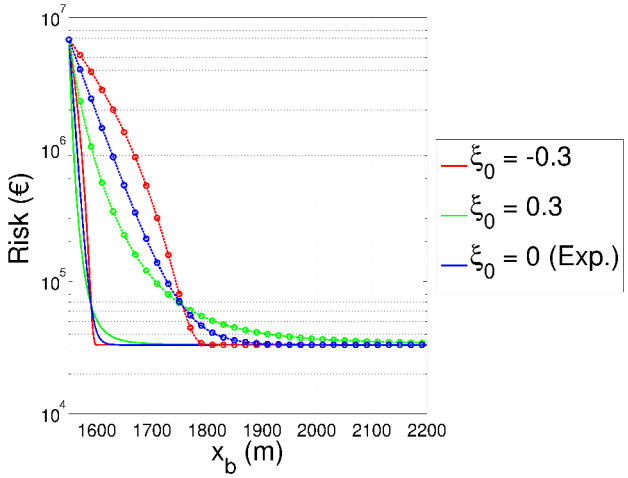

(a) Residual risk functions for various ξ_0 values with the energy dissipation interaction law (solid line) and the volume catch interaction law (dashed line with circles).

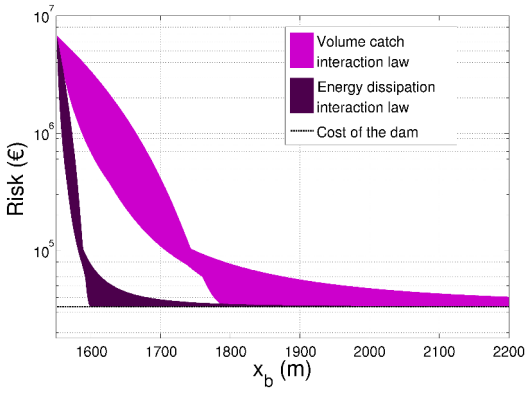

(b) Residual risk bounds constructed according to the $\xi_0 = \{-0.3; -0.1; 0; 0.1; 0.3; 0.5\}$ sample with the two interaction laws.

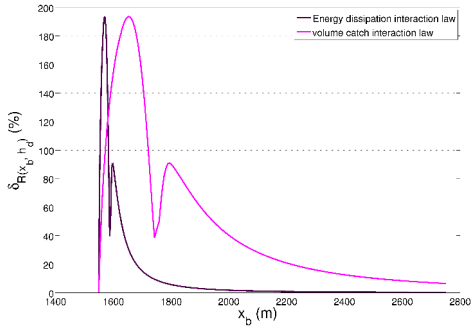

(c) Sensitivity index $\delta_{R(x_b,h_d)}$ (Eq. (5.22)) to the runout tail shape as function of the building position x_b for the two interaction laws, $\xi_0 = \{-0.3; -0.1; 0; 0.1; 0.3; 0.5\}$.

Figure 5.5 – Residual risk sensitivity to the GPD parametrisation. $h_0 = 1\ m$, $\alpha = 0.14$, $V = 50,000\ m^3$, $\ell_{fz} = 100\ m$, $\phi = 0°$ and $h_d = 6\ m$.

limit height is 5.9 m with $V = 50,000$ m^3, $\phi = 9°$ and $\ell_{fz} = 50$ m). As expected, the residual risk increases when the deposit shape angle becomes increasingly negative, and, hence, the dam, under the volume catch interaction law, less efficient. For this 5.5 m dam height, for which none of the interaction laws is able to stop all avalanches, the energy dissipation interaction law remains the most optimistic regarding the beneficial action of the dam. Risk estimates provided by the volume catch interaction law become close to the energy dissipation ones only with the maximal $\phi = 9°$ value, and much higher with "less optimistic" lower deposit shape angles (Figure 5.6(a)).

From the set of risk curves of Figure 5.6(a), for each position in the path, two risk bound couples can be built: the first one considers the minimum and maximum risk estimates with the volume catch interaction law according to the variability on ϕ only (Figure 5.6(b) (i)). The second one takes into account, in addition, the minimal risk value provided by the energy dissipation interaction law (Figure 5.6(b) (ii)). In other words, due to the higher efficiency postulated by the energy dissipation law, upper risk bounds are the same in the two cases, whereas lower bounds differ sightly. For example, without considering the energy dissipation law, the residual risk is estimated to be in the interval $[35,172 - 104,233]$ €for a building situated at a position corresponding to the centennial runout without dam (with $\xi_0 = 0.3$). And with the inclusion of the energy dissipation law in the bounds definition, it is in the interval $[31,808 - 104,233]$ €.

The resulting sensitivity to the interaction law index $\delta'_{R(x_b,h_d)}$ (Eq. (5.25)) evaluated all over the runout zone ascertains that a maximal error of 130% (including the energy dissipation law) / 105% (with the volume catch interaction law only) can be made on the risk quantification if the interaction law chosen is wrong in terms of postulated mechanism and/or deposit shape angle. As for the sensitivity to the GPD parametrisation, the width between these risk bounds and hence the $\delta'_{R(x_b,h_d)}$ sensitivity index are small for buildings very close to the dam (highly exposed), as well as very far down in the path (positions reached by the most extreme avalanches only). Sensitivity to interaction law is therefore maximal for buildings situated at "intermediate" abscissa positions (Figure 5.6(c)).

5.3.4 Optimal dam heights

With the GPD versus the Exponential runout model

For now, we consider the various residual risk functions at hour hand as functions of the dam height, searching the height that minimizes the residual risk according to Eq. (5.19). Optimal design sensitivity to GPD parametrisation is still evaluated on the $\xi_0 = [-0.3 - 0.5]$ range. Since the building position in the risk minimisation is fixed, four positions are chosen: the minimal and the maximal decennial and centennial abscissas provided by these possible parameterisations without dam, that is to say

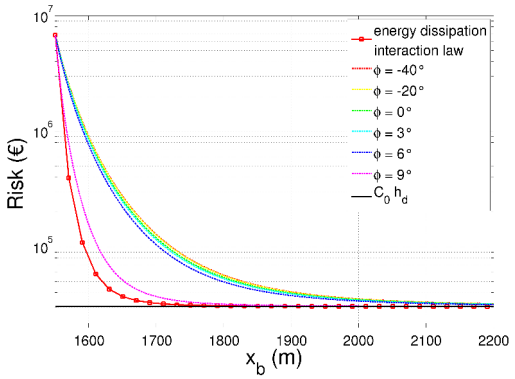

(a) Residual risk function according to various deposit shape angles ϕ (volume catch interaction law). For comparison, the residual risk with the energy dissipation interaction law is plotted in solid line with squares. The dam construction cost $C_0 h_d$ appears in black.

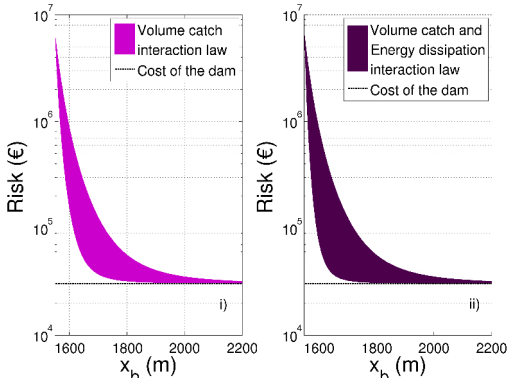

(b) Residual risk bounds constructed according to the $\phi = \{-40°; -20°; 0°; 3°; 6°; 9°\}$ sample (volume catch interaction law), without (i) or with (ii) the energy dissipation interaction law. The dam construction cost $C_0 h_d$ appears in black.

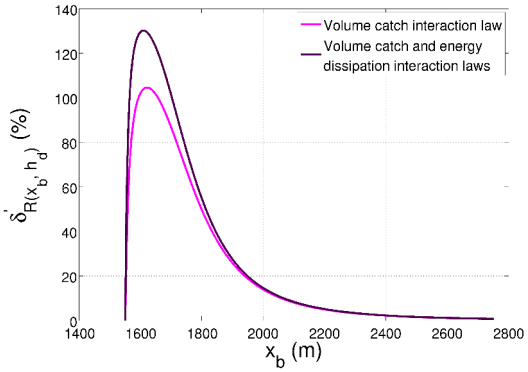

(c) Sensitivity index to the interaction law $\delta'_{R(x_b,h_d)}$ (Eq. (5.25)) as function of the building position x_b without or with the energy dissipation interaction law, $\phi = \{-40°; -20°; 0°; 3°; 6°; 9°\}$.

Figure 5.6 – Residual risk sensitivity to the interaction law, with focus on the ϕ deposit shape angle: $h_0 = 1\ m$, $\alpha = 0.14$, $V = 50,000\ m^3$, $\ell_{fz} = 50\ m$, $\xi_0 = 0.3$ and $h_d = 5.5\ m$.

$[1,600\ m; 1,690.6\ m; 1,718.4\ m; 1,765.2\ m]$.

Figures 5.7 shows, for these four positions and the different tested ξ_0 values, the obtained residual risk curves, as functions of the dam height h_d, with the energy dissipation law. For each curve, the optimal height minimising the risk is highlighted. It is more or less clear, depending on the abscissa position x_b and the ξ_0 value considered, but, as a general rule, a minimum can well be found on the range of h_d values allowed by the positivity constraint. As intuitively expected, optimal dam heights are higher for buildings situated closer to the dam than for buildings located further down in the path, since it is economically more sound to protect more exposed elements at risk. Also, for very high dam heights, the risk converge to the construction cost $C_0 h_d$. This occurs as soon as the dam is high enough to stop all avalanches before the considered building abscissa, making the additional construction effort unnecessary.

The same evaluation can be done considering the volume catch interaction law instead of the energy dissipation one. At this stage, we consider $\phi = 9°$, $l_{fz} = 100\ m$ and $V = 50,000\ m^3$, *i.e.* parameter values for which the dam is "efficient" so that it is easier to determine optimal heights minimizing the residual risk. This is not always the case with this interaction law, see Sect 5.3.4.

Table 5.6 summarizes optimal dam heights and associated risk estimates $R(x_b, h_d^*)$ for the two interaction laws. As first glance it appears that Fréchet like positive ξ_0 values lead higher optimal heights and higher corresponding minimum estimates whith regards to the ones lead by Weibull or Gumbell like ξ_0 values. This conclusion reflects the fact that heavy tailed GPD distributions forecast more extreme avalanches than the two other tail types considered. This makes higher constructions economically advantageous, but the remaining risk after dam construction still higher. Note that the increase with ξ_0 is very clear with the energy dissipation interaction law, and somewhat less clear with the volume catch interaction law. This is attributable to the fact that with the advantageous volume catch parameters used here, low dam heights are quite efficient. For instance, the 4.18 m limit height is sufficient to stop all avalanches, and it is economically sound to construct uo to this height for many of the ξ_0 and x_b values tested.

To confirm this shape parameter effect, previous calculations were generalized, with the energy dissipation law, to a large range of building positions (Figure 5.8) and to a quasi continuous sample of ξ_0 values (Figure 5.9), retaining in each case h_d^* and $R(x_b, h_d^*)$. Overall, results illustrate very clearly that, for a given building position, the higher ξ_0, the higher the optimal dam height and corresponding minimum risk. However, it also appears that the differences in optimal dam heights and corresponding residual risks obtained with different ξ_0 values strongly increase with increasingly high x_b positions up to very high x_b values. For example, Figure 5.8(a) illustrates the results of the optimisation procedure all along the path with a typical Fréchet-type choice ($\xi_0 = 0.3$), the symmetrical Weibull-type

choice ($\xi_0 = -0.3$), and the intermediate Gumbel-type case ($\xi_0 = 0$). Fréchet-type optimal heights and corresponding risks estimates are systematically higher than Gumbel-type ones, themselves systematically higher that the Weibull-type ones, and these differences increase with x_b. Same conclusions still hold with the volume catch interaction law, even if the decreasing pattern is weaker (Figure 5.8(b)). These results simply traduce again the fact that difference in tail types especially affects the most extreme return levels, and, as a consequence, the design choices controlled by these. Note, however, that for $_b$ values so high that they are "never" reached by avalanches, the optimal height and the associated residual risk logically drop to zero. This occurs for x_b abscissas all the more small than ξ_0 is low (Figure 5.9(a)).

In terms of optimal design sensitivity indexes $\delta_{x_b,R(h_d^*)}$ and δ_{x_b,h_d^*} reflecting the sensitivity of the risk minimisation procedure to the GPD parametrisation, values a bit lower than for the risk sensitivity indexes $\delta_{R(x_b,h_d)}$ and $\delta'_{R(x_b,h_d)}$ are obtained. Still, they remain quite high, up to 120% with the energy dissipation law and 40% with the volume catch interaction law, depending on the x_b position (Figure 5.8(c)). Hence, optimal dam heights and associated minimum risk estimates can well be misvalued by a factor two if a wrong ξ_0 value is considered, for instance at high (obviously, not too high to be unattainable) abscissas in the path, where, as discussed before, the sensitivity to the tail behaviour is the highest. Finally, the scatter plot of the two indexes (Figure 5.8(c)) shows that the ξ_0 choice is slightly more influential on the optimal design than on the corresponding risk estimate, but this effect is not very marked.

Table 5.6 – Optimal dam height h_d^* and corresponding minimum risk $R(x_b, h_d^*)$ with the two interaction laws at the four abscissas $x_b = [1,600\ m; 1,690.6\ m; 1,718.4\ m; 1,765.2\ m]$. These correspond to $[\min_{\xi_0}(x_{T10}), \max_{\xi_0}(x_{T10}), \min_{\xi_0}(x_{T100}), \max_{\xi_0}(x_{T100})]$, respectively, for $\xi_0 \in \{-0.3; -0.1; 0; 0.1; 0.3; 0.5\}$. The used parameter set is $C_0 = 5,530$ €$.m^{-1}$, $C_1 = 300,000$ €, $\alpha = 0.14$, $h_0 = 1$ m, $V = 50,000\ m^3$, $\ell_{fz} = 100\ m$, and $\phi = 9°$. With these, the maximal dam height is 7.14 m with the energy dissipation law and 4.18 m with the volume catch one. .

ξ_0	Energy dissipation: h_d^* (m), $R(x_b, h_d^*)$ (k€)		Volume catch: h_d^* (m), $R(x_b, h_d^*)$ (k€)	
-0.3	[6.0; 3.6; 2.8; 1.5]	[33.3; 20.2; 16.1; 9.2]	[4.1; 3.6; 3.3; 2.6]	[22.8; 20.1; 18.6; 14.8]
-0.1	[6.3; 4.2; 3.5; 2.3]	[35.1; 24.3; 20.9; 14.9]	[4.18; 3.9; 3.7; 3.2]	[23.0; 21.6; 20.7; 18.7]
0 (*Exp*)	[6.4; 4.4; 3.7; 2.5]	[36.0; 26.3; 23.0; 17.4]	[4.18; 4.0; 3.8; 3.5]	[23.0; 22.2; 21.6; 20.1]
0.1	[6.5; 4.6; 3.9; 2.6]	[36.8; 28.1; 25.0; 19.5]	[4.18; 4.1; 4.0; 3.7]	[23.1; 22.6; 22.3; 21.3]
0.3	[6.9; 5.2; 4.6; 3.3]	[38.6; 32.7; 30.3; 25.8]	[4.18; 4.18; 4.18; 4.1]	[23.1; 23.1; 23.1; 23.0]
0.5	[7.14; 6.6; 6.2; 5.5]	[40.0; 38.2; 37.3; 35.4]	[4.18; 4.18; 4.18; 4.18]	[23.1; 23.1; 23.1; 23.1]

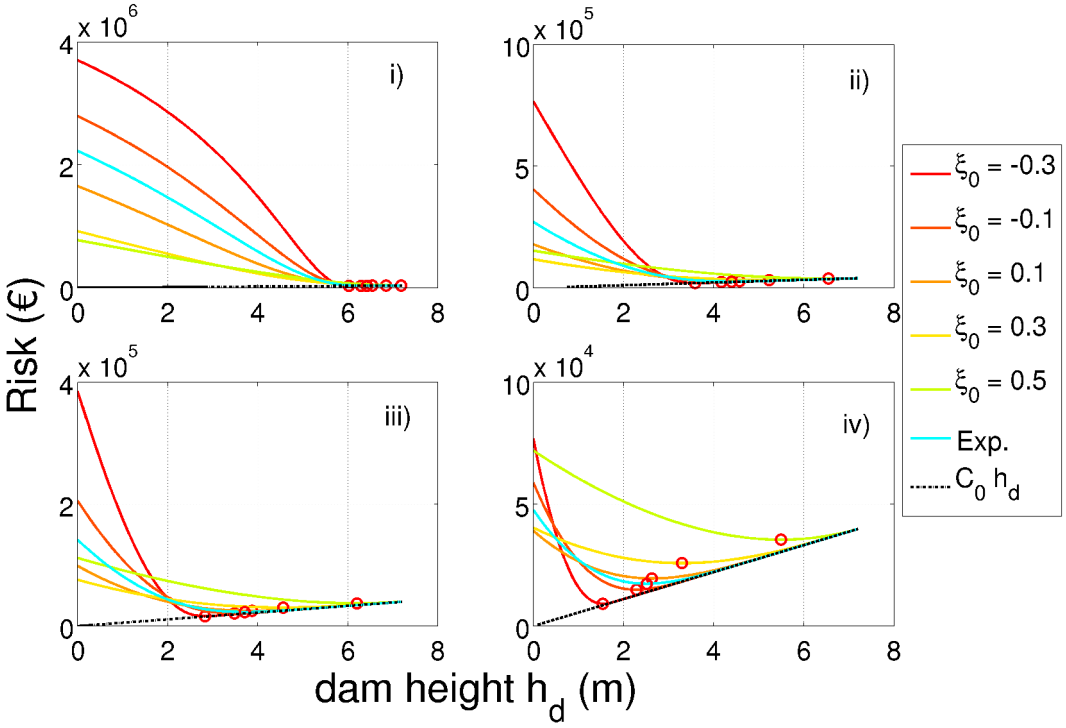

Figure 5.7 – Optimal design with the energy dissipation law for different GPD parametrisations and at diffent building abscissas x_b: (i) $1,600\ m$, (ii) $1,690.6\ m$, (iii) $1,718.4\ m$, (iv) $1,765.2\ m$. Red circles denote the minimum of each residual risk curve. The dashed black line is the asymptotic dam construction cost $C_0 h_d$. Decisional model parameters are $C_0 = 5,530\ €.m^{-1}$, $C_1 = 300,000\ €$, $\alpha = 0.14$, and $h_0 = 1$ m, which imposes $h_d \leq 7.14\ m$

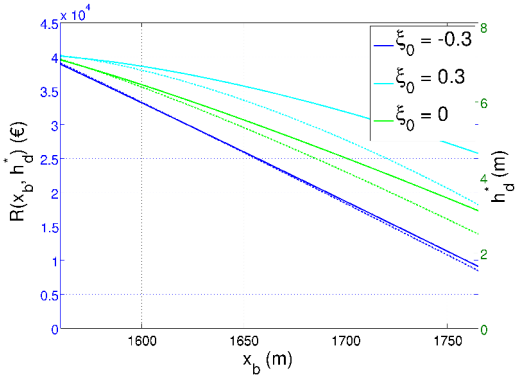

(a) Optimal height $h_d = h_d^*$ (dashed line) and corresponding minimum residual risk $R(x_b, h_d^*)$ (solid line) as functions of the building position x_b with the energy dissipation interaction law.

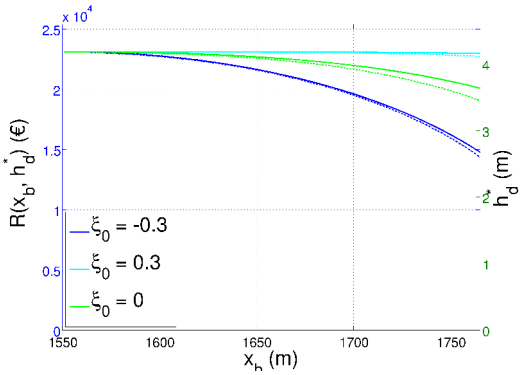

(b) Optimal height $h_d = h_d^*$ (dashed line) and corresponding minimum residual risk $R(x_b, h_d^*)$ (solid line) as functions of the building position x_b with the volume catch interaction law.

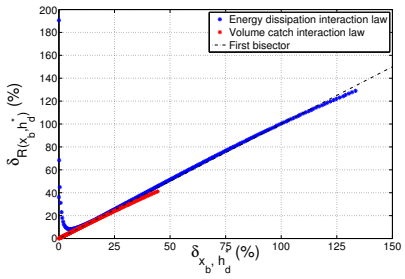

(c) Risk sensitivity index $\delta_{R(x_b,h_d^*)}$ (Eq. (5.24)) as function of the optimal design sensitivity index δ_{x_b,h_d^*} (Eq. (5.23)) for the two interactions laws. Each point of the plot corresponds to a different building abscissa x_b. Black dashed line is the first bisector of the scatter plot.

Figure 5.8 – Optimal design sensitivity to the runout tail shape. $C_0 = 5,530$ €$.m^{-1}$, $C_1 = 300,000$ €, $\alpha = 0.14$, $h_0 = 1$ m, $V = 50,000$ m^3, $\ell_{fz} = 100$ m, $\phi = 9°$.

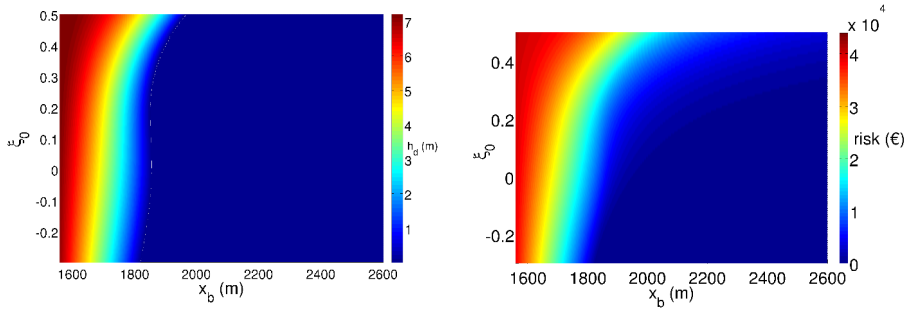

(a) Optimal dam height. (b) Risk value at the optimal dam height.

Figure 5.9 – Optimal dam height and corresponding minimum risk estimate as continuous functions of the GPD shape parameter ξ_0 and building position x_b, energy dissipation law. $C_0 = 5,530$ €$.m^{-1}$, $C_1 = 300,000$ €, $\alpha = 0.14$, and $h_0 = 1$ m.

With the volume catch versus the energy dissipation interaction laws

Figure 5.10 shows the residual risk curves as function of the dam height h_d for various deposit shape angles at the same abscissas studied in Figure 5.7, and with a constant $\xi_0 = 0.3$ value. Whereas things were rather simple with the energy dissipation law, here, as a result of the higher complexity of the volume catch interaction law, many cases are likely to occur. First, green squares (■) are optimal heights resulting from the positivity constraint in the interaction law. Second, from the second abscissa studied until the last one, it is observed that, for the lowest deposit shape angles tested, the risk curves never stop increasing: the cost of the dam is then always high enough to dominate the total cost. Such curve shapes induce an optimal height equal to zero (black star $*$), which never occured for the same abscissas with the energy dissipation law (Figure 5.7). Third, red circles (●) denote "true" optimal heights resulting from the residual risk minimization on a dam height range where the risk derivative exists. As said before, Appendix 5.6.2 details these three different cases. Finally, for highly negative deposit shape angles and low abscissas in the path ($-40°$ and $-20°$ in (i)), the risk decreases over a very large h_d range and the the maximal value allowed by the positivity constraint is very high. In that cases, we have stopped the analysis at 30 m, assuming that higher dams would't be allowed for environmental or engineering reasons even if they would apparently be sound from the purely economical perspective of our computational framework. Such limits, rather than truly optimal dam heights, are all equal to 30 m. They appear as black triangles (▲).

As for the GPD parametrisation, to fully quantify the sensitivity of the optimal design and corresponding minimum risk estimate to the interaction law, Figure 5.11 was drawn. It spans a large set of building positions and deposit shape angles with the deposit volume

interaction law, and the energy dissipation law is also considered. Figure 5.11(a) shows that with the deposit volume interaction law and with regards to the energy dissipation law, atypical patterns are observed in the h_d^* and $R(x_b, h_d^*)$ curves as functions of x_b: for each deposit shape angle ϕ, an abscissa x_b in the path can be found where the optimal dam height drops brutally from a more or less high h_d^* value to zero, whereas the residual risk switches to the baseline risk without dam. This behaviour comes from the fact that, with the deposit volume interaction law, for high abscissas in the avalanche path, strictly increasing risk curves where the dam construction cost dominates the risk reduction due to the dam protective effect are always obtained, as illustrated in Figure 5.10 (ii-iv). The path position at which this optimal height drop to zero is observed decreases with ϕ, since a lower value of ϕ implies a less efficient dam.

More generally, Figure 5.11(a) suggests that, for a given GPD parametrisation, when the optimal dam height exists, except for the highest ϕ value tested, it is higher with the volume catch interaction law than with the energy dissipation law, and that the corresponding remaining risk is higher as well. These effects are due to the generally lower risk reduction for a given dam height with the volume catch interaction law, except when ϕ is close to its maximal possible value, as discussed in Sect. 5.3.3. This is all the more true than ϕ is low, making the dam less and less efficient. For example, at the centennial abscissa $x_b = 1,718.4$m ($\xi_0 = 0.3$), optimal heights and corresponding minimum risk are 0 m (no optimum) and $75,800e$ (baseline risk) with $\phi = -40\circ$, 10.6 m and $59,500e$, respectively, and 4.6 m and $30,300e$ with the energy dissipation law. On the contrary, for $\phi = 9\circ$, optimal height (4.18 m) and corresponding risk ($23,100e$) are lower than with the energy dissipation law, since the limit height that stops all avalanches is reached.

Finally, Figure 5.11(b) shows the spread of the optimal dam height, when it exists, as a continuous function of the deposit shape angle and the building position, with, as said before, a maximal dam height set to 30 m. For low deposit shape angles, say $\phi < -15°$, this maximal value is easily attained, but as the dam is weakly useful, it is rapidly (*i.e.* when one goes down in the path) observed that no protection is economically more advantageous than a huge dam. This in black no-optimum domain where the best economical choice is $h_d = 0$ begins at abscissa 1625 m, for $\phi = -40°$, at abscissa 1662 m, for $\phi = -20°$ and at abscissa 1677 m, for $\phi = -10°$. For higher deposit shape angles, the no optimum area becomes narrower and narrower, and the maximal optimal height decreases. As a limit case, for $\phi = 9°$, the optimal height exists all over the investigated x_b range, but it is very small ((4.18 m, and, as said before, even smaller than the optimal height provided by the energy dissipation law at the same abscissa. This lastly illustrates the higher complexity of the volume catch interaction law. With the energy dissipation law, high optimal dam heights are found for abscissa positions close to the dam and, the higher the dam, the

higher its efficiency in reducing the risk, so that h_d^* tends to zero with x_b rather smoothly. On the contrary, with the volume catch interaction law, h_d^* is controlled primarily by ϕ rather than by x_b. Low values close or equal to the limit value sue to the positivity constraint correspond to the highest ϕ value and the risk reduction is important, whereas very high h_d^* values can be obtained over a large range of positions in the path for low ϕ. The dam is then rather inefficient in reducing risk, but still economically sound, before brutally dropping to zero when the construction is no longer justified.

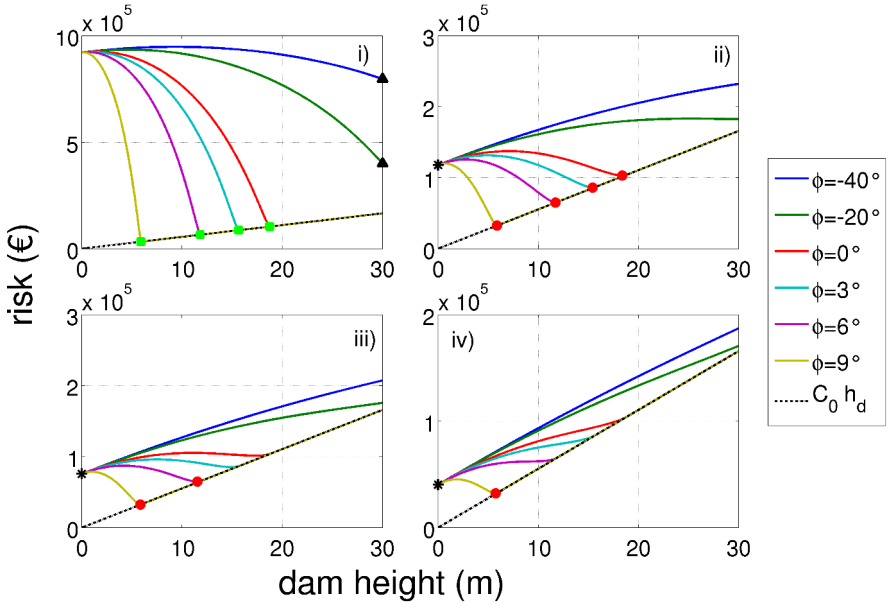

Figure 5.10 – Optimal design with the volume catch interaction law for different deposit shape angles and at different building abscissas x_b: (i) $1,600.0$ m, (ii) $1,690.6$ m, (iii) $1,718.4$ m, (iv) $1,765.2$ m. The dashed black line is the asymptotic dam construction cost $C_0 h_d$. Decisional model parameters are $C_0 = 5,530$ €$.m^{-1}$, $C_1 = 300,000$ €, $V = 50,000$ m^3, $\ell_{fz} = 100$ m, $\xi_0 = 0.3$. The positivity constraint depends on the considered deposit shape angle ϕ, but is not very restrictive for low deposit shape angles, *e.g*, $h_d \leq 34.5$ m for $\phi = -40°$, $h_d \leq 13.3$ m for $\phi = 0°$, and $h_d \leq 4.18$ m for $\phi = 9°$. When the maximal dam height allowed by the interaction law is above 30 m, the numerical minimum search is restricted to the $[0 - 30$ $m]$ interval. Symbology regarding the different residual risk minima refers to the different optimum types pointed out in Appendix 5.6.1 and is detailed in text (Sect. 5.3.4).

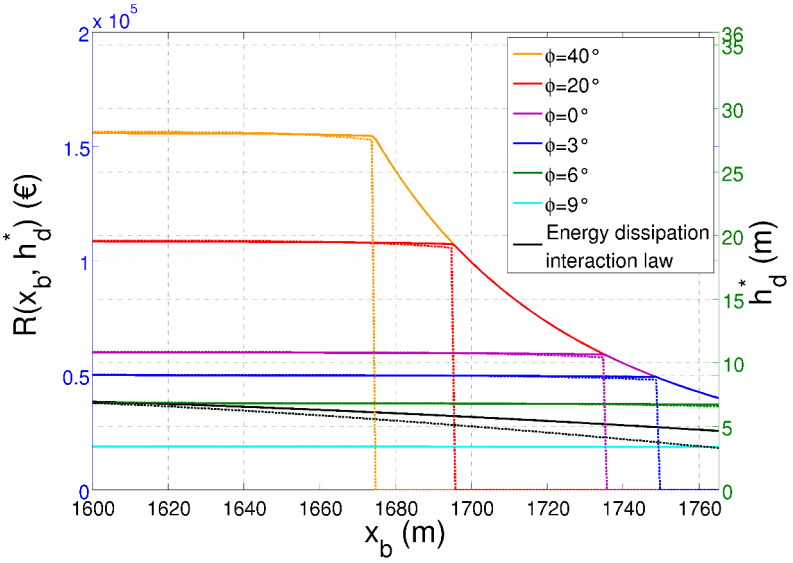

(a) Optimal height $h_d = h_d^*$ (dashed line) and corresponding minimum residual risk $R(x_b, h_d^*)$ (solid line) as functions of the building position x_b with different interaction laws: energy dissipation and volume catch with various deposit shape angles.

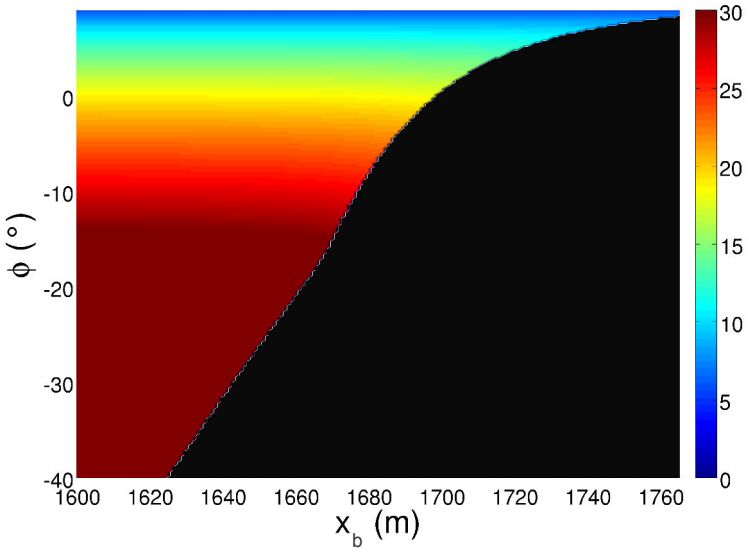

(b) Optimal dam height as continuous function of the abscissa x_b and of the deposit shape angle ϕ. The black area is the region where no optimal design exists.

Figure 5.11 – Optimal design sensitivity to interaction law, $C_0 = 5,530$ €$.m^{-1}$, $C_1 = 300,000$ €, $\alpha = 0.14$, $h_0 = 1$ m, $V = 50,000\ m^3$, $\ell_{fz} = 100\ m$, $\xi_0 = 0.3$.

5.4 Discussion and conclusion

5.4.1 Summary of the work done

In snow avalanche long term forecasting, existing risk and optimal design methods are computationally intensive and, therefore, rarely used in a real engineering context. In addition, they ground on discussible assumptions for hazard modelling, for instance, regarding the distribution of extreme runouts, and their interaction with defense structures. In this work, we addressed these limitations by expanding a pre-existing quasi analytical decisional model (Eckert et al., 2008a) to make it usable with a much wider class of avalanche runout models based on extreme value statistics and of avalanche - defense structure interaction laws.

Specifically, we replaced the classical exponential runout model by the more general Generalised Pareto one. This latter has, coupled with a Poisson model for occurrences, theoretical justifications that promotes its use for modelling "all" possible tails of distributions. This is a huge advantage that should make it sufficient for determining high return period events and perform the risk and optimal design computations on most of the avalanche paths. Indeed, whereas the exponential distribution may fit runout data on runout zones having a rather regular topography compatible with a light tail behavior only, the GPD distribution may cope also for bounded or heavy tailed runout distance distributions controlled by more complex/irregular topographies. However, when the runout zone topography is really extravagant, even the GPD may fail, and a statistical-numerical approach should be proffered, see Sect.5.4.4.

Regarding the defense structure, a simple flow-dam law based on local dissipation of kinetic energy was confronted to a more flexible law based on the volume stored upstream of the dam. The energy dissipation interaction law provides a formula linking the runout distance in the path without a dam to the runout with a dam of height h_d, depending on only the height of the flow h_0. The volume catch interaction law provides the same output, but depending on the deposit volume upstream the dam $V_{obs}(h_d)$ and on the total volume of the avalanche V. Intricately, the value of $V_{obs}(h_d)$ not only depends on the dam height but also on the dam width and on the shape angle of the deposit upstream the dam. It is admitted that, as reported in the Table 5.1, the deposit shape angle can be related either to the humidity rate of the snow, the velocity of the avalanche and/or the μ frictional effect. As a consequence, the volume catch interaction law is more flexible, allowing a more insightful inclusion of the avalanche hazard model one considers into the analysis.

Hence, combining these elementary bricks, we have obtained simple risk formulae to quantify risk and perform the optimal design of an avalanche dam in a quick and efficient

way that cover a variety of situations corresponding to different paths topographies (tail type) and/or types of snow (deposit shape angle). From these, we showed how a detailed uncertainty propagation and sensitivity study (data quantity, stochastic avalanche modelling and flow-obstacle interaction assumptions) can be conducted, leading intervals and bounds for risk estimates and optimal design choices. Practical implementation has been made on a typical case study from the French Alps, illustrating the approach and allowing to more broadly discuss and evaluate the sensitivity of risk quantification and minimisation procedures to avalanche hazard modelling choices (see Sect. 5.4.2 for a summary of main findings).

A somewhat criticizable point of the approach is that we used an extremely rough quantification of the costs. The reason was to be able to obtain analytical equations function of the dam height and the stochastic hazard model. In fact, such analytical solutions exist as soon as the residual risk can be written as:

$$R_b(x_b, h_d) = C_0(h_d) + k_p \times p(x_{stop} > x_b | h_d), \tag{5.26}$$

where k_p is a proportionality to the exceedence probability $p(x_{stop})$ coefficient. Hence, the approach works as soon as the damage is supposed not to vary with avalanche intensity (pressure, flow depth, etc.). In Eq. (5.18), we considered the worst-case: $k_p = C_1 A\lambda$, *i.e.* a total C_1 loss as soon as the building of value C_1 at the abscissa x_b is attained. This is compatible with an economical point of view saying that a building loses all of its value as soon as it has been hit one time by an avalanche because nobody will be ready to buy it afterwards.

However, implementing other choices more compatible with data regarding damages by avalanches to various types of constructions is straightforward, *e.g.* $k_p = A\lambda C_1 \overline{V_i}$, with $\overline{V_i} = \int p(y) V_b(y)\, dy$ the average vulnerability towards the whole range of avalanche intensities that can be derived from the vulnerability curves of, *e.g.* Favier et al. (2014a). In practice, $\overline{V_i}$ may be roughly in the $[0.05-0.5]$ interval, depending on the considered building technology and local hazard distribution, leading to residual risk estimates systematically lower than those provided by our worst case approach. Also, the A actualisation factor was used to obtain finite total risk estimates on the long range, but there is nothing against working at the annual time scale instead, as often done in risk assessment methods in the snow avalanche field, *e.g.* (Keylock et al., 1999). This only requires transforming the total construction cost $C_0(h_d)$ into an annual construction cost $C_0^{'}(h_d) = C_0(h_d)/A$. This shows that the actualisation factor is interpretable, with our simple risk/costs expression, as an amortizing period for our dam.

Eventually, Eq. (5.26) highlights well the that the approach, even if originally designed as individual-risk based (Arnalds et al., 2004), should rather be seen as "local-risk"

based: risk is evaluated and minimised with regards to the abscissa x_b, without considering elements at risk possibly located at other positions in the path, but with possible consideration of many elements at risk together at the abscissa x_b as soon as they can be combined into a single C_1 value. For instance, here, only damages to a building were studied, but similar computations could easily be performed with, *e.g.*, furniture or even humans inside the considered building as elements at risk. For the latter, recent developments relating lethality rates to avalanche impacts could be used (Favier et al., 2014b). However, this would also imply monetizing human life, and we prefer avoid this ethically contestable issue at this stage. Finally, note that, according to Eq. (5.26), the construction cost $C_0(h_d)$ does not need to be linear with the dam height, a choice we made for simplicity. The approach works with any other explicit function of h_d, since, anyhow,the risk minimum search (Eq.(5.19)) is done numerically.

5.4.2 Main findings of the sensitivity analysis

Despite the theoretical interest of the GPD distribution with regards to simpler distributions (modelling "all" possible tails of extreme avalanche runouts), the case study has well shown the high difficulty to practically fit it on real runout data. Specifically, it was impossible to obtain a realistic shape parameter estimate by simply maximizing the likelihood of the data sample at our hand. We strongly believe that this may occur more often that not for avalanche runout data, by definition scarce and recorded with a high level of uncertainty. Since the shape parameter is specifically the one that fully determines the tail behavior type (Fréchet, Gumbel or Weibull), this may cause huge miss-specification of high return levels, and, therefore, induce a bad assessment of the related risk. Here, we have proposed a practical way to tackle the difficulty: implement a profile likelihood maximisation method given a reasonable set of possible shape parameters containing the different tail types (for our case study, $[-0.3 - 0.5]$, with a preferred value $\xi_0 = 0.3$), and consider the whole range of return level plots this set leads within a sensitivity analysis in (residual) risk estimation and optimal design of a defense structure.

Also, for the defense structure effect, it is in practice not easy to make a single choice between the two we considered, and, for the deposit volume one, which deposit shape angle / snow type should be preferred. Furthermore, it can even be reasonably argued that risk mapping /defense structure design should be efficient according to all possible interaction processes/laws, so that taking land use planning decisions on the basis of one single scenario may be contested. We therefore addressed this question as well within the sensitivity analysis, with the goal of having a comprehensive picture of the sensitivity to the different assumptions made in hazard modelling (the way the flow interacts with the structure is for us included in the hazard modelling).

In summary, the risk sensitivity to the GPD shape parameter was assessed as being a bit more influential with regards to the interaction law choice: up to 200% relative error according to Eq.(5.22)), versus up to 130% relative error according to (Eq. (5.25). However, these sensitivity indexes are both very high, and on the same order of magnitude. Hence, the analyses done in Sect. 5.3.3 lead to conclude that the statistical distribution of runouts (and, for instance, the tail type), as well as the interaction law are both crucial if one wants to properly estimate the residual risk in the runout zone according to a given dam height.

In addition, the two sensitivity indexes $\delta_{R(x_b,h_d)}$ (Eq.(5.22)) and $\delta'_{R(x_b,h_d)}$ (Eq. (5.25)) showed more (the former) or less (the latter) complex behaviours according to the abscissa position in the path, but both of them took their highest values for abscissas positions of interest for hazard mapping/zoning procedures. Indeed, modelling assumptions, for instance the tail behavior, most strongly affects high magnitude events, but become insignificant at abscissa (nearly) never reached by avalanches. As a consequence, the very high sensitivity to hazard modelling assumptions we have highlighted may well be critical in practice for engineers and stake-holders concerned by land-use planning decisions. This is a good argument to recommend the bounds approach we have proposed instead of dealing with safety considerations on the basis of a single estimate that may be far from the true risk.

In 5.3.4 the sensitivity study was conducted for the decisional procedure. Here also, sensitivity to the ξ_0 GPD shape parameter choice has been shown to be quite high whatever the considered interaction law. For instance, the higher ξ_0, the higher the optimal height, and the higher the remaining residual risk after the dam construction. Furthermore, we highlighted that the sensitivity to ξ_0 measured by the decisional sensitivity indexes δ_{x_b,h_d^*} (Eq.(5.23)) and $\delta_{x_b,R(h_d^*)}$ (Eq.(5.24)) is also especially high (up to 120%) for buildings situated far down in the path, but still sometimes reached by avalanches. This is consistent with results obtained for residual risk estimates, and is more generally related to the extreme sensitivity of high return levels to the tail behavior.

Regarding the sensitivity of the optimal design procedure to the interaction law choice, it was first shown that the volume catch interaction law has a less stable behaviour than the energy dissipation one, because of its higher number of parameters and more complex dependency to h_d. Hence, the higher flexibility of the volume catch law and, especially, its ability to better reflect the variability of the nature of the flowing snow has a practical drawback: the optimal design procedure is more difficult to carry out, with the different cases discussed in Appendix 5.6.1 needing to be carefully identified and accounted for. Meanwhile, it was possible to show that the lower the deposit shape angle ϕ, the higher the optimal dam height, when it exists, but the higher the residual risk after the dam construction. This simply comes from the fact that the lower the deposit shape angle one

considers, the less efficient the dam is in reducing the risk. Because of this effect, for nearly all possible ϕ values, h_d^* is a strongly discontinuous function of x_b. The position in the path beyond which an optimal height no longer exists increases with the deposit shape angle, until disappearing (on the range of reasonable building positions x_b considered) for the maximal possible value $\phi = 9°$. For the latter, the dam is the most efficient, making its construction nearly always rewarded by a cost reduction up to, *e.g.* 4.18 m for $\ell_{fz} = 100$ m, the limit value that stops everything. It is the only deposit volume interaction law parametrisation for which a given dam height is more efficient in reducing the risk than with the energy dissipation law. Therefore, it is the only case for which the optimal height and the remaining risk are lower, for a given x_b position, with the volume catch law than with the energy dissipation law. For all other ϕ values tested, and whatever the position in the path, the optimal height (when it exists) and the remaining risk are higher with the volume catch law.

All in all, risk and optimal design sensitivity to hazard modelling assumptions regarding the behaviour of extreme runout and the perturbation of the flow by a permanent defense structures seem to be both very strong. Even if some more case studies may be needed to be fully affirmative, this may well be true for a large variety of avalanche paths, and even for a range of defense structures and flow/structures interaction processes much wider than those considered in this study. It is a very important outcome for practice which somewhat differs from what is observed regarding sensitivity to vulnerability / costs. Indeed, according to theoretical (Abraham and Cadre, 2004) and practical (Favier et al., 2014b) evidences, rough vulnerability/cost estimates may be sufficient to determine the defense structure that minimizes the risk even if the true risk is then (rather) badly estimated. Here, on the contrary, we have shown that both risk and optimal design evaluations will fail in producing sensible results if hazard modelling assumptions are even slightly fallacious.

5.4.3 Modelling variability and uncertainty in risk and optimal design procedures

The sensitivity /uncertainty analysis has been carried out through various ways. First, a rather classical uncertainty propagation approach has been implemented to derive confidence intervals for high return levels from the Poisson-GPD point estimates and the related standard errors. To do so, we have adapted two approaches to our profile likelihood context (Appendix 5.6.2), and shown that, for it, the deviance-based one may be the most robust, providing apparently coherent results all over the different Fréchet, Gumbel and Weibull runout tail domains. Such confidence interval fairly represent the uncertainty resulting from the limited size of the data sample available.

In a second time, we considered a reduced range of ξ_0 values, and, conditional to these, plugged the point estimates for the other Poisson-GPD model parameters provided by the profile likelihood maximisation in the residual risk functions. At this stage, we forgot the data quantity related uncertainty (parameters standard errors), focusing on the sensitivity to ξ_0 in risk and optimal design approaches through the indexes $\delta_{R(x_b,h_d)}$, δ_{x_b,h_d^*}, and $\delta_{R(x_b,h_d^*)}$. Our approach was driven by both practical considerations (the impossibility to fit a reliable ξ_0 value with the full likelihood maximisation on our data set) and more theoretical ons (getting some broader insights about the sensitivity of risk estimates and optimal dam heights to the runout tail shape).

Yet, such a two-step approach is somewhat contestable since it would be conceptually more satisfactory to take the parameter uncertainty into account into the sensitivity analysis. A possible way to achieve this would be to switch to a Bayesian approach of the problem, averaging the residual risk functions over the *posterior* distribution of model parameters and evaluating the optimal dam heights and sensitivity indexes accordingly. Conditionally to ξ_0, the approach can still be partly implemented analytically thanks to so called conjugation properties. However, residual risk functions are then presumably no longer fully explicit, which is the main reason we preferred working under the classical paradigm in this paper. Further details about such a possible extension of our work is provided in Appendix 5.6.3.

Furthermore, the limitation of working conditionally to ξ_0 thus remains. As a consequence, the real added value of a Bayesian consideration of the problem would probably be to work with informative priors on all GPD parameters, for instance ξ. To construct them, one could use the results reported in the literature regarding the tail behavior of avalanche runouts in other areas/paths (with care since the result of a presumable Fréchet-type tail behavior obtained for our case study contradicts the evidences of a Weibull type behaviour obtained on larger samples, Keylock (2005); Ancey (2012)). This extra-data information would be of great help in practice, avoiding the ξ_0 choice we had to make because of our limited data set and, presumably reducing the width of high return level confidence intervals. However, in that case, there would be clearly be no full analytical solution of the problem, since no conjugate distribution exists for ξ (Parent and Bernier, 2003a,b).

Regarding the interaction law choice, we proceeded as for ξ_0 (sensitivity index $\delta'_{R(x_b,h_d)}$), but things are a little bit different. Clearly, here, one deals not with uncertainty related to a limited data sample, but with a real modelling assumption regarding the type of dam /flow interaction and consecutive deposit shape angle. Hence, what should be done in practice with the high sensitivity highlighted remains a difficult question: *e.g.* to chose always the energy dissipation one, no matter the rheological behaviour it hides, because it is the most stable numerically? Or to take a mean or a maximum

value provided by each of the interactions laws so as to maximize the safety with the final decision? If some expert information about the most probable amount and type of snow and, hence, deposit shape angle, is available, the volume catch interaction law is probably a good option. However, this is clearly not often the case. To help the engineer to make a sensible choice, Appendix refappendix4 pushes forward the comparison between the two interaction laws we used.

All in all, lots of work remains to be done to find appropriate ways to better quantify and represent the different uncertainty sources that combines while trying to estimate avalanche risk and design the most appropriate defense structure in the context of limited funds. However, we believe that, from a practical perspective, our approach is already a nice refinement with regards to earlier attempts, showing how, on a practical case, bounds and sensitivity indexes to runout tail types or to possible interaction processes can be (rather) easily computed to add information into the decision making, and, hopefully, make the stake holder's choice more appropriate

5.4.4 Other outlooks for further work

Even if extreme value statistics are used, for example, in the different variations of the runout ratio approach, *e.g.* McClung (2000, 2001), our feeling is that, for snow avalanche problems, their use could probably be more intense that it is currently the case. By replacing the exponential distribution by the much more general GPD one, our work may contribute to the diffusion of important extreme value concepts such as the tail behaviour in this specific community. However, much work on this question remains to be done, for instance, to more deeply analyse extreme runouts on data sample as large and clean as possible within this framework. Symmetrically, in the extreme value community, optimal design approaches in which a real effort on costs and decision modelling is made remain, at our knowledge, seldom (*e.g.* Rietsch et al. (2013)), and our work main encourage further developments in this promising direction.

Second, the bridge remains to be done with similar risk and optimal design approaches involving an avalanche numerical propagation model (Barbolini et al., 2004a; Cappabianca et al., 2008; Eckert et al., 2009; Favier et al., 2014b). Since the expected damage can easily be computed according to existing vulnerability curves and the multivariate avalanche model outputs, these have the advantage to avoid the assumptions we have made regarding a constant loss whatever the avalanche impact on a considered element at risk. Also, they are able to deal with the most complex path topographies on which runout extrapolation beyond the further recorded value will fail, even with a GPD tail. On the other hand, if such statistical-numerical approaches have desirable extreme value properties (tail behaviour, etc.), which could be crucial for well evaluating the most damageable events,

remains a critical and rather open question. Also, clearly, their inherent computation cost will remain an obstacle to their use in engineering practice, which justifies the development of simpler alternatives such as ours.

Finally, avalanches - defense structures interaction remains a research field of high practical relevance, very active, but also where lots of work remains to be done to better understand the complex physics it involves. However, it would already be clearly useful to expand our work to other types of defence structures and avalanche flow interaction laws already available. For instance, it must be remembered that the two we considered correspond to idealised cases only (typical but limited Froude number ranges). Hence, first ideal candidates to enlarge the applicability of our approach would be interaction laws combining runout shortening by energy dissipation and volume catch. Such laws account for both the storage effects and the local dissipation of kinetic energy and are therefore able to work at intermediate Froude numbers (Faug et al., 2004a). Potentially, they could be implemented within the same framework, making the results of the risk and optimal design computations less specific to one type of flow obstacle interaction (and/or to one given snow type), which would, in turn, facilitate the engineer's choice. However, if the convenience of having analytical risk equations at hand would still be true remains to be investigated.

5.5 Acknowledgements

The authors thank the ANR research program MOPERA (Modélisation probabiliste pour l'Étude du Risque d'Avalanche - www.avalanches.fr/mopera-projet/) and the MAP3 Alcotra Interreg program for financially supporting this work.

5.6 Appendices

5.6.1 Existence of optimal heights with the volume catch interaction law

For the general GPD case, when $\xi \neq 0$, the derivative of Eq. (5.21) with regards to the dam height is:

$$\begin{aligned}
\frac{\partial R(x_b,h_d)}{\partial h_d} &= C_0 + \lambda C_1 A \frac{\partial}{\partial h_d}\left(\left(1+\frac{\xi(x_b-x_d)}{\sigma\left(1-\frac{h_d^2}{2A_a\tan\alpha_s}\right)^{1/2}}\right)^{\frac{-1}{\xi}}\right) \\
&= C_0 + \lambda C_1 A \frac{-1}{\xi}\left(1+\frac{\xi(x_b-x_d)}{\sigma\left(1-\frac{h_d^2}{2A_a\tan\alpha_s}\right)^{1/2}}\right)^{\frac{-1-\xi}{\xi}} \frac{\partial}{\partial h_d}\left(1+\frac{\xi(x_b-x_d)}{\sigma\left(1-\frac{h_d^2}{2A_a\tan\alpha_s}\right)^{1/2}}\right) \\
&= C_0 + \lambda C_1 A \frac{-1}{\xi}\left(1+\frac{\xi(x_b-x_d)}{\sigma\left(1-\frac{h_d^2}{2A_a\tan\alpha_s}\right)^{1/2}}\right)^{\frac{-1-\xi}{\xi}} \frac{\xi(x_b-x_d)}{\sigma}\frac{\partial}{\partial h_d}\left(\left(1-\frac{h_d^2}{2A_a\tan\alpha_s}\right)^{-1/2}\right) \\
&= C_0 - \frac{\lambda C_1 A h_d}{2\sigma A_a\tan\alpha_s}(x_b-x_d)\left(1+\frac{\xi(x_b-x_d)}{\sigma\left(1-\frac{h_d^2}{2A_a\tan\alpha_s}\right)^{1/2}}\right)^{\frac{-1-\xi}{\xi}}\left(1-\frac{h_d^2}{2A_a\tan\alpha_s}\right)^{-3/2}
\end{aligned} \quad . \quad (5.27)$$

This expression allows better understanding of the different cases likely to occur. Figure 5.12 a-b shows the no optimum case, where the risk derivative is positive all over the range of possible h_d values, and, hence, the residual risk is a strictly increasing function of h_d. This is typically observed for buildings situated at large abscissas in the path and/or for low values of the deposit shape angle ϕ. According to the volume catch interaction law, the dam has then a very small protective effect, so that the loss reduction with increasing h_d values is always lower than the concomitant construction cost increase.

Figure 5.12 c-d shows the case of a pseudo-optimum due to the positivity constraint in Eq. (5.13). The risk derivative is always negative over the range of possible h_d values, so that the minimum risk obtained corresponds to the maximal investigated h_d value. This is typically observed for buildings situated just beyond the dam abscissa in the path and/or for high values of the deposit shape angle ϕ. The dam has then a very high protective efficiency, making the additional construction effort rewarded all over the possible h_d range. Noteworthy, the maximal investigated height is, in this case, $h_d = \left(\frac{V\times 2\tan(\alpha_s)}{\ell_{fz}}\right)^{1/2}$, the limit value just sufficient to stop all avalanches before the considered element at risk. From a practical point of view, this height can be considered an optimal choice.

Finally, Figure 5.12 e-f shows the case of a real optimum occurring on the investigated h_d range. In fact, the residual risk derivative has even two zeros in this case, but only the one corresponding to the local minimum of the residual risk function is of interest. It

highlights the dam height above which the additional protective effect no longer compensates the additional construction costs. This is typically observed for reasonable building positions / deposit shape angles, intermediate between the two extreme cases previously discussed.

5.6.2 Confidence intervals for return levels with profile likelihood GPD estimates

With the delta method

According to Eq. (5.4), the σ, ξ and λ derivatives of the return level x_T (the indices "stop" and "0" are dropped in the return level, for simplicity, and so is the $x_T > x_d$ condition), are, respectively:

$$\frac{\partial x_T}{\partial \sigma} = \frac{1}{\xi}((\lambda T)^{\xi} - 1), \tag{5.28}$$

$$\frac{\partial x_T}{\partial \xi} = -\frac{\sigma}{\xi^2}((\lambda T)^{\xi} - 1) + \frac{\sigma}{\xi}(\lambda T)^{\xi} \ln(\lambda T)), \tag{5.29}$$

$$\frac{\partial x_T}{\partial \lambda} = \sigma T^{\xi}(\lambda)^{\xi - 1}. \tag{5.30}$$

In our profile-likelihood approach, we set the ξ_0 value, and determine $\hat{\sigma}(\xi_0)$, which yields:

$$\hat{x_T}(\xi_0) = x_T(\xi_0, \hat{\sigma}(\xi_0), \hat{\lambda}) = x_d + \frac{\hat{\sigma}(\xi_0)}{\xi_0}((\hat{\lambda} T)^{\xi_0} - 1). \tag{5.31}$$

The delta method considers $\hat{x_T}$ to be asymptotically normally distributed (theorem 2.4 of Coles (2001)). In our case, this writes:

$$\hat{x_T}(\xi_0) \sim N(x_T(\xi_0, \hat{\sigma}(\xi_0), \hat{\lambda}), V_{x_T}(\xi_0)), \tag{5.32}$$

where $V_{x_T}(\xi_0) = \nabla x_T^T(\xi_0) V_{\sigma(\xi_0),\lambda} \nabla x_T(\xi_0)$. $V_{\sigma(\xi_0),\lambda}$ is the approximate variance-covariance matrix of the profile likelihood estimates and $\nabla x_T(\xi_0) = \begin{pmatrix} \frac{\partial x_T(\xi_0)}{\partial \sigma} \\ \frac{\partial x_T(\xi_0)}{\partial \lambda} \end{pmatrix}$ is evaluated at $(\hat{\sigma}(\xi_0), \hat{\lambda})$. It follows that an approximate $(1 - \alpha)$ confidence interval for $x_T(\xi_0)$ is:

$$\hat{x_T}(\xi_0) \pm z_{\frac{\alpha}{2}} \sqrt{V_{x_T}(\xi_0)}, \tag{5.33}$$

where $z_{\frac{\alpha}{2}}$ is the $(1 - \frac{\alpha}{2})$ quantile of the standard normal distribution.

On the basis of the deviance statistics

The deviance statistics defined in Sect. 5.2 in the context of the GPD - Exponential model choice allows obtaining another confidence interval for high return levels. In our case, one needs to evaluate the profile deviance at the ξ_0 value. To do so, according to Eq. (5.4),

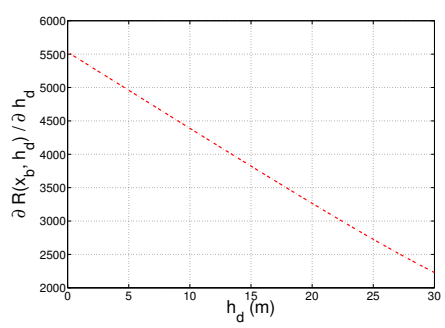

(a) Derivative plot.

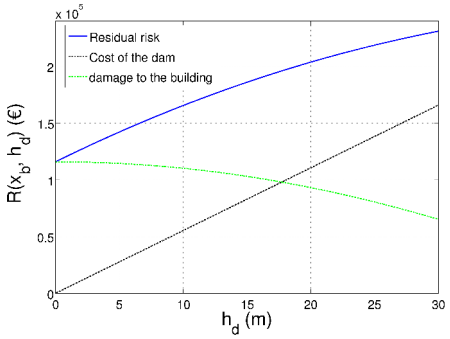

(b) Risk plot.

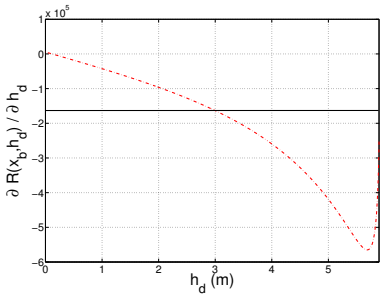

(c) Derivative plot.

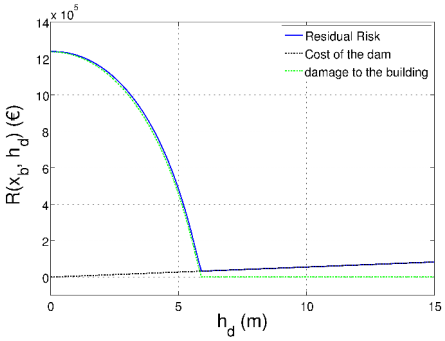

(d) Risk plot.

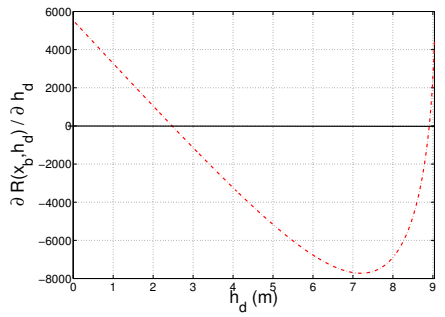

(e) Derivative plot.

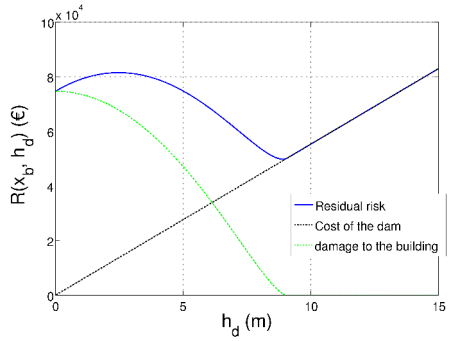

(f) Risk plot.

Figure 5.12 – Existence of optimal heights with the volume catch interaction law, $C_0 = 5,530$ €$.m^{-1}$, $C_1 = 300,000$ €, $V = 50,000\ m^3$, and $\xi_0 = 0.3$. (a)-(b) No optimum case: The used parameter set is: $\phi = -40°$, $\ell_{fz} = 50\ m$ and $x_b = 1,690.7\ m$; (c)-(d) Pseudo-optimum case induced by the positivity constraint in the volume catch interaction law. The damage to the building costs are zero for h_d values exceeding the positivity constraint $h_d = 5.9$ m in this case. For higher dams, all avalanches are stopped below or at the dam abscissa and the risk derivative does not exist. The used parameter set is: $\phi = 9°$, $\ell_{fz} = 50\ m$, and $x_b = 1,589.7\ m$; (e)-(f) Real optimum case corresponding to residual risk minimization. The used parameter set is: $\phi = 3°$, $\ell_{fz} = 150\ m$, $x_b = 1,718.7\ m$.

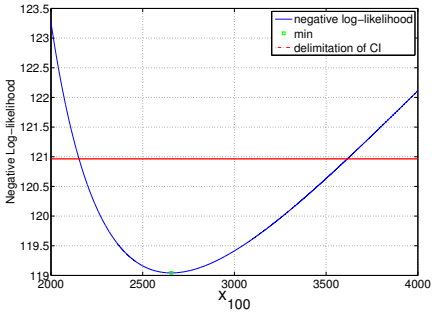

Figure 5.13 – Deviance based 95% confidence interval (CI) for the 100 years return level, $\xi_0 = 0.3$. The green square denotes the minimum of the negative log-likelihood curve. The red straight line is the Chi-squared based 95% threshold. Its intersection with the negative log likelihood curve delimitates the 95% confidence interval for the centennial runout distance.

for $\xi_0 \neq 0$, we can write $\sigma(\xi_0) = \frac{(\xi_0(x_T(\xi_0)-x_d)}{((\lambda T)^{(\xi_0)}-1}$. Replacing all the occurrence of σ in the log-likelihood function by this expression leads the searched profile deviance as function of ξ_0, λ and $x_T(\xi_0)$. According to the theorem 2.5 of Coles (2001), its asymptotic distribution is, again, the one degree of freedom χ^2 distribution, which provides easily the searched $(1-\alpha)$ confidence interval for the true value of $x_T(\xi_0)$, with α the considered significance level.

Figure 5.13 applies this result to the evaluation of the 95% confidence interval for the centennial runout. The best guess $\hat{x_{100}}$ is at the minimum of the profile log-likelihood. The cut-off straight line corresponds to $\frac{1}{2}\ \chi^2_1(0.05) = 1.921$. Its intersection with the profile log–likelihood corresponds to the bounds of the searched interval 95%. Note that these are non symmetric around the best guess $\hat{x_{100}}$, an important difference with the delta method, where the asymptotic normality assumption imposes symmetry of confidence intervals on return levels.

5.6.3 A Bayesian outlook of the problem

The Bayesian framework proposes an alternative paradigm for inference. Statistical estimates are considered as random variables whose joint *posterior* distribution given the data is evaluated (Parent and Bernier, 2007). This framework has been recently popularised in the avalanche literature because of its ability to treat various problems, for instance, calibration of flow codes (Ancey, 2005; Straub and Gret-Regamey, 2006; Eckert et al., 2010c) or spatio-temporal assessment of climate change impacts (Eckert et al., 2010d,a), but also because there is a strong link between the Bayesian paradigm and statistical theory of

decision under uncertainty (Raiffa, 1968; Berger, 1985).

Posterior distribution of the POT model conditional to ξ_0

Let us first recall that, with the dam height h_d and our two interaction laws, the distribution of runout distances exceeding the dam abscissa x_b (the $x_b > x_d$ condition is dropped) is:

$$x_{stop}(h_d) \sim GPD(\sigma_{h_d}, \xi) \tag{5.34}$$

with $\sigma_{h_d} = \frac{1}{\sigma(1-\alpha\frac{h_d}{h_0})}$ under the energy dissipation law and $\sigma_{h_d} = \frac{1}{\sigma\sqrt{1-\frac{h_d^2}{2A_a \tan\alpha_s}}}$ under the volume catch interaction law.

Conditionally to a fixed ξ_0 value, applying Bayes' theorem to our sample $x_{stop}(h_d) = x_{stop_i}(h_d)$, i in $[1, n]$ of runouts shortened by the dam h_d leads the *posterior* distribution:

$$p(\sigma_{h_d}|x_{stop}(h_d), \xi_0) \propto \pi(\sigma_{h_d}) l(x_{stop}(h_d)|\sigma_{h_d}, \xi_0) \tag{5.35}$$

where $\pi(\sigma_{h_d})$ is the *prior* probability distribution of the modified scale parameter σ_{h_d} and $l(x_{stop}(h_d)|\sigma_{h_d}, \xi_0)$ the profile GPD likelihood of the available modified sample with the dam height h_d and the chosen shape parameter ξ_0.

To benefit more easily of so-called conjugation properties, it is easier to work again with the inverse scale parameter $\rho_{h_d} = 1/\sigma_{h_d}$. Then, under the convenience choice of:

$$\pi(\rho_{h_d}) \sim Gamma(a_\rho(h_d), b_\rho(h_d)), \tag{5.36}$$

it should be possible to proof that the *posterior* distribution is:

$$p(\rho_{h_d}|x_{stop}(h_d), \xi_0) \sim Gamma(a'_\rho(h_d), b'_\rho(h_d)) \tag{5.37}$$

with $a'_\rho(h_d) = a_\rho(h_d) + S_n(h_d)$ and $b'_\rho(h_d) = b_\rho(h_d) + n$, where $S_n(h_d) = \sum_{i=1}^{n}(x_{stop_i}(h_d) - x_d)$ is the sum of exceedences in the available sample or runout distances shortened by one of the two interaction laws.

The annual probability of reaching the dam abscissa x_d is not modified whatever the dam height, which writes $\lambda(h_d) = \lambda$. Furthermore, with the POT approach, magnitude and frequency of threshold exceedences are independent. As a consequence, it is straightforward that the full joint *posterior* of the POT model writes:

$$p(\lambda, \rho_{h_d}|x_{stop}(h_d), \xi_0) = p(\lambda|x_{stop}) p(\rho_{h_d}|x_{stop}(h_d), \xi_0). \tag{5.38}$$

Finally, under the assumption of the conjugate $\pi(\lambda) \sim Gamma(a_\lambda, b_\lambda)$ distribution for λ:

$$p(\lambda|x_{stop}) \sim Gamma(a'_\lambda, b'_\lambda), \tag{5.39}$$

with $a'_\lambda = a_\lambda + T_{obs}$ and $b'_\lambda = b_\lambda + n$. T_{obs} is simply the length of the observation period on which the runout sample has been recorded.

Bayesian risk, optimal design and sensitivity indexes

As a generic expression, the Bayesian (exposant B) residual risk function writes:

$$R^B(x_b, h_d) = \int R(x_b, h_d, \theta(h_d)) p(\theta(h_d)|x_{stop}(h_d)) d\theta(h_d), \tag{5.40}$$

where $R(x_b, h_d, \theta(h_d))$ is the residual risk function provided by, Eq. (5.17) conditional to the model parameters $\theta(h_d)$ and $p(\theta(h_d)|x_{stop}(h_d))$ the joint *posterior* distribution of the parameters of the stochastic hazard model given the available shortened sample.

With our POT model, still conditionally to ξ_0, this writes

$$R^B(x_b, h_d|\xi_0) = C_0 h_d + C_1 A \int\int \lambda P(x_{stop}(h_d) > x_d|\rho(h_d), \xi_0) p(\lambda, \rho_{h_d}|x_{stop}(h_d), \xi_0) d\lambda d\rho(h_d). \tag{5.41}$$

Because of the magnitude-frequency independence, this simplifies into:

$$R^B(x_b, h_d|\xi_0) = C_0 h_d + C_1 A \frac{b'_\lambda}{a'_\lambda} \int P(x_{stop}(h_d) > x_d|\rho(h_d), \xi_0) p(\rho_{h_d}|x_{stop}(h_d), \xi_0) d\rho(h_d), \tag{5.42}$$

since the integral over λ is simply the posterior expectancy, close to the empirical observation rate if the *prior* parameters (a_λ, b_λ) are chosen so that $\pi(\lambda)$ is poorly informative.

Hence, only the integral over the *posterior* distribution of the modified scale parameter ρ_{h_d} remains, and $P(x_{stop}(h_d) > x_d|\rho(h_d), \xi_0) = (1 + \rho(h_d)\xi_0(x_b - x_d)^{-1/\xi_0}$, $\xi_0 \neq 0$ is simply the exceedence probability under the GPD model. At this stage, even if Eq. (5.37) truly holds, if the full analytical computation is possible or not remains to be investigated in more details.

However, in any case, an standard numerical computation should lead $R^B(x_b, h_d|\xi_0)$ as function of h_d, which can easily be minimised exactly as it is done for $R(x_b, h_d, \theta)$ in Eq.(5.19) for the classical risk evaluated conditional to point estimates (*plug-in* approach). The big difference is that the λ and σ / ρ parameters are then no longer fixed, so that uncertainty concerning them resulting from the limited data sample available is explicitly taken into account in the risk assessment, and in the optimal design procedure. This could be very useful for, in the future, evaluating for example the sensitivity to interaction processes, but taking into account parameter uncertainty in addition to possible variability among interaction laws and deposit shape angles. For this, the Bayesian sensitivity index analogous to Eq. (5.25) is simply:

$$\delta'^B_{R(x_b,h_d)} = \int \delta'_{R(x_b,h_d,\rho_{h_d}|\xi_0)} p(\rho_{h_d}|x_{stop}(h_d), \xi_0) d\rho(h_d). \tag{5.43}$$

5.6.4 Is it possible to further compare the two flow-dam interaction laws?

It is tempting to push forward the direct comparison between the two flow-dam interaction laws used in the present paper. By considering $n = 1/2$ (confined zone upstream of the dam) and by making use of Taylor expansion, the volume's catch interaction (see Eq. (5.12)) law yields:

$$\frac{x_{stop}(h_d) - x_d}{x_{stop_0} - x_d} \approx 1 - \frac{1}{2}\frac{V_{obs}}{V} \ . \tag{5.44}$$

The avalanche volume and the volume stored upstream of the dam can be expressed, respectively, as: $V = h_0 L_0 l_f z = k_0 h_0^2 \ell_{fz}$ and $V_{obs} = k_s L \ell_{fz} h_d$, under the assumption of a rough proportionality for the avalanche length $L_0 = k_0 h_0$, L the deposit length and k_s a coefficient representing deposit's shape. This leads:

$$\frac{x_{stop}(h_d) - x_d)}{x_{stop_0} - x_d} \approx 1 - \frac{1}{2}\frac{k_s L h_d}{k_0 h_0^2} \ . \tag{5.45}$$

By making use of $k_s = 1$ and $L = h_d/(2\tan(\alpha_s))$ (triangular-shaped deposit upstream of the dam), it yields:

$$\frac{x_{stop}(h_d) - x_d)}{x_{stop_0} - x_d} = 1 - \left(\frac{1}{4k_0 \tan(\alpha_s)}(\frac{h_d}{h_0})^2\right) \ . \tag{5.46}$$

This above equation is equivalent to the linear model (see equation (5.11)) only if:

$$\alpha = \frac{1}{4k_0 \tan(\alpha_s)}\frac{h_d}{h_0} \ . \tag{5.47}$$

For this latter equation to be true, either the righthandside term must be kept constant or α must be a function of h_d/h_0. The first option leads to a somewhat non-physical result: the length of the deposit and the volume stored upstream of the dam are constant whatever the dam height. The second option can give more physical results, but only with small values of α, ten times smaller than the typical value of 0.14 that was used in this study. This factor 10 explains why the volume's catch law generally evaluates a residual risk higher than the one obtained with the energy dissipation law, as discussed in the present paper.

More generally, this second option also shows that the two interaction laws are definitely different models, difficult to directly compare. For instance, the run-out shortening derived from the Taylor's expansion of the volume's catch law is no longer a linear function of h_d/h_0). However, better understanding the similarities and differences between the two interaction laws we considered may make it possible in the future to better describe flows characterised by intermediate Froude numbers, in link with the more general formulations previously advocated that combines the two shortening processes (Faug et al., 2004b). This may be important since the $1-5$ Froude range, to which none of our two interaction laws is perfectly adapted, is typical for snow avalanche flows in many paths.

CHAPTER 6

Conclusion

In this thesis, a framework for the evaluation of the vulnerability of elements at risk towards snow avalanches and its consideration in risk assessment and optimal design procedures was proposed. First, fragility curves for ten reinforced concrete structures were obtained considering four limit states. Then the efforts were concentrated on improving the mechanical model, but keeping a good effectiveness/computation time ratio for the fragility curve assessment. Third, the risk sensitivity to fragility relations was assessed on a simple case. Finally, analytical risk formula were obtained to make practitioners benefit from extreme value theory. The flow/structure interaction law influence in the decisional framework was also investigated on a case study. What follows sums up the main outcomes of the work and points out further outlooks.

6.1 Civil engineering approaches

Classical RC design approaches

The method we worked on consisted in finding good approximations of the distribution of the ultimate uniform avalanche-like pressure on a RC wall. We assumed that the bending failure is the dominant failure mode when a RC wall is loaded by an avalanche. We considered four limit states based on four specific bending moments the wall can undergo. The four limit states were defined as the moments where (1) the elastic limit within concrete is reached, (2) the steel yielding occurs weighted by a coefficient of safety, (3) the steel yielding occurs (no safety coefficient is considered) and (4) the wall collapses. These were evaluated at low computational costs *via* abacus.

Fragility assessment with the classical RC design approaches

The mechanical model was based on abacus relations that enable to calculate the maximal bending moment which develops within the RC wall for a given applied pressure. A Monte Carlo sampling was used to build the CDF of the ultimate pressure of the RC wall which corresponds to the fragility relation of the structure. Because a very low CPU time was needed to perform the ultimate pressure calculation, massive sets of fragility curves were derived. Ten walls were considered, differing from each others by their boundary conditions. Thus, forty fragility curves were obtained ranging from 2.8 kPa to 218.6 kPa (the range is defined by the minimum 2.5% quantile and the maximum 97.5% quantile among all the fragility curves). The sensitivity of the approach was analysed by two different ways. First, various statistical inputs distributions for the mechanical model were tested to underline the effect of this choice on the fragility relation. The marginal variances had the strongest effect in our case. Then the Sobol indices were calculated for independent inputs to understand the role of the inputs for each limit states calculation.

Fragility assessment with the SDOF non linear model

In a second time, the approach was enlarged to less stringent mechanical assumptions. Finite elements methods provide good approximations of the behaviour of a RC wall structure, but the time needed for calculations remains too high for establishing fragility relations. The idea was to perform a meta-modelling based on physical considerations. A meta-model based on statistical assumption (polynomial approximation, regression ...) could have fit our problem, but the interest of our approach is that, with our choice, the main physics is kept. The choice was made of a single-degree-of-freedom (SDOF) model. We showed that it gives satisfactory results when modelling the ultimate behaviour of the RC structure. Indeed, the comparison with limit analysis and Finite Element Analysis showed that the SDOF model well reproduces the load-displacement behaviour.

With the SDOF model, four reliability methods were investigated to highlight their pros and cons for evaluating a fragility curve. An accuracy analysis was conducted to find out which of the four fragility assessment methods provides the best computation time-accuracy compromise. The non parametric Kernel smoothing one appeared as a good choice, making no strong assumptions regarding the shape of the fragility curve but allowing smooth approximations to be obtained.

6.2 Risk and decisional analysis

Sensitivity to the fragility relations for various buildings

We took advantage of having at hand a large set of vulnerability curves to improve our risk understanding. A case study was used to calculate the annual risk of reaching a given limit state and to evaluate dam heights that minimise the risk. We obtained minimal and maximal values using all the fragility relations. We showed that the difference between the minimal and maximal values for risk was ten times higher than for the optimal design value. We choose not to integrate on all the fragility relations we had but to use the available set to build risk bounds. Thus, the risk is not any more presented as a single estimate but as an interval that takes into account various building technologies, showing the high sensitivity to the fragility relations choice.

Human fragility relations derivation for risk quantification

This conclusion was consolidated by the use of human vulnerability relations in the risk study. We assumed that a numerical link exists between fragility relations for buildings and human death probability for people inside these buildings. A set of lethality rates as function of avalanche loading for people inside buildings was thus obtained. It has been pointed out how human risk quantification is highly dependent on the vulnerability curve choice. As an evidence, we showed that acceptable risk levels may be reached with certainty further down in the path than predicted by return period based zoning policies.

Sensitivity to hazard modelling assumptions

The risk sensitivity to the hazard distribution was also assessed: (1) by using analytical expression for modeling avalanche runout distribution and (2) by considering two avalanche - defense structure interaction laws. Avalanche runout models were analytically modelled using the generalized Pareto distribution (GPD) from extreme value statistics. Thus, we obtained simple analytical risk formulae to quantify risk and perform the optimal design of an avalanche dam in a quick and efficient way. A simple avalanche - defense structure interaction law based on kinetic energy dissipation was confronted to a law based on the volume stored upstream of the dam whose flexibility make it able to cope for various types of snow. We showed that the energy dissipation one generally postulates a higher risk reduction, but the flexibility of the volume catch one makes the case of high deposit shape angles due to wet snow flows an exception to this rule. Eventually, here also, we demonstrated how a detailed uncertainty propagation and sensitivity study can be conducted, leading intervals and bounds for risk estimates and optimal design values.

6.3 Main perspectives

Improve the mechanical model

Ultimate bending moments were used to describe a damage level of the RC structure. However, as function of the complexity of the structure and the loading features, RC structures can develop several failure modes (direct shear, punching, etc.) which should be better accounted for by the structure model than we did. For this, it is important to mention that experimental work has already been achieved to better understand the behaviour of a RC structure loaded by a snow avalanche, and that some studies are under progress to better assess possible quasi-static, dynamic or impulsive responses of the structure. Consequently, as shown in Chap. 3, inertial effects could have an influence and our curves could be revisiting according to this result.

Fragility assessment *via* other reliability methods

We also used simple reliability methods to assess fragility relations, *i.e.* Monte Carlo sampling, kernel smoothing and parametric approaches based on fixed shapes of the fragility curve. If more complex mechanical are put in use in the future, efforts should be made to well choose more efficient reliability methods suitable for time consuming models. Several choices may be possible such as improved MC methods or adapted meta-models.

We also suggest that the tail behaviour of the fragility curve may be important in various relaibility problems. Indeed, for risk quantification, for instance, it can be of high interest to know precisely very low quantiles of the fragility curve indicating loadings for which the structure failure becomes possible. Including this aspect into the analysis, for instance using a GPD tail such as illustrated in Chap. 3 would be interesting, making the link with the extreme value framework used in Chap. 5.

Use the Bayesian approach to integrate the parameters uncertainties

In this work, we did not use Bayesian approaches but "played" with uncertainty to obtain risk bounds. For example, in Chap. 4, we did not integrate all over the fragility curves set. Also in Chap 5, in order to keep analytical risk formulas, we did not take parameter uncertainty into account in these. Considering these choices in the future would be worthily.

Using other flow/structure interaction laws and perform a "global" sensitivity study

Another perspective may be to test other flow/structure interaction relations within the same framework. Indeed, even if the two interaction laws we considered take into account two types of avalanche flows, some underlying assumptions remain strong and could lead to wrongly evaluate risk and optimal design decisions.

Also, from a wider perspective, the risk sensitivity analysis has been conducted for each of the sub-models but not in a global way, checking how the uncertainty/variability regarding the different sub-models may interact in the final outputs. In the future, it would be interesting from an operationnal perspective to confront all the inputs of the model in the same sensitivity study, giving access to more general bounds for risk suitable for all the tested configurations.

Bibliography

Abraham, C. and Cadre, B. (2004). Asymptotic global robustness in bayesian decision theory. *The annals of Statistics*, 32:1341–1366.

Ancey, C. (2005). Monte Carlo calibration of avalanches described as Coulomb fluid flows. *Philosophical Transactions of the Royal Society A: Mathematical, Physical and Engineering Sciences*, 363(1832):1529–1550.

Ancey, C. (2006). *Dynamique des avalanches*. Presses polytechnique et universitaires romandes.

Ancey, C. (2012). Are there "dragon-kings" events (i.e. genuine outliers) among extreme avalanches? *European Physical Journal: Special Topics*, 205(1):117–129.

Ancey, C., Gervasoni, C., and Meunier, M. (2004). Computing extreme avalanches. *Cold Regions Science and Technology*, 39(2-3):161 – 180. Snow And Avalanches: Papers Presented At The European Geophysical Union Conference, Nice, April 2003. Dedicated To The Avalanche Dynamics Pioneer Dr. B. Salm.

Ancey, C., Rapin, F., Martin, E., Coleou, C., Naaim, M., and Brunot, G. (2000). L'avalanche de péclerey du 9 février 1999. *La Houille Blanche*, 5:45–53.

Arnalds, D., Jonasson, K., and Sigurdsson, S. (2004). Avalanche hazard zoning in iceland based on individual risk. *Annals of Glaciology*, 38:285–290. International Symposium on Snow and Avalanches, Davos, Switzerland.

Barbolini, M., Cappabianca, F., and Sailer, R. (2004a). Empirical estimate of vulnerability relations for use in snow avalanche risk assessment. In *Risk Analysis IV*, volume 9, pages 533–542.

Barbolini, M., Cappabianca, F., and Savi, F. (2004b). Risk assessment in avalanche-prone areas. In *Annals of Glaciology*, volume 38, pages 115–122.

Barbolini, M. and Keylock, C. (2002). A new method for avalanche hazard mapping using a combination of statistical and deterministic models. *Natural Hazards and Earth System Sciences*, 2:239–245.

Bares, R. (1969). *Tables pour le calcul des dalles et des parois*. Dunod, Paris (French).

Baroudi, D., Sovilla, B., and Thibert, E. (2011). Effects of flow regime and sensor geometry on snow avalanche impact-pressure measurements. *Journal of Glaciology*, 57(202):277–288.

Baroudi, D. and Thibert, E. (2009). An instrumented structure to measure avalanche impact pressure: Error analysis from monte carlo simulations. *Cold Regions Science and Technology*, 59:242–250.

Bartelt, P., Salm, B., and Gruber, U. (1999). Calculating dense-snow avalanche runout using a Voellmy-fluid model with active/passive longitudinal straining. *Journal of Glaciology*, 45:242–254.

Bazant, Z. P. and Oh, B. H. (1983). Deformation of cracked net-reinforced concrete walls. *Journal of Structural Engineering*, 109(1):93–108.

Bellot, H., Naaim Bouvet, F., Naaim, M., Caccamo, P., Faug, T., and Ousset, F. (2013). Taconnaz avalanche path: pressure and velocity. In *International Snow Science Workshop (ISSW 2013), Grenoble Chamonix-Mont-Blanc, France, October 7-11, 2013 : a merging of theory and practice, p. 1378-1383*.

Berger, J. O. (1985). *Statistical Decision Theory and Bayesian Analysis*.

Bernier, J. (2003). Decisions and attitude of decision makers facing hydrological risk. *Hydrological Sciences Journal*, 48(3):301–316.

Berthet-Rambaud, P. (2004). *Structures rigides soumises aux avalanches et chutes de blocs : modélisation du comportement mécanique et caractérisation de l'interaction phénomène-ouvrage*. PhD thesis, Université Grenoble 1 - Joseph Fourier.

Berthet-Rambaud, P., Limam, A., Baroudi, D., Thibert, E., and Taillandier, J. (2008). Characterisation of avalanche loading on impacted structures: a new approach based on inverse analysis. *Journal of Glaciology*, 54:525–541.

Berthet-Rambaud, P., Limam, A., Roenelle, P., Rapin, F., Tacnet, J., and Mazars, J. (2007). Back-analysis of the collapse of taconnaz reinforced concrete deflective walls by february 11th 1999 avalanche. *Cold Reg Sci Technol*, 47:16–31.

Bertrand, D., Naaim, M., and Brun, M. (2010). Physical vulnerability of reinforced concrete buildings impacted by snow avalanches. *Natural Hazard and Earth System Sciences*, 10(7):1531–1545.

Biggs, J. (1964). *Introduction to structural dynamics*. New York: McGraw-Hill Book Company.

Blanchet, J. and Davison, A. (2011). Spatial modeling of extreme snow depth. *Annals of Applied Statistics*, 5(3):1699–1725.

Bozhinskiy, A., Nazarov, A., and Chernouss, P. (2001). Avalanches : a probabilistic approach to modelling. *Annals of Glaciology*, 32:255–258.

Bründl, M., Romang, H., Bishof, N., and Rheinberger, C. (2009). The risk concept and its application in natural hazard risk management in swotzerland. *Natural Hazard and Earth System Sciences*, 9:801–813.

Caccamo, P., a. C. B., Faug, T., Bellot, H., and Naaim-Bouvet, F. (2012). Small-scale tests to investigate the dynamics of finite-sized dry granular avalanches and forces on a wall-like obstacle. *Granular Matter*, 14:577–587.

Caccamo, P. (2012). *Experimental study of the ifluence of protection structures on avalanches and impact pressures*. PhD thesis, Université de Grenoble, spécialité : Science de la Terre, de l'Univers et de l'Environnement.

Cappabianca, F., Barbolini, M., and Natale, L. (2008). Snow avalanche risk assessment and mapping: A new method based on a combination of statistical analysis, avalanche dynamics simulation and empirically-based vulnerability relations integrated in a GIS platform. *Cold Regions Science and Technology*, 54:193–205.

Carta, G. and Stochino, F. (2013). Theoretical models to predict the flexural failure of reinforced concrete beams under blast loads. *Engineering structures*, 49:306–315.

CEB-FIP (2010). Model code 2010, first complete draft, volume 1: fib, bulletin 55. Technical report, Federal Institute of Technology, Lausanne (Switzerland).

Coles, S. (2001). *An Introduction to Statistical Modeling of Extreme Values*. Springer.

Coles, S., Heffernan, J., and Tawn, J. (1999). Dependence measures for extreme value analyses. *Extremes*, 2:4:339–365.

Committee, C. T. (2004). *Eurocode 2: Design of concrete structures - Part:1-1 - general rules and rules for buildings (EN 1992-1-1:2004)*.

Daudon, D., Baroth, J., Ma, Y., Perrotin, P., and Mommessin, M. (2013). Sensitivity of a reinforced concrete protective gallery under a snow avalanche load. *Structural Safety*, 41:47–56.

De Borst, R. and Guitiérrez, M. A. (1999). A unified framework for concrete damage and fracture models including size effects. *International Journal of Fracture*, 95:261–277.

De Haan, L. (1984). A spectral representation for max-stable processes. *The Annals of Probability*, 12:1194–1204.

Eckert, N., Baya, H., and Deschâtres, M. (2010a). Assessing the response of snow avalanche runout altitudes to climate fluctuations using hierarchical modeling: application to 61 winters of data in France. *Journal of Climate*, 23(12):3157–3180.

Eckert, N., Coleou, C., Castebrunet, H., Deschatres, M., Giraud, G., and Gaume, J. (2010b). Cross-comparison of meteorological and avalanche data for characterising avalanche cycles: The example of december 2008 in the eastern part of the french alps. *Cold Regions Science and Technology*, 64(2):119–136.

Eckert, N., Deschâtres, M., Bonnefoy, M., and Rapin, F. (2009). La crue avalancheuse de décembre 2008 dans les alpes françaises : Quelques éclairages fournis par l'epa et autres dispositifs gérés par le cemagref. Technical report, Cemagref, TR RIVAGE.

Eckert, N., Gaume, J., and Castebrunet, H. (2011). Using spatial and spatial-extreme statistics to characterize snow avalanche cycles. In *Procedia Environmental Sciences*, volume 7, pages 224–229.

Eckert, N., Keylock, C., Bertrand, D., Parent, E., Faug, T., Favier, P., and Naaim, M. (2012). Quantitative risk and optimal design approaches in the snow avalanche field: Review and extensions. *Cold Regions Science and Technology*, 79-80:1–19.

Eckert, N., Naaim, M., and Parent, E. (2010c). Long-term avalanche hazard assessment with bayesian depth-averaged propagation model. *Journal of Glaciology*, 56:563–583.

Eckert, N., Parent, E., and Belanger, L. (2007a). Hierarchical modelling for spatial analysis of the number of avalanche occurrences at the scale of the township. *Cold Regions Science and Technology*, 50:97–112.

Eckert, N., Parent, E., Faug, T., and Naaim, M. (2008a). Optimal design under uncertainty of a passive defense structure against snow avalanches: from a general Bayesian framework to a simple analytical model. *Natural Hazard and Earth System Sciences*, 8(5):1067–1081.

Eckert, N., Parent, E., Kies, R., and Baya, H. (2010d). A spatio-temporal modelling framework for assessing the fluctuations of avalanche occurrence resulting from climate change: application to 60 years of data in the northern French Alps. *Climatic change*, 101(3-4):515–553.

Eckert, N., Parent, E., Naaim, M., and Richard, D. (2008b). Bayesian stochastic modelling for avalanche predetermination: from a general system framework to return period computations. *Stochastic Environmental Research and Risk Assessment*, 22:185–206.

Eckert, N., Parent, E., and Richard, D. (2007b). Revisiting statistical-topographical methods for avalanche predetermination: Bayesian modelling for runout distance predictive distribution. *Cold Regions Science and Technology*, 49:88–107.

Ellingwood, B. R. (2001). Earthquake risk assessment of building structures. *Reliability Engineering and System Safety*, 74:251–262.

Embrechts, P., Klüppelberg, C., and Mikosch, T. (1997). *Modelling extremal events for insurance and finance*. Springer Verlag.

Faivre, R., Iooss, B., Mahévas, S., Makowski, D., and Monod, H. (2013). *Analyse de sensibilité et exploration de modéles. Application aux sciences de la nature et de l'environnement.*

Faug, T. (2004). *Simulation sur modèle réduit de l'influence d'un obstacle sur un écoulement à surface libre Application aux ouvrages de protection contre les avalanches de neige*. PhD thesis, Université Joseph Fourier.

Faug, T., Chanut, B., Beguin, R., Naaim, M., Thibert, E., and Baroudi., D. (2010). A simple analytical model for pressure on obstacles induced by snow avalanches. *Ann. Glaciol.*, 51(54):1–8.

Faug, T., Gauer, P., Lied, K., and Naaim, M. (2008). Overrun length of avalanches overtopping catching dams: Cross-comparison of small-scale laboratory experiments and observations from full-scale avalanches. *Journal of Geophysical Research F: Earth Surface*, 113(3).

Faug, T., Naaim, M., Bertrand, D., Lachamp, P., and Naaim-Bouvet, F. (2003). Varying dam height to shorten the run-out of dense avalanche flows: developing a scaling law from laboratory experiments. *Surveys in Geophysics*, 24(5/6):555–568.

Faug, T., Naaim, M., and Naaim-Bouvet, F. (2004a). An equation for spreading length, centre of mass and maximum run-outs shortenings of avalanche flows by obstacle. *Cold Regions Science and Technology*, 39(2/3):141–151.

Faug, T., Naaim, M., and Naaim-Bouvet, F. (2004b). Experimental and numerical study of granular flow and fence interaction. *Annals of Glaciology*, 38:135–138.

Favier, P., Bertrand, D., Eckert, N., and Naaim, M. (2014a). A reliability assessment of physical vulnerability of reinforced concrete walls loaded by snow avalanches. *Natural Hazards and Earth System Sciences*, 14:689–704.

Favier, P., Eckert, N., Bertrand, D., and Naaim, M. (2014b). Sensitivity of avalanche risk to vulnerability relations. *Cold Regions Science and Technology*, Accepted.

Favre, R., Jaccoud, J., Burdet, O., and Charif, H. (1990). *Dimensionnement des structure en béton - Aptitude au service et éléments de structures*. Presses Polytech. et Univ. Romandes.

Fisher, R. A. (1922). On the mathematical foundations of theoretical statistics. *Philosophical Transactions of the Royal Society of London. Series A, Containing Papers of a Mathematical or Physical Character*, 222:309–368.

Fuchs, S. and Bründl, M. (2005). Damage potential and losses resulting from snow avalanches in settlements in the canton of grisons, switzerland. *Natural Hazards*, 34:53–69.

Fuchs, S., Thoeni, M., McAlpin, M. C., Gruber, U., and Bruendl, M. (2007a). Avalanche hazard mitigation strategies assessed by cost effectiveness analyses and cost benefit analyses - evidence from Davos, Switzerland. *Nat Hazards*, 41(1):113–129.

Fuchs, S., Thoeni, M., McAlpin, M. C., Gruber, U., and Bruendl, M. (2007b). Avalanche hazard mitigation strategies assessed by cost effectiveness analyses and cost benefit analyses - evidence from Davos, Switzerland. *Nat Hazards*, 41(1):113–129.

Gauer, P., Issler, D., Lied, K., Kristensen, K., Iwe, H., Lied, E., Rammer, L., and Schreiber, H. (2007). On full-scale avalanche measurements at the ryggfonn test site. *Cold Reg Sci Technol*, 49:39–53.

Gauer, P., Kronholm, K., Lied, K., Kristensen, K., and Bakkehøi, S. (2010). Can we learn more from the data underlying the statistical α-β model with respect to the dynamical behavior of avalanches? *Cold Regions Science and Technology*, 62:42–54.

Gaume, J., Chambon, G., Eckert, N., and Naaim, M. (2012). Relative influence of mechanical and meteorological factors on avalanche release depth distributions: An application to french alps. *Geophysical Research Letters*, 39(12).

Gaume, J., Eckert, N., Chambon, G., Naaim, M., and Bel, L. (2013). Mapping extreme snowfalls in the french alps using max-stable processes. *Water Resources Research*, 49(2):1079–1098.

Givry, M. and Perfettini, P. (2004). Construire en montagne : la prise en compte du risque d'avalanche (french). Technical report, Ministère de l'écologie et du développement durable.

Hakonardottir, K. M. (2000). Retarding effects of braking mounds: Granular flows. Master's thesis, School of Mathematics, University of Bristol.

Hendrikx, J. and Owens, I. (2008). Modified avalanche risk equations to account for waiting traffic on avalanche prone roads. *Cold Regions Science and Technology*, 51(2-3):214–218.

Issler, D. (1997). Modelling of snow entrainment and deposition in powder snow avalanches. *Annals of glaciology*, 26:253–258.

Jansen, M. (1999). Analysis of variance designs for model output. *Computer Physics Communications*, 117:35–43.

Jarry, F. (2011). 40 ans d'accidents d'avalanches... 40 ans de prévention. *Neige et Avalanches*, 135:18–22.

Johannesson, T. and Arnalds, D. (2001). Accidents and economic damage due to snow avalanches and landslides in iceland. *Jökull*, 50:81–94.

Johansen, K. (1962). *Yield Line Theory*. Cement and Concrete Association, London, UK.

Joint Committee on Structural Safety, J. (2001). Probabilistic model code, part i-iii.

Jones, J., Wu, C., Oehlers, D., A.S. Whittaker, a. W. S., Marks, S., and Coppola, R. (2009). Finite difference analysis of simply supported rc slabs for blast loadings. *Engineering Structures*, Volume 31, Issue 12:2825–2832.

Jordaan, I. (2005). *Decisions under Uncertainty. Probabilistic Analysis for Engineering Decisions*. Cambridge University Press.

Jónasson, K., Sigurðsson, S. T., and Arnalds, D. (1999). Estimation of avalanche risk. Report No. R99001-URO, Reykjavík, Veðurstofu Íslands.

Kassem, F., Bertrand, D., Brun, M., and Limam, A. (June 16-20, 2013). Reliability analysis of reinforced concrete slab subjected to low velocity impact accounting of material damage. *11th International Conference on Structural Safety & Reliability - Columbia University - New York, NY*.

Katz, R., Parlange, M., and Naveau, P. (2002). Statistics of extremes in hydrology. *Advances in Water Resources*, 25(8-12):1287–1304.

Keylock, C. (2005). An alternative form for the statistical distribution of extreme avalanche runout distances. *Cold Regions Science and Technology*, 42(3):185–193.

Keylock, C. and Barbolini, M. (2001). Snow avalanche impact pressure - vulnerability relations for use in risk assessment. *Canadian Geotechnical Journal*, 38(2):227–238.

Keylock, C., McClung, D., and Magnusson, M. (1999). Avalanche risk mapping by simulation. *Journal of Glaciology*, 45 (150):303–314.

Kyung, H. L. and Rosowsky, D. V. (2006). Fragility analysis of woodframe buildings considering combined snow and earthquake loading. *Structural safety*, 28:289–303.

Lagaros, N. D. (2008). Probabilistic fragility analysis: A tool for assessing design rules of rc buildings. *Earthquake engineering and engineering vibration*, 7:45–56.

Lavigne, A. (2013). *Modélisation statistique régionale de l'activité avalancheuse*. PhD thesis, AgroParisTech.

Lavigne, A., Bel, L., Parent, E., and Eckert, N. (2012). A model for spatio-temporal clustering using multinomial probit regression: application to avalanche counts. *Environmetrics*, 23:522 – 534.

Leadbetter, M., Lindgren, G., and Rootzén, H. (1983). *Extremes and related properties of random sequences and processes*.

Lemaire, M. (2005). *Fiabilité des structures - Couplage mécano-fiabiliste statique*.

Leprêtre, C., Millar, A., Combescure, A., and Janet, P. (1988). Report demt 88/330. Technical report, Atomic Energy Comission, Saclay, France.

Li, Y. and Ellingwood, B. R. (2007). Reliability of woodframe residential construction subjected to earthquakes. *Structural Safety*, 29(4):294 – 307. Probabilistic Concepts in the Design of Timber Structures.

Lied, K. and Bakkehoi, S. (1980). Empirical calculations of snow-avalanche run-out distances based on topographic parameters. *Journal of Glaciology*, 26 (94):165–176.

Low, H. Y. and Hao, H. (2001). Reliability analysis of reinforced concrete slabs under explosive loading. *Structural Safety*, 23:157 – 178.

Low, H. Y. and Hao, H. (2002). Reliability analysis of direct shear and flexural failure modes of rc slabs under explosive loading. *Engineering Structures*, 24:189–198.

Lu, R., Luo, Y., and Conte, J. (1994). Reliability evaluation of reinforced concrete beams. *Structural Safety*, 14:277–298.

MacGregor, J. G., Mirza, S. A., and Ellingwood, B. (1983). Statistical analysis of resistance of reinforced and prestressed concrete members. *ACI Journal*, 80:167–176.

Maggioni, M., Caimi, A., Godone, D., Freppaz, M., Bertea, A., Cordola, M., Prola, M., Bertoglio, V., and Frigo, B. (2009). The avalanche events of december 2008 in ceresole reale (piedmont western italian alps). In *International Snow Science Workshop, Davos 2009, Proceedings*.

Maggioni, M., Gruber, U., Purves, R., and Freppaz, M. (2006). Potential release areas and return period of avalanches: is there a relation ? In *International Snow Science Workshop, 2006, Proceedings*.

Margreth, S. and Romang, H. (2010). Effectiveness of mitigation measures against natural hazards. *Cold Regions Science and Technology*, 64(2):199–207.

Margreth, S., Stoffel, L., and Wilhelm, C. (2003). Winter opening of high alpine pass roads-analysis and case studies from the swiss alps. *Cold Regions Science and Technology*, 37(3):467–482.

Mattock, A. H. (1967). Discussion of rotational capacity of reinforced concrete beams. *J. Struct. Div.*, 93(ST2):519–522.

Mavrouli, O. and Corominas, J. (2010a). Rockfall vulnerability assessment for reinforced concrete buildings. *Natural Hazards and Earth System Science*, 10(10):2055–2066.

Mavrouli, O. and Corominas, J. (2010b). Vulnerability of simple reinforced concrete buildings to damage by rockfalls. *Landslides*, 7(2):169–180.

Mazars, J. (1986). A description of micro- and macroscale damage of concrete structures. *Engineering Fracture Mechanics*, 25(5–6):729 – 737.

McClung, D. (2000). Extreme avalanche runout in space and time. *Canadian Geotechnical Journal*, 37(1):161–170.

McClung, D. (2001). Extreme avalanche runout: a comparison of empirical models. *CANADIAN GEOTECHNICAL JOURNAL*, 38:1254–1265.

McClung, D. (2003). Time arrival of slab avalanche masses. *Journal of Geophysical Research B: Solid Earth*, 108 (10):ETG 3–1 – ETG 3–11.

McClung, D. and Lied, K. (1987). Statistical and geometrical definition of snow avalanche runout. *Cold Regions Science and Technology*, 13(2):107–119.

Merz, B., Kreibich, H., Schwarze, R., and Thieken, A. (2010). Review article "assessment of economic flood damage". *Natural Hazards and Earth System Science*, 10(8):1697–1724.

Meunier, M. and Ancey, C. (2004). Towards a conceptual approach to predetermining long-return-period avalanche run-out distances. *Journal of Glaciology*, 50(169):268–278.

Millard, A. (1993). *CASTEM 2000, Manuel d'utilisation, Rapport no CEA-LAMBS 93/007*. Commissariat à l'Energie Atomique, www-cast3m.cea.fr., Saclay.

Mirza, S., Hatzinikolas, M., and J.G., M. (1979). Statistical descriptions of strength of concrete. *Journal of the Structural Division, ASCE*, 105(6):1021–1037.

Mirza, S. A. and MacGregor, J. G. (1979). Variations in dimensions of reinforced concrete members. *ASCE J Struct Div*, 105(4):751–766.

Mollon, G., Dias, D., and Soubra, A.-H. (2013). Probabilistic analyses of tunneling-induced ground movements. *Acta Geotechnica*, 8(2):181–199.

Mosley, B., Bungey, J., and Hulse, R. (2007). *Reinforced Concrete Design: to Eurocode 2*. Palgrave Macmillan (6th ed.).

Naaim, M. (1998). *Contribution to snow drift and avalanches flows modelling.* Habilitation thesis, University Joseph Fourier, Grenoble, France.

Naaim, M., Bertrand, D., Faug, T., Fuchs, S., Cappabianca, F., and Bründl, M. (2008a). Vulnerability to rapid mass movements. Technical report, Irasmos - WP4 Project no. 018412.

Naaim, M., Durand, Y., Eckert, N., and Chambon, G. (2013). Dense avalanche friction coefficients : influence of physical properties of snow. *Journal of Glaciology*, 59:771–782.

Naaim, M., Faug, T., Eckert, N., Chambon, G., Naaim, F., and Bellot, H. (2008b). Snow avalanche pressure on obstacles. In *International Snow Science Workshop, Whistler 2008, Proceedings*.

Naaim, M., Faug, T., N, E., Chambon, G., and Naaim, F. (2008c). A macroscopic formulation of the total drag coefficient of rapid shallow mass flows. *J. Geophys. Res.*

Naaim, M., Faug, T., Naaim, F., and Eckert, N. (2010). Return period calculation and passive structure design at the taconnaz avalanche path, france. *Annals of Glaciology*, 51(54):89–97.

Naaim, M., Naaim-Bouvet, F., Faug, T., and Bouchet, A. (2004). Dense snow avalanche modeling: flow, erosion, deposition and obstacle effects. *Cold regions science and technology*, 39(2):193–204.

Nassr, A., Razaqpur, A., Tait, M., Campidelli, M., and Foo, S. (2012). Single and multi degree of freedom analysis of steel beams under blast loading. *Nucl Eng Des*, 242:63–77.

Naveau, P., Guillou, A., Cooley, D., and Diebolt, J. (2009). Modelling pairwise dependence of maxima in space. *Biometrika*, 96(1):1–17.

Naveau, P., Toreti, A., Smith, I., and Xoplaki, E. (2014). A fast nonparametric spatio-temporal regression scheme for generalized pareto distributed heavy precipitation. *Water Resources Research*, 50(5):4011–4017.

Newmark, N. (1959). A method of computation for structural dynamics. *ASCE Journal of Engineering Mechanics Division*, 85:67–94.

Ngo, T., Mendis, P., Gupta, A., and Ramsay, J. (2007). Blast loading and blast effects on structures - an overview. *Electronic Journal of Structural Engineering*, 7:76–91.

Nicot, F. (2010). *Neige, paravalanches et constructions*.

Nielsen, M. and Hoang, L. (2011). *Limit Analysis and Concrete Plasticity*. CRC Press, Boca Raton, FL, USA.

Nolde, N. and Joe, H. (2013). A bayesian extreme value analysis of debris flows. *Water Resources Research*, 49(10):7009–7022.

Ousset, I., Bertrand, D., Brun, M., Limam, A., and Naaïm, M. (2013). Vulnerability of a reinforced concrete wall loaded by a snow avalanche: experimental testing and fem analysis. *International Snow Science Workshop Grenoble*, Chamonix Mont-Blanc - 2013.

Ousset, I., Bertrand, D., Carjaval, C., Limam, A., and Naaim, M. (2014). Etude fiabiliste d'une dent déflectrice en béton armé sollicitée par une avalanche de neige dense. In *8èmes Journées Fiabilité des Matériaux et des Structures*.

Papathoma-Köhle, M., Kappes, M., Keiler, M., and Glade, T. (2010). Physical vulnerability assessment for alpine hazards: state of the art and future needs. *Natural Hazards*, pages 1–36.

Papathoma-Köhle, M., Kappes, M., Keiler, M., and Glade, T. (2011). Physical vulnerability assessment for alpine hazards: state of the art and future needs. *Natural Hazards*, 58(2):645–680. 10.1007/s11069-010-9632-4.

Papathoma-Köhle, M., Keiler, M., Totshing, R., and Glade, T. (2012). Improvement of vulnerability curves using data from extreme events: debris flow event in south tyrol. *Natural Hazards*, 64 (3):2083–2105.

Parent, E. and Bernier, J. (2003a). Encoding prior experts judgments to improve risk analysis of extreme hydrological events via pot modeling. *Journal of Hydrology*, 283(1-4):1–18.

Parent, E. and Bernier, J. (2003b). Encoding prior experts judgments to improve risk analysis of extreme hydrological events via pot modeling. *Journal of Hydrology*, 283(1-4):1–18.

Parent, E. and Bernier, J. (2007). *Le raisonnement bayésien: modélisation et inférence*. Springer.

Pasanisi, A., Keller, M., and Parent, E. (2012). Estimation of a quantity of interest in uncertainty analysis: Some help from bayesian decision theory. *Reliability Eng. System Safety*, 100:93–101.

Peyras, L., Carvajal, C., Felix, H., Bacconnet, C., Royet, P., Becue, J.-P., and Boissier, D. (2012). Probability-based assessment of dam safety using combined risk analysis and reliability methods-application to hazards studies,. *Euro. J. Environ. Civil Eng.*, 16:795–817.

Pickands, J. (1975). Statistical inference using extreme order statistics. *The Annals of Statistics*, 3(1):pp. 119–131.

Raiffa, H. (1968). *Decision Analysis: Introductory Lectures on Choices Under Uncertainty*. Addison-Wesley.

Ravanat, X., Bellot, H., Ousset, F., Thibert, E., and Naaim, M. (2012). Lautaret avalanche test site: outcomes from the 11th april 2012 event. In *Proceedings, 2012 International Snow Science Workshop, Anchorage, Alaska, p. 622-627*.

Resnick, S. (1987). *Extreme Values, Point Processes and Regular Variation*. Springer Verlag.

Rheinberger, C., Bründl, M., and Rhyner, J. (2009). Dealing with the white death: Avalanche risk management for traffic routes. *Risk Analysis*, 29(1):76–94.

Rietsch, T., Naveau, P., Gilardi, N., and Guillou, A. (2013). Network design for heavy rainfall analysis. *Journal of Geophysical Research D: Atmospheres*, 118(23):13075–13086.

Roudnitska, S. (2013). Retour sur l'avalanche de saint-françois-longchamp, un an après. *Neige et Avalanches*, 141:12–15.

Salm, B., Burkard, A., and Gubler, H. (1990). Berechnung von fliesslawinen, eine anleitung für praktiker mit beispielen. Tech. Rep. No. 47, Eidgenössisches Institut für Schnee -und Lawinenforschung, Davos.

Saltelli, A., Annoni, P., Azzini, I., Campolongo, F., Ratto, M., and Tarantola, S. (2010). Variance based sensitivity analysis of model output. design and estimator for the total sensitivity index. *Computer Physics Communications*, 181:259–270.

Saltelli, A., Tarantola, S., Campolongo, F., and Ratto, M. (2004). *Sensitivity analysis in practice: A guide to assessing scientific models.*

Savage, S. and Hutter, K. (1989). The motion of a finite mass of granular material down a rough incline. *Journal of Fluid Mechanics*, 199:177–215.

Sawczuk, A. and Jaeger, T. (1963). *Grenztragfdhigkeits-Theorie der Flatten.* Springer-Verlag.

Schaer, M. and Issler, D. (2001). Particle densities, velocities and size distributions in large avalanches from impact-sensor measurements. *Ann. Glaciol.*, 32:321–327.

Schlather, M. and Tawn, J. (2003). A dependence measure for multivariate and spatial extreme values: Properties and inference. *Biometrika*, 90(1):139–156.

Schläppy, R., Eckert, N., Jomelli, V., Stoffel, M., Grancher, D., Brunstein, D., Naaim, M., and Deschatres, M. (2014). Validation of extreme snow avalanches and related return periods derived from a statistical-dynamical model using tree-ring techniques. *Cold Regions Science and Technology*, 99:12–26.

Schwendtner, B., Papathoma-Köhle, M., and Glade, T. (2013). Risk evolution: How can changes in the built environment influence the potential loss of natural hazards. *Natural Hazards and Earth System Sciences*, 13:2195–2207.

Sobol, I. (2001). Global sensitivity indices for nonlinear mathematical models and their monte carlo estimates. *Mathematics and Computers in Simulation*, 55:271–280.

Sovilla, B., Schaer, M., Kern, M., and Bartelt, P. (2008a). Impact pressures and flow regimes in dense snow avalanches observed at the vallée de la sionne test site. *J. Geophys. Res.*, 113.

Sovilla, B., Shaer, M., and Rammer, L. (2008b). Measurements and analysis of full-scale avalanche impact pressure at vallée de la sionne test site. *Cold Reg Sci Technol*, 51(2-3):122–137.

Spence, R. J., Kelman, I., Baxter, P. J., Zuccaro, G., and Petrazzuoli, S. (2005). Residential building and occupant vulnerability to tephra fall. *Natural Hazards and Earth System Sciences*, 5:477–494.

Straub, D. and Gret-Regamey, A. (2006). A Bayesian probabilistic framework for avalanche modelling based on observations. *Cold Reg. Sci. Tech.*, 46(3):192–203.

Sudret, B., Mai, C., and Konakli, K. (2014). Computing seismic fragility curves unsing non-parametric representations. *Earthquake engineering and structural dynamics*.

Thibert, E., Baroudi, D., Limam, A., and Berthet-Rambaud, P. (2008). Avalanche impact pressure on an instrumented structure. *Cold Regions Science and Technology*, 54:206–215.

Val, D., Bljuger, F., and Yankelevsky, D. (1997). Reliability evaluation in nonlinear analysis of reinforced concrete structures. *Structural Safety*, 19(2):203–217.

Van Danzig, D. (1956). Economic decision problems for flood prevention. *Econometrica*, 24:276–287.

Von Neumann, J. and Morgenstern, O. (1953). *Theory of Games and Economic Behaviour*. Princeton University Press.

Wand, M. and Jones, M. (1995). *Kernel smoothing*.

Wang, T. and Hsu, T. T. (2001). Nonlinear finite element analysis of concrete structures using new constitutive models. *Computers & Structures*, 79(32):2781 – 2791.

Wilhelm, C. (1997). Wirtschaftlichkeit im lawinenschutz. methodik und erhebungen zur beurteilung von schutzmassnahmen mittels quantitativer risikoanalyse und ökonomischer bewertung. *Mitt.Eidgenöss. Inst. Schnee- Lawinenforsch*, 203:288–293.

Wilhelm, C. (1998). Quantitative risk analysis for evaluation of avalanche protection projects. In *Norwegian Geotechnical Institute, Norway*.

APPENDIX A

Résumé étendu

Contexte

Les avalanches de neige sont une menace pour les populations de montagne. En particulier, tous les ans, on dénombre des victimes parmi les pratiquants de sports d'hiver. Lors des hivers rigoureux des années 1970, 1999 et 2008 en France, des victimes et des dommages matériels importants sont également à déplorer. Ces dommages sont observés jusqu'en fond de vallée, lá où se trouvent les principaux enjeux exposés. Pour ces avalanches extrêmes arrivant en fond de vallée différentes stratégies de protection peuvent être employées. On peut citer comme exemples, la prévention à court terme *via* la mise en alerte de la population, ou alors la gestion de la crise *via* l'évacuation de la population ou encore le déclenchement préventif de l'aléa. Cependant, l'imprévisibilité et la brutalité d'une avalanche rendent cette option difficile en pratique. La gestion du développement du territoire passe avant tout par la vision à long terme : par exemple étendre l'urbanisation dans les zones où le risque est acceptable pour la population ou encore choisir et optimiser les mesures de protection à mettre en place (digues, tas freineurs, etc.). Cette étape de zonage et d'élaboration de mesures de protection se basent sur la quantification du risque à long terme.

Actuellement, celle-ci est généralement restreinte à l'étude de l'aléa de référence. En France, c'est l'estimation de l'avalanche centennale qui prime. En Europe, d'autres seuils sont employés. Aucune méthode systématisée ou normalisée d'estimation de ces événements de période de retour donnée, *i.e.* l'avalanche atteignant l'abscisse centennale pour la France, n'est prédominante. En pratique, les cartes des plans de prévention des risques naturels utilisées comme délimitation des zones à risque sont faites par le croisement de données historiques, d'analyses de terrain, de photos aériennes, de modélisations numériques et/ou statistiques, de jugements d'experts, *etc.* Un pays européen fait figure d'exception : l'Islande a opté pour une approche intégrée du risque, prenant en compte non seulement

l'étude de l'aléa (fréquence, intensité) mais aussi la vulnérabilité des personnes à l'intérieur de bâtiments potentiellement exposés.

La recherche appliquée en ingénierie paravalancheuse pour l'estimation du risque à long terme se focalise sur deux problématiques majeures : comment améliorer l'estimation des avalanches de période de retour élevée, et quels sont les méthodes qui pourraient améliorer le zonage afin d'augmenter la sécurité des personnes et pallier aux défauts découlant de l'utilisation de méthodes purement "aléa-centrées". Cette thèse tente de répondre à la deuxième problématique. Nous proposons de nouvelles approches pour tout d'abord construire des courbes de fragilité caractérisant la vulnérabilité de l'enjeu considéré *via* sa probabilité de défaillance, et ensuite effectuer des calculs de risque dans un cadre intégré utilisant les courbes de fragilité déduites à l'échelle de l' enjeu. Enfin, nous avons essayer de répondre au probléme de l'optimisation des moyens de protections à partir d'outils issus de la théorie décisionnelle.

Les objectifs de cette thèse sont multiples et sont présentés en détails dans la suite de cette partie introductive. Par la suite, chacun des chapitres sera détaillé dans une section dédiée. Les deux premiers chapitres s'intéressent à la mise en place de courbes de fragilité avec différents modèles mécaniques et différentes méthodes fiabilistes. Les deux derniers chapitres cherchent à quantifier la sensibilité du risque intégré. La sensibilité est d'abord étudiée par rapport aux courbes de vulnérabilité précédemment développées, puis par rapport au modèle d'aléa (distribution des distances d'arrêt basée sur la théorie statistique des valeurs extrêmes et deux lois d'interactions fluide/structure). Une conclusion est proposée afin de clore ce résumé étendu du travail effectué.

Chaque chapitre peut être lu indépendamment des autres ; le premier est publié dans le journal international *Natural Hazards and Earth System Sciences*, le troisième est en cours de finalisation pour publication dans le journal international *Cold Regions Science and Technology* et les deux autres ont vocation à être soumis prochainement pour publication.

Objectifs

Transposer et assembler

Autant pour les risques anthropiques que pour les risques naturels, des méthodes ont été développées de manière rigoureuse et validées sur de nombreux cas. Un des objectifs a été d'adapter ces approches au cadre risque avalanche dans lequel s'insère ce travail de recherche. Ce dernier s'intéresse à l'étude des "briques élémentaires" permettant le calcul de risque. Des améliorations notables ont été proposées d'une part pour la description de vulnérabilité des enjeux et d'autres part pour la description de l'aléa avalancheux. En outre, un autre objectif est l'utilisation de ces nouveaux outils de calcul de risque dans le

cadre de la théorie de la décision afin de rechercher les structures de protection optimales.

Mettre à profit les techniques de génie civil

Le domaine du génie civil fournit des modèles mécaniques plus ou moins raffinés permettant de décrire les dommages occasionnés par un champ de pression sur une structure. Des structures en béton armé ont été étudiées. Le champ d'étude de la fiabilité permet de calculer la fragilité des structures fournissant la probabilité de survenue de ces dommages en fonction d'une sollicitation donnée. Ce cadre nous permet de pallier aux limites des approches actuelles de mise en place de courbe de vulnérabilité aux avalanches. Celles-ci restent essentiellement basées sur des approches empiriques. Ces approches reposent sur des données rares et imparfaites issues de cas réels bien documentés. En particulier, nous avons chercher à proposer une alternative à ce type de courbes de vulnérabilité en proposant des jeux systématisés de courbes de fragilité de structures en béton armé chargées par une avalanche pour une très large gamme de type de structures définies par leurs conditions aux limites.

Mieux évaluer le risque pour les personnes et les biens

Les courbes de fragilité sont déjà largement utilisées en génie parasismique. Leur utilisation commence pour les aléas gravitaires, notamment les éboulements rocheux. Nous avons cherché à mettre en place des courbes de fragilité aux avalanches de structures en BA pouvant permettre de mieux évaluer les risques matériels et humains. Il est ainsi possible de connaître dans quelle mesure le développement de plusieurs courbes de fragilité fournissant la probabilité d'atteinte d'un état limite donné peut améliorer le calcul de risque. D'autre part, la vulnérabilité des habitants est directement liée à la vulnérabilité des structures dans lesquelles ils se trouvent. La recherche de liens quantitatifs reliant la vulnérabilité structurelle à la vulnérabilité humaine est de ce fait un champ d'étude pertinent. L'objectif suivant est donc de quantifier les intérêts liés au développement de plusieurs courbes de fragilité. Le risque et des bornes pour le risque peuvent être calculés, d'abord pour une structure (risque de destruction ou d'atteinte d'un état donné) puis pour la vie humaine (risque de mort). L'apport de tels outils est particulièrement important pour le praticien en charge de la prise de décision.

Améliorer la modélisation de l'aléa via la statistique des extrêmes

L'un des sous-modèles influents du calcul de risque est le modèle d'aléa, et en particulier son comportement au niveau des queues de distribution qui vont induire des dommages sur les éléments à risque étudiés. Dans cette thèse nous avons utilisé des modèles de valeurs

extrêmes appliqués aux données d'avalanches. Par rapport aux modèles d'ingénierie classique, cela évite de restreindre le modèle d'aléa à l'étude de quelques scénarios rares et donc de disposer d'une distribution plus complète et réaliste. Par rapport aux méthodes de calcul de risque utilisant un modèle numérique de propagation, un effort a été fait ici pour utiliser ces modèles de manière analytique, de manière à disposer de relations simples et rapides à mettre en œuvre. L'objectif était de voir le potentiel d'application de tels outils tout en analysant leur limite d'utilisation (difficulté d'inférence, réalisme des périodes de retour prédites, etc.). En pratique, il est important de connaître le bénéfice à utiliser de tels modèles statistiques pour le calcul de risque et à l'intérieur du modèle décisionnel en découlant.

Améliorer l'interaction fluide/structure dans le calcul décisionnel

Enfin, le dernier objectif était d'exploiter les développements récents semi-empiriques de relations d'interactions fluides/structures. Ces relations permettent de prendre en compte l'effet de la structure de protection sur la distribution de l'aléa. Dans la littérature, plusieurs lois d'interactions ont été établies, notamment en fonction de la nature de l'avalanche dévalant la pente (vitesse, taux d'humidité, etc.). De ce fait, le risque peut être calculé en utilisant la distribution originale d'aléa ou celle modifiée par la prise en compte de l'effet de la structure sur l'intensité de l'aléa. En faisant directement intervenir les paramètres structurels dans le calcul de risque, nous avons la possibilité de poursuivre le calcul jusqu'à la recherche de la structure minimisant les pertes matérielles et humaines. Nous cherchons à comprendre comment, dans ce cadre, le choix d'une loi d'interaction plutôt qu'une autre influence la sortie décisionnelle.

Chapitre 2 : Obtention de courbes de fragilité de structures en béton armé *via* une approche fiabiliste couplée avec des modéles mécaniques classiques de l'ingénierie civil

Des modèles utilisés classiquement en bureau d'études basés sur la théorie des plaques et sur la théorie des lignes de ruptures sont utilisés. Ils ont l'avantage de fournir une bonne approximation de la réponse mécanique de la structure en des temps de calculs très courts. L'obtention des courbes de fragilité est effectuée à partir de la caractérisation de différents états de dommages de la structure. Ces derniers permettent de définir les critères de défaillance pour le calcul de la probabilité de défaillance qui, compte tenu des temps de calcul du modèle déterministe, est effectué avec la méthode de Monte Carlo. Différentes techniques de propagation des incertitudes permettent de quantifier le poids des différents paramètres ainsi que l'influence des différentes hypothèses concernant la modélisation probabiliste de la distribution des variables d'entrée. Les indices de Sobol

ont été utilisés dans le cas de variables d'entrées indépendantes.

Chapitre 3 : Obtention de courbes de fragilité *via* des approches fiabilistes couplées à des modèles enrichit de type masse-ressort ou éléments finis

L'objectif de cette partie est la mise en place d'un modèle restant simple mais gardant une bonne représentation de la physique et l'optimisation des méthodes d'approximation de la fragilité. Ainsi, l'approche précédente est étendue à la construction de modèles numériques plus sophistiqués et permettant de tenir compte d'un plus grands nombre de processus physiques comme le développement de potentiels effets dynamiques. Les deux modèles mécaniques sont basés respectivement sur une approche masse-ressort et une approche éléments finis. Des comportements mécaniques plus réalistes de la structure chargée par une avalanche peuvent être ainsi obtenus tout en gardant un temps de calcul raisonnable. Quant bien même ces temps de calculs restent faibles, leur implémentation dans un cadre fiabiliste nécessite d'avoir recours a des méthodes de calcul de la probabilité de défaillance qui réduisent le nombre d'appels au code déterministe. Ainsi, quatre méthodes sont proposées et comparées.

Chapitre 4 : Sensibilité du calcul de risque aux relations de fragilité

Dans la troisième partie, nous saisissons l'opportunité d'avoir à disposition un large éventail de relations de fragilité pour des bâtiments en BA pour proposer de nouvelles relations de probabilité de mort de personnes à l'intérieur de ces bâtiments chargés par une avalanche. Les courbes de fragilité de bâtiments correspondent à quatre états limites ; les courbes de vulnérabilité des personnes sont issues de quatre méthodes quantitatives différentes. Ces deux séries de courbes de fragilité, pour les bâtiments et les humains, sont exploitées dans une analyse complète de sensibilité du risque au modèle de dommage. De cette manière, nous mettons en évidence l'écart qui peut exister entre le zonage basé sur l'estimation de la période de retour d'avalanches rares ou extrêmes et les seuils de risques acceptables. Nous montrons aussi combien les approches décisionnelles sont robustes à la vulnérabilité sur un cas de conception de digue paravalanche typique. Ces résultats sont particulièrement intéressants pour la pratique en ingénierie paravalanche.

Chapitre 5 : Sensibilité du calcul de risque aux distributions de l'aléa d'entrée: utilisation de la statistique des extrêmes et de deux lois d'interaction écoulement/ouvrage

En quatrième partie, nous proposons des formules de risque analytiques simplifiées basées sur la statistiques des valeurs extrêmes. Ainsi, nous effectuons la recherche du design optimal d'une digue paravalanche par un moyen rapide et efficace. Deux lois d'interactions

fluides/structures sont testées, l'une issue du calcul de dissipation d'énergie par une digue de hauteur donnée, l'autre basée sur des critères géométriques de retenue du volume de neige en amont de la digue. Une étude de sensibilité détaillée est effectuée pour évaluer l'influence des distributions statistiques choisies et les lois d'interaction écoulement/obstacle. L'importance d'une évaluation précise de la queue de distribution des dépôts d'avalanches ainsi que de la relation régissant l'interaction fluides/structures est montrée au travers de la recherche des erreurs relatives induites par l'étendue possible des modèles d'aléas considérés, notamment en terme de domaine d'attraction.

Conclusion et perspectives

Ce travail de thèse apporte de nouvelles connaissances concernant les possibilités et les limites de modélisation des "briques élémentaires" impliquées dans le calcul de risque, ainsi que leur effet sur des calculs effectués dans un cadre décisionnel. La caractérisation de la vulnérabilité des structures en béton armé impactées par des avalanches de neige a été proposée *via* l'obtention de courbes de fragilité déduites à partir de plusieurs approches. Tout d'abord, la fragilité de onze structures en béton armé, différenciées par leurs conditions aux limites, a été éstimée à partir d'approches issues de l'ingénierie civil particulièrement économes en temps de calcul. Ensuite, le raffinement des modéles déterministes a permis une meilleure description des phénomènes physiques mais engendrant des coût de calculs plus importants. Ainsi des méthodes fiabilistes alternatives ont été proposées dont les résultats sont pleinement satisfaisants. Le besoin de modèles déterministes rapides en terme de temps CPU pour le calcul de fiabilité et l'actuelle méconnaissance de la réponse mécanique des structures face à des avalanches de neige ouvrent des perspectives sur de futures études dédiées à la proposition de nouveaux modèles mécaniques. Par exemple, ces derniers permettraient de prendre en compte plusieurs modes de ruine en fonction de la structure considérée.

D'autre part, l'étude de la sensibilité du risque aux données d'entrée est, pour la pratique, intéressante et plaide pour une intensification des efforts à mieux caractériser la vulnérabilité des structures et des personnes à l'intérieur. Nous avons montré la faiblesse des approches actuelles. Les risques acceptables sont dépassés pour les abscisses légalement admises, *i.e.* centennales. L'étude analytique d'une distribution extrême de Pareto généralisée permet d'obtenir des résultats probants sur l'influence des paramètres du modèle statistique sur le risque. Une approche bayésienne pourrait prendre en compte l'incertitude de leur estimation. Cependant, l'accent sur cette thèse a été mis sur la valorisation de l'incertitude des hypothèses du problème comme un outil d'aide à la décision. Les plages de risques et le calcul d'erreurs relatifs en fonction de la décision de protection optimales révèlent l'étendue et combien une unique valeur peut être difficile à interpréter.

APPENDIX B

Article de review

Cold Regions Science and Technology 79-80 (2012) 1–19

Contents lists available at SciVerse ScienceDirect

Cold Regions Science and Technology

journal homepage: www.elsevier.com/locate/coldregions

Quantitative risk and optimal design approaches in the snow avalanche field: Review and extensions

N. Eckert [a,*], C.J. Keylock [b], D. Bertrand [c], E. Parent [d], T. Faug [a], P. Favier [a,c], M. Naaim [a]

[a] IRSTEA, UR ETGR, 38 402 Saint Martin d' Hères, France
[b] Department of Civil and Structural Engineering, Mappin Street, University of Sheffield, S1 3JD, UK
[c] INSA de Lyon, L.G.C.I.E., Laboratoire de Génie Civil en Ingénierie Environnementale, 69100, Villeurbanne cedex, France
[d] Equipe MORSE, UMR 518 INRA-AgroParisTech, 16 rue C Bernard, 75005, Paris, France

ARTICLE INFO

Article history:
Received 20 May 2011
Accepted 8 March 2012

Keywords:
Snow avalanche risk analysis
Vulnerability
Formal risk framework
Risk zoning
Decision theory
Optimal design
Uncertainty

ABSTRACT

Standard engineering procedures, such as adopting high return periods as reference events, are a simplified means of handling the complex and multivariate nature of snow avalanches. Furthermore, such methods do not explicitly take into account the elements at risk and/or possible budgetary constraints. In recent years, many authors from a variety of fields have tried to overcome these limitations with quantitative risk evaluations including cost–benefit analyses. Their proposals are based on different modelling assumptions, and often on different definitions for certain important concepts including scenarios, vulnerability relations and time effects. The first goal of this paper is to propose a state of the art, and to discuss the common points, advantages and drawbacks of the various proposals within a unified formal framework based on decision theory. Most of the applications already in use concern long term risk assessment in land use planning and traffic road regulation, but some potential also exists for short term problems including risk assessment to back-country skiing. In a second time, new extensions of a simple decisional model for the optimal design of an avalanche dam are proposed to illustrate the key point of the place of uncertainty in risk analyses. Finally, to stimulate further research efforts, other important outlooks including computational issues, multivariate optimal design and measures of risk alternative to the standard expected loss minimisation are discussed.

1. Introduction

Long term avalanche hazard assessment is generally based on high return period reference events. For the design of a passive defence structure, several variables such as impact pressure, flow depth and snow volume must be considered whereas only univariate random variables show a one-to-one correspondence between a return period and an exceedence probability (Ancey et al., 2004; Eckert et al., 2007a). This difficulty can be somewhat overcome by considering different combinations of variables corresponding to the same return period, see Naaim et al. (2010) for an example of the design of a complex avalanche defence structure using a bivariate analysis of volumes and Froude numbers. However, such an approach, common in structural engineering, remains hard to implement in practice when the variables to be considered are numerous. Furthermore, for hazard zoning, return-period-based approaches are even more problematic. Indeed, two return periods derived from runout distances and impact pressures are generally retained (Salm et al., 1990), but the return period of the reference event considered is then somewhat undefined from the perspective of the runout-pressure joint distribution. This all indicates that the multivariate nature of snow avalanche hazard creates difficulties when trying to use legal thresholds such as the 100 year return period in practice.

Similarly, in avalanche forecasting, a high danger can have several origins: a generalised high probability of release of small natural avalanches, a more localised high probability of release of major natural avalanches, a high probability of human triggers due to a weak layer with a large spatial extent…, etc. The raw avalanche danger, generally expressed on a 1–5 scale, is therefore always completed by a more detailed bulletin that makes precise the exact nature of the threat. This clearly implies that, in short term hazard assessment also, hazard is too complex to be reduced to a single quantity that can be used for taking decisions such as closing ski tracks without interpretation.

Cappabianca et al. (2008) list other important reasons that make hazard-oriented approaches somewhat insufficient to quantify avalanche risk. First, they do not consider the elements at risk, which makes it impossible to compare the level of exposure of different mountain communities to avalanche hazard, and of a given mountain community to different natural hazards such as debris flows,

* Corresponding author. Tel.: +33 476762822.
E-mail address: nicolas.eckert@irstea.fr (N. Eckert).

0165-232X/$ – see front matter © 2012 Elsevier B.V. All rights reserved.
doi:10.1016/j.coldregions.2012.03.003

and rock falls. Second, hazard-oriented approaches do not allow comparison between different mitigation strategies such as land use planning policies, temporary evacuations or construction of permanent defence structures. This is clearly not adapted to the current context of limited public funds which requires cost–benefit analyses of different competing solutions and a search for optimality.

Taking inspiration from other related fields such as hydrology and flood mitigation (e.g. Bernier, 2003), several authors have, over the last years, proposed formal (i.e. quantitative and model based) avalanche risk quantification procedures to overcome these limitations. The principle is to combine the model describing avalanche hazard with a quantitative assessment of its consequences for one or several elements at risk, mainly people, buildings and traffic roads. These methods are now gaining popularity among stakeholders, and take increasing importance in practice (Bründl et al., 2009). However, the definitions used and modelling assumptions made remain different from one proposal to another. Furthermore, confusion regarding certain key concepts such as scenario/decision, uncertainty/variability or stationarity/time effects remains frequent so that it may be difficult for avalanche engineers and practitioners willing to use the different proposals to understand their differences and to compare them to each other on the cases studies of interest. Finally, even when an integrated risk approach is claimed, often only one aspect of the problem is addressed, e.g. randomness in snow stability simulations (Chernouss and Fedorenko, 2001), evaluation of damage potential with respect to one or several scenarios (e.g. Fuchs and Bründl, 2005), or communication and management of organisational measures during intense avalanche cycles (Bründl et al., 2004).

The first goal of this work is therefore to propose a state of the art of the existing quantitative risk (Section 2) and optimal design (Section 3) approaches in the snow avalanche field, and to discuss their common points, advantages and drawbacks within the unified and clarified formal framework of decision theory. This might make them more accessible for Cold Regions scientists and engineers. Because the majority of recent work has been focussed towards long term risk assessment in land-use planning, and to civil engineering structures such as buildings as elements at risk, these applications provide the primary focus of this paper. However, short term and traffic road risk assessment are also considered, and potential for risk evaluation to back-country skiing and for including less material elements at risk into the analysis are discussed. Second, starting from this basis, the key point of the place of uncertainty in risk analyses is illustrated with respect to some new extensions of a simple decisional model for the optimal design of an avalanche dam (Section 4). Finally, to stimulate research efforts, possible additional developments that have great potential for developing innovative mitigation strategies are pointed out (Section 5).

2. A formal framework for quantifying avalanche risk

2.1. Formal risk framework

2.1.1. Risk as an expected damage

In the field of natural hazards, risk is generally defined by the product of hazard and vulnerability, i.e. a combination of the damageable phenomenon and its consequences. For instance, as pointed out by Barbolini et al. (2004a), this is widely adopted in the landslide community (IUGS, 1997). Also, in the avalanche field, the existence of different components to risk was already recognised and analysed by Burkard (1992). However, such a definition remains insufficiently precise for a quantitative risk assessment. Following Wald (1950)'s seminal work in statistical decision, (for a modern exposition accessible to engineers and scientists interested in applications of probability and risk, see Jordaan, 2005), the risk R_w affecting the system at risk w can be expressed as the expected damage:

$$R_w = E_y\left[\sum_{z\in w} q(z_w) z_w V(z,y)\right] = \sum_{z\in w} q(z_w) z_w \int p(y) V(z,y) dy. \quad (1)$$

Eq. (1) says that R_w is the expectation (or mathematical average), E_y, of the consequences of avalanche activity for the whole system at risk w. $p(y)$ is the local probability distribution of avalanches y. w is a set of any element or combination of elements, z_w, that may be at risk including physical factors such as persons, traffic roads, a full mountain village…, etc., and less tangible aspects such as the spirit of the inhabitants of the village or the image and aesthetics of the village. The consequences for any element z_w included in w of any avalanche y are measured by the product $z_w V(z,y)$. z_w refers to the nature and value of the considered, specific element of w. $V(z,y)$ is the vulnerability of the general type of element z to the hazard y, i.e. the damage susceptibility for any element from type z affected by the hazard y. The term $q(z_w)$ is simply a weighting factor representing the exposure of z_w, generally a fraction of time that corresponds to the probability of the element z_w to be exposed at the time of the avalanche event.

The major advantage with respect to simpler formulations of this approach is that it permits separation of what depends on the case study, i.e. identifying the different elements at risk z_w included in the studied system w, quantifying their exposures $q(z_w)$ and evaluating the local distribution of avalanche hazard $p(y)$, from what can be used for any case study involving one or several elements at risk from the type z, namely the vulnerability relation $V(z,y)$. As an example, w can be an avalanche prone area including two elements at risk, a building and a car, which have their own socio-economic value and exposure depending on local characteristics, but much more general damage susceptibilities that would be the same if they were placed in another runout area.

Eq. (1) uses the linearity of integration to take the summation outside the integral. This emphasises the dimensionless quantity $r_z = \int p(y)V(z,y)dy$, sometimes denoted the specific risk for the element z (e.g. Cappabianca et al., 2008), which depends on its damage susceptibility and on the local avalanche distribution only. Individual risk $R_z = zr_z$ which is used in risk mapping applications, see Section 2.5.1, is obtained by multiplying the specific risk by the value of the considered element. It is also obtained by posing $(\sum_{z\in w} z_{w=z})$ in Eq. (1). If a unitary element at risk is considered, the only difference with the specific risk is that the individual risk is no longer dimensionless. Finally, the total risk for the full system w is simply the sum of individual risks for each of the different elements z_w of w weighted by their exposure, i.e.:

$$R_w = \sum_{z\in w} q(z_w) R_z = \sum_{z\in w} q(z_w) z_w r_z. \quad (2)$$

2.1.2. Computations in practice

This sum of integrals R_w can rarely be computed analytically. As early shown by Keylock et al. (1999), it can however be approximated by the sum of Monte Carlo integrals $R_w \approx \sum_{z\in w} z_w q(z_w) \frac{1}{N} \sum_{k=1}^{N} V(z,y_k)$ where the y_k, $k\in[1,N]$ is a large enough sample of $p(y)$.

Summation in Eqs. (1)–(2) implies that one is able to express all of the elements z_w of the system w by the same unit. For instance, a critical point is how to take human lives into account, and compare them to pieces of equipment. Similarly, difficulties also arise if one wants to consider the less tangible elements at risk and compare them to material values. Mathematical convenience is to follow insurance techniques and to express everything in the same monetary currency. The risk is then the total expected loss for the system at risk. Alternatively, all the computations can be carried out by considering only one

kind of element at risk, for instance human lives or buildings, leading to a risk that has to be interpreted as an expected number of deaths or destroyed buildings, see Section 2.5.1.

2.1.3. Link with other well-known definitions

As noted by McClung (2005), risk definitions vary among disciplines, and none will be universally accepted. However, clear connections between the different fields can be found. For instance, in the field of statistical decision theory, risk is not considered independently from the probability model $p(y)$ or from a set of potential decisions d (for example, various levels of protection) whose socio-economical consequences on the system at risk are made explicit by writing $R_w(d,p(y))$. The function $R_w(d,p(y))$ is termed as the expected disutility of decision d under the model $p(y)$, and the definition of risk requires the additional concept of decision rule (Wald, 1950), which takes into account that only a sample, denoted y_{obs}, of past observations is available at the time of decision. Decision rules are mappings $\delta()$ between the samples of observations and the elements of the decision set such that $\mathrm{d}=\delta(y_{obs})$. This framework permits the mappings that have optimal properties (admissible rules) to be determined given that the probability model $p(y)$ might be imperfectly known because of the limited sample y_{obs} available. The statistical risk $R_w(\delta,p(y))$ is then obtained by integrating out all possible samples that can be generated by the statistical model $p(y)$ such that $R_w(\delta,p(y))=\int_{y_{obs}} R_w(\delta(y_{obs}),p(y))\times p(y_{obs})dy_{obs}$. For now, these refinements are however unfruitful, since no action on the system at risk is considered, and uncertainty regarding the hazard model $p(y)$ is neglected, so that the correspondence between a limited sample and what works to design is not yet investigated. Both points are reconsidered in Sections 3 and 4, respectively.

In avalanche engineering, a simpler risk definition is often adopted. The distribution of avalanche hazards is assumed to be reducible to a single scenario y_k, leading to:

$$R_w(y_k)=\sum_{z\in w} q(z_w)z_w V(z,y_k), \tag{3}$$

which corresponds to the total damage to be expected if the y_k event occurs. Note that Eqs. (1) and (2) are equivalent if a Dirac distribution is postulated for y, i.e. the discrete probability $p(y=y_k)=1$. However, neglecting any possible randomness of the damageable phenomenon is of course a strongly questionable simplification that should be avoided. The reason is that the risk/total loss may be highly sensitive to the hazard magnitude, i.e. may greatly increase with a small increase in avalanche runout. For example, it is shown by Fuchs and McAlpin (2005) on a case study in Switzerland, with y_k taken as the 300 year return period avalanche. The important risk increase arises from an undesirable consequence of a land use planning policy that has been based on a single reference event, so that many buildings have been constructed very close to the limit of the hazard zones. Similarly, according to Wastl et al. (2011) for a case study in Iceland, the risk to traffic on roads is directly proportional to the total length of threatened road sections, i.e. to the sum of the widths of the retained avalanche scenarios that cross the threatened road. These two examples show well that if no randomness around the possible reference scenario is considered, the obtained risk estimate cannot be robust.

Finally, in the field of human geography, a scenario approach is generally retained, but the risk equation is written with additional terms C and M representing local capacity for protective actions in time of crisis and larger mitigation measures, respectively (e.g. Wisner et al., 2004). For us, C can be included in the $q(z_w)$ and z_w terms of Eqs. (1)–(3), since, if protective actions in times of crisis are taken, they indeed contribute to restrict the number/value/exposure of the elements at risk. Furthermore, M corresponds to a particular case of the decisional setting discussed in Section 3.1.

2.2. The different bricks of the risk framework in detail

2.2.1. Stochastic avalanche modelling

The stochastic avalanche model $p(y)$ describes the variability of snow avalanches affecting the considered system. Obtaining reliable models for $p(y)$ in long term and short term hazard assessments is one of the most frequently addressed problems in the avalanche community. In short term avalanche hazard assessment, probabilistic models generally aim at evaluating the release probability or at least the avalanche danger level as a function of a set of snow and weather covariates. Classical approaches include nearest neighbours (e.g. Gassner and Brabec, 2002) and discriminant analyses (e.g. McClung and Tweedy, 1994). Spatial scale is generally a discrete grid of massifs/elevations/aspects (e.g. Durand et al., 1999; McCollister et al., 2003).

In long term avalanche hazard assessment, the proposed models are generally working at the path scale, and aim at determining the magnitude–frequency relationship in the runout zone. The dichotomy between statistical relations (Keylock, 2005; Lied and Bakkehoi, 1980; McClung and Lied, 1987) and deterministic propagation models (e.g. Bartelt et al., 1999; Naaim et al., 2004) associated with extreme value analyses of snow depths (e.g. Blanchet and Lehning, 2010) has produced controversy for some time. However, in the last few years, statistical–dynamical models have been proposed (Barbolini and Keylock, 2002; Bozhinskiy et al., 2001; Meunier and Ancey, 2004). A joint probability distribution $p(x)$ is chosen for the random vector of input variables x of the deterministic propagation model G, and fictitious avalanches are generated to reconstruct the probability distribution $p(y)=G(p(x))$. An up-to-date example derived from Eckert et al. (2010a) is given in Fig. 1. The statistical–dynamical model calibrated on the local data provides the one-to-one relation between runout distance and return period. Furthermore, for each runout distance/return period (here 10 years), the joint distribution of all other variables is evaluated conditional to its exceedence.

2.2.2. The elements at risk

The definition and analysis of the system at risk, w, is more of a social science/geography problem. It includes identifying the system, w, carefully counting the different elements at risk, determining their nature (e.g., for a building, the fabrication methods: masonry, reinforced concrete, steel structure, wood frames…, etc.) and evaluating their value z_w as well as their exposure $q(z_w)$. Note that Eq. (1) is implicitly written for independent elements. Formally, it should always be possible to define the set w such that it includes only independent elements by considering possible correlations as additional elements. Nevertheless, in practice, identifying and evaluating these dependences may be far from easy, except for simple cases, e.g. longer stays in exposed buildings because of a road closure.

Detailed studies of elements at risk can be found in the risk literature for different countries. For example, Fuchs et al. (2004, 2005) have studied in details the region of Davos, Switzerland, and Keiler (2004), the region of Galtür, Austria. In these approaches, the system at risk is delimited by considering the avalanche prone areas corresponding to the current legal hazard maps. Counting the number and type of buildings within these areas and their inhabitants leads to the total loss associated with the reference scenario, which is also called the probable maximal loss, a common insurance concept. It is obtained by setting $V(y,z)=1\,\forall z,y>0$ in Eq. (1), i.e. under the assumption of total destruction of the different elements at risk as soon as they are attained by the flow. In Keiler et al. (2005), the approach is expanded to mobile values such as cars. Over a larger spatial scale, Johannesson and Arnalds (2001) review avalanche accidents

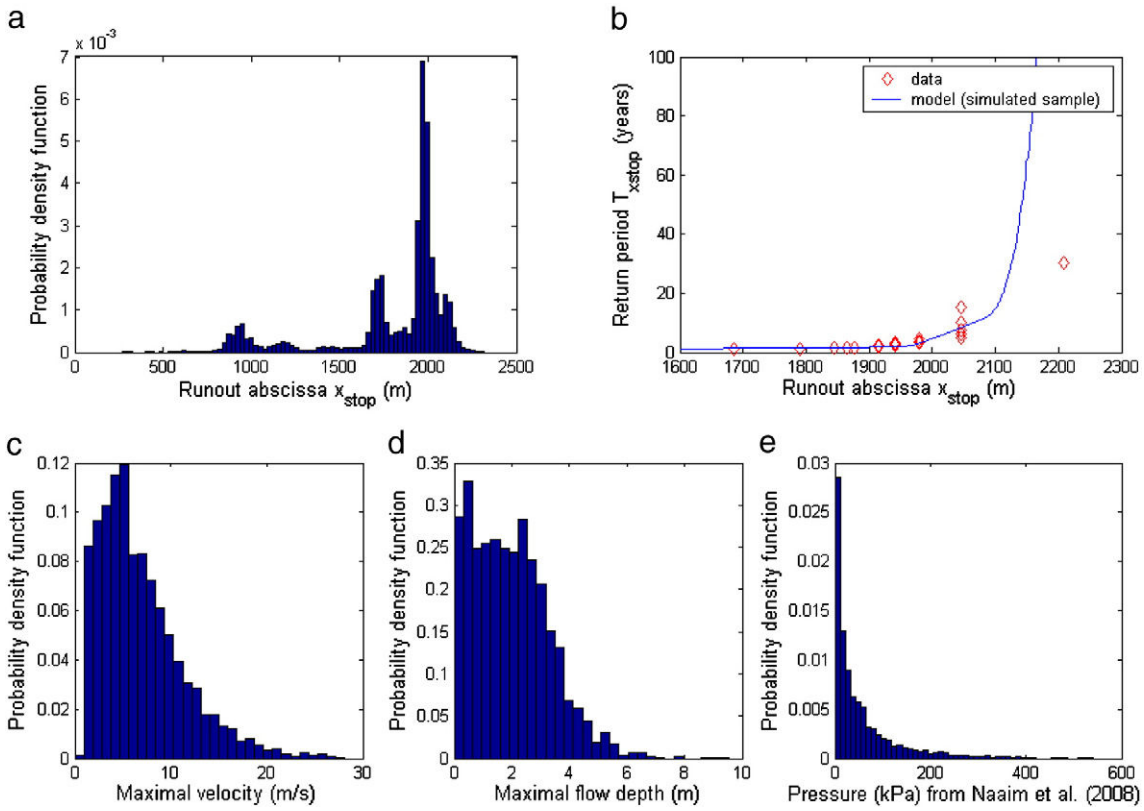

Fig. 1. Multivariate statistical–dynamical avalanche model. Avalanche model and case study from Eckert et al. (2010a): a) local runout distance distribution. b) one-to-one relation between runout distance and return period. For a runout distance corresponding to a 10 year return period, the conditional distribution of c) maximal velocity, d) maximal flow depth, and e) impact pressure computed following Naaim et al. (2008), taking the rheology of snow into account.

and economic damage in Iceland, showing the high exposure of the country to avalanche danger since its settlement.

2.2.3. Vulnerability relations

In the classical definition, where risk is a product of hazard and vulnerability, one would call vulnerability of the system w the full term $\sum_{z \in w} q(z_w) z_w V(z, y_k)$, which is in fact nothing more than the loss associated with the scenario y_k, i.e. the risk in a scenario approach. The chosen definition of vulnerability as a damage susceptibility for a given type of element z is much more restrictive but, again, has the advantage of being independent of the considered system at risk, so that it can be determined once for all. A generic representation of $V(z,y)$ for a given type of element at risk z is a non-strictly monotonically increasing function of y limited by [0,1] (Fig. 2).

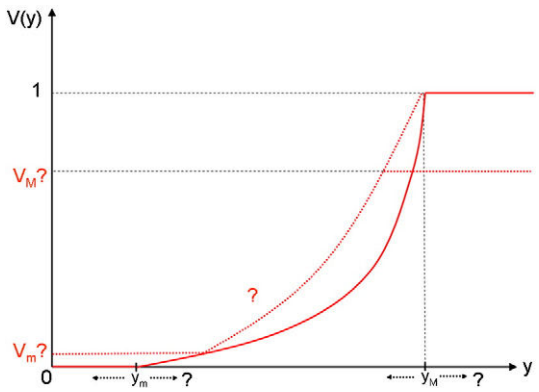

Fig. 2. Schematic representation of a vulnerability relation. "?" indicates the main uncertainty sources: the threshold values y_m and Y_M for which the damage is minimal/maximal respectively, the damage V_m and V_M corresponding to these thresholds, and the shape of the curve between y_m and Y_M.

Precursor formulations for material elements at risk were proposed by Wilhelm (1998) linking the damage potential for five building classes to avalanche pressure. For humans, Jonasson et al. (1999) first proposed relations between avalanche velocity and probability of surviving inside buildings obtained by back calculation of a few well documented catastrophic avalanches. A first review of available vulnerability relations for standalone people, buildings of different types, people inside buildings of different types, and cars has been made by Barbolini et al. (2004b). Since then, the work has been extended to different rapid mass movements (Bertrand et al., 2008; Papathoma-Köhle et al., 2011). Nevertheless, the compiled data remain rather scarce and imprecise. Furthermore, for the less tangible elements at risk, damage susceptibility has been very rarely even quantified, and only hard to validate formulations provided by social science or economical analyses are available (Fuchs, 2009).

Particular points that remain discussed and/or vary from one type of element at risk to another are indicated in Fig. 2: the existence and values of thresholds y_m and Y_M for which the damage is minimal/maximal respectively, the damage corresponding to these thresholds (i.e. $V_m = V(y_m) \geq 0$ and $V_m \leq V_M = V(Y_M) \leq 1$), and the shape of the curve between y_m and Y_M. For example, it is generally admitted that $V_M = 1$ for standalone people because the survival probability is close to zero for somebody caught by a very large and/or intense avalanches, whereas $V_M < 1$ (and equals 0.27 according to Barbolini et al., 2004b) for people inside reinforced houses. It must also be noted that, even if vulnerability is dimensionless, there may be a significant difference for a given hazard value between the damage level to a physical element and the economical damage level. For instance, a building can lose all (or nearly all) its value if it is reached by an avalanche even if it is only damaged slightly. Indeed, potential buyers may renounce the purchase because of fear of even greater avalanches, or

it may cost more to fully repair the building than to build a new one. This somewhat justifies using a probable maximal loss approach ($V(z,y)=1\forall\ y>0$) rather than employing more complex vulnerability curves when risk is measured in an economic currency.

Another great concern is the choice of the variable y. In the case of material elements at risk and/or human lives, impact pressure is most commonly used (e.g. Keylock and Barbolini, 2001). However, during the interaction of an avalanche flow with, e.g., a building, pressure evolutes in space and time, and the respective contributions of maximal pressure, total loading duration, pressure fluctuations…, etc., to the overall damage state is imperfectly understood. Second, the link between impact pressure and flow properties remains unclear (Naaim et al., 2008; Sovilla et al., 2008). Third, one variable such as pressure, is presumably not enough to estimate the damage level that may also depend on the avalanche duration, its depth…, etc. Interactions between flow and structures using full-scale measurements on real test sites (e.g. Thibert et al., 2008), small scale numerical simulations (e.g. Chanut et al., 2010; Faug et al., 2009), and laboratory tests (Caccamo et al., 2010) have provided some insights on the relation between impact forces and properties of the incoming flow. However, much work is still to be done to reach a fair and precise quantification of the basic response of an element at risk to the different space and time dependent avalanche variables.

Recently, an interesting way of progressing has been proposed: the numerical modelling of full-scale simplified civil engineering structures subjected to avalanche loading. The avalanche loading is described by a pressure field applied on the wall exposed to the avalanche, and appropriate numerical methods have been used for modelling the building technology. For instance, reinforced masonry walls have been modelled by the discrete element method (Bonnevie et al., 2003). Moreover, Bertrand et al. (2010) have used the finite element method to explore the dynamic response of reinforced concrete walls. For a given impact pressure, the damage level is formulated as the ratio between the maximum displacement over the maximum allowable displacement. Fig. 3 shows how the damage level evolves with avalanche loading for several structure configurations differing in terms of geometrical and internal mechanical parameters, leading to the corresponding vulnerability relations.

2.3. Randomness in damages and link with structural reliability

An important characteristic of the chosen formalism is that the relation $V(z,y)$ is purely deterministic, and free from any randomness or uncertainty. However, existing formulations and many papers introduce some doubt regarding the way $V(z,y)$ should be interpreted: as a fraction of the considered element z destroyed ("deterministic" point of view); or, as a probability for the entire element to be fully destroyed ("probabilistic" point of view)? This is the difference between *vulnerably curves* in the strict sense of the term, and *fragility curves*. The distinction is commonly made in the community of earthquake engineering (e.g. Ellingwood, 2001; Kyung and Rosowsky, 2006; Lagaros, 2008), but generally not in the avalanche community.

The "deterministic" point of view is appealing, because, at the scale of interactions between avalanches and elements at risk, there is presumably no "true" randomness. It is compatible with numerical evaluations of vulnerability curves, since, for a given type of element at risk, one gets a unique relation between the damage level and avalanche magnitude. However, this point of view means that, for risk computations, a realistic $V(z,y)$ relation must be determined for each very precise type of element at risk z, which is nearly impossible in practice. This is clearly shown in Fig. 3, with different vulnerability curves for slight changes in configuration and/or mechanical

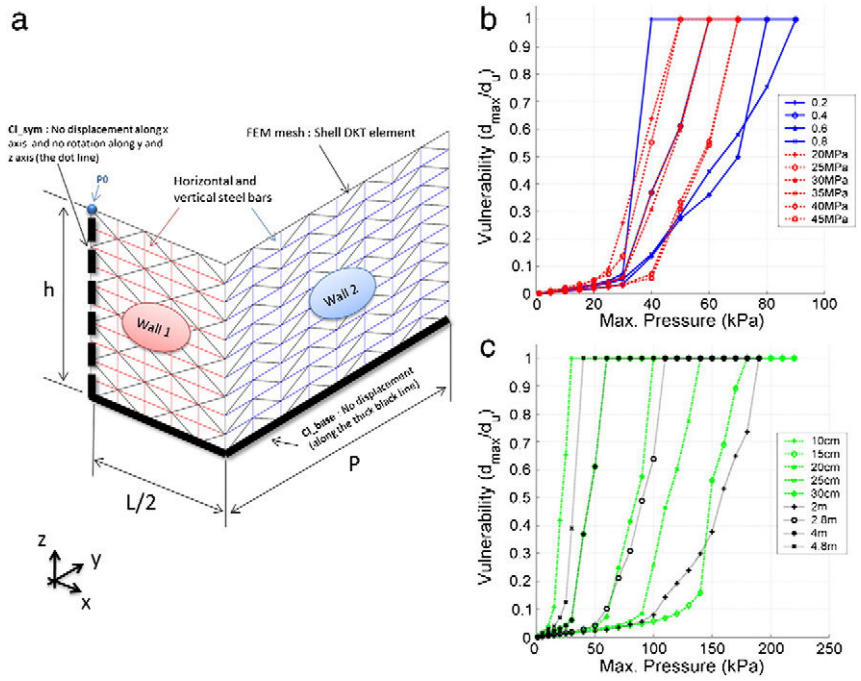

Fig. 3. Physical vulnerability defined as a damage level for reinforced a concrete civil engineering structure derived from Bertrand et al. (2010). For a given loading pressure, the damage level is the ratio between the maximum displacement and the ultimate displacement. a) Finite Element Model (FEM) of the u-shape reinforced concrete structure where shell DKT elements have been used. b) Vulnerability as a function of structure's mechanical properties: reinforcement's density (steel density) from 0.2% to 0.8% and ultimate concrete strength from 20 to 45 MPa. c) Vulnerability as a function of structure's dimensions: L (form 2m to 4.8m) and wall thickness (from 10 cm to 30 cm).

parameters of an already somewhat oversimplified civil engineering structure.

The main objective of structural reliability is to estimate the failure probability of a given system with regard to the variability of certain inputs/parameters taken as random (see, e.g., Lemaire, 2009). For instance, for civil engineering structures, many physical parameters (stability, resistance, fatigue, maximal deformation…, etc.) can be used to define the limit state separating the safe state from the failure state under a given external load, for example a damageable phenomenon. In details, under the loading y and for random inputs/parameters u, the failure probability is:

$$P(f(y) > f_l) = \int_{u_{\min}}^{u_{\max}} p(u) \times I_{\{f(y,u)>f_l\}} du, \tag{4}$$

where f is the response of the considered structure to the loading y under the input/parameter u, $p(u)$ the joint probability distribution of the inputs/parameters, f_1 the limit state of the structure, and $I_{\{f(y,u)>f_l\}}$ the 1–0 indicator function indicating if the limit state is attained or not (other notations are of more common use in the physical reliability community, see e.g. Papadrakis et al., 1996).

Considering the more general case of the element at risk z, and posing in Eq. (4) $v(z,y,u) = I_{\{f(y,u)>f_l\}}$ the "elementary" deterministic 0–1 vulnerability relation indicating if the element z is viable under the (y,u) conditions or not leads to the conditional expectancy $E_u[v(z,y,u)|y]$, which is also the probability for z to be destroyed for the loading y, taking into account the effect of the additional variability $p(u)$. Noting this conditional expectancy $V(z,y)$ clearly shows that the "probabilistic" interpretation of vulnerability curves is compatible with the one of structural reliability.

Reliability analysis has been widely used to assess the vulnerability of buildings of specific technology: reinforced concrete beams (e.g. Frangopol et al., 1996; Lu et al., 1994) or slabs (e.g. Low and Hoa, 2001), masonry infilled walls (Park et al., 2009)…, etc. Moreover, different kinds of hazards have been considered (e.g. Rizzano and Tolone, 2009; Ruiz-Garcia and Miranda, 2010), as well as combination of different hazards (Asprone et al., 2010; Lee and Mosalam, 2004). Taking inspiration from these approaches, systematic reliability analyses could be performed in the snow avalanche field for different types of elements at risk. This could complete the seldom data collected after real events, and reduce the number of configurations to be explored with regard to very precise but computationally intensive deterministic numerical approaches such as the one of Bertrand et al. (2010).

It is important to state that evaluating Eq. (1) using a "probabilistic" vulnerability curve $V(z,y)$ instead of the elementary deterministic vulnerability relation $v(z,y,u)$ defined earlier is consistent from a mathematical point of view because the specific risk $r_z = E_{u,y}[v(z,y,u)]$ coincides with $\int p(y)V(z,y)dy = E_y[E_u[v(z,y,u)|y]]$, a consequence of the rather intuitive *Theorem of Iterated Expectation*. This shows that the difference between *vulnerability* and *fragility* curves is not that important when they are used within a risk framework. Distinction will therefore not be made in the rest of the paper. This also indicates that, by averaging over the influence of certain factors *prior* to risk evaluation, "probabilistic" vulnerability relations are very useful, not only because they are valid over a larger range of situations than "deterministic" ones, but also because they reduce computations by lowering the number of factors over which integration has to be made for each case study.

However, one last point remains to be discussed: where does the randomness $p(u)$ comes from? From slightly different elements at risk subject to the same avalanche hazard y and/or from the same element associated with slightly different avalanche hazard values? For example, the probability of a building to be destroyed for a given maximal pressure may be linked to spatio-temporally different pressure signals with same maximal peak and/or to buildings apparently similar, but that differ in terms of spatial variability of their mechanical parameters. Similarly, the probability of surviving an avalanche may depend to a certain extent on avalanche characteristics which are not accounted for in the $V(z,y)$ relation, e.g. flow depth for a vulnerability relation that depends on velocity only), but also on survival chances as a function of the age/sex/fitness of the people caught.

Presumably, these two cases are not distinguished in the available data concerning catastrophic avalanches. However, even if they lead to the same risk evaluation for a given case-study, it is important to interpret them differently. Variability related to the element at risk may be taken into account into probabilistic vulnerability relations derived from a reliability analysis, with the advantages previously listed in terms of complexity and computation time reductions. On the other hand, as soon as avalanche variables are also considered, the result should be interpreted as a partial (in the sense that integration is not "finished") specific risk rather than as a vulnerability, because the assumption of a $V(z,y)$ relation independent from the system at risk and usable for any case study is then no longer fulfilled. Hence, reliability analyses devoted to evaluating vulnerability relations should concentrate on the variability of the considered elements at risk rather than on hazard variables.

2.4. Time effects

As discussed in Keiler et al. (2006), temporal changes in risk can result from changes in hazard and/or in the system at risk. In contrast, with the chosen formalism, time effects do not affect vulnerability curves, since they are defined as independent of the system at risk. Changes in hazard can be either natural (e.g. under climate change) or under human influence (e.g. because of the construction of active defence structures such as fans that reduce the release probability). Changes in the system at risk often result from changes in land use: e.g. new buildings, or reinforcement of existing ones. The construction of passive defence structures (e.g. deflecting dams) that prevent the elements at risk from being hit without affecting the release probability can affect both the hazard (because the magnitude–frequency relation is modified at certain locations of the runout zone) and the system at risk (because the number of exposed buildings may be reduced because of a smaller "maximal" runout area). Finally, the opposite case of an ageing and therefore less efficient defence structure can increase the hazard for certain elements at risk, and/or the size of the system at risk.

Practically, the question of temporal changes in the system at risk can be investigated by considering different time windows, counting the different elements included in the system at risk for each time window, associating them with their vulnerability and adding/subtracting the terms changing from one time window to another in Eq. (1). This is difficult, since it involves finding reliable data regarding the evolution of land use, but technically it is similar to evaluating the elements at risk in a stationary case. For example, in Fuchs et al. (2004), it is demonstrated that avalanche risk has substantially decreased around Davos, Switzerland, between 1950 and 2000, presumably because of enhanced active defence structures in the release zones. On the contrary, according to Keiler et al. (2006), no clear risk trend is visible in Galtür, Austria, over the same period, because the construction of new countermeasures has been compensated by the increase of the number and value of the elements at risk.

Things are more complicated for changes in hazard. Eq. (1) is written under stationarity, i.e. under the assumption that, for any time increment δt,

$$p(y|t) = p(y|t + \delta t). \tag{5}$$

However, for existing risk approaches computing risk values at shorter time scales (generally days), the avalanche model is possibly different for each time window. The important thing to note is that

the damage expectation remains nevertheless computed over the full avalanche distribution as expressed in Eq. (1) for each time window. For example, in Zischg et al. (2005a), the hazard model is taken as the daily binomial variable indicating if an avalanche occurs on the considered day or not, depending on the daily snow and weather conditions. This permits estimation of the temporal variability of risk to traffic roads and, comparing it to the long term mean risk, shows the existence of sharp and short risk peaks resulting from high snow instabilities and/or intense traffic. In Zischg et al. (2005b), similar work is done for wet snow avalanches with a fuzzy logic release model.

On the other hand, the assumption of stationarity of the hazard model is always made in existing long term avalanche risk analyses. An actualisation is then needed for obtaining converging estimates (e.g. finite total or annual risk values), which is essentially similar to considering a depreciation period for the elements at risk, see Section 3. Hence, work remains to be done to perform long term risk computations taking into account the growing evidences of recent structured changes in avalanche activity (Eckert et al., 2010b, 2010c; Keylock, 2003), and/or expected changes (Lazar and Williams, 2008; Martin et al., 2001) due to snowpack modifications under predicted climate warming (López-Moreno et al., 2009; Räisänen, 2008). The problem is that under nonstationarity, quantities of interest such as the expected mean time between two extreme avalanches of given magnitude/return period is time dependent and must be conditioned on the initial system state. The modelling task is therefore not easy, and further developments of the formal framework of Eq. (1) are required before this appealing goal can be reached.

2.5. Specific applications

2.5.1. Risk zoning

Long term risk zoning was one of the early applications of formal risk computations in the avalanche field. First methodological developments and applications were proposed in Iceland (Jonasson et al., 1999; Keylock and Barbolini, 2001; Keylock et al., 1999), with rapid introduction in the legislation and engineering practice, both in Iceland (Arnalds et al., 2004) and Italy (Barbolini et al., 2004a). Risk zoning is an individual risk approach for a person inside a building or a standalone building. The considered element z_w is generally taken as fully exposed, which implies $q(z_w) = 1$.

Proposed methods use the semi-empirical vulnerability curves relating damage susceptibility for buildings or people to pressure or velocity described in Section **2.2.3** and avalanche probability models ranging from explicit statistical models to coupled statistical–dynamical simulations. Implementation is generally performed along 1D topographical profiles, but lateral spread is sometimes taken into account, so as to evaluate the risk in the whole runout zone rather than only along the main flow path. In all cases, the results of the computations, which are generally made on an annual basis, is a long-term death rate as a function of space for people, and a long-term destruction rate for a building.

In the early work of Keylock et al., 1999 illustrated in Fig. 4, the risk computations are based on the runout ratio (McClung and Lied, 1987) statistical model for runout distance expanded to the avalanche width. Statistical distributions are formulated for different size classes of avalanches, and vulnerability is evaluated as a death

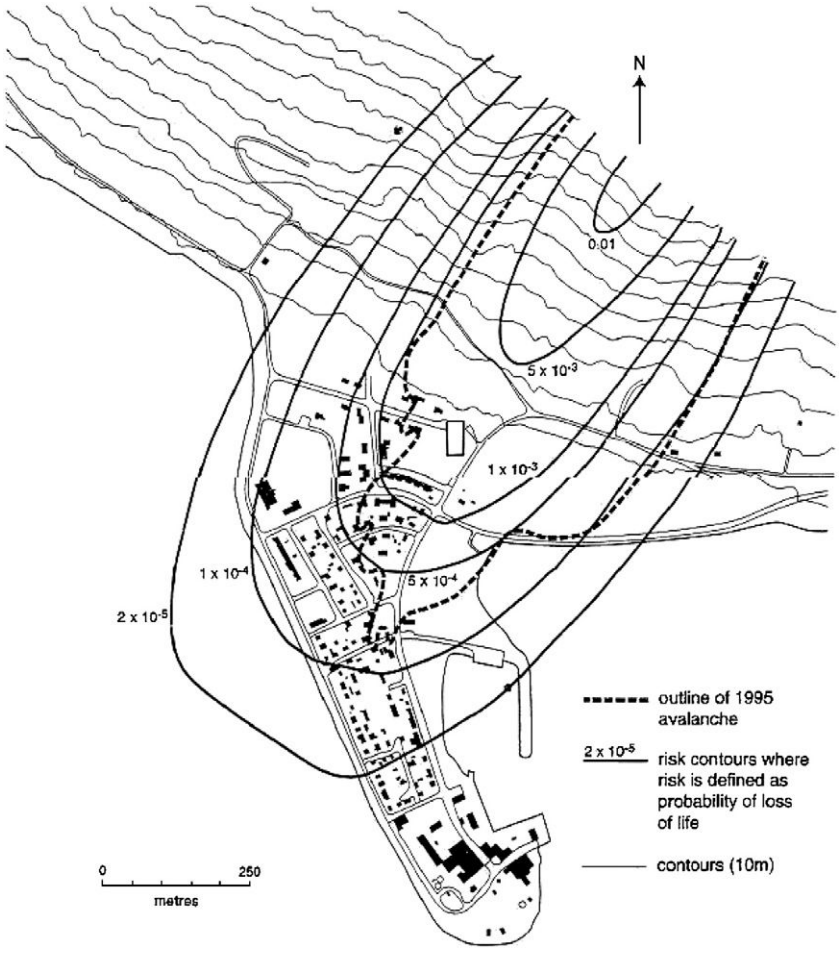

Fig. 4. Precursor risk model and case-study from Keylock et al. (1999). Flateyri, Iceland: risk contours versus outline of the 1995 avalanche. Figure reprinted from the Journal of Glaciology with permission of the International Glaciological Society. The risk for people inside buildings is expressed as an annual probability of death.

probability function of avalanche size for people inside buildings. In Arnalds et al. (2004), the PCM (Perla et al., 1980) sliding block avalanche propagation model is used instead. The probability distribution of runouts in each path is evaluated by transfer onto a model path on which comparison with a large data set of extreme events is possible (Sigurdsson et al., 1998). In Barbolini et al. (2004a), a depth-averaged propagation model is coupled with statistical simulations of release depths, and a deterministic relation between the release depth and the friction parameters is used. In Cappabianca et al. (2008) a relatively similar approach is proposed, but in a 2D framework. The risk evaluation is approximated by showing and using a deterministic relation between release depth and impact pressure at a given location of the path, so as to reduce computation times.

The main problem for switching from risk mapping to risk zoning is the definition of acceptable risk limits for allowing urbanisation and/or deciding that countermeasures are unavoidable. As discussed in Cappabianca et al. (2008), proposed methods to evaluate acceptable risk levels include considering the other types of risks faced in everyday life such as domestic fatalities, and confronting them to avalanche risk. For example, protection goals in Switzerland are reported in Ammann (2006).

Remarkably, as extensively discussed by McClung (2005), hazard zoning procedures using return periods may be seen as worst case risk zoning methods with an accepted risk equal to the chosen return period, a dimensionless unitary element at risk z at position x_o and $V(z,y)=1\,\forall z,y(x_o)>0$, i.e. total destruction of the element at risk as soon as it is attained. For example, in the French practice that generally retains the centennial avalanche as the reference event, the equivalent accepted risk is then 10^{-2} per year.

2.5.2. Risk assessment to traffic roads

Risk assessment to traffic road is another important application of formal risk computations in the avalanche field. Precursor work was made by Wilhelm (1997) in Switzerland, and then transposed in several other countries (Europe, North America, New-Zealand…, etc.) by various authors. Individual and collective risks are estimated for a single path, or for a system at risk constituted of a road section threatened by several paths. Total risk is then the sum of the risks corresponding to each path according to the summation of Eq. (1), but with possibly different avalanche hazard levels for each path. Wilhelm's approach was made in a scenario perspective, i.e. by assuming that the avalanche corresponding to a given return period was known, thus avoiding integration over hazard variability. Similarly, Hendrikx and Owens (2008) use Schearer (1989)'s avalanche hazard index to represent avalanche magnitude in each threatened road section. However, extension to an α/β-like statistical framework (e.g. Wastl et al., 2011), or even to a stochastic avalanche model including dynamical simulations (Zischg et al., 2005b) is straightforward.

The main contributions of Wilhelm (1997)'s work are a way to evaluate the exposure rate of cars travelling on a road affected by avalanches and a usable value for the death rate λ_d of people in a vehicle hit by an avalanche. The proposed formula is a semi-empirical function of the daily traffic volume, the mean number of passengers in cars, the speed of the vehicle and the length of the exposed road section. It has been extended to account for waiting traffic (Hendrikx and Owens, 2008). The proposed death rate λ_d was obtained by analyses of past accidents, leading to the value 0.2. Variations around this value have been discussed, with regard to the type of vehicle or avalanche path. For instance, Kristensen et al. (2003) propose the value 0.4 for Norwegian paths, to take into account longer rescue times in remote regions that increase the probability of death after an accident.

With regard to the discussion of Section 2.3, it must be noted that if λ_d is supposed to vary with the type of vehicle z only, it can be seen as the vulnerability $V(z,y)=\lambda_d\,\forall y>0$. On the contrary, if it depends on local topographic and/or climatologic constraints, it is rather the specific risk for an individual crossing the considered path within its car since integration over the local avalanche activity is implicitly performed, making the value no longer usable, without care, for another path.

Because of the low loss that represents the destruction of a car with regard to one or several human fatalities, Wilhelm chose to measure risk to traffic roads in terms of long term death rate, i.e. to neglect all other kind of losses. This is enough to compare the risk on different roads to each other and to acceptable thresholds, as well as for a rough analysis of the benefit of different mitigation strategies. For instance, in Margreth et al. (2003), winter opening of three Alpine passes is studied, and it is stated that death number reduction is too low to justify full protection using permanent countermeasures. However, considering human lives only becomes insufficient as soon as detailed cost–benefit analyses are undertaken because the reduction of fatalities must then be compared to investment costs using the same units. Therefore, Rheinberger et al. (2009) have proposed within a risk perspective (i.e. with a Gumbel stochastic model of runout distances instead of scenarios "only") a monetary extension of Wilhelm's framework to express all losses in the same economic currency, see Section 3.

2.5.3. Risk for mountaineers/back-country skiers

Existing methods to assess risk for mountaineers/back-country skiers consist in the detailed analysis of the respective weight of the different factors leading to accidents. The factors considered are either only natural (e.g. Grímsdóttir and McClung, 2006), or both natural and human. In the latter case, precursor work was done by Munter (1992), followed by several authors (e.g. McCammon and Hägeli, 2007). For instance, Pfeifer (2009) has proposed logit/zero inflated models to evaluate the probability of an accident as a function of different covariates, providing a quantitative decision support for going/not going on a ski slope a given day.

However, although obviously very useful, these approaches cannot totally be viewed within the formal framework of Eq. (1) because they do not consider the damage susceptibility component of risk. Hence, there is surely potential for future developments of formal risk analyses for mountaineers/back-country skiers combining long or short term avalanche release probability maps, vulnerability curves for standalone people, such as those proposed in Barbolini et al. (2004b), and statistics concerning the frequency of visits to estimate exposure. This would give more support to decisions that restrict in ski resorts access to certain areas (or at least advise against visiting them) in the long term, or during specific situations (a function of snow pack depth and meteorological conditions).

3. Decision and optimisation

3.1. The decisional setting

Risk can be modified by a decision/action d such as the construction of a defence structure, a road closure, artificial avalanche releases…, etc., in fact nothing more than a particular case of time effects discussed in Section 2.4. Decision can influence the hazard model $p(y|d)$ and the exposure $q(z_w|d)$, the notation indicating that hazard and exposition are now conditioned by the decision d, but not the vulnerability relations that characterise the different types of elements at risk. Decision can also influence the system at risk, by modifying the number of elements at risk, their nature and/or value, the latter because better protected elements at risk may be valued more highly. The total risk is therefore a function of the (possibly multidimensional) decisional variable d. Since the work of Van Dantzig (1956) applied to flood prevention in Holland, an additive form is generally chosen:

$$R_w(d) = C_o(d) + \sum_{z\in w}(z_w|d)q(z_w|d)\int p(y|d)V(z,y)dy, \tag{6}$$

where $C_o(d)$ is the loss resulting from the decision d independently of any avalanche damage. As stated before, $R_w(d)$ is termed the expected disutility in statistical theory. $C_o(d)$ is generally expressed in terms of costs, but the problem of being able to express all losses including $C_o(d)$ in the same units, mentioned for Eq. (1), is obviously even more critical here.

According to decision theory (Berger, 1985), the optimal decision that should be retained is $d^* = \text{Arg min}_d(R_w(d))$, i.e. the value of the decisional variable that minimises the expected damages/losses. The *baseline* risk considered up to here is the specific case $d = 0$. Therefore, risk is sometimes expressed with respect to the reference state, i.e. $R_w(d) - R_w(0)$. Obviously, the optimum is identical for $R_w(d) - R_w(0)$ and $R_w(d)$, since $R_w(0)$ does not depend on d.

The idea that decision makers shall behave in risky situations as optimizers of some generalisation of Eq. (6) (via a utility function mapping rewards to real numbers in such a way that preserves preference over those rewards) and that their state of knowledge can be described by the means of a random variable is derived from the precursor work in economics of Von Neumann and Morgenstern (1953). It was promoted by Raiffa (1968) to help in making the best from indirect relevant information. This normative theory generally known as *maximisation of expected utility* is grounded on five mathematical axioms formalised by Pratt et al. (1964). Extension to situations when there is more than a single attribute to take into account when deciding have been theorised by Keeney and Raiffa (1976). During the last fifty years, their followers have exhibited a series of "paradoxes" (Allais, 1953, 1979) by experiments on behaviour under risk, mostly linked to discrepancies between the observable rationality of a decision maker (Piattelli-Palmarini, 1995) and the expected utility optimisation principle. New models of behaviour have therefore been developed (Machina, 1982; Quiggin, 1982; Tvesky and Kahneman, 1992), trying to take into account these other types of rationality under risk and to develop a coherent descriptive theory (Machina, 1987; Munier, 1988). However, we stick to the rationale associated with expected loss minimisation in most of what follows, since it agrees with common actuarial practice for optimising public funds, and because it guarantees an always positive value of information (i.e. a better state of information can never worsen the decision in a sequential setting), which is not necessarily the case with more recent approaches. We nevertheless discuss the potential of alternative risk measures in Section 5.4.

Standard/traditional cost–benefit analyses can be seen as a way of computing the function $R_w(d)$ for a few discrete values of d only, i.e. without investigating all possible values of the decision. In the avalanche field, they are now commonly used as a basis for comparing different competing risk reduction methods in land use planning (e.g. Ceriani, 2010; Wilhelm, 1997). For example, Fuchs et al. (2007) compared 16 mitigations strategies in Davos, showing that the one currently in use is close to the maximal economical efficiency. Other applications include the a posteriori evaluation of one or several already existing permanent defence structures (Fuchs and McAlpin, 2005), and the risk to traffic roads minimisation previously discussed (Margreth et al., 2003).

Most often, a scenario approach is adopted, i.e. only a few hazard values are considered such as in Eq. (3). Incidentally, confusion arises about what the scenario is: the hazard value y_k and/or the decision d? We suggest reserving the scenario terminology to the hazard value, and viewing a discrete set of decisions rather as a numerical approximation of the risk function in the decision space, which is unavoidable as soon as Eq. (6) cannot be computed and/or minimised analytically. However, as discussed in Section 2.1 for risk mapping, the optimality of the retained decision may be highly sensitive to such approximations/discretisations, so that they must be made with care.

On the contrary, in the avalanche field, complete optimal design methods following Eq. (6) are, at our knowledge, for now limited to two contributions. In Rheinberger et al. (2009), a quantitative comparison of organisational (temporary) and structural (permanent) risk to traffic road reduction options is performed. The decision space consists in a finite set of mitigation measures — including combinations — and it is shown that site-specific characteristics of avalanche paths and the economic importance of the considered traffic roads are decisive factors for the choice of optimal mitigation strategy. However, the different competing decisions are too different from each other to allow a sound representation of the risk as the function of decision. In Eckert et al. (2008a, 2009) the decision space is continuous and simpler. These papers study the effect of including an avalanche–obstacle interaction law in a stochastic model of avalanche magnitude, and the size of the dam that maximises the economical benefit of its construction is searched for. As an illustration of the potential of a decision theoretical framework in avalanche engineering and of the feasibility of all computations, the next subsections recall and expand the main steps of this work.

3.2. Example: optimal design of the height of an avalanche dam

3.2.1. Analytical formulation

The simplified setting considered is a one dimensional topographical profile with a single fully exposed building without any inhabitants located at the abscissa position x_b within the runout zone. The construction of a vertical protective dam at the abscissa position x_d is envisaged, and the problem is to choose the dam height h_d that minimises economic losses. This is therefore an individual risk approach with $\sum_{z \in W} z_w = z = C_1$, with C_1 the value of the building expressed in €, $q(z_w) = 1$, and a continuous monovariate decisional variable, the dam height $d = h_d$.

The choice is made to work in terms of total risk rather than in annual values. This implies, under the assumption of stationarity of the avalanche phenomenon (see Section 2.4), introducing the actualisation factor $A = \sum_{t=1}^{+\infty} \frac{1}{(1+i_t)^t}$ for expressing the costs of future damages in the current monetary unit. It depends only on predicted annual interest rates i_t, $t \in [1, +\infty[$. The construction cost is assumed to increase linearly with the dam height, with a unitary cost C_o expressed in €.m^{-1}, so that $C_o(d) = C_o h_d$. Other formulations are obviously possible and straightforward.

Finally, the damages to the dam are neglected, i.e. assumed as negligible with regard to those inflicted to the building. If this is considered as a too strong assumption, another way of thinking is to accept that certain avalanches damage the dam, but not enough to reduce its protective effect. This has the advantage to allow including the reparation costs needed after each damageable event into the construction costs C_o (a standard computation as soon as a depreciation period is fixed for the dam) instead of considering the more complex case of a modified system at risk with the dam as an additional threatened element.

Avalanche magnitude is measured in terms of runout distance x_{stop} only, so that $\{y = x_{stop}\}$. The runout distances exceeding the dam abscissa are assumed to be exponentially distributed, which can be expressed with a single parameter ρ as:

$$p\left(x_{stop} \middle| \rho, x_{stop} > x_d\right) = \rho \exp\left(-\rho\left(x_{stop} - x_d\right)\right). \tag{7}$$

Furthermore, the number a of exceedences of the dam abscissa occurring during a given winter is assumed to be Poisson-distributed, which can be expressed with a single parameter λ as:

$$p(a) = \frac{\lambda^a}{a!} \exp(-\lambda). \tag{8}$$

This very simple stochastic avalanche model is well known in hydrology (Parent and Bernier, 2003) as a particular case of the Peak

Over Threshold (POT) model family (Coles, 2001) which models the exceedences of any stationary process as soon as the threshold is high enough (Pickands, 1975).

Following Faug et al. (2008), the influence of the dam on relatively rapid avalanche flows is expressed as a linear relation between the runout distance reduction and the ratio, h_d/h_o, between the dam height, h_d, and the depth of the flow without the dam, h_o. The runout distance without the dam, x_{stop_o}, is therefore reduced to $x_{stop}(h_d)$, the runout distance of the same avalanche with a dam height h_d, with a proportionality coefficient α quantifying the first-order effect of the dam:

$$\frac{x_{stop}(h_d)-x_d}{x_{stop_o}-x_d}=1-\alpha\frac{h_d}{h_o}. \tag{9}$$

For simplicity, in the rest of the paper, we will consider the fictitious case corresponding to the known and fixed value $h_o=1m$. However, all the proposed developments and results can be understood and interpreted more realistically as functions of the scaled variable h_d/h_o.

With this avalanche–dam interaction law, the cumulated probability of exceeding the building abscissa $P(x_{stop}\geq x_b)=\exp(-\rho(x_b-x_d))$ is reduced, leading to the residual probability for the building of being hit with the dam:

$$P\left(x_{stop}\geq x_b|h_d\right)=\exp\left(\frac{-\rho(x_b-x_d)}{1-\alpha(h_d/h_o)}\right). \tag{10}$$

This shows that $(1-\alpha(h_d/h_o))/\rho$ is the scale parameter for the exponential distribution of runouts with the dam h_d, leading to the annual quantile:

$$x_{stop_T}(h_d)=\left(\frac{1-\alpha(h_d/h_o)}{\rho}\right)\ln(\lambda T)+x_d, \tag{11}$$

i.e. to the runout distance $x_{stop_T}(h_d)$ corresponding to the return period T with the dam height h_d. It represents the residual hazard after the dam construction. It is represented in Fig. 5a for different dam heights, including the baseline case $h_d=0$.

Finally, the very rough worst case vulnerability relationship is assumed: maximal damage as soon as the building is attained, whereas it remains obviously undamaged if the avalanche does not reach its abscissa:

$$V(z,y)=V\left(C_1,x_{stop}\right)=I_{\{x_{stop}\geq x_b\}}. \tag{12}$$

All these modelling assumptions can be seen as very strong. Their limits and implications, as well as detailed results for a case study are extensively discussed in the original paper (Eckert et al., 2008a). Their advantage is that they permit easy computation of Eq. (6) analytically, leading to:

$$\begin{aligned}R(h_d)&=C_oh_d+A\lambda C_1\int_{\frac{x_b-x_d}{1-\alpha(h_d/h_o)}}^{+\infty}\rho\exp\left(-\rho\left(x_{stop}-x_d\right)\right)dx_{stop}\\&=C_oh_d+A\lambda C_1\exp\left(\frac{-\rho(x_b-x_d)}{1-\alpha(h_d/h_o)}\right),\end{aligned} \tag{13}$$

which nicely illustrates the contribution of the different terms to the total expected losses. The construction cost, C_oh_d, depends on the size of the obstacle only. Avalanche hazard is involved through the expectation of the annual distribution of avalanche numbers reaching the dam abscissa, i.e. the annual exceedence rate λ, and through the reduced probability of hitting the building $P(x_{stop}\geq x_b|h_d)$. The actualisation factor A corresponds to the equivalent number of years that has to be considered for the annual risk computation to coincide with the total damage starting from the date of the dam construction. Another way to see it is as an equivalent number of buildings that weights the annual risk for a single building.

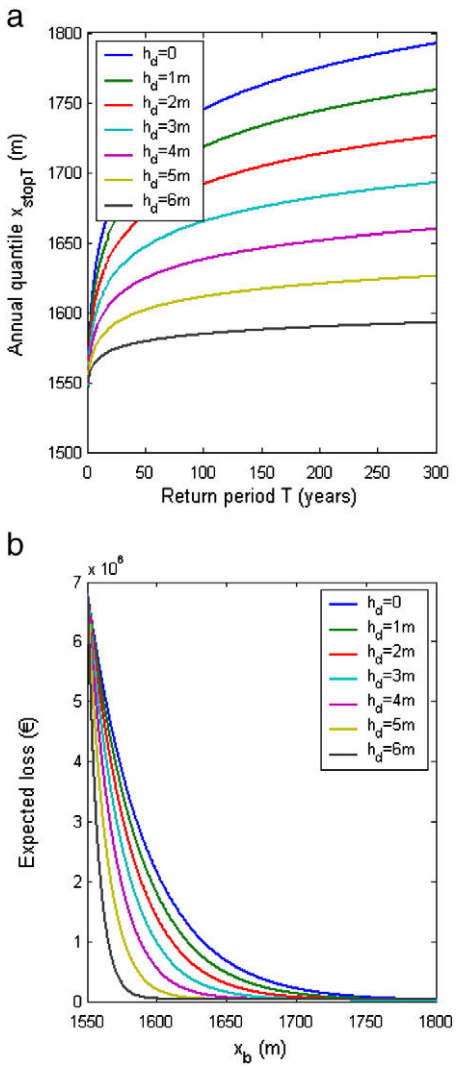

Fig. 5. Residual hazard and residual risk. Analytical model and case study from Eckert et al. (2008a). a) Residual hazard is the annual quantile x_{stop_T} from Eq. (11) for different dam heights h_d. b) Residual risk represents the total expected loss as a function of the abscissa position of a single building x_b for different dam heights. $h_o=1m$ is fixed.

$R(h_d)$ is plotted as functions of x_b in Fig. 5b. The baseline risk is $R_0=R(0)=A\lambda C_1\exp(-\rho(x_b-x_d))$. For all other dam heights, $R(h_d)$ is the residual risk in the runout zone. This family of curves illustrates the reduction of expected losses with the increase of the dam height for "small" values of x_b, as well as the convergence to the constant C_oh_d (different for each dam height) for "large" values of x_b because the building is then constructed at a safe position.

Finally, the difference in expected losses if the dam h_d is constructed instead of no dam built:

$$\begin{aligned}R(h_d)-R_0&=C_oh_d\\&\quad+A\lambda C_1\left[\exp\left(\frac{-\rho(x_b-x_d)}{1-\alpha(h_d/h_o)}\right)-\exp(-\rho(x_b-x_d))\right],\end{aligned} \tag{14}$$

is simply the opposite of the benefit expected from the dam construction.

Seen rather as functions of h_d, Eqs. (13)–(14) can be minimised for each building position, x_b, which can be used to maximise the benefit from the dam construction. Fig. 6 shows the risk functions obtained for buildings situated at annual quantile positions $x_{stop_T}(0)$ ranging

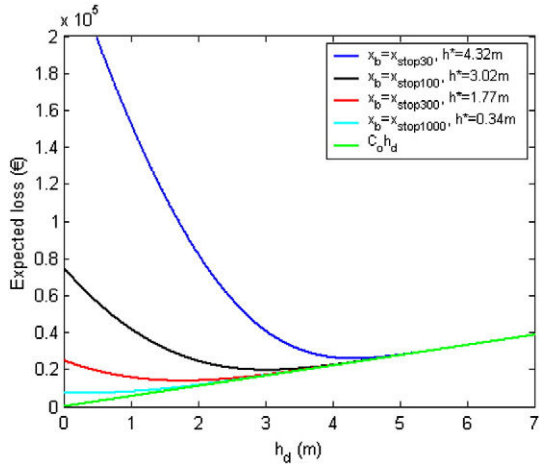

Fig. 6. Risk function and optimal design of an avalanche dam. Analytical risk model and case study from Eckert et al. (2008a). Risk functions given by Eq. (13) for a single building situated at abscissa positions x_{stopT} corresponding to return periods ranging from 30 to 1000 years without dam.

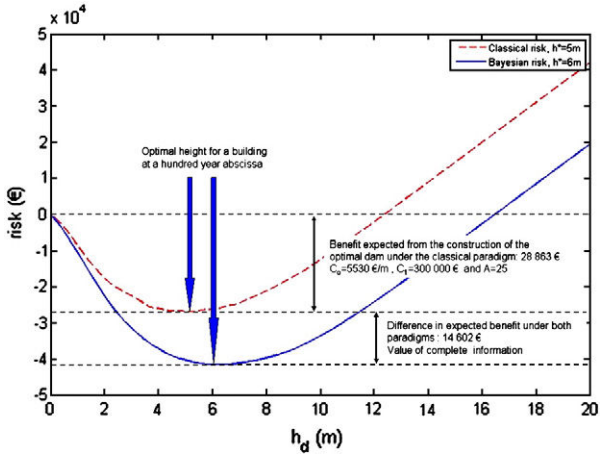

Fig. 7. Classical and Bayesian optimal designs of an avalanche dam. Numerical risk model and case study from Eckert et al. (2009). Risk represents the opposite of the expected benefit as a function of the dam height, i.e. the baseline risk is subtracted from the expected loss for each dam height. A single building situated at a 100-year abscissa position without dam is considered.

from 30 to 1000 year return periods. For any building position, the risk function is nicely shaped, with a clear optimal height h^* corresponding to the minimisation of expected losses. For dam heights lower than the optimum, the expected losses decrease when the dam height increases. For higher dams, the expected losses increase again, indicating that the additional protective effect no longer compensates the additional construction cost. For example, for a building situated at a centennial abscissa (i.e. at a position reached every 100 years on average without a dam, which is provided by Eq. (11) with $T=100$ and $h_d=0$), the optimal height is 3.02 m. Note that this may appear very small, but it is a direct consequence of the chosen system at risk, a single building with no inhabitants, so that it cannot be economically justified to build a huge permanent defence structure.

Fig. 6 also shows that the optimal dam height decreases from 4.32 m to 0.34 m when the return period of the considered abscissa increases from 30 to 1000 years. This is caused by the fact that the dam construction is less profitable and harder to justify for elements that are less often attained (e.g. for buildings never hit, it is not sound to construct at all, so that the optimal height is 0 m!). Note finally that, for all building positions, the risk function tends to the same linear increase with the dam height. The asymptotic behaviour $C_o h_d$ is attained as soon as the dam becomes high enough to stop all avalanches before the building, which is obviously the case for lower dams for buildings situated at less exposed positions. In practice, these curves can be computed very easily for any case study, giving a first rough approximation of the maximal (because of the 0–1 vulnerability relation) expected loss, reasonable as long as the assumption of exponentially distributed runouts is tenable.

3.2.2. Numerical formulation

In Eckert et al. (2009) the oversimplified hazard and vulnerability models of Eqs. (7), (8) and (12) are replaced by still simplified but more realistic formulations. The explicit stochastic model of avalanche runout is replaced by a multivariate statistical–dynamical model similar to the one presented in Fig. 1. The vulnerability formulation used is derived from those reported in Section 2.2.3, with velocity taken as the single variable to relate avalanche magnitude to damage level. An additional equation is used to model the energy dissipation at the dam abscissa, i.e. how the avalanche–obstacle interaction disrupts the velocity profile. These more sophisticated modifications increase the reliability and usability of the risk formulation obtained, but do not change anything from a formal point of view, except that Eq. (6) is no longer analytically integrable, and must be computed numerically for a set of dam heights.

The difference $R(h_d) - R_0$ obtained for the case study of the paper is presented in Fig. 7 for a building situated at a centennial abscissa. For dam heights lower than 12 m, this cost is negative, which indicates that the construction of a dam is economically sound, with an optimum for $h^*=5$m, providing an expected benefit of around 30 000€. Other differences to Fig. 6 are related to the differences in the case studies considered and in the additional effects taken into account in the hazard and vulnerability models, mainly the real topography of the path (which does not appear in Eqs. (12)–(14)) and the dependence of damage on velocity and runout distance, instead of runout distance only. The latter modification makes the expected losses systematically lower than when a total destruction is assumed as soon as the building is attained.

4. Uncertainty in risk evaluation and optimal design

4.1. Risk as an integrated measure

Commonsense associates risk with uncertainty. However, a very important and often badly understood point is that risk, when defined as an expected damage, is an integrated measure and should therefore no longer be associated with any uncertainty level. From this point of view, the concepts of risk and confidence interval are antagonistic, since being able to give a confidence interval implies that an error distribution is known, meaning that an additional integration is possible. This has already been pointed out for elements at risk while discussing randomness in vulnerability relations and links with structural reliability in Section 2.3, but it is also true for uncertainty regarding the hazard model $p(y)$.

A good example is how to deal with parameter uncertainty in risk analyses. Let us consider again the obstacle effect in the analytical optimal design setting presented previously. Rather than a single estimated value α to be taken as a surrogate for the "true" α, lab and full scale experiments provide a range of possible values $[\alpha_{\min},\alpha_{\max}]$, depending on small variations of experimental conditions and flowing material (Faug et al., 2008). A sensitivity analysis is possible to evaluate Eq. (13) with these values, leading to a $[R_{\min},R_{\max}]$ risk interval, but this contradicts the definition of risk as a single loss expectation for any value of the decisional variable h_d. Therefore, it is more consistent to compute:

$$R'(h_d) = E_\alpha[R(h_d,\alpha)] = \int R(h_d,\alpha) \times p(\alpha) \times d\alpha, \quad (15)$$

where $R(h_d,\alpha)$ is the risk with a fixed value of α given by Eq. (13), and $p(\alpha)$ a probability distribution quantifying the possible values of the parameter and their respective *credibilities*, i.e. a probabilistic judgement ascertaining a degree of belief. If one is willing to assume the uncertainty on α to be represented by the uniform distribution $p(\alpha)=\frac{1}{\alpha_{\max}-\alpha_{\min}}$ on $]\alpha_{\min},\alpha_{\max}[$, $R'(h_d)$ is then:

$$R'(h_d)=C_o h_d+\frac{A\lambda C_1}{\alpha_{\max}-\alpha_{\min}}\int_{\alpha_{\min}}^{\alpha_{\max}}\exp\left(\frac{-\rho(x_b-x_d)(h_o/h_d)}{(h_o/h_d)-\alpha}\right)d\alpha. \quad (16)$$

Integration is still analytically feasible, leading to:

$$R'(h_d)=C_o h_d+\frac{A\lambda C_1}{\alpha_{\max}-\alpha_{\min}}\left[\begin{array}{l}(\alpha_{\max}-(h_o/h_d))\exp\left(\frac{-\rho(x_b-x_d)(h_o/h_d)}{(h_o/h_d)-\alpha_{\max}}\right)\\-(\alpha_{\min}-(h_o/h_d))\exp\left(\frac{-\rho(x_b-x_d)(h_o/h_d)}{(h_o/h_d)-\alpha_{\min}}\right)\\+\rho(x_b-x_d)(h_o/h_d)\,\mathrm{expint}\left(\frac{\rho(x_b-x_d)(h_o/h_d)}{(h_o/h_d)-\alpha_{\max}}\right)\\-\rho(x_b-x_d)(h_o/h_d)\,\mathrm{expint}\left(\frac{\rho(x_b-x_d)(h_o/h_d)}{(h_o/h_d)-\alpha_{\min}}\right)\end{array}\right], \quad (17)$$

where $\mathrm{exp\,int}(x)=\int_{-\infty}^{x}\frac{1}{t}\exp(-t)dt$ is the exponential integral function which is tabulated by most computational software. By comparison to Eq. (13), the risk R' depends on the bounds $(\alpha_{\min},\alpha_{\max})$ rather than on a single value of α.

Logically, Eq. (17) converges to the risk function given by Eq. (13) for very sharp distributions of α. Uniform "flat" distributions for the credibility about α have large variances, meaning that when little is known about α except bounds, probabilistic bets can be scattered on a large range of possible values. Hence, the optimal height and expected losses tend to increase with the variance of the credibility regarding α, and convergence to the asymptote $C_o h_d$ is slower when α is poorly known (Fig. 8). This is all attributable to the explicit incorporation of an additional uncertainty source into the decisional process. It makes the expected losses higher for a given dam height, and requires a more cautious design when α is not known perfectly, which is logical.

Finally, it is noteworthy that optimality is more conservative than risk., i.e. that the optimal height increases more slowly with the uncertainty level regarding α than the expected losses at the optimum, i.e. of around 8% versus of around 17% on the investigated uncertainty range (Table 1).

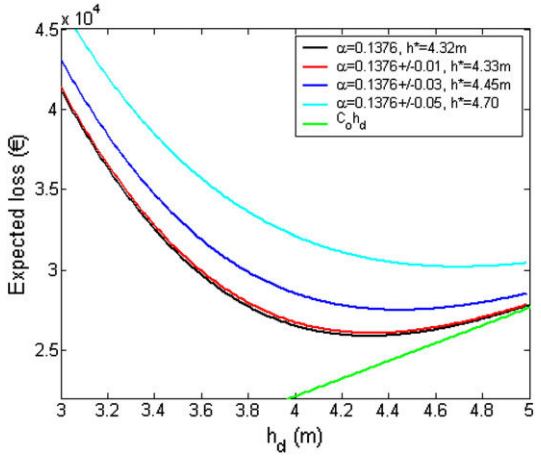

Fig. 8. Sensitivity of the optimal design to the uncertainty regarding the avalanche–obstacle interaction law. Case study from Eckert et al. (2008a). Risk functions are evaluated using Eq. (17). They represent the total expected loss as a function of the dam height for different uncertainty levels regarding the α parameter. A single building situated at a 30-year abscissa position without dam is considered.

Table 1
Effect of the uncertainty regarding the avalanche–obstacle interaction law on the optimal height and associated risk. Risk model and case study from Eckert et al. (2008a). The element at risk is a single building at an abscissa position corresponding to a 30 year return period. Δ_{h^*} represents the difference in optimal height h^* between $\alpha=\hat{\alpha}$ and the considered uncertainty range. $\Delta_{R(h^*)}$ is the corresponding difference in expected loss.

	$\alpha=\hat{\alpha}=0.1376$	$\hat{\alpha}\pm0.01$	$\hat{\alpha}\pm0.03$	$\hat{\alpha}\pm0.05$
h^* (m)	4.32	4.33	4.45	4.7
Δ_{h^*} (m)	/	0.01	0.13	0.38
Δ_{h^*} (%)	/	0.2	2.9	8.1
$R(h^*)$ (€)	25 873	26 057	27 500	30 193
$\Delta_{R(h^*)}$ (€)	/	184	1627	4320
$\Delta_{R(h^*)}$ (%)	/	0.7	6.3	16.7

4.2. Variability and uncertainty in the risk framework

Another point which needs clarification is the difference between uncertainty and variability (O'Hagan and Oakley, 2004). The former results from a lack of knowledge (for example, about critical parameters) and is called uncertainty by ignorance or epistemic uncertainty by some authors, whereas the second (sometimes called uncertainty by essence or rather confusingly random uncertainty) is related to natural variations of the studied phenomenon, here snow avalanches, driven by variable snow and weather conditions. Therefore, uncertainty and variability imply totally different modelling assumptions since, in reality, there is only a fixed single value for every uncertain unknown but many different outcomes can occur from the same variable mechanism.

However, it must be emphasised that both are treated in a similar way with the mathematical toolbox of probabilities in the risk framework. As an example of this non-distinction, one may consider the case, important in practice, of a risk evaluation with a scenario approach, but taking into account a given uncertainty level around the chosen reference value. This is the basis of the analysis of Fuchs and McAlpin (2005) discussed earlier to highlight the sensitivity of risk evaluation to a reference hazard value. In the decisional context, the risk function associated to the scenario y is the total loss expected if the y event occurs:

$$R_w(d,y)=C_o(d)+\sum_{z\in w}(z_w|d)q(z_w|d)V(z,y). \quad (18)$$

A classical representation for the uncertainty around the reference scenario is the Gaussian distribution $y\sim N(y_k,{\sigma_{y_k}}^2)$, i.e. centred on the chosen reference scenario y_k, with a variance ${\sigma_{y_k}}^2$ modelling the associated distribution of uncertainty. In other words y_k is the best guess, but one believes to make a winning bet with odds 95 against 5 that the scenario y lies between $y_k-1.96\sigma_{y_k}$ and $y_k+1.96\sigma_{y_k}$. This leads to the integrated risk function:

$$R_w'(h_d)=\int\frac{1}{\sigma_{y_k}\sqrt{2\pi}}\exp\left(\frac{(y-y_k)^2}{2\sigma_{y_k}^2}\right)R_w(h_d,y)dy. \quad (19)$$

This function R_w' is the result of epistemic uncertainty concerning the reference scenario y_k. However, the same function is obtained by evaluating Eq. (6) with $p(y)\sim N(y_k,{\sigma_{y_k}}^2)$, i.e. under the assumption that the variability of snow avalanches in the considered system at risk can be modelled by a perfectly known Gaussian probability model.

Application to the chosen optimal design illustrative example leads to evaluating Eq. (13) with the normal distribution $p(x_{stop})\sim N(x_{stop_k},{\sigma_{x_{stop_k}}}^2)$ instead of an exponential one. For homogeneity with Eq. (13), a total cost

approach is kept, adding the A and λ factors to weight the loss expected from a single event, which gives:

$$R'(h_d) = C_o h_d + A\lambda C_1 \int_{\frac{x_b - x_d}{1-\alpha(h_d/h_o)}}^{+\infty} \frac{1}{\sigma_{x_{stop_k}}\sqrt{2\pi}} \exp\left(\frac{\left(x_{stop} - x_{stop_k}\right)^2}{2\sigma^2_{x_{stop_k}}}\right) dx_{stop} = C_o h_d + A\lambda C_1 \left[1 - \phi\left(\frac{x_b - x_d}{1-\alpha(h_d/h_o)}\right)\right], \quad (20)$$

where $\phi\left(\frac{x_b - x_d}{1-\alpha(h_d/h_o)}\right)$ represents the normal cumulative distribution function of mean x_{stop_k} and standard deviation ${\sigma_{x_{stopk}}}^2$ evaluated in $\frac{x_b - x_d}{1-\alpha(h_d/h_o)}$. Hence, $R'(h_d)$ represents the total losses to be expected from the successive occurrences of the x_{stop_k} reference event on the long term, but taking into account the associated uncertainty. The alternative interpretation as a result of the variability of snow avalanches on the considered case study is mathematically plausible, but practically highly unlikely because the assumption of normally distributed runout distances is never fulfilled.

Intuitively, without uncertainty about x_{stop_k}, the dam construction is unsound if $x_{stop_k} < x_b$ because the building is then constructed at a safe position, On the contrary, if $x_{stop_k} > x_b$, the building is exposed without the dam, and the height $h^* = \frac{h_o}{\alpha}\left(1 - \frac{x_b - x_d}{x_{stop_k} - x_d}\right)$ just sufficient to stop the reference event at the building abscissa should be advised. For uncertainty levels represented by $\sigma_{x_{stopk}} > 0$, the building is not fully safe even for $x_{stop_k} < x_b$, and Eq. (20) can be evaluated for any dam height and minimised, leading to results very useful in an operational context to test the economical efficiency of a hazard zoning map based on a reference event and its modification by a dam.

For example, Fig. 9 shows the risk functions obtained with different building positions x_b, different uncertainty levels, $\sigma_{x_{stopk}}$, and the reference event x_{stop_k} taken as the centennial quantile from Eq. (11) without a dam, a classical hazard zoning limit. The three curves in Fig. 9a represent a building within the extension of the considered reference event (blue), just at the limit of the extension of the reference event (black), and beyond its extension (red), respectively. They are nicely shaped, with, in all cases, first a rapid decrease of expected losses with the dam height, then a clear optimal height, and finally a rapid convergence to the asymptotic behaviour $C_o h_d$ for higher dams. This is even true in the case of the building situated outside the extension of the reference event because its probability of being hit is significant for low dam heights with the considered uncertainty level. Differences with the case of exponentially distributed runouts of Fig. 6 are, for a given building position, a lower optimal height, lower expected losses and a sharper shape before and after the optimum. They are related to the greater dispersion and asymmetry of an exponential tail with regard to the bell-shaped Gaussian case. Fig. 9b corresponds to the case of a building situated just at the extension limit of the reference event (black line in 9a), but with different uncertainty levels, $\sigma_{x_{stopk}}$. The different curves show the increase in optimal height and expect losses with the uncertainty level, because, with high uncertainty levels, the probability of hitting the building remains high even for relatively high dams.

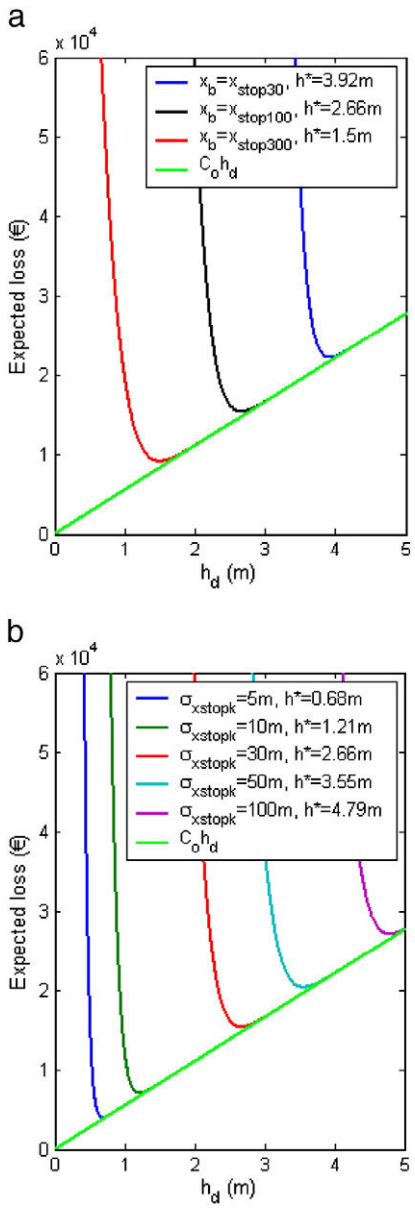

Fig. 9. Risk functions and optimal design for Gaussian uncertainty around reference scenarios. Case study from Eckert et al. (2008a). Risk functions evaluated using Eq. (20): a) for various building positions x_b with $x_{stop_k} = x_{stop_{100}}$ and $\sigma_{x_{stopk}} = 30$m, b) for various uncertainty levels $\sigma_{x_{stopk}}$ with $x_{stop_k} = x_b = x_{stop_{100}}$.

4.3. Calibration, parameter uncertainty and Bayesian risk

Another particular case of the variability/uncertainty distinction is the one related to the calibration of the stochastic avalanche model and the related estimation error. Indeed, avalanche models are still far from perfect, so that they need local calibration to give reliable results. Classical notation for the avalanche model is $p(y|\theta)$, where θ is the vector of unknown parameters. For example, $\theta = \{\lambda, \rho\}$ in the POT model of Eqs. (7)–(8), and includes the friction coefficients of the propagation model as additional component of θ when a statistical–dynamical model such as the one of Fig. 1 is used.

The typical calibration challenge is to get a point estimate, $\hat{\theta}$, using the available data in order to use $p\left(y\middle|\hat{\theta}\right)$ for risk computations or, more classically, quantifying reference hazards. Beyond the possible technical difficulty of the calibration task, such an approach has the drawback that it neglects the estimation error around $\hat{\theta}$, which is unrealistic with regard to the generally poor local information available. Furthermore, this may bias the decision in an undesirable way, because calibration is generally performed by minimisation of a variance criterion (e.g. mean square error minimisation), which is a symmetrical quadratic function, whereas, in the context of natural hazards, the penalty to be applied for the decision is clearly asymmetrical. As an obvious example, the total costs increase much more strongly if an avalanche dam height is overestimated by a given value than if it is underestimated by the same amount. These problems are fairly addressed within the

Bayesian framework by first computing the *posterior* distribution of the parameters given the available data sample y_{obs} such as:

$$p(\theta|y_{obs}) \propto p(\theta) \times p(y_{obs}|\theta), \tag{21}$$

where $p(y_{obs}|\theta)$ is the probability of the data under the assumption that they are (generally independent) realisations of $p(y|\theta)$, and $p(\theta)$, a (possibly non or poorly informative) *prior* distribution representing extra-data information (Berger, 1985). In this framework, the Bayesian definition of probability quantifies directly the degree of uncertainty of a scientific judgement, the probability of an event being the price at which one would buy or sell a bet that rewards one currency unit if it happens, and nothing if it fails (Kadane, 2011). Accordingly, the *posterior* distribution expresses mathematically the uncertainty source stemming from partial knowledge of θ in the risk equation, in turn leading to the Bayesian risk by integrating over parameter uncertainty:

$$R_{Bw}(d, y_{obs}) = \int p(\theta|y_{obs}) \times R_w(d,\theta) d\theta, \tag{22}$$

where $R_w(d,\theta)$ is the risk function for the system, w, provided by Eq. (6) with the model parameter value θ. From a practical point of view $R_{Bw}(d,y_{obs})$ is, a function of d only instead of being a function of model parameters also, making the search of the optimal decision $d_B{}^* = \text{Arg min}_d(R_{Bw}(d,y_{obs}))$ that minimises the expected losses easier.

From the more theoretical point of view of statistical decision theory, it can be shown that choosing $d_B{}^*$ instead of other decisions has suitable properties with regard to the statistical risk defined in Section 2.1.3. First, $d_B{}^*$ minimises the averaged opportunity loss $\Lambda\bar{R}_w = \int (R_w(d^*,\theta) - R_w(d,\theta)) \times p(\theta|y_{obs}) d\theta$, i.e. the loss to be expected because of an imperfect knowledge of the hazard model if the decision d is taken instead of the optimal one d^*. Second, when considered as a function of data, $d_B{}^*$ is the decision rule $d_B{}^* = \delta(y_{obs})$, which belongs to the set of so-called Bayes' rules obtained by varying the prior distribution. Such rules are known to dominate other decision rules under low restrictive regularity conditions (Wald, 1950). An example of a comparison of Bayes' rule to other intuitive rules including safety factors can be found in Parent et al. (2010) in the related case of the optimal design of a dam protecting against river floods.

Applications of Bayesian methods to various forms of avalanche models can be found in McClung and Tweedy (1994), Harbitz et al. (2001), Ancey (2005), and Eckert et al. (2007b, 2008b). For example, Bayesian risk computations have been applied to avalanche risk mapping over large areas in a GIS environment (Grêt-Regamey and Straub, 2006). This leads to a risk value as a function of space as detailed in Section 2.5.1, but taking into account the imperfect local information. On the other hand, no decisional variable is considered in this particular study, and only a finite set of possible friction parameters values for the statistical–dynamical hazard model is used.

Application of Bayesian optimal design procedures and comparison with classical ones can be found in the previously mentioned papers (Eckert et al., 2008a, 2009). In the case of the analytical illustrative example, integration of Eq. (13) leads to:

$$R_B(h_d, y_{obs}) = C_o h_d + AC_1 \int_{\lambda=0}^{\infty} \int_{\rho=0}^{\infty} \lambda \exp\left(\frac{-\rho(x_b - x_d)}{1-\alpha(h_d/h_o)}\right) p(\lambda,\rho|y_{obs}) d\rho d\lambda. \tag{23}$$

Analytical computation remains possible, if so called conjugate Gamma *priors* are chosen for $\{\lambda,\rho\}$:

$$p\left(\rho \middle| a_\rho, b_\rho\right) = \frac{a_\rho{}^{b_\rho}}{\Gamma\left(b_\rho\right)} \rho^{b_\rho - 1} \exp\left(-a_\rho \rho\right), \text{and} \tag{24}$$

$$p\left(\lambda \middle| a_\lambda, b_\lambda\right) = \frac{a_\lambda{}^{b_\lambda}}{\Gamma(b_\lambda)} \lambda^{b_\lambda - 1} \exp(-a_\lambda \rho). \tag{25}$$

(a_ρ, b_ρ) and (a_λ, b_λ) are two pairs of parameters to be specified representing the knowledge about avalanche magnitude and frequency on the studied site *prior* to local data analysis, and possibly resulting from expert knowledge concerning their regional behaviour (Kadane and Wolfson, 1998). *Posterior* distributions for λ and ρ are then still Gamma distributed, with the parameter pairs $(a_\rho^{'}, b_\rho^{'})$ and $(a_\lambda^{'}, b_\lambda^{'})$ combining the *prior* knowledge and the information conveyed by the data. More precisely, with a data set y_{obs} of n avalanches exceeding the threshold x_d in m years and $S(n)$ the sum of these exceedences, $a_\lambda^{'} = a_\lambda + m$, $b_\lambda^{'} = b_\lambda + n$, $a_\rho^{'} = a_\rho + S(n)$ and $b_\rho^{'} = b_\rho + n$, which indicates that, when n and m are large enough, the *prior* knowledge does not play much of a role. Computations detailed in Eckert et al. (2008a) lead to:

$$R_B(h_d, y_{obs}) = C_o h_d + AC_1 \frac{b_\lambda^{'}}{a_\lambda^{'}} \left(\frac{a_\rho^{'}}{a_\rho^{'} + \frac{x_b - x_d}{1-\alpha(h_d/h_o)}}\right)^{b_\rho^{'}}, \tag{26}$$

i.e. to a risk function similar to Eq. (13) since $b_\lambda^{'}/a_\lambda^{'}$ is the *posterior* expectancy of λ (i.e. the most probable exceedence rate given the data), and $\left(\frac{a_\rho^{'}}{a_\rho^{'} + x_b - x_d}\right)^{b_\rho^{'}}$ the *posterior* probability of exceeding the distance x_b without dam, which is reduced by the avalanche–obstacle interaction law.

Results obtained for different building positions are summarised in Table 2. For all dam heights, the Bayesian optimum is higher than the classical one leading to a more cautious recommendation, due to imperfect knowledge. This result is coherent with those obtained regarding the influence of the α parameter in Section 4.1, and $\sigma_{x_{stopk}}$ in Section 4.2: the additional uncertainty source, here parameter uncertainty resulting from the lack of local information, calls for a more cautious optimal design $h_B{}^*$ and higher expected losses. Note that, in fact, Eq. (17) can be seen as a Bayesian risk if the chosen uniform distribution $p(\alpha)$ is interpreted as a *posterior* distribution derived from observations.

Moreover, the systematic difference between the Bayesian and classical optimal heights increases from 5% to 250% for return periods of the building abscissa ranging from 10 to 1000 years. Taking estimation error into account therefore affects, in particular, the optimal design of a defence structure protecting buildings threatened only by the most extreme events. This is another intuitive result given that estimation error affects the evaluation of the highest quantiles of the hazard distribution more strongly, making extreme runout distances more probable than if perfect knowledge is assumed.

Going back to the numerical model of Fig. 7 yields similar results, with the Bayesian optimal height 20% higher (6 m versus 5 m) than the classical one, and the benefit expected from the construction of the optimal dam higher when the Bayesian computation is used (41 465 €) than when the classical computation is used (28 863 €), with a relative difference of 54%. The absolute difference $R_B(h_B{}^*) - R(h^*) = 14\,602$ € can be interpreted as the expected opportunity loss $\Lambda\bar{R}$ for the Bayesian decision rule against the minimisation of expected losses under the classical paradigm. It is attributable to the limited sample of avalanche runouts on the case study. In other words

Table 2
Classical and Bayesian optimal heights for buildings situated at abscissa positions corresponding to different return periods. Risk model and case study from Eckert et al. (2008a). $\Delta_{h^*} = h_B^* - h^*$ represents the difference between the Bayesian $h_B{}^*$ and classical h^* optimal heights.

	T_{10}	T_{30}	T_{100}	T_{300}	T_{1000}
h^* (m)	5.42	4.32	3.02	1.77	0.34
$h_B{}^*$ (m)	5.69	4.73	3.58	2.47	1.19
Δ_{h^*} (m)	0.27	0.41	0.56	0.7	0.85
Δ_{h^*} (%)	5	9.5	18.5	39.6	250

this is the value of information, i.e. the value quantifying what the decision maker should be ready to pay to obtain perfect information $\theta = \hat{\theta}$ with full confidence, i.e. to fund an exhaustive data collection protocol. Optimal properties of Bayes' decision rules grant that other decisional procedures would yield a lower expected profit for the decision maker.

4.4. Decisional sensitivity analyses

Even if the risk concept is designed to integrate as many variability/uncertainty sources as possible, it cannot take into account those for which it is unsound to consider them as being expressible in terms of probability distributions. For instance, this concerns quantities such as the position of the elements at risk. The risk function itself can nevertheless be computed for different values, so as to investigate their influence on the risk function and on the optimal solution, thus leading to (classical or Bayesian) *decisional* sensitivity analyses. Previous developments have already illustrated decisional sensitivity analyses, with e.g. the evolution of the total risk and of the optimal dam height with the position of the building in Fig. 6. Much more detailed results regarding the effects of the different parameters on risk functions can be found in Eckert et al., 2008a. A particularly important case is the one related to the vulnerability relation. Keylock and Barbolini (2001) postulated simple hypothetical functions for the vulnerability relation and showed that risk zoning is relatively robust to the vulnerability formulation used. This finding has been confirmed in Eckert et al. (2009) where the risk functions obtained were quite similar with a set of different vulnerability relations. Furthermore, the optimal dam height was shown to be even less sensitive to the choice of the damage formulation, in a similar way that the uncertainty regarding α affected the optimal decision less than the total losses corresponding to the optimal decision in the example of Section 4.1.

These results can be explained by the fact that, for a disastrous phenomenon such as a snow avalanche, the "first order effect" is whether or not the element at risk is attained by the flow or not. It is therefore understandable that results remain mainly unchanged for damage formulations that only differ in the precise way in which the dependency between damage and flow velocity or pressure is accounted for. More generally, these results are also compatible with theoretical work showing the robustness of optimal decisions with regard to a relatively large class of loss functions (Abraham and Cadre, 2004). All this suggests that the main results from risk analyses can already be used with reasonable confidence for avalanche engineering projects, even if important efforts remain to be done to improve our knowledge about vulnerability relations.

5. Open questions and directions for further work

5.1. Improvements to the different sub-models

Risk analyses combine different sub-models for avalanche hazard and vulnerability. The influence of decisions must also be modelled in cases of an optimal design approach, e.g. the effect of an obstacle (such as a dam) on the flow dynamics as a function of its size and shape. Nevertheless, according to our review, existing applications, even if they give interesting preliminary results such as the maximal expected loss in the case of the proposed illustrative analytical computations, often rely on simplified sub-models instead of the most up-to-date ones. For example, simple statistical models of avalanche runout are generally used as hazard models rather than fully multivariate statistical–dynamical models with avalanche flows described in the framework of continuum mechanics. Similarly, semi-empirical, simplified vulnerability curves are generally put in use rather than the most recent results of systematic numerical investigations. Therefore, improving the reliability of risk estimations involves putting more effort into adapting state-of-the-art sub-models to the risk setting. To do so, one major difficulty is the possible incompatibilities of the input/outputs of the different sub-models. For example, as shown with the illustrative analytical model, existing simplified formulations for the effect of an obstacle on avalanche flows consider a unique flow depth value (the maximum avalanche flow depth), which is difficult to reconcile with, e.g., flow depths that vary at each time step of the simulation.

Even if a certain robustness to the choice of the vulnerability relation exists (Section 4.4), priority should be given to improvements in their formulation for both the tangible and less tangible elements at risk. For civil engineering structures, numerical approaches, such as those developed by Bertrand et al. (2010) but coupled with the structural reliability approach detailed in Section 2.3 seem promising for estimating the probability of destruction for classes of elements at risk large enough to be used in practice. In the short term, this should help improve the methods currently in use for the design of permanent defence structures, thus allowing a more optimal use of limited public funds.

Another important point is that it should be possible to improve existing methods for describing systems at risk, i.e. for identifying, counting and evaluating the elements at risk, especially the less tangible aspects of risk, whose value is certainly underestimated in existing approaches. This may require involving more people with social science backgrounds into quantitative risk analyses.

Finally, the avalanche hazard models themselves may require some degree of re-thinking to move away from the old-fashioned conflict between deterministic and statistical schools of modelling. For example, statistical avalanche models often neglect the existence of different types of avalanche flows, different phases in the flow…, etc., and we do not know if the distributions they provide for extreme avalanches under various forcing inputs are always consistent with Extreme Value Theory (Coles, 2001). Similarly, when a more physical description of the flow is used, crucial questions such as the dependency of impact pressure on hydrodynamic conditions (flow depth and velocity), rheological properties (friction parameters on topography and snow quality) and/or geometrical conditions (shape of the impacted element) remain at least partially unclear. Therefore, much work remains to be done for a better physical representation of the flow, including an assessment of the stochasticity of the avalanche phenomenon, e.g. of the variable properties of all possible avalanches on a given site under study and of avalanches with the same starting mass but varying dynamics due to variable mass entrainment, density, or mass partitioning between powder and dense components.

5.2. Multivariate decisional approaches

Decision analyses performed within a risk framework can better account for the multivariate nature of avalanche hazard than standard return-period based approaches. However, the seldom existing decisional models reviewed in this work mostly consider a univariate decision variable such as a mitigation strategy chosen from a small number of alternatives, or the choice of a dam height. This is a limitation that does not really describe situations faced by stakeholders that have to make several choices simultaneously, e.g. the extension of an area to be evacuated during an avalanche cycle and the duration of the evacuation. Existing decision models can therefore arguably be seen rather as toy-models or mathematical exercises than as useful tools in operational contexts. This pleads in favour of expanding the existing decision models towards a multivariate decisional framework. For instance, useful improvements would be the joint optimisation of the different dimensions (height, width, length) of a defence structure, or of the time and duration of a road closure for traffic regulation.

5.3. Computational issues in risk evaluation

Computational limitations are closely related to the necessity of using the most up to date sub-models and of working in a multivariate

decisional framework. Indeed, with advanced sub-models based on a set of differential equations requiring a long time of computer occupation to be solved and/or complex decisional variables, the thousand runs with different avalanche combinations of avalanche hazard and decision necessary to evaluate Eqs. (1)–(6) by standard Monte Carlo procedures cannot be launched (remember the typical statistical convergence rate, i.e. $1/\sqrt{n}$ where n is the number of simulations). This is especially true for short term problems such as road closures when it is not possible to wait several days (or weeks!) to take decisions.

Therefore, existing methods for approximating Monte Carlo integrals more rapidly than random searches should be adapted to the avalanche field, so as to significantly reduce the number of simulations necessary for obtaining robust approximated solutions for the problem of risk minimisation. This could be done by putting in use the numerous methods that have been developed in structural reliability for approximating small probabilities in an efficient manner (Lemaire, 2009), with (e.g. First or Second Order Reliability Method — FORM/SORM) or without (e.g. directional or stratified Monte Carlo searches) approximations regarding the shape of the response surface, or even with emulation of the entire model using stochastic processes as in Sacks et al. (1989) or Kennedy and O'Hagan (2001).

5.4. Several measures of risk

A major characteristic of the decisional setting of Eq. (6) is that it offers a unique optimal solution to a given problem. In most cases, this is a positive attribute, but it can also have undesirable effects. First, statistical decision theory is a "personal" theory in the sense that it minimises losses according to the stakeholder's valuation of the considered system at risk. On the contrary, in an operational context, there are many different concerned protagonists to discuss and negotiate different trade-offs between protection and costs (exposed people may prefer a higher protection even if it is not fully "sound" from the economical point of view). Second, the five behaviour principles of Pratt et al. (1964) define a very strict rationale whereas stakeholders may act rationally, but have their own definition of rationality, depending on their personality or psychology, for instance on their risk perception. Third, from an even more theoretical point of view, choosing to define optimality as the minimisation of expected losses may be a dangerous strategy for a small mountain community because of very limited funds available for recovering after a major catastrophic event. Indeed, in the standard loss expectation, nothing is said about the time necessary to reach the expected loss, and to the maximal loss that may be feared during this time. This is well known in finance as a major cause of bankruptcies, especially in the context of extreme damageable phenomena, because the amount of money available to compensate very high losses is not infinite (Embrechts et al., 1997).

These different problems could be overcome by using measures of risk alternative to the simple loss expectation. This would restore possibilities for negotiations, and leave to the stakeholders the final decision, depending on their personality and on their political, social and/or budgetary constraints. For instance, as discussed in Bernier (2003) for hydrological problems, the behaviour of stakeholders facing risk can be taken into account by distorting the costs in the risk equation via a coefficient representing a careful, neutral or risk-prone personality. Even if it is not easy to quantify the marginal attitude towards risk as a distortion of perceived potential incomes (Munier, 1988), distorting costs into utility functions presents the advantage of staying under the mathematical framework grounded by the axioms of Pratt et al. (1964), which introduces only little changes to the general decisional framework of Eq. (6).

More radically, financial and insurance techniques have developed a large range of risk measures. Optimal decision is then based on the full distribution of random losses rather than on the maximised expected utility only. The most usual of these alternative measures is the Value at Risk (VaR), nothing more than a quantile of the distribution of random losses that is not exceeded at a certain confidence level. Many others exist, with mathematical properties and practical advantages/limits that remain discussed (e.g. Landsman and Sherris, 2001). The most validated ones could be used in avalanche engineering, leading, for a given case study, to different optimal solutions (one for each measure of risk), but corresponding to different behaviours against risk and/or strategies of loss minimisation, e.g. at long term only, or both at short and long terms by granting that a certain amount of losses is not exceeded on a given time window.

6. Conclusion

Risk analyses and optimal design approaches are appealing, since they combine different methods and sub-models that were developed separately, leading to real knowledge integration, both from semantic and mathematical (Eqs. (1) and (6)) points of views. With the ambition of breaking the walls between disciplines, this work has provided an up-to-date review of existing developments in the snow avalanche field. Special emphasis has been given to the clarification of key points such as time effects, links with structural reliability, and the difference between a scenario and a decision. Furthermore, the quantitative examples given in Section 4 have demonstrated how additional uncertainty sources can be processed and incorporated into decision making, generally leading to more cautious decisions, especially through a fully Bayesian approach of the decisional problem, from model calibration to risk minimisation. Our hope is that this work will stimulate further interdisciplinary research, not only at the stage of risk evaluation, but also at the early stage of the construction of the different sub-models, because we firmly believe that only by working together can physicists, engineers and statisticians better represent the different sources of variability/uncertainty that exist in avalanche flows, from one element at risk to another, and across the mechanical parameters of one given element at risk.

It is also important to note that the framework discussed herein, although developed from a science and engineering perspective, is able to integrate information provided by multidisciplinary and social-science oriented approaches as soon as the effort (not necessarily trouble-free) is made to express them in a quantitative way. This is especially true for taking the less tangible elements at risk into account. Furthermore, as shown by pre-existing applications, this is relevant not only for long term risk assessment in land use planning, but also for short term and traffic road risk assessment, and potentially for back-country skiing.

However, fully usable decision models remain for the moment seldom applied, computationally intensive, and oversimplified in terms of modelling assumptions. This latter point is especially critical because, once the optimal solution is provided, there is no more space for uncertainty since it is hidden in the modelling assumptions themselves. As discussed in Section 5, there is therefore much room for further development to bridge the gap between theory and practice, and adapts this framework to the various situations for which it is theoretically suited. This involves expanding the already existing decisional models for risk zoning, traffic road regulation and optimal design of defence structures, developing new ones, checking more deeply their sensitivity by using a variety of case studies, attempting to reduce computation times to permit greater use of such methods in real time and proposing measures of risk alternative to the standard loss expectation that can more readily accommodate complex, multivariate processes and budgetary or political constraints.

Finally it is noteworthy that all the developments presented here for snow avalanches are, in essence, usable for a wide range of natural hazards including all other rapid mass movements. For instance, similar developments have been recently proposed for rock falls, including modelling different variability and uncertainty sources (Bourrier

et al., 2009), quantifying physical vulnerability of structures/buildings using numerical simulation campaigns (Mavrouli and Corominas, 2010a; 2010b) and integrating the different sub-models in a formal risk framework (Agliardi et al., 2009). Even the hydrological community, from which inspiration has been taken at the beginning of risk implementations in the avalanche field, could benefit in turn from the experience acquired. This is particularly the case for statistical–dynamical simulations including rainfall-runoff models that try to mimetic the variability of damageable floods with reasonable physical realism (e.g. Kuczera and Parent, 1998). Hence, idea exchange/transfer between the different communities could be initiated/pursued with mutual benefit.

Acknowledgements

This work was mainly achieved in the framework of the MOPERA project funded by the French National Research Agency (ANR-09-RISK-007-01). For the French/British exchanges, it has benefited from the support of the British Council and the French *Ministère des Affaires Etrangères et Européennes*. Our statistical considerations have been sharpened by many personal communications from Jacques Bernier, retired research engineer from *Electricité de France*. Finally, the authors are grateful to the International Glaciological Society for allowing the reprint of Fig. 4, and to the anonymous referee that helped in improving the paper.

References

O' Hagan, A., Oakley, J., 2004. Probability is perfect, but we can't elicit it perfectly. Reliability Engineering and System Safety 85, 239–248.
Abraham, C., Cadre, B., 2004. Asymptotic global robustness in Bayesian decision theory. The Annals of Statistics 32, 1341–1366.
Agliardi, F., Crosta, G.B., Frattini, P., 2009. Integrating rockfall risk assessment and countermeasure design by 3D modelling techniques. Natural Hazards and Earth System Sciences 9, 1059–1073.
Allais, M., 1953. Le comportement de l'homme rationnel devant le risque : critique des postulats et axiomes de l'école américaine. Econometrica 21 (4), 503–546.
Allais, M., 1979. The so-called Allais paradox and rational decisions under uncertainty. In: Allais, M., Hagen, O. (Eds.), Expected Utility Hypotheses and the Allais Paradox. Reidel publishing, pp. 437–681.
Ammann, W.J., 2006. Risk concept, integral risk management and risk governance. In: Ammann, W.J., Dannenmann, S., Vuilliet, L. (Eds.), RISK 21 — Coping with Risks due to Natural Hazards in the 21st Century. Balkema Press, Rotterdam, pp. 3–23.
Ancey, C., 2005. Monte Carlo calibration of avalanches described as Coulomb fluid flows. Philosophical Transactions of the Royal Society of London, Series A 363, 1529–1550.
Ancey, C., Gervasoni, C., Meunier, M., 2004. Computing extreme avalanches. Cold Regions Science and Technology 39, 161–184.
Arnalds, P., Jonasson, K., Sigurdson, S.T., 2004. Avalanche hazard zoning in Iceland based on individual risk. Annals of Glaciology 38, 285–290.
Asprone, D., Jalayer, F., Prota, A., Manfredi, G., 2010. Proposal of a probabilistic model for multi-hazard risk assessment of structures in seismic zones subjected to blast for the limit state of collapse. Structural Safety 32, 25–34.
Barbolini, M., Keylock, C.J., 2002. A new method for avalanche hazard mapping using a combination of statistical and deterministic models. Natural Hazards and Earth System Sciences 2, 239–245.
Barbolini, M., Cappabianca, F., Savi, S., 2004a. Risk assessment in avalanche-prone areas. Annals of Glaciology 38, 115–122.
Barbolini, M., Cappabianca, F., Sailer, R., 2004b. Empirical estimate of vulnerability relations for use in snow avalanche risk assessment. In: Brebbia, C.A. (Ed.), Atti del Convegno Risk Analysis 2004, pp. 533–542. 27–29 Settembre, Rodi, Grecia.
Bartelt, P., Salm, B., Gruber, U., 1999. Calculating dense-snow avalanche runout using a Voellmy-fluid model with active/passive longitudinal straining. Journal of Glaciology 45, 242–254.
Berger, J.O., 1985. Statistical Decision Theory and Bayesian Analysis, Second edition. Springer-Verlag. 617 pp.
Bernier, J., 2003. Décisions et comportements des décideurs face au risque. Journal des Sciences Hydrologiques 48 (3), 301–316.
Bertrand, D., Bründl, M., Cappabianca, F., Chambon, G., Eckert, N., Faug, T., Fuchs, S., Naaim, F., 2008. Vulnerability to rapid mass movements. In: Naaim, M. (Ed.), Integral Risk Management of Extremely Rapid Mass Movements-IRASMOS, Delivrable 4. Sixth Framework Programme (2002–2006). 112 pp. available at: http://irasmos.slf.ch/results_wp4.htm.
Bertrand, D., Naaim, M., Brun, M., 2010. Physical vulnerability of reinforced concrete buildings impacted by snow avalanches. Natural Hazards and Earth System Science 10 (7), 1531–1545.
Blanchet, J., Lehning, M., 2010. Mapping snow depth return levels: smooth spatial modeling versus station interpolation. Hydrology and Earth System Sciences 7, 6129–6177.
Bonnevie, C., Berthet Rambaud, P., Nicot, F., 2003. Assessment of the vulnerability of masonry buildings subjected to avalanche loadings. Ingénieries-EAT. Numéro spécial Risques naturels et aménagement du territoire, pp. 137–150.
Bourrier, F., Eckert, N., Nicot, F., Darve, F., 2009. Bayesian stochastic modeling of a spherical rock bouncing on a coarse soil. Natural Hazards and Earth System Sciences 9, 831–846.
Bozhinskiy, A.N., Nazarov, A.N., Chernouss, P.A., 2001. Avalanches: a probabilistic approach to modelling. Annals of Glaciology 32, 255–258.
Bründl, M., Etter, H.-J., Steiniger, M., Klingler, C., Rhyner, J., Ammann, W.J., 2004. IFKIS — a basis for managing avalanche risk in settlements and on roads in Switzerland. Natural Hazards and Earth System Sciences 4, 257–262.
Bründl, M., Romang, H.E., Bischof, N., Rheinberger, C.M., 2009. The risk concept and its application in natural hazard risk management in Switzerland. Natural Hazards and Earth System Sciences 9, 801–813.
Burkard, A., 1992. Composition of the avalanche risk. Université européenne d'été sur les risques naturels : neige et avalanches, Chamonix, 14–25 Septembre 1992: Cemagref publication, 1995, pp. 213–216.
Caccamo, P., Chanut, B., Faug, T., Bellot, H., Naaim-Bouvet, F., 2010. Small-scale laboratory tests on granular avalanches overflowing a flat obstacle: flow regimes, dead zone and induced forces. Proceedings of the EPFL Doctoral Conference in Mechanics.
Cappabianca, F., Barbolini, M., Natale, L., 2008. Snow avalanche risk assessment and mapping: a new method based on a combination of statistical analysis, avalanche dynamics simulation and empirically-based vulnerability relations integrated in a GIS platform. Cold Regions Science and Technology 54, 193–205.
Ceriani, E., 2010. La mitigazione del rischio in relazione al rapporto Costi/Benefici e alla valutazione di impatto ambientale. Université d' Eté des Risques Naturels. Module 10.1. 13–17 Septembre 2010. Les Deux Alpes, France. 13 pp. Availaible at http://www.obs.ujf-grenoble.fr/risknat/pages/universites/session2010.html.
Chanut, B., Faug, T., Naaim, M., 2010. Time varying force from dense granular avalanches on a wall. Physical Review E 82, 041302. doi:10.1103/PhysRevE.82.041302.
Chernouss, P.A., Fedorenko, Y., 2001. Application of statistical simulation for avalanche risk evaluation. Annals of Glaciology 32, 182–186.
Coles, S., 2001. An introduction to statistical modelling of extreme values. Springer Ed. 208 pp.
Durand, Y., Giraud, G., Brun, E., Merindol, L., Martin, E., 1999. A computer based system simulating snowpack structures as a tool for regional avalanche forecasting. Journal of Glaciology 45 (151), 469–484.
Eckert, N., Parent, E., Richard, D., 2007a. Revisiting statistical–topographical methods for avalanche predetermination: Bayesian modelling for runout distance predictive distribution. Cold Regions Science and Technology 49, 88–107.
Eckert, N., Parent, E., Belanger, L., Garcia, S., 2007b. Hierarchical modelling for spatial analysis of the number of avalanche occurrences at the scale of the township. Cold Regions Science and Technology 50, 97–112.
Eckert, N., Parent, E., Naaim, M., Richard, D., 2008a. Bayesian stochastic modelling for avalanche predetermination: from a general system framework to return period computations. Stochastic Environmental Research and Risk Assessment 22, 185–206.
Eckert, N., Parent, E., Faug, T., Naaim, M., 2008b. Optimal design under uncertainty of a passive defense structure against snow avalanches: from a general Bayesian framework to a simple analytical model. Natural Hazards and Earth System Sciences 8, 1067–1081.
Eckert, N., Parent, E., Faug, T., Naaim, M., 2009. Bayesian optimal design of an avalanche dam using a multivariate numerical avalanche model. Stochastic Environmental Research and Risk Assessment 23, 1123–1141.
Eckert, N., Naaim, M., Parent, E., 2010a. Long-term avalanche hazard assessment with a Bayesian depth-averaged propagation model. Journal of Glaciology 56 (198), 563–586.
Eckert, N., Parent, E., Kies, R., Baya, H., 2010b. A spatio-temporal modelling framework for assessing the fluctuations of avalanche occurrence resulting from climate change: application to 60 years of data in the northern French Alps. Climatic Change 101 (3–4), 515–553.
Eckert, N., Baya, H., Deschâtres, M., 2010c. Assessing the response of snow avalanche runout altitudes to climate fluctuations using hierarchical modeling: application to 61 winters of data in France. Journal of Climate 23, 3157–3180.
Ellingwood, B., 2001. Earthquake risk assessment of building structures. Reliability Engineering and System Safety 74, 251–262.
Embrechts, P., Kluppelberg, C., Mikosch, T., 1997. Modelling Extremal Events: for Insurance and Finance. Springer Ed. 648 pp.
Faug, T., Gauer, P., Lied, K., Naaim, M., 2008. Overrun length of avalanches overtopping catching dams: cross-comparison of small-scale laboratory experiments and observations from full-scale avalanches. Journal of Geophysical Research 113, F03009. doi:10.1029/2007JF000854.
Faug, T., Beguin, R., Chanut, B., 2009. Mean steady granular force on a wall overflowed by free-surface gravity-driven dense flows. Physical Review E 80, 021305. doi:10.1103/PhysRevE.80.021305.
Frangopol, D., Ide, Y., Spacone, E., Iwaki, I., 1996. A new look at reliability of reinforced concrete columns. Structural Safety 18, 123–150.
Fuchs, S., 2009. Susceptibility versus resilience to mountain hazards in Austria — paradigms of vulnerability revisited. Natural Hazards and Earth System Sciences 9, 337–352.
Fuchs, S., Bründl, M., 2005. Damage potential and losses resulting from snow avalanches in settlements in the Canton of Grisons, Switzerland. Natural Hazards 34, 53–69.
Fuchs, S., McAlpin, M.C., 2005. The net benefit of public expenditures on avalanche defense structures in the municipality of Davos, Switzerland. Natural Hazards and Earth System Sciences 5, 319–330.

Fuchs, S., Bründl, M., Stötter, J., 2004. Development of avalanche risk between 1950 and 2000 in the municipality of Davos, Switzerland. Natural Hazards and Earth System Sciences 4, 263–275.
Fuchs, S., Keiler, M., Zischg, A., Bründl, M., 2005. The long-term development of avalanche risk in settlements considering the temporal variability of damage potential. Natural Hazards and Earth System Sciences 5, 893–901.
Fuchs, S., Thöni, M., McAlpin, M.C., Gruber, U., Bründl, M., 2007. Avalanche hazard mitigation strategies assessed by cost effectiveness analyses and cost benefit analyses — evidence from Davos, Switzerland. Natural Hazards 41 (1), 113–129.
Gassner, M., Brabec, B., 2002. Nearest neighbour models for local and regional avalanche forecasting. Natural Hazards and Earth System Sciences 2, 247–253.
Grêt-Regamey, A., Straub, D., 2006. Spatially explicit avalanche risk assessment linking Bayesian networks to a GIS. Natural Hazards and Earth System Sciences 6, 911–926.
Grímsdóttir, H., McClung, D., 2006. Avalanche risk during backcountry skiing — an analysis of risk factors. Natural Hazards 39, 127–153.
Harbitz, C., Harbitz, A., Farrokh, N., 2001. On probability analysis in snow avalanche hazard zoning. Annals of Glaciology 32, 290–298.
Hendrikx, J., Owens, I., 2008. Modified avalanche risk equations to account for waiting traffic on avalanche prone roads. Cold Regions Science and Technology 51, 214–218.
IUGS, 1997. Quantitative risk assessment for slopes and landslides — the state of the art. In: Cruden, D.M., Fell, R., Balkema, A.A. (Eds.), Landslide Risk Assessment, Proceedings of the International Workshop on Landslide Risk Assessment, 19–21 Feb. 1997, Honolulu, Hawaii, pp. 3–12. Rotterdam, The Netherlands.
Johannesson, T., Arnalds, T., 2001. Accidents and economic damage due to snow avalanches and landslides in Iceland. Jokull 50, 81–94.
Jonasson, K., Sigurdson, S.T., Arnalds, P., 1999. Estimation of avalanche risk. Vedurstofu Islands. Reykjavik. VI-R99001-UR01. 44 pp.
Jordaan, I., 2005. Decisions Under Uncertainty: Probabilistic Analysis for Engineering Decisions. Cambridge University Press. 672 pp.
Kadane, J., 2011. Principles of uncertainty. Texts in Statistical Science. Chapman & Hall. 475 pp.
Kadane, J.B., Wolfson, D.B., 1998. Experiences in elicitation. The Statistician 47, 1–20.
Keeney, R.L., Raiffa, H., 1976. Decisions with Multiple Objectives: Preferences and Value Tradeoffs. J. Wiley, New York. 569 pp.
Keiler, M., 2004. Development of the damage potential resulting from avalanche risk in the period 1950–2000, case study Galtür. Natural Hazards and Earth System Sciences 4, 249–256.
Keiler, M., Zischg, A., Fuchs, S., Hama, M., Stötter, J., 2005. Avalanche related damage potential — changes of persons and mobile values since the mid-twentieth century, case study Galtür. Natural Hazards and Earth System Sciences 5, 49–58.
Keiler, M., Sailer, R., Jörg, P., Weber, C., Fuchs, S., Zischg, A., Sauermoser, S., 2006. Avalanche risk assessment — a multi-temporal approach, results from Galtür, Austria. Natural Hazards and Earth System Sciences 6, 637–651.
Kennedy, M.C., O'Hagan, A., 2001. Bayesian calibration of computer models. Journal of the Royal Statistical Society. Series B. Methodological 63, 425–464.
Keylock, C.J., 2003. The North Atlantic Oscillation and snow avalanching in Iceland. Geophysical Research Letters 30 (5), 1254. doi:10.1029/2002GL016272.
Keylock, C.J., 2005. An alternative form for the statistical distribution of extreme avalanche runout distances. Cold Regions Science and Technology 42, 185–193.
Keylock, C.J., Barbolini, M., 2001. Snow avalanche impact pressure — vulnerability relations for use in risk assessment. Canadian Geotechnical Journal 38, 227–238.
Keylock, C.J., McClung, D., Magnusson, M., 1999. Avalanche risk mapping by simulation. Journal of Glaciology 45 (150), 303–314.
Kristensen, K., Harbitz, C.B., Harbitz, A., 2003. Road traffic and avalanches — methods for risk evaluation and risk management. Surveys in Geophysics 24 (5–6), 603–616.
Kuczera, G., Parent, E., 1998. Monte Carlo assessment of parameter uncertainty in conceptual catchment models: the Metropolis algorithm. Journal of Hydrology 211 (1–4), 69–85.
Kyung, H., Rosowsky, D., 2006. Fragility analysis of woodframe buildings considering combined snow and earthquake loading. Structural Safety 28, 289–303.
Lagaros, N., 2008. Probabilistic fragility analysis: a tool for assessing design rules of RC buildings. Earthquake Engineering and Engineering Vibration 7, 45–56.
Landsman, Z., Sherris, M., 2001. Risk measures and insurance premium principles. Insurance: Mathematics and Economics 29, 103–115.
Lazar, B., Williams, M., 2008. Climate change in western ski areas: potential changes in the timing of wet avalanches and snow quality for the Aspen ski area in the years 2030 and 2100. Cold Regions Science and Technology 51 (2–3), 219–228.
Lee, T., Mosalam, M., 2004. Probabilistic fiber element modeling of reinforced concrete structure. Computers and Structures 82, 2285–2299.
Lemaire, M., 2009. Structural Reliability. ISTE/Wiley ed. 488 pp.
Lied, K., Bakkehoi, S., 1980. Empirical calculations of snow-avalanche run-out distances based on topographic parameters. Journal of Glaciology 26 (94), 165–176.
López-Moreno, J.I., Goyette, S., Beniston, M., 2009. Impact of climate change on snowpack in the Pyrenees: horizontal spatial variability and vertical gradients. Journal of Hydrology 374 (3–4), 384–396.
Low, H., Hoa, H., 2001. Reliability analysis of reinforced concrete slabs under explosive loadings. Structural Safety 23, 157–178.
Lu, R., Luo, Y., Conte, J., 1994. Reliability evaluation of reinforced concrete beams. Structural Safety 14, 277–298.
Machina, M.J., 1982. Expected utility without the independence axiom. Econometrica 50, 277–323.
Machina, M.J., 1987. Choice under uncertainty: problems solved and unsolved. The Journal of Economic Perspectives 1 (1), 121–154.
Margreth, S., Stoffel, L., Wilhelm, C., 2003. Winter opening of high alpine pass roads — analysis and case studies from the Swiss Alps. Cold Regions Science and Technology. 37 (3), 467–482.
Martin, E., Giraud, G., Lejeune, Y., Boudart, G., 2001. Impact of climate change on avalanche hazard. Annals of Glaciology 32, 163–167.
Mavrouli, O., Corominas, J., 2010a. Vulnerability of simple reinforced concrete buildings to damage by rockfalls. Landslides 7, 169–180.
Mavrouli, O., Corominas, J., 2010b. Rockfall vulnerability assessment for reinforced concrete buildings. Natural Hazards and Earth System Sciences 10, 2055–2066.
McCammon, I., Hägeli, P., 2007. An evaluation of rule-based decision tools for travel in avalanche terrain. Cold Regions Science and Technology 47 (1–2), 193–206.
McClung, D., 2005. Risk-based definition of zones for land-use planning in snow avalanche terrain. Canadian Geotechnical Journal 42, 1030–1038.
McClung, D., Lied, K., 1987. Statistical and geometrical definition of snow-avalanche runout. Cold Regions Science and Technology 13, 107–119.
McClung, D., Tweedy, J., 1994. Numerical avalanche prediction: Kootenay Pass, British Columbia, Canada. Journal of Glaciology 40 (135), 350–358.
McCollister, C., Birkeland, K., Hansen, K., Aspinall, R., Comey, R., 2003. Exploring multiscale spatial patterns in historical avalanche data, Jackson Hole Mountain Resort, Wyoming. Cold Regions Science and Technology 37, 299–313.
Meunier, M., Ancey, C., 2004. Towards a conceptual approach to predetermining high-return-period avalanche run-out distances. Journal of Glaciology 50 (169), 268–278.
Munier, B., 1988. Risk, Decision and Rationality. Reidel Publishing Company, Dordrecht. 707 pp.
Munter, W., 1992. Neue Lawinenkunde: Ein Leitfaden für die Praxis. Verlag des SAC, Bern, Switzerland.
Naaim, M., Naaim-Bouvet, F., Faug, T., Bouchet, A., 2004. Dense snow avalanche modelling: flow, erosion, deposition and obstacle effects. Cold Regions Science and Technology 39, 193–204.
Naaim, M., Faug, T., Thibert, E., Eckert, N., Chambon, G., Naaim, F., 2008. Snow avalanche pressure on obstacles. Proceedings of the International Snow Science Workshop. Whistler. Canada. September 21st–28th 2008.
Naaim, M., Faug, T., Naaim, F., Eckert, N., 2010. Return period calculation and passive structure design at Taconnaz avalanche path, France. Annals of Glaciology 51 (54), 89–97.
Papadrakis, M., Papadopoulos, V., Lagaros, D., 1996. Structural reliability analysis of elastic–plastic structures using neural networks and Monte Carlo simulation. Computer Methods In Applied Mechanics and Engineering 136, 145–163.
Papathoma-Köhle, M., Kappes, M., Keiler, M., Glade, T., 2011. Physical vulnerability assessment for alpine hazards: state of the art and future needs. Natural Hazards 58, 645–680.
Parent, E., Bernier, J., 2003. Bayesian P.O.T. modelling for historical data. Journal of Hydrology 274, 95–108.
Parent, E., Pasanisi, A., Keller, M., Bousquet, N., Bernier, J., 2010. Considérations décisionnelles pour la construction d'un ouvrage de protection contre les crues. Luminy, France. 37 pp.
Park, J., Towashiraporn, P., Craig, J., Goodno, B., 2009. Seismic fragility analysis of low-rise unreinforced masonry structures. Engineering Structures 31, 125–137.
Perla, R., Cheng, T., Mc Clung, D., 1980. A two-parameter model of snow-avalanche motion. Journal of Glaciology 26, 197–207.
Pfeifer, C., 2009. On probabilities of avalanches triggered by alpine skiers. An empirically driven decision strategy for backcountry skiers based on these probabilities. Natural Hazards 48 (3), 425–438.
Piattelli-Palmarini, M., 1995. La réforme du jugement: ou comment ne plus se tromper, Odile Jacob ed. . 273 pp.
Pickands, J., 1975. Statistical inference using extreme order statistics. The Annals of Statistics 3, 11–130.
Pratt, J.W., Raiffa, H., Schlaifer, R., 1964. The foundations of decision under uncertainty: an elementary exposition. Journal of the American Statistical Association 59 (306), 353–375.
Quiggin, J., 1982. A theory of anticipated utility. Journal Of Economic Behavior and Organization 3, 323–343.
Raiffa, H., 1968. Decision Analysis — Introductory Lectures on Choices under Uncertainty. Addison Wesley, Reading, MA. 309 pp.
Räisänen, J., 2008. Warmer climate: less or more snow? Climate Dynamics 30, 307–319.
Rheinberger, C., Bründl, M., Rhyner, J., 2009. Dealing with the White Death: avalanche risk management for traffic routes. Risk Analysis 29 (1), 76–94.
Rizzano, G., Tolone, I., 2009. Seismic assessment of existing RC frames: probabilistic approach. Journal of Structural Engineering 135 (7), 836–852.
Ruiz-Garcia, J., Miranda, E., 2010. Probabilistic estimation of residual drift demands for seismic assessment of multi-story framed buildings. Engineering Structures 32, 11–20.
Sacks, J., Welch, W.J., Mitchell, T.J., Wynn, H.P., 1989. Design and analysis of computer experiments. Statistical Science 4, 409–423.
Salm, B., Burkard, A., Gubler, H.U., 1990. Berechnung von Fliesslawinen : eine Anleitung für Praktiker mit Beispilen. SLF Davos technical report 47.
Schaerer, P., 1989. The avalanche hazard index. Annals of Glaciology 13, 241–247.
Sigurdsson, S., Jonasson, K., Arnalds, K., 1998. Transferring avalanches between paths. Proceedings of the anniversary conference 25 years of snow avalanche research, Voss, 12–16 May. Norwegian Geotechnical Institute Publication, 203, pp. 259–263.
Sovilla, B., Schaer, M., Kern, M., Bartelt, P., 2008. Impact pressures and flow regimes in dense snow avalanches observed at the Vallée de la Sionne test site. Journal of Geophysical Research 113, F01010. doi:10.1029/2006JF000688.
Thibert, E., Baroudi, D., Limam, A., Berthet-Rambaud, P., 2008. Avalanche impact pressure on an instrumented structure. Cold Regions Science and Technology 54 (3), 206–215.

Tvesky, A., Kahneman, D., 1992. Advances in prospect theory: cumulative representation of uncertainty. Journal of Risk and Uncertainty 5, 297–321.
Van Dantzig, D., 1956. Economic decision problems for flood prevention. Econometrica 24 (3), 276–287.
Von Neumann, J., Morgenstern, O., 1953. Theory of Games and Economic Behaviour. Princeton University Press, New Jersey, USA.
Wald, A., 1950. Statistical Decision Functions. Wiley ed. 179 pp.
Wastl, M., Stötter, J., Kleindienst, H., 2011. Avalanche risk assessment for mountain roads: a case study from Iceland. Natural Hazards 56, 465–480.
Wilhelm, C., 1997. Wirtschaftlichkeit im Lawinenschutz. Methodik und Erhebungen zur Beurteilung von Schutzmassnahmen mittels quantitativer Risikoanalyse und ökonomischer Bewertung: Mitt. Eidgenöss. Inst. Schnee- Lawinenforsch, 54, pp. 1–309.
Wilhelm, C., 1998. Quantitative risk analysis for evaluation of avalanche protection projects. Proc. of 25 Years of Snow Avalanche Research, Voss, Norway, 12–16 May 1998: Norwegian Geotechnical Institute Publications, 203, pp. 288–293.
Wisner, B., Blaikie, P., Cannon, T., Davis, I., 2004. At Risk: Natural Hazards, People's Vulnerability and Disasters, 2nd ed. Routledge, London. 124 pp.
Zischg, A., Fuchs, S., Keiler, M., Stötter, J., 2005a. Temporal variability of damage potential on roads as a conceptual contribution towards a short-term avalanche risk simulation. Natural Hazards and Earth System Sciences 5, 235–242.
Zischg, A., Fuchs, S., Keiler, M., Meißl, G., 2005b. Modelling the system behaviour of wet snow avalanches using an expert system approach for risk management on high alpine traffic road. Natural Hazards and Earth System Sciences 5, 821–832.